UNIVERSITÀ DI PARMA

Università degli Studi di Parma

Dottorato di Ricerca in Tecnologie dell'Informazione

XXXI Ciclo

NUMERICAL SIMULATION OF HIGH-EFFICIENCY CIGS-BASED SOLAR CELLS

Coordinatore:

Chiar.mo Prof. Marco Locatelli

Tutor:

Chiar.ma Prof.ssa Giovanna Sozzi

Chiar.mo Prof. Roberto Menozzi

Dottorando: *Simone Di Napoli*

Anni 2015/2018

To my family...

Contents

List of Figures

Introduction

In the future the energy demand will increase more and more; to supply that, new sources of energy must be explored.

The close link between the socio-economic development and the exploitation of every form of energy present on our planet is evident. However, the resulting progress represents the only good news and in fact this unlimited abuse involves in a wrong way everything that surrounds us. The continuous increment of people and the consequent raise of energy demand lead to a progressive boost of environmental pollution.

One of the most important effects caused by this increase is the *Climate Change*, in particular the raise of temperature due to the growing accumulation of greenhouse gases in the atmosphere.

To address these issues, in December 1997 the United Nations Framework Convention on Climate Change (UNFCCC) drafted the Kyoto Protocol that set targets for reducing greenhouse gas emissions for industrialized countries. By signing this document the European Community promised the emission reduction of 8.65% respect to the emission recorded in 1985, considered as the base year, in the period 2008-2012.

For the period following the end of the Kyoto Protocol the European Union has established a set of measures with the Directive 2009/29/EC: the 20 20 20 Plan. The objectives set are three:

- reduce emissions by 20% of greenhouse gases (CO_2);
- increase the share of energy produced from renewable sources to 20%;
- bring energy savings to 20% respect the 1990;

all these goals must be reached within the 2020.

Cooperation to reduce climate change was improved in 2015 in Paris, where an ONU international meeting was held in which a further agreement was stipulated to limit the increase in temperature to 1.5 celsius degrees compared to the pre-industrial era. Moreover, since 2020, the countries of old industrialization have become available to provide one hundred billion a year to spread green energy all over the world and "decarbonise" the economy.This is a very important step because at the moment most of the energy production in the world is obtained using fossil fuels, but this type of sources are not renewable and they are running out; some experts have estimated the exhaustion of resources in about forty years.

The ultimate goal of all these agreements is to oppose the continuous climate change and preserve the well-being of the planet by promoting the use of renewable energy sources, through the achievement of binding targets for the countries of the European Union. This strong push towards the use of green energy sources has led industries, research centers and universities to work to improve the efficiency of systems, in order to reduce the cost of energy generated from renewable sources which is currently higher than that energy derived from fossil fuel.

Most of the investments in renewable energy concern the photovoltaic field with the aim of improving the efficiency of solar cells and reducing costs. The thin-film technology for solar cells fits in this context: in fact they use less material than normal cells and in general require a much smaller amount of energy to be manufactured but on the other hand they are less efficient. One of the most promising materials used for the realization of thin-film solar cells is the $Cu(In_{1-x}Ga_x)Se_2$ ($CIGS$). It has the potential to be produced by European industry at lower costs while yielding comparable efficiency to the more classical silicon-based solar cell.

This is demonstrated by Swiss Federal Laboratories for Materials Science and Technology (EMPA) which holds the record efficiency of 20.4% [1] for solar cells on a flexible plastic film, and Zentrum für Sonnenenergie-und Wasserstoff-Forschung Baden-Württemberg (ZSW) which held the record efficiency of 22.6% [2] for cells on rigid glass substrate. Recently ZSW has been surpassed by Solar Frontier with the actual record of 22.9% [26] for cells on rigid glass substrate.

All these structures are comparable with Silicon based solar cells.

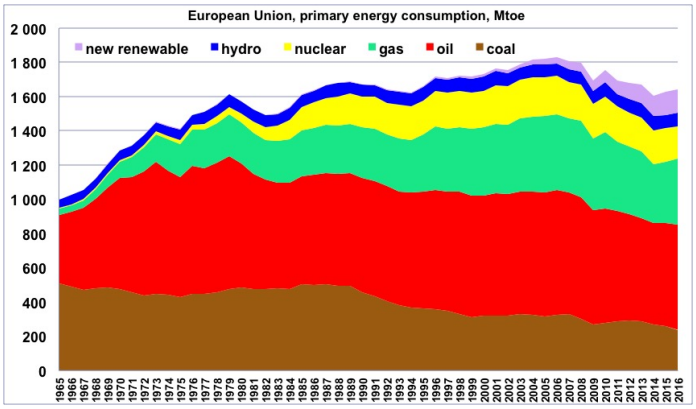

Figure 1: The energy consumption of the European Union is shown in this graph, it is possible to notice that in recent years the use of fossil fuels is decreasing, whereas that of renewable energy is increasing [3]

These CIGS record efficiencies identify the CIGS photovoltaic technology as a prime candidate for meeting the cost and performance criteria for a next generation photovoltaic technology, which ultimately will contribute to the backbone of Europe's electricity sources in the future.

To stimulate research, the European Union has launched a funding program (Horizon 2020) for innovative projects through the European Commission. Sharch25 is one of the projects that have been financed and the Department of Engineering and Architecture (DIA) of University of Parma has been directly involved. The goal of the project was to develop thin-film CIGS solar cells with a 25% efficiency within three years (2015-2018).

This thesis aims to quantitatively identify and study through numerical simulations the main factors that limit the state of the art of the performance of CIGS solar cells and develop new solutions aimed at increasing the efficiency of this type of solar cells.

One of the studied factors is the Post Deposition Treatment with Alkali fluorides because it has significantly improved the performance of CIGS solar cells, playing a major role in the achievement of efficiencies above 20%. Although the mechanisms

responsible for this efficiency improvements are not completely clear yet, the beneficial effects of PDT have been associated to modified properties of the *CIGS* surface directly affecting the optoelectronic properties at the *p-n* junction and providing better surface for subsequent buffer layer deposition, as well as to improved bulk properties. The studied effects of variations of bulk or interfaces properties,presented in this thesis, can be also useful to understand the possible impact of alkali post deposition treatments on the cell performance.

In the first chapter the behavior of solar cells is presented with particular attention to those with thin films, and a first mention is made of the CIGS material. Then in the second, the two record cells (EMPA, ZSW) on which the whole thesis is based are shown and the Synopsys Sentaurus TCAD software used for all the simulations is presented. In the third chapter the behavior of the CIGS semiconductor and its properties are studied in depth with the help of the simulations. The fourth chapter is completely dedicated to the limiting factors of the performance of CIGS solar cells. Finally, new solutions to increase cell efficiency are presented in chapter five, focusing attention on the study of the effects of passivation and light management.

Chapter 1

Solar Cells

In this chapter the photovoltaic effect and the solar cells behavior will be described, starting from the simple p-n junction. It will be analyzed the classical Silicon-based solar cells with particular attention to the thin film, also will be showed the CIGS and its potentiality. In addiction a description of the solar cells circuit model and of the figures of merit will be made.

1.1 Photovoltaic Effect

The description of solar cells starts from the photovoltaic effect that was discovered by the French physicist Edmond Bequerel in 1839 [4]; he verified the direct conversion of light radiation into electrical energy by detecting how the intensity of the current in an electrolytic cell increased with direct exposure to the Sun. These studies together with those of Hertz in 1887 [5] showed to the scientific community the singular properties of semiconductors and in particular of silicon.

In 1954 the first silicon solar cell was produced in the Bell laboratory [6]; the high cost, however, limited its application to the space sector, where reliable and inexhaustible sources of energy were required. In recent decades, photovoltaic technology has spread very rapidly even for terrestrial applications, to meet the energy needs of isolated users, and also to provide additional energy to buildings already connected

to a pre-existing electricity grid.

The behavior of all the photovoltaic devices is based on a junction between a p-doped and a n-doped semiconductors, of the same (homojunction cells) or different (heterojunction cells) material. The energy production of these p-n junctions is strictly related to the photovoltaic effect: this physical phenomenon occurs when an electron in the valence band of a semiconductor moves into the conduction band thanks to the absorption of a photon incident on the material. Photons in the solar radiation have different energies:

$$E_{ph} = \frac{hc}{\lambda} \tag{1.1}$$

where:

- h is the Plank constant ($6.626 \cdot 10^{-34}$ $[Js]$);
- c is the speed of light in the vacuum ($2.99792458 \cdot 10^{8}$ $[\frac{m}{s}]$);
- λ is the wavelength of the photon $[m]$;
- E_{ph} is the photon energy $[J]$;

From the formula (1.1) it is possible to note that photons with different wavelength have different energy: high λ means low energy and low λ means high energy. This is very important to know because the transfer of energy from the electromagnetic field to the matter takes place only in a discrete way; indeed, if the photon as enough energy it is absorbed and excites an electron into the conduction band. When the energy of an incident photon is equal to or greater than the band gap of the material, it is absorbed by the material and excites an electron into the conduction band.

The absorption coefficient determines how far a photon of a particular wavelength can penetrate into a material before it is absorbed.

$$\alpha = \frac{4\pi k}{\lambda} \tag{1.2}$$

where:

- k is the extinction coefficient of the material;

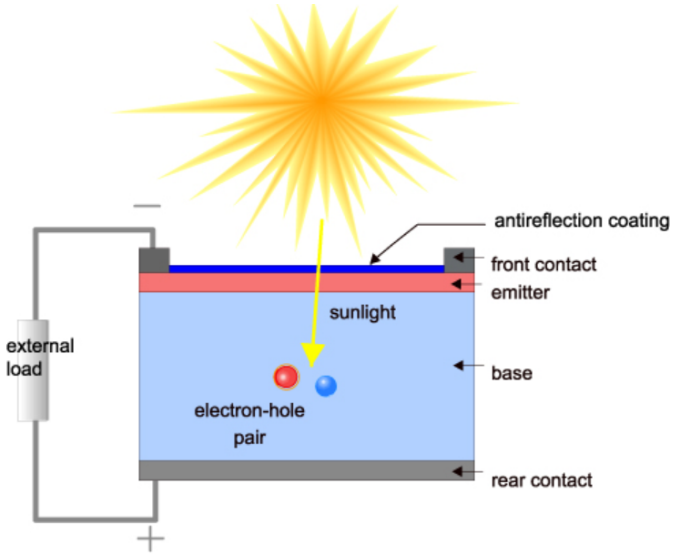

Figure 1.1: Rapresentation of photovoltaic effect [7]

- λ is the wavelength of the photon $[m]$;

In a material with low absorption coefficient for a wavelength, photons with this λ are scarcely absorbed and if the material is thin enough it could be transparent to that wavelength. The absorption coefficient depends on the material and also on the wavelength: semiconductors have large absorption coefficient for wavelengths corresponding to energies larger than or equal to the energy gap of the material.

As described before the photon absorption generates an electron-hole pair so that in order to have a separation of the charges and therefore a current, an electric field is required which is provided by the p-n junction which is at the base of all photovoltaic devices.

1.2 Theory of p-n junction

In this section the behavior of a p-n junction will be shown, only the homojunction case will be analyzed (same material for the two regions) but similar formulas can be

used for a heterojunction.

A p-n junction is composed by a p-doped region and a n-doped region, the p-type region has a high hole concentration while the n-type has a high electron concentration. The union of these two region, in particular the strong difference in doping, causes the diffusion of free carriers in the semiconductor thus generating a diffusion current. The diffused carriers leave the ionized atoms of the dopants unbalanced by establishing a potential difference and therefore an electric field between the positive ion cores in the n-type material and negative ion cores in the p-type material. An electric field builds up around the junction "depletion region", where free carriers are swept away so that this part of the structure is depleted.

The profiles of charge density, electric field and electric potential are showed in Figure 1.2: the electric field drives the holes towards p-region and the electrons towards the n-region. At the edges of the space charge region a potential difference called built-in voltage is then established. Under the following assumptions:

- complete ionization of dopant;
- complete depletion of space charge region;
- negligible voltage drop in the neutral region.

it is possible to calculate the built-in voltage:

$$\phi_{BI} = \frac{kT}{q} ln \left(\frac{N_D N_A}{n_i^2} \right) \tag{1.3}$$

where:

- k is the Boltzmann constant ($1.38 \cdot 10^{-23} [JK^{-1}]$);
- T is the temperature;
- q is the electron charge ($1.6 \cdot 10^{-19} [C]$);
- N_D is the concentration of donors in the n-region $[cm^{-3}]$;
- N_A is the concentration of acceptors in the p-region $[cm^{-3}]$;

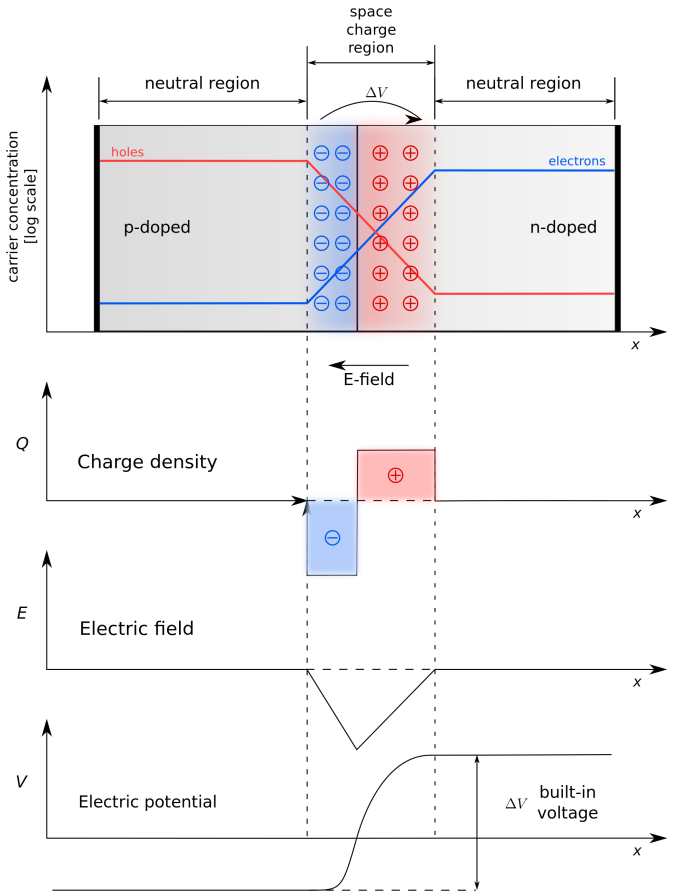

Figure 1.2: Charge density, electric field and electric potential versus depth inside the p-n junction [8]

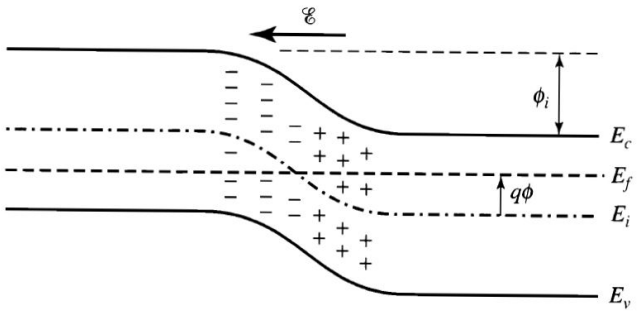

Figure 1.3: Band diagram of a p-n junction [9]

- n_i is the intrinsic concentration of carriers $[cm^{-3}]$.

The thermodynamic equilibrium is reached when the Fermi level is constant throughout the structure as shown in Figure 1.3.

Solving the Poisson equation it is possible to calculate the extension of the depletion region in the p-side and the n-side of the junction:

$$x_p = \sqrt{\frac{2\varepsilon}{qN_A}\left(1+\frac{N_A}{N_D}\right)^{-1}\phi_{BI}} \tag{1.4}$$

$$x_n = \sqrt{\frac{2\varepsilon}{qN_D}\left(1+\frac{N_D}{N_A}\right)^{-1}\phi_{BI}} \tag{1.5}$$

where:

- ε is the dielectric constant of the semiconductor $\left[\frac{F}{cm}\right]$.

1.3 Silicon based solar cells

The most produced solar cell is a p-n junction made of silicon (homojunction). Silicon is the semiconductor most used for its good attitude to processing, refining and doping; another advantage is its abundance and the possibility of being recycled

by the photovoltaic industry. Depending on the application, the silicon can be monocrystalline (it is the same material used for electronic components) or polycrystalline (this is characterized by lower efficiencies but at a lower cost) and even amorphous.

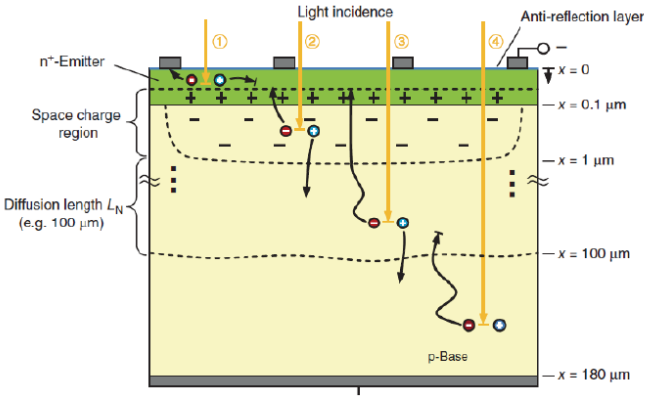

Figure 1.4: A classical silicon solar cell is shown and the four possible regions where photons could be absorbed [7]

An example of silicon based solar cell is showed in Figure 1.4: from the top to the bottom of the structure there are the n^+-region, which is called emitter, and the p-region with a doping of several orders of magnitude lower. Due to the difference of doping the depletion region lies almost completely inside the p-region.

On the top of the cell there is a metallic grid with two different scopes: make the contact with the external world and collect the electrons. This grid results from the compromise between the need of small contact resistance and narrow shadow regions. At the bottom, instead, problems of shadow does not exist and the contact is made by metalizing the whole surface.

Photons enter the cell from the top and they are absorbed at different depth depending on their wavelength however, if the energy is too low they can pass through all the cell. Photons with a high energy have a reduced absorption depth, and therefore generate in the highest part of the cell; gradually, moving downwards, the less energetic ones are absorbed.

The absorption of a photon and the consequent generation of an electron-hole pair

can take place in four different region as illustrated in Figure 1.4.

In the first case the generation take place in the neutral n^+-region, the generated electron can be collected by the front contact instead the hole, which is a minority carrier in that region, should reach the back contact instead it will recombine in the emitter region. In this case the generated carriers do not contribute to the overall current, and photons absorbed in this region must be minimized.

The best case is the second one because the absorption and consequent generation take place in the depletion region. The electric field present in this part of the structure separates the carriers: electrons are collected at front contact and hole are accelerated towards the back contact. In this region the number of absorbed photon must be maximized, because of the low recombination probability of generated carriers.

Towards the back of the cell, the region that extends from the end of the depletion region to a distance equal to the diffusion length of the electrons, L_N, within the p-doped region is considered to be the generation zone. The diffusion length is the distance that minority carriers can travel before recombining and can be calculated as:

$$L_N = \sqrt{D_N \tau_N} \tag{1.6}$$

where:

- D_N is the diffusivity coefficient of electrons within the p-region $\left[\frac{cm^2}{s}\right]$;
- τ_N is the lifetime of electrons inside the p-region [s].

In this part of the structure, therefore, the generated electrons can reach the depletion region where they are driven by the electric field towards the front contact, while holes are easily collected by the back contact.

In the region near to the back contact, the generated carriers do not contribute to the photo-generated current because the holes are collected while electrons, which are minority carriers, recombine.

1.4 Solar cells circuit model

The solar cell can be electrically modeled as follows:

- a diode (classical p-n junction as described previously) whose current is the only contribution in the case of a non-illuminated cell, therefore called "dark current" (Figure 1.5 (a));
- a current generator to model the photo-generated current in parallel with the previous diode. The I-V curve is shifted down into the fourth quadrant where power can be extracted from the diode (the larger the light intensity the larger is the shift Figure 1.5 (b));
- a shunt resistor R_{sh} to model the parasitic effect due to the structure;
- a series resistor R_s intrinsic of the cell.

The resulting circuit is shown in Figure 1.6. The total output current is the difference between photo-generated and dark current:

$$J_{light} = J_{Photo} - J_{Diode} \tag{1.7}$$

where J_{Diode} is the classical current of a diode:

$$J_{Diode} = J_0 \left(e^{\frac{qV}{kT}} - 1 \right) \tag{1.8}$$

and J_{Photo} is the photo-generated current; these two currents depend on both the illumination density and the applied voltage [10].

1.5 Figures of merit

The main figures of merit of a solar cell [11] are: the short circuit current (I_{SC}), the open circuit voltage (V_{OC}), the Fill Factor (FF) and the efficiency (η).

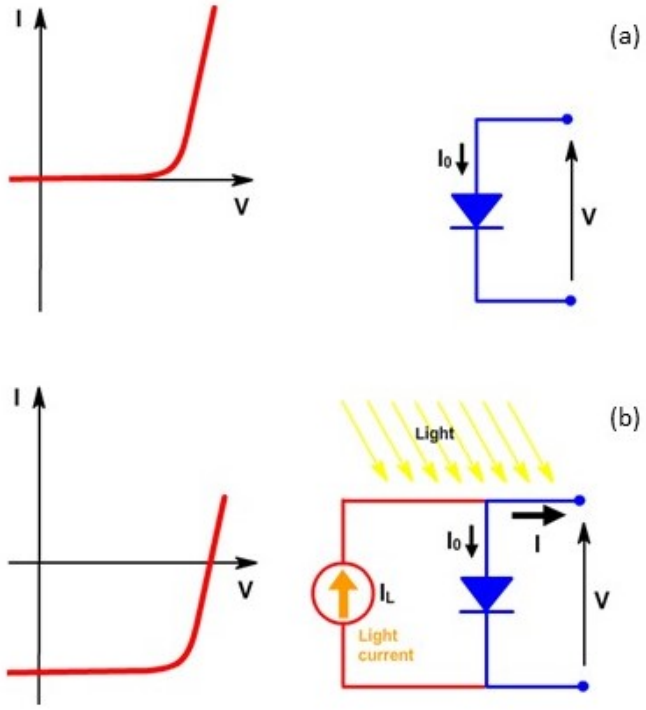

Figure 1.5: Solar cell I-V characteristics: (a) in dark where only the "dark current" is present; (b) under light. [7]

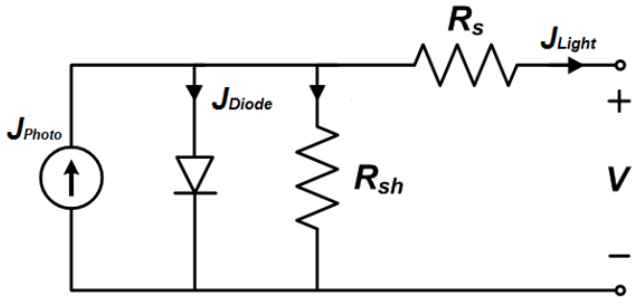

Figure 1.6: One diode equivalent circuit of a solar cell

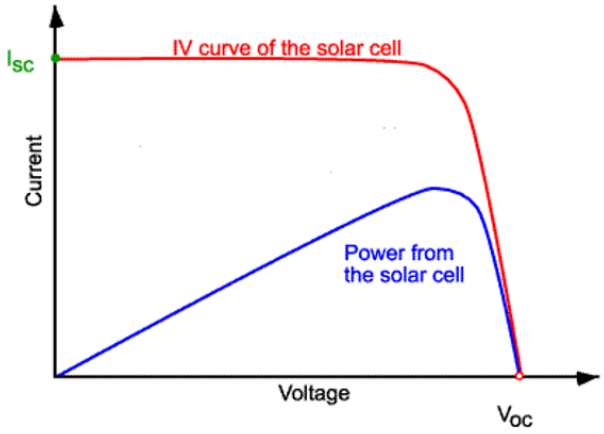

Figure 1.7: In this graph are shown the I-V characteristic (red line) and the generated power (blu line).

All these parameters are of fundamental importance to understand how much the cell is optimized for the conversion of solar energy and they can be derived from the IV characteristic shown in Figure 1.7.

The short circuit current is defined as maximum current flowing in a solar cell under illumination, occurs when the voltage across the device is zero; in an ideal cell this current correspond to the photo-generated one. The I_{SC} is mainly influenced by several factors including: portion of cell area that is illuminated, power of the incident radiation and correct collection of the generated carriers.

The open circuit voltage is the maximum voltage that can be obtained from a solar cell and occurs when the current is zero. The fill factor is defined as the ratio between the maximum power generated, P_{MPP}, by the cell and the product between I_{SC} and V_{OC}.

$$FF = \frac{P_{MPP}}{I_{SC}V_{OC}} \tag{1.9}$$

From the I-V curve, shown in Figure 1.8, is also possible to identify the P_{MPP} and it can be expressed as:

$$P_{MPP} = V_{MPP} \cdot I_{MPP} \tag{1.10}$$

where I_{MPP} and V_{MPP} are respectively the current and the voltage at the maximum power point.

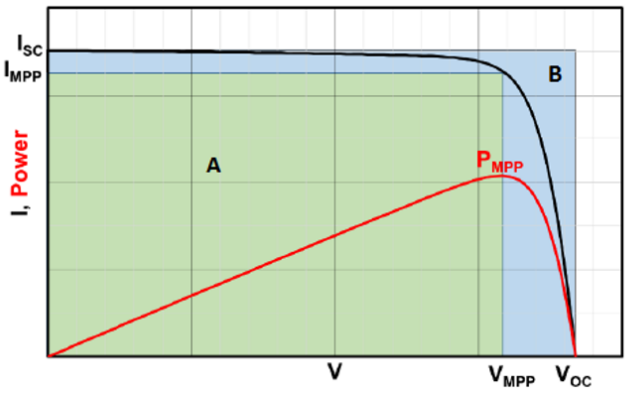

Figure 1.8: Maximum Power Point P_{MPP} and correspondly voltage V_{MPP} and current I_{MPP}.

Finally the efficiency of the solar cell (η) is defined as the ratio between the produced energy and the input energy supplied by the sun.

$$\eta = \frac{I_{SC} V_{OC} FF}{P_{in}} \tag{1.11}$$

where $I_{SC} V_{OC} FF$ is the maximum power output.

1.6 Thin film solar cell CIGS based

In recent years, another technology has entered the market, conquering a part of it: the thin-film solar cells. The main differences compared to the classical ones are the reduced thickness and the possibility of being deposited on flexible substrates [12] [13] [14].

The thin film market is increasingly also because these cells are cheaper and have a comparable efficiency to the more classical crystal silicon-based solar cell. One of the most efficient materials used for the realization of thin-film solar cells is the *CIGS* (Figure 1.9 [15]) which is demonstrated by EMPA and ZSW with their record of efficiency [1] [2] comparable with Silicon based solar cells.

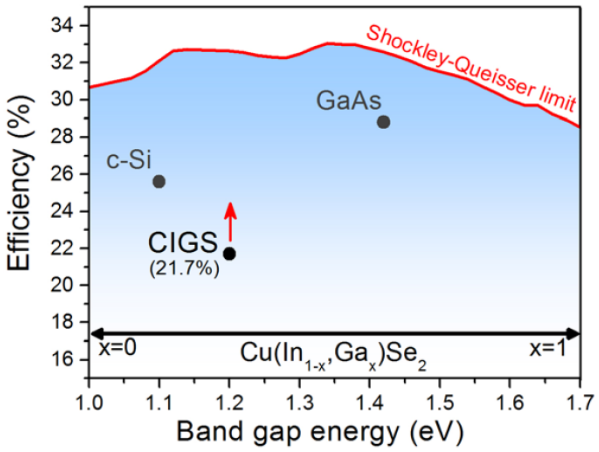

Figure 1.9: The Shockley-Queisser limit which indicates the theoretical efficiency limit of materials in function of its energy-gap.

The Copper Indium Gallium (di)Selenide (*CIGS*) is a direct band gap semiconductor with poly-crystalline nature: it is a solid solution of copper indium selenide (*CIS*) and copper gallium selenide (*CGS*).

It is a tetrahedrally bonded semiconductor, with the chalcopyrite crystal structure (Figure 1.10) with chemical formula $Cu\,(In_{1-x}, Ga_x)\,Se_2$, where the value of the x can vary from *0* (pure *CIS*) to *1* (pure *CGS*) as follows [16].

$$x = \frac{[Ga]}{[In] + [Ga]} \tag{1.12}$$

The band gap of the *CIGS* can vary between $1eV$ and $1.7eV$ [17] and it is strongly dependent on x:

- $x = 0$ means pure *CIS* and a band gap of $E_g = 1eV$

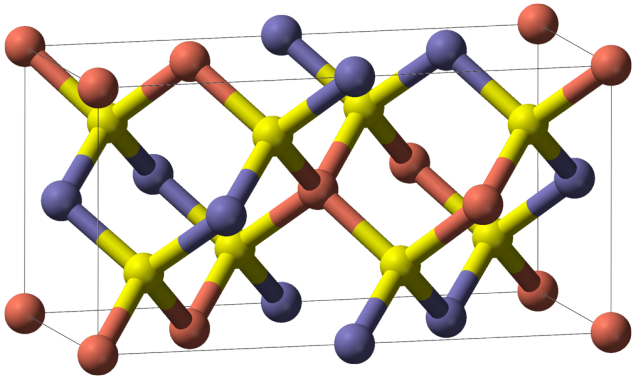

Figure 1.10: Tetrahedral structure of bonds in *CIGS*: copper in red, selenium in yellow and indium or gallium in blue.

- $x = 1$ means pure *CGS* and a band gap of $E_g = 1.7eV$

This property is fundamental in the process of optimization of the material where a different x value corresponds to different optical and collection properties [16] [18]. Moreover the choice of the ideal band gap is a key aspect for the performance of solar cells which come from a compromise between open circuit voltage (V_{OC}) and short circuit current density (J_{SC}), requiring high and low E_g value respectively.

The p-doped *CIGS* is used as absorber layer in thin film solar cells. To achieve the desired doping, during the growth of the material the incorporation of copper vacancies should be encouraged; therefore the selenium atoms near the copper vacancy are deficient in electrons, so they tend to accept electrons and the material is p-doped.

1.7 Structure of CIGS solar cells

Differently from Silicon-based solar cells, *CIGS* cells are heterostructures, that is to say formed by different materials. The peculiar characteristic of this heterostructure is the band offset that occurs between two different materials. It happens because

the two semiconductors have different band gap and when they are put in contact a discontinuity and a band-bending can form (Figure 1.11 (b) [10]).

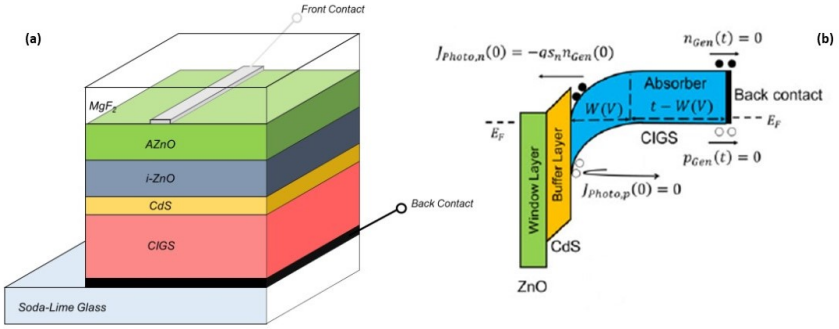

Figure 1.11: The structure of a classical thin-film *CIGS* solar cell (a) and the corresponding band diagram are shown (b).

The structure in Figure 1.11 (a) is a classical thin film *CIGS* solar cell, it is formed by five layer of different materials:

- MgF_2 or *Magnesium fluoride*, is the anti-reflective coating and its main characteristic is to be transparent for a wide range of wavelength. It is used to minimize the total reflection of the cell, in particular at wavelengths corresponding to the maximum intensity of solar radiation.

- *AZnO* or *Aluminum-doped Zinc Oxide*, is, together with i-ZnO, the **window** layer. It has a high band-gap (3.3eV) in order to be transparent to most part of incident photons. It is heavily doped in order to form a good ohmic contact with the overlying contact grid.

- $i - ZnO$ or *intrinsic Zinc Oxide*, is the second part of the **window** layer, as the AZnO it has a high band-gap (3.3eV).

- *CdS* or *Cadmium sulfide*, is the **buffer** layer. Forms the p-n junction with the *CIGS*. It is n-doped with a band gap of 2.4eV lower than the ZnO but higher

than the *CIGS*. Even if it is a toxic material, it forms a junction with the *CIGS* of very high quality, so that it has not been replaced so far.

- The *CIGS* or *Copper Indium Gallium (di)Selenide*, is the **absorber** layer. It is the layer that has to absorb the most part of solar radiation and that is why it is the thickest and with the lowest band-gap.

Usually the substrate is made of the Soda-Lime Glass, even if it can be replaced by lighter materials such as plastic. On the glass substrate, a layer of molybdenum (Mo) is deposited which has a dual function: to act as a back contact, collecting holes, and reflect in the cell the unabsorbed photons.

Chapter 2

CIGS solar cells modeling

In this chapter the numerical model developed for the latest generation cells produced by EMPA and ZSW will be described. This work puts the basis of the arguments presented in the following and describes the importance of having a model for the simulations as realistic as possible. The modeling of the two cells differs mainly because the structures differ in thickness and gradation. Initially, the software and the physical model used will be presented.

2.1 Software and physical models

The software used to perform all the described electro-optical simulations is the Synopsys Sentaurus T-CAD suite [19], one of the most used in the field of device simulation. Sentaurus T-CAD is an advanced multidimensional (1D, 2D, 3D) code to perform different type of analysis:

- Electrical, it is the simulation from the electrical point of view of a device only;
- Optical, it is the simulation from the optical point of view of a device only;
- Electro-optical, it is the combination of electrical and optical simulations and the most used to simulate the solar cells;

- Transient, it is a type of simulation used to study the evolution over time of certain physical quantity (i.e. voltage, current);
- Small-Signal AC analysis, it is the simulation used to apply a small signal to the device (for example it is used for the capacitance-frequency simulations);
- Capacitance-Voltage, it is the simulation used to calculate the capacitance of a device over the voltage;
- Electromagnetic, it is the simulation from the electromagnetical point of view of a device only;
- Mixed mode analysis, this type of simulation mixes the circuital simulation with the device simulation.

The Sentaurus suite is composed by different tools, the most important are listed below:

- Sentaurus Structure Editor: it is used to create the structure to be simulated. It is possible to define the regions of the device, the thicknesses of layer and the various doping; after this, the mesh is created and will be used by the simulator to solve the equations describing the physical problem. The degree of fineness of the mesh is fundamental for the accuracy and convergence of the simulations.
- Sentaurus Device: it is used to define the physical behavior of the device, set the type of simulation to be performed and select the desired parameters to be plotted. Furthermore, it is possible to specify the properties of the materials composing the device and their physical characteristics.
- Sentaurus Visual: it is used for the visualization of results.
- Sentaurus Inspect: as the previous one, this tool is used for the visualization of the results.

After this brief introduction to the simulator, in the rest of this section the physical model used [9] in all the simulation will be described.

2.1.1 Electrical Model

In this work all the simulations were performed under DC steady-state conditions, hence the following model description is restricted to this case.

The electrostatics is described by the Poisson equation:

$$\nabla\cdot(\varepsilon_0\varepsilon_r\nabla\Psi) = q\,(p - n + N_D - N_A) - \rho_T \tag{2.1}$$

where $\varepsilon_0\varepsilon_r$ is the dielectric constant, $\nabla\Psi$ is the electrostatic potential, p and n are the free carrier concentrations, N_D and N_A are the donor and acceptor doping densities and ρ_T is the additional trapped charge density.

The Poisson's equation is solved self-consistently with the continuity equations:

$$\nabla\cdot\vec{J_n} = -\nabla\cdot\vec{J_p} = q(R - G) \tag{2.2}$$

where $\vec{J_n}$ and $\vec{J_p}$ are the current densities respectively of electrons and hole, R is the recombination rate and G is the generation rate.

The software gives the opportunity to simulate three different types of recombination:

- Radiative: typical of direct band gap semiconductors, they occur when an electron in the conduction band recombines with a hole in the valence band thus emitting a photon.
- Shockley-Read-Hall (SRH):they are due to defects in the material or at interface between different materials. They occurs when an electron/hole remains trapped in forbidden states introduced by these defects, and recombine with a hole/electron.
- Auger: typical of heavily doped semiconductors, they occurs when the energy resulting from the recombination of an electron with a hole is transfered to a third electron in the conduction band.

Shockley-Read-Hall (SRH) recombinations are the only ones not negligible in the solar cell simulation, so they are the only ones taken into consideration in this thesis.

The SRH model can be described by the following formula:

$$R = \frac{N_0 v_{THn} v_{THp} \sigma_n \sigma_p \left(np - n_i^2\right)}{v_{THn}\sigma_n \left(n + n_1\right) + v_{THp}\sigma_p \left(p + p_1\right)} \tag{2.3}$$

with

$$n_1 = n_i \cdot e^{\frac{E_T - E_i}{kT}} \tag{2.4}$$

$$p_1 = n_i \cdot e^{\frac{E_i - E_T}{kT}} \tag{2.5}$$

where N_0 and E_T correspond to the trap density and the energy level, v_{THn} and v_{THp} are the electron and hole thermal velocities, σ_n and σ_p are the electron and hole capture cross-section and n_i and E_i correspond to the intrinsic carrier concentration and intrinsic Fermi level.

In this work the occupation probability of a state at energy E is given by the Fermi-Dirac statistics:

$$f(E) = \frac{1}{1 + e^{\frac{E - E_F}{kT}}} \tag{2.6}$$

where E_F is the Fermi energy.

The current densities are expressed by the drift-diffusion equations; in the low-field regime, the mobility and diffusivity are related by the equations of Einstein:

$$D = \frac{kT}{q}\mu \tag{2.7}$$

and the current densities can be written as:

$$\overrightarrow{J_n} = n\mu_n \nabla E_{Fn} \tag{2.8}$$

$$\overrightarrow{J_p} = p\mu_p \nabla E_{Fp} \tag{2.9}$$

where E_{Fn} and E_{Fp} are the quasi-Fermi levels, which for a non-degenerate semiconductor are linked with the carrier densities by:

$$n = N_C e^{\frac{E_{Fn} - E_C}{kT}} \tag{2.10}$$

$$p = N_V e^{\frac{E_V - E_{Fp}}{kT}} \tag{2.11}$$

where N_C and N_V are the effective densities of states correspondingly in the conduction and valence band, and E_C and E_V are the respective band edges.

2.1.2 Optical Model and photo-generation

In the simulations described in this thesis, the light propagation through the cell is described by the Transfer Matrix Model (TMM). This model is based on two assumptions:

- ideal and flat interfaces between layers;
- coherent propagation, that is to say layers that are thinner than the optical coherence length.

The second assumption is generally accurate enough; the first one, on the other hand, is a coarse approximation in the case of thin-film polycrystalline cells: however, since measured optical coefficients are used in the simulations, the effect of surface roughness is to some extent incorporated in the model, and TMM simulations can be considered accurate enough.

Other models are available in the simulator for optical propagation (e.g., Ray Tracing), but they are not employed in the simulations described in this work.

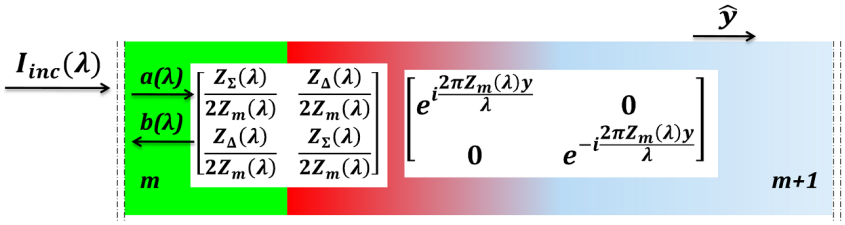

Figure 2.1: Transfer matrix at a generic interface and inside a layer for normal incident light.

In Figure 2.1 is illustrated the TMM, the symbols in the picture can described as follows:

$$Z_{\Sigma}(\lambda) = Z_m(\lambda) + Z_{m+1}(\lambda) \tag{2.12}$$

$$Z_{\Delta}(\lambda) = Z_m(\lambda) - Z_{m+1}(\lambda) \tag{2.13}$$

$a(\lambda)$ is the forward propagating wave, $b(\lambda)$ is the backward propagating wave, $I_{inc}(\lambda)$ is the incident wave.

For normal incidence, the complex wave impedance Z equals the complex refractive index of the material:

$$Z = \widetilde{n} = n + ik \tag{2.14}$$

where n is the refractive index and k the extinction coefficient.

By considering the product of all transfer matrices, for a given incident wave $I_{inc}(\lambda)$ and no backward propagating wave at the final interface of the structure, the complex waves $a(\lambda)$ and $b(\lambda)$ can be computed at each position y, and the optical intensity and optical generation rate can be calculated as:

$$I(y, \lambda) = n(\lambda)|a(\lambda) + b(\lambda)|^2 I_{inc}(\lambda) \tag{2.15}$$

$$G^{opt}(y, \lambda) = \frac{4\pi k(\lambda) I(y, \lambda)}{hc} \tag{2.16}$$

In this work every absorbed photon is considered to generate an electron-hole pair, then the quantum yield equals one.

2.2 EMPA cell

The record efficiency of 20.4% for thin-film CIGS solar cells on flexible polymer substrate [1] is held by the Swiss Federal Laboratories for Materials Science and Technology (EMPA) and it was obtained with a novel low temperature (350 °C) deposition process; this cell is used as one of the two baseline structures of this thesis.

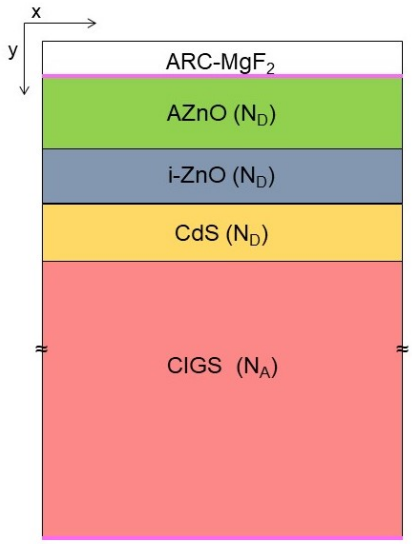

Figure 2.2: EMPA simulated structure

The simulated structure used to reproduce the EMPA record cell is made of, from bottom to top, back contact (Mo), p-type $Cu(In, Ga)Se_2$ (*CIGS*) absorber, n-type *CdS* buffer, *i-ZnO / ZnO:Al* (*AZnO*) window, MgF_2 Anti-Reflective-Coating (ARC). The base contact has a distributed series resistance of 0.5 Ωcm^2

As written in the previous chapter, a thin-film *CIGS* solar cell is a heterojunction, so in the structure there are several materials with different band-gaps. When two materials are joined together there is the formation of two discontinuities: Conduction Band Offset (CBO), and Valence Band Offset (VBO) [20]. The values of these discontinuities depends on the matching of the materials, but for the behavior of the cell the most important is the CBO and in this thesis the focus is only on that discontinuity.

In this structure there are two CBOs: at Buffer/Window interface (Δ_{BW}), and at Buffer/Absorber interface (Δ_{AB}).

The value of the conduction band offset (CBO) between *ZnO* and *CdS* (Δ_{BW}) is taken from literature and fixed at $-0.2eV$ [21] [22]; this mean that the edge of the conduction band of *CdS* is above the edge of the *ZnO*. This particular band alignment

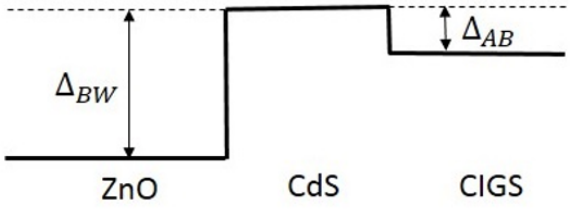

Figure 2.3: Schematic band alignment, showing a "cliff" ($\Delta_{BW} < 0$) between window and buffer and a "spike" ($\Delta_{AB} > 0$) between buffer and absorber.

is called *cliff* (Figure 2.4 (B)).

The situation is different for the CBO between *CdS* and *CIGS* (Δ_{AB}), indeed it changes with the Gallium molar fraction of the absorber [23]. In case of EMPA cell this value is $0.3eV$; this mean that the edge of the conduction band of *CIGS* is below the edge of the *CdS*. This band alignment is called *spike* (Figure 2.4 (A)).

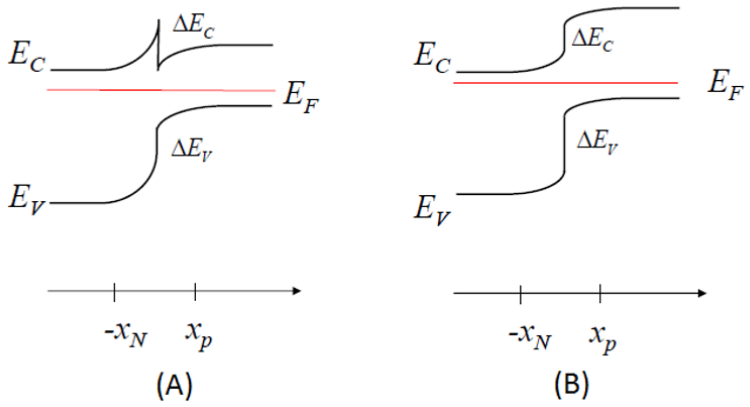

Figure 2.4: Two conduction band offsets (CBO) are shown: (A) *spike*, (B) *cliff*.

The absorber is compositionally-graded and the formula linking *Eg* (in *eV*) and the *Ga/(Ga + In)* ratio (*GGI*) is [16]:

$$E_g = E_g\,(CuInSe_2) + \left(E_g\,(CuGaSe_2) - b - E_g\,(CuInSe_2)\right) \cdot GGI + b \cdot GGI^2 \quad (2.17)$$

where $E_g\,(CuGaSe_2)$ is $1.7eV$, $E_g\,(CuInSe_2)$ is $1.0eV$ and the bowing coefficient b is *0.2*; all these values are taken from the literature [17].

In table are listed the electrical parameter used for the EMPA baseline cell; the experimental *GGI* profile [1] introduced in the simulation is shown in Figure 2.5. Another important parameter, in particular from an optical point of view, is the quantity of copper inside the *CIGS*, this can be defined as

$$CGI = \frac{[Cu]}{[In] + [Ga]} \tag{2.18}$$

In the baseline EMPA cell, the *CGI* is considered constant and equal to 0.8 according to literature [1].

	AZnO	i-ZnO	CdS	CIGS
E_g [eV]	3.3	3.3	2.4	graded
Doping density $[cm^{-3}]$	$4{\cdot}10^{20}$ (donor)	$1{\cdot}10^{17}$ (donor)	$2{\cdot}10^{16}$ (donor)	$1{\cdot}10^{16}$ (acceptor)
Bulk trap concentration $[cm^{-3}]$	$1{\cdot}10^{16}$ (mid-gap acceptor)	$1{\cdot}10^{16}$ (mid-gap acceptor)	$3{\cdot}10^{15}$ (mid-gap acceptor)	$6.67{\cdot}10^{14}$ (mid-gap donor)
Bulk trap cross-sections $[cm^2]$	$1{\cdot}10^{-12}$ (h) $1{\cdot}10^{-15}$ (e)	$1{\cdot}10^{-12}$ (h) $1{\cdot}10^{-15}$ (e)	$1{\cdot}10^{-12}$ (h) $1{\cdot}10^{-15}$ (e)	$1{\cdot}10^{-15}$ (h) $1{\cdot}10^{-15}$ (e)
N_C $[cm^{-3}]$	$2.3{\cdot}10^{18}$	$2.3{\cdot}10^{18}$	$2.3{\cdot}10^{18}$	$6.7{\cdot}10^{17}$
N_V $[cm^{-3}]$	$3.3{\cdot}10^{19}$	$3.3{\cdot}10^{19}$	$1.8{\cdot}10^{19}$	$1.5{\cdot}10^{19}$
μ_e $[cm^2V^{-1}s^{-1}]$	100	100	100	100
μ_h $[cm^2V^{-1}s^{-1}]$	25	25	25	25

As far as optical parameters are concerned, except where otherwise noted, the values measured at EMPA were used for all the materials [24].

In addition since the absorber have graded composition, the optical coefficients are position-dependent: the coefficients corresponding with *GGI* values for which literature data was not available were determined by linear interpolation. In some

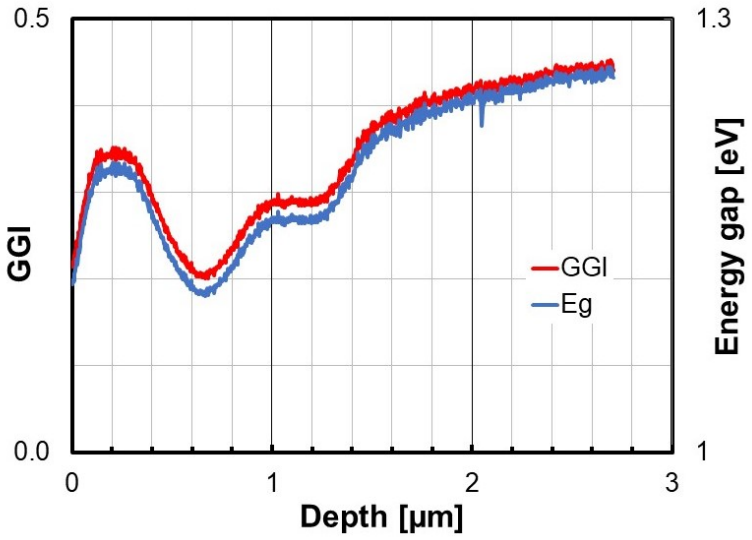

Figure 2.5: Absorber compositional and bandgap grading (EMPA cell, with power conversion efficiency η = 20.4%).

cases, linear interpolation was necessary to increase the wavelength resolution with respect to the available literature data.

The comparison between the best case obtained from the simulation of EMPA structure and the values of the EMPA record cell are shown in Table below:

	$V_{OC}[V]$	$J_{SC}\left[\frac{mA}{cm^2}\right]$	$FF[\%]$	$\eta[\%]$
Record cell [1]	0.736	35.1	78.9	20.4
Simulation	0.741	36.8	80.1	22.0

2.3 ZSW cell

In 2015 the record efficiency of 21.7% [25] for thin-film CIGS solar cells on glass substrate was held by the Zentrum für Sonnenenergie-und Wasserstoff-Forschung Baden-Württemberg (ZSW) as 22.6% [2] in 2017, but Solar Frontier, with the actual record of 22.9% [26], surpass in the same year (2017). All these solar cells were

obtained using a high temperature (600°C) process for the growth of *CIGS*.

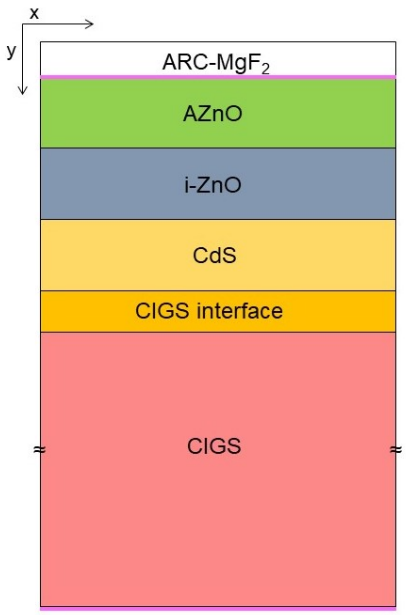

Figure 2.6: ZSW simulated structure

Toghether with EMPA cell, described in the section before, the ZSW cell was used as another baseline structure of this thesis.

The simulated structure used to reproduce the ZSW record cell is made of, from bottom to top, back contact (Mo), p-type $Cu(In,Ga)Se_2$ (*CIGS*) absorber, n-type *CdS* buffer, *i-ZnO / ZnO:Al (AZnO)* window, MgF_2 Anti-Reflective-Coating (ARC).

This structure (Figure 2.6) differs from the EMPA one, for the *CIGS* doping near the interface: in fact, the surface of the absorber is n-doped for 5 nm depth in order to obtain a buried junction and enhance the performance of the cell, in particular the V_{OC} value. No distributed series resistance at base contact was considered for the ZSW cell.

The ZSW cell (Figure 2.6) is a hetero-structure as the EMPA one, but the CBO are different because the grading inside the *CIGS* is different (Figure 2.7); in this structure it was used a Δ_{BW} of $-0.2eV$ and a Δ_{AB} of $0.1eV$ [23].

In table below are listed the electrical parameter used for the ZSW baseline cell; the experimental *GGI* profile [25] introduced in the simulation is shown in Figure 2.7.

The quantity of copper (*CGI*) inside the *CIGS* is considered constant and equal to 0.9 according to literature [25].

	AZnO	i-ZnO	CdS	CIGS
E_g [eV]	3.3	3.3	2.4	graded
Doping density $[cm^{-3}]$	$4{\cdot}10^{19}$ (donor)	$1{\cdot}10^{17}$ (donor)	$1{\cdot}10^{17}$ (donor)	$8{\cdot}10^{16}$ (acceptor)
Bulk trap concentration $[cm^{-3}]$	$1{\cdot}10^{16}$ (mid-gap acceptor)	$1{\cdot}10^{16}$ (mid-gap acceptor)	$3{\cdot}10^{15}$ (mid-gap acceptor)	(a) $1{\cdot}10^{13}$ (E_C-E_T = 0.24 eV donor) (b) $1{\cdot}10^{13}$ (E_C-E_T = 0.34 eV donor) (c) $1{\cdot}10^{13}$ (E_T-E_V = 0.29 eV acceptor) (d) $1{\cdot}10^{13}$ (E_T-E_V = 0.58 eV acceptor)
Bulk trap cross-sections $[cm^2]$	$1{\cdot}10^{-12}$ (h) $1{\cdot}10^{-15}$ (e)	$1{\cdot}10^{-12}$ (h) $1{\cdot}10^{-15}$ (e)	$1{\cdot}10^{-12}$ (h) $1{\cdot}10^{-15}$ (e)	(a) and (b) $1{\cdot}10^{-17}$ (h) $1{\cdot}10^{-15}$ (e) (c) and (d) $1{\cdot}10^{-15}$ (h) $1{\cdot}10^{-17}$ (e)
N_C $[cm^{-3}]$	$2.3{\cdot}10^{18}$	$2.3{\cdot}10^{18}$	$2.3{\cdot}10^{18}$	$6.7{\cdot}10^{17}$
N_V $[cm^{-3}]$	$3.3{\cdot}10^{19}$	$3.3{\cdot}10^{19}$	$1.8{\cdot}10^{19}$	$1.5{\cdot}10^{19}$
m_e $[cm^2V^{-1}s^{-1}]$	100	100	100	100
m_h $[cm^2V^{-1}s^{-1}]$	25	25	25	25

Also in this case, as far as optical parameters are concerned, except where otherwise noted, the values measured at EMPA were used for all the materials [24].

As for the EMPA cell also for the ZSW cell, since the absorber have graded composition, the optical coefficients are position-dependent.

The comparison between the best case obtained from the simulation of ZSW structure and the values of the ZSW record cell are shown in table below:

	$V_{OC}[V]$	$J_{SC}\left[\frac{mA}{cm^2}\right]$	$FF[\%]$	$\eta[\%]$
Record cell [25]	0.746	36.59	79.29	21.7
Simulation	0.814	35.55	85.6	24.7

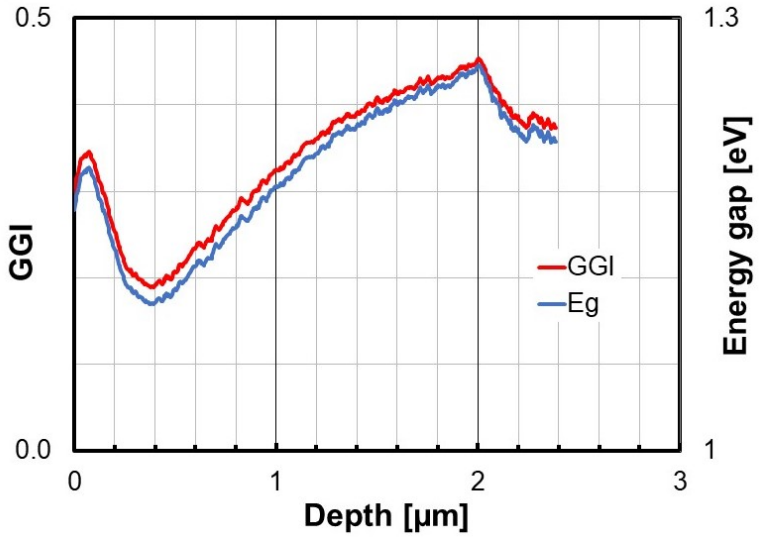

Figure 2.7: Absorber compositional and bandgap grading (ZSW cell, with power conversion efficiency $\eta = 21.7\%$).

Chapter 3

CIGS properties

In this chapter the CIGS and its properties will be analyzed, In particular will be studied the behavior of the solar cell when the material properties change, starting from the variation of the Gallium profile, and the variation of the conduction band offsets. Finally the admittance spectra simulations and their interpretation will be introduced.

3.1 Ga content profile inside CIGS (GGI)

One of the most important properties of the *CIGS* is the dependence of the energy band-gap on the *[Ga]/([Ga]+[In])* ratio (*GGI*) [18]; the increase of *Ga* content widens the band-gap, while its reduction decreases the band gap. This behavior mainly takes place through the movement of the conduction band edge [16]. Intentional grading of the *CIGS* absorber is commonly used in high efficiency solar cells [2] [1] in order to increase the absorption and collection and hence the efficiency.

In this section the EMPA cell was used as baseline, after that it was deeply modified (different *GGI* and *CGI*). The optical coefficients used for *CIGS* in all the simulations correspond to a value of $CGI = 0.9$, and vary consistently with the *GGI* profile.

In order to study the sensitivity of cell parameters on the *GGI* grading profile, the simplified model of notch grading shown in Figure 3.1 [18] was considered.

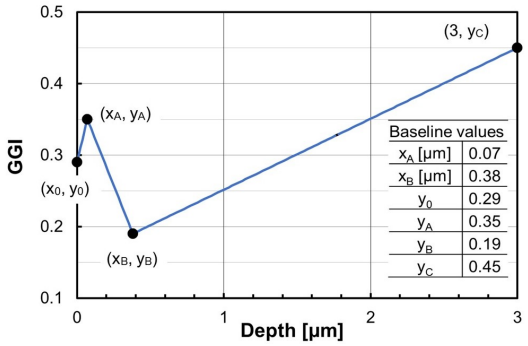

Figure 3.1: Simulated *[Ga]/([Ga]+[In])* (GGI) profile, for $CGI = 0.9$. The coordinates $y_0, x_A, y_A, x_B, y_B, y_C$ were varied in the simulations. The inset reports the coordinates corresponding with the baseline profile.

Different band-gap profiles are simulated by varying the coordinates of points 0 $(0, y_0)$, A (x_A, y_A), B (x_B, y_B), and C $(3\mu m, y_C)$, where x is the depth inside the *CIGS* layer and y is the corresponding *GGI* ratio.

The baseline *GGI* profile (Figure 3.1) corresponds to a cell with an efficiency of 21%, $J_{SC} = 34.4\frac{mA}{cm^2}$, $V_{OC} = 0.745V$ and $FF = 81.9\%$. Only one of the coordinates is varied at a time, while the others are kept at their baseline values.

3.1.1 Variation of x_A and x_B

In this subsection, the focus is on x_A and x_B in order to understand if the change in depth can lead to an increase in efficiency. In particular, it is very important that the notch (x_B, y_B), which is the part of the structure with the highest absorption, is within the depletion region in order to favor the collection of all the generated carriers.

Varying the depth of the *GGI* peak x_A (in the range 0.03 - 0.13 μm) and the depth of the notch x_B (in the range $0.14 \div 0.32$ μm), has negligible effect on all the figures of merit. In Figure 3.2 the efficiency is shown in function of x_A and x_B; it is possible to note that the changes of η are less than 0.3%.

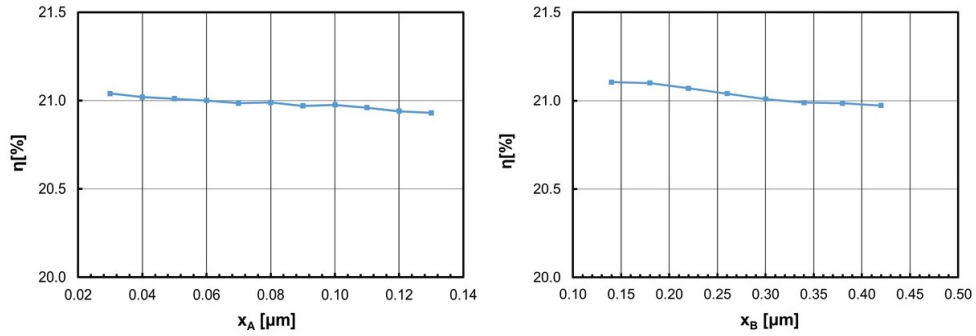

Figure 3.2: Simulated efficiency versus x_A and x_B.

3.1.2 Variation of y_0, y_A, y_B and y_C

In this subsection, the focus is on the content of gallium y_i at different positions that can lead to different effect on the cell parameters.

The increase of the surface *GGI*, y_0, mainly affects FF and η which respectively earn almost 2% and 1% absolute, for y_0 varying from *0.20* to *0.38*. (Figure 3.3)

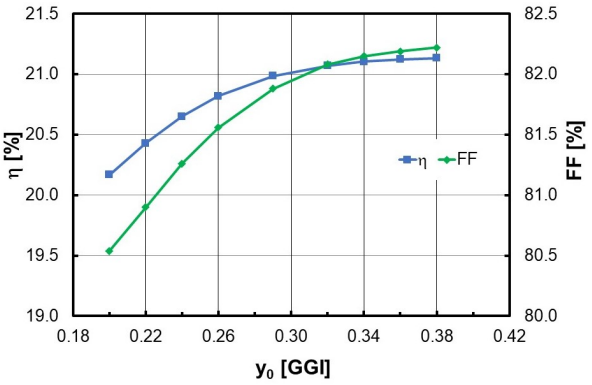

Figure 3.3: Simulated η and FF versus y_0.

The opposite happens for the *GGI* peak, y_A: an increase from *0.3* to *0.4* lead to J_{SC} losses of about 1 $\frac{mA}{cm^2}$ due to a minor absorption in the part of the cell where the intensity of the radiation is maximum (*CIGS* surface). Controlled by the short-circuit

current, the efficiency, η, also decreases by almost 1% absolute, as shown in Figure 3.4.

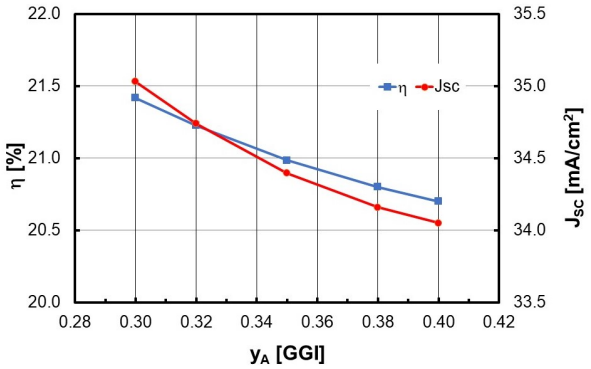

Figure 3.4: Simulated η and J_{SC} versus y_A.

Similarly to y_A, an increase from *0.12* to *0.24* of the minimum *GGI* y_B leads to a J_{SC} and η decrease (Figure 3.5).

Also in this case these efficiency reductions are due to a low absorption in the notch, which is the part of the cell that most contributes to the short-circuit current, since it is the part of the structure with the highest absorption.

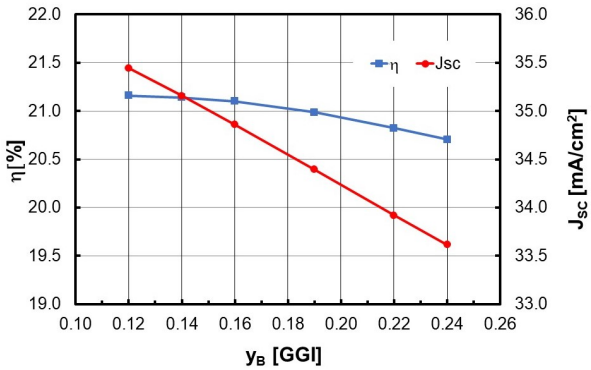

Figure 3.5: Simulated η and J_{SC} versus y_B

The last point to vary is the back side *GGI* value y_C: its variation leads to a

significant efficiency gain due to the increase of V_{OC} (Figure 3.6).

It is possible to explain the observed behaviors with the formation of a electric field: in fact, with an increase of y_C there is an increase in the electric field on the back side of the cell that improves the collection and reduces the recombinations. However, for $y_C > 0.55$ this performance enhancement shows a saturation.

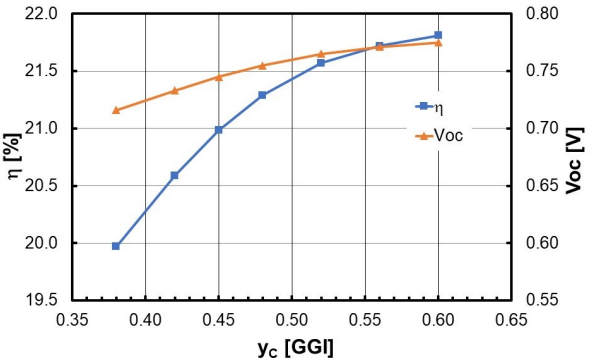

Figure 3.6: Simulated η and V_{OC} versus y_C

The analysis described so far shows that the increase of *GGI* at the molybdenum side of the *CIGS* absorber (y_C) is expected to give the best results [18].

3.2 Cu content of CIGS (CGI)

Another important property of CIGS is the dependence on the *Cu* content (*CGI*) [18] [27]; different *CGI* inside the CIGS causes a variation of the band-gap mainly by moving the valence band edge. A low *CGI* can lead to low absorption and high *CGI* can lead to high absorption [28].

To study the way *CGI* can affect the cell performances, four samples with average *[Cu]/([In]+[Ga])* (***CGI****) ratios of *0.8, 0.85, 0.9, 0.93* were considered; all the structures have a graded *CIGS*.

The measured performance parameters of the 4 cells, performed under the AM 1.5 spectrum at 25 °C, show that increasing *CGI** adversely affects the fill factor, FF, and open circuit voltage, V_{OC}, while the short circuit current density, J_{SC}, increases

by some 3% when *CGI** changes from *0.80* to *0.85*, then more gently increases as *CGI** is raised from *0.85* to *0.93*.

As a result, the efficiency is maximum (19%) for *CGI** = *0.80* and *0.85*, then decreases by some 1% absolute as *CGI** is increased to *0.93*. The measured EQEs reflect the effect on J_{SC}: the increased near infra-red (NIR) response observed when *CGI** moves from *0.80* to *0.85* tends to saturate for *CGI**> *0.85*.

To better understand the observed device behavior, some simulations were performed where is considered the *GGI* profiles, which are loaded into the model, and the *CGI* average (*CGI**). The optical behavior is described by complex refractive indexes depending on both *GGI* and *CGI** ratios and coming from the literature [29].

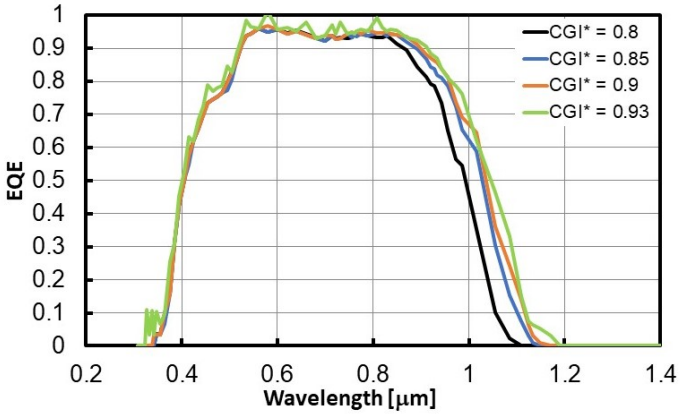

Figure 3.7: Simulated external quantum efficiencies of the cells with different *CGI** ratios and *GGI* grading.

The simulated EQEs are shown in Figure 3.7, it is possible to note a shift in the near infra-red (NIR) between *CGI** = *0.80* and *0.85*, that is due to a strong variation of the absorption coefficients.

A direct comparison between simulated and measured EQEs is shown in Figure 3.8 where the measurements do not show a shift, but rather a slope change; instead both measurements and simulations do not show any significant change for *CGI** > *0.85*.

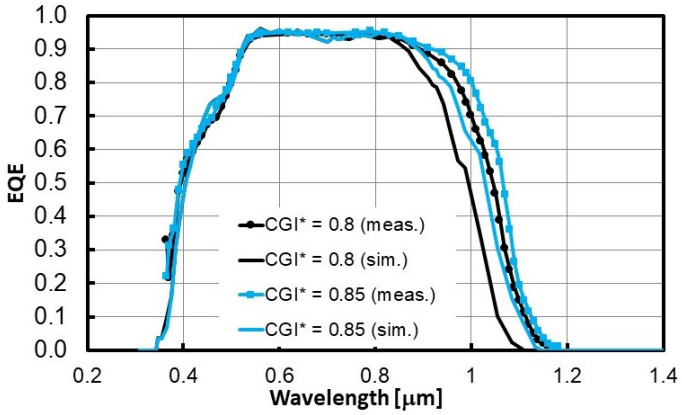

Figure 3.8: Measured and simulated external quantum efficiencies for $CGI^* = 0.8$ and *0.85*. The red line is a simulation with average *Cu* content $CGI^* = 0.80$ but non-uniform *CGI*.

From Figure 3.8 is also possible to note that the simulations underestimate the response of the cell at wavelength larger than $0.85\mu m$, especially for *CGI* = 0.80*. In fact in the simulations an uniform *CGI = CGI** is assumed in the whole absorber, while in the real cell the *CGI* profile is not constant.

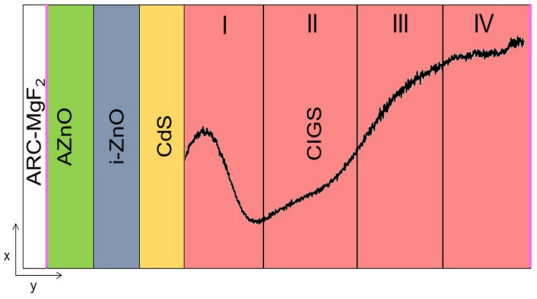

Figure 3.9: A schematic representation of the simulated structure. The profile drawn in the *CIGS* is the measured *GGI* ratio. In the simulations, instead, the *CGI* ratio is varied throughout regions I-IV as detailed in the text.

To investigate this point, the structure shown in Figure 3.9 has been simulated, where the *CIGS* is divided into four regions, and the *CGI* ratio is varied as detailed in the table below:

	Reg I CGI*	**Reg II CGI***	**Reg III CGI***	**Reg IV CGI***
Case 1	0.7	0.7	0.7	**0.9**
Case 2	0.7	0.7	**0.9**	0.7
Case 3	0.7	**0.9**	0.7	0.7
Case 4	**0.9**	0.7	0.7	0.7

The simulated EQEs for the four cases reported in the table above are shown in Figure 3.10. It is possible to note that the regions close to the front of *CIGS* and to the notch of the *GGI* profile (case 3 and 4) determine the cell NIR absorption. These parts of the structure are the most important for the absorption because at the front the intensity of the radiation is maximum and the notch has the lowest *GGI*.

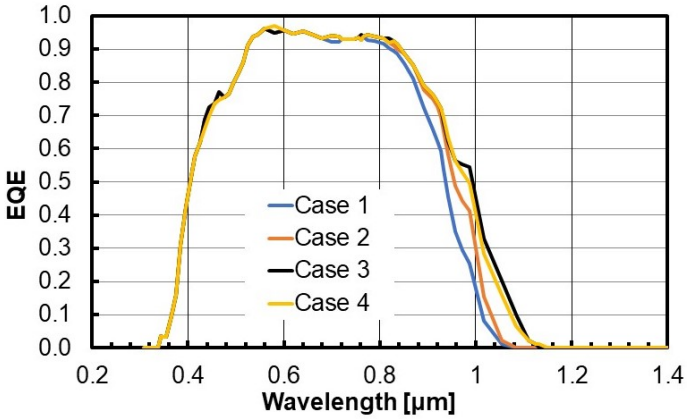

Figure 3.10: Simulated external quantum efficiencies for different *CGI* profiles, as detailed in Figure 3.9 and previous table.

Although the non uniformity of *CGI* displayed in previous table is purely speculative, Figure 3.10 shows that assuming constant *CGI** over the whole *CIGS* layer might be the reason of the gap between the measured and simulated EQEs in the NIR range when *CGI*< 0.85* (black lines in Figure 3.8).

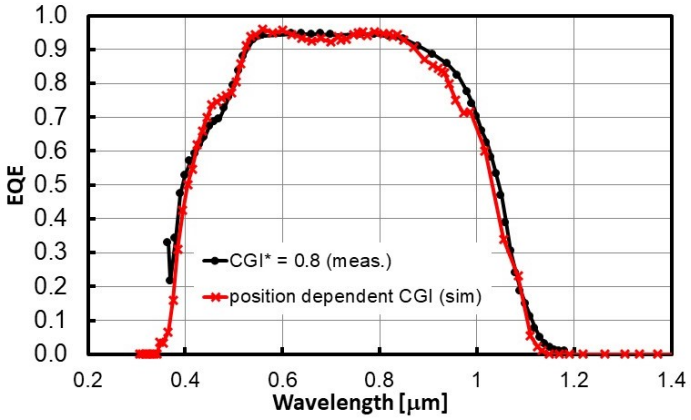

Figure 3.11: Comparison between measured external quantum efficiency and the simulated one for a structure with a position dependent *CGI*.

Based on these results, it has been simulated a cell with *CGI* = 0.80* (average value), but non-uniform *CGI* (lower at the front and at the bottom, higher in the central part of the absorber): in this case, the simulated EQE (red line in Figure 3.11) is very close to the measured one [1] (black line with dots in Figure 3.11) in the NIR range.

It is possible to conclude that absorption coefficients corresponding to an average *CGI* < 0.85* will not adequately describe carrier generation in the *CIGS* regions where the non-uniform *CGI* is > *0.85*, because of the step variation of the absorption coefficients described above.

This set of simulations show how *CGI* affects the performance of *CIGS* solar cells [18], and that the *CGI* value must be properly taken into account to model the absorption of the cell in the NIR range accurately, and that increasing the average *CGI* above *0.85* leads only to slight increment of J_{SC}.

3.3 Conduction band offset

As described in chapter before, the *CIGS* solar cell is a heterojunction structure: hence different materials hence formation of band-offsets [17] at the interface of thus

materials with different energy-gap. Two band offsets may form: the Valence Band Offset (VBO) and the Conduction Band Offset (CBO). As described before, also in this section only the CBO is considered because it is the most important for the behavior of the cell [30] [31].

The results inserted in this section are obtained with the EMPA cell simulated with the Minoura coefficients [29] for the CIGS with a *CGI* of 0.9 and the Hara coefficients [32] for all the other materials.

This structure is characterized by two CBOs: at Buffer/Window interface (Δ_{BW}), and at the Buffer/Absorber interface (Δ_{AB}). The value of the conduction band offset (CBO) between *ZnO* and *CdS* (Δ_{BW}) is taken from literature and is $-0.2eV$ (cliff) [21] [22]. The CBO between *CdS* and *CIGS* (Δ_{AB}) instead change with the changing of the molar fraction of the absorber [23], in case of EMPA cell this value is $0.3eV$ (spike).

The simulation for variable Δ_{BW} are not reported here because this CBO has no effect on the cell performance if the value is negative but $> -0.4eV$, and there is no evidence in literature which affirm that Δ_{BW} can be $< -0.4eV$.

Different is the situation for the Δ_{AB} indeed its variation can influence the performance of the cell as shown in Figure 3.12.

The decrease of efficiency for Δ_{AB} larger than $0.4eV$ is completely due to a decrease of fill-factor; a possible explanation of this behavior is a stronger depletion of the *CdS* which can increase the resistance of the cell then decreasing the *FF*. The parameters of the cell for different Δ_{AB} are listed in the table below.

	Δ_{AB} [eV]					
	0	0.1	0.2	0.3	0.4	0.5
$V_{OC}[V]$	0.74	0.74	0.74	0.74	0.74	0.74
$J_{SC}\left[\frac{mA}{cm^2}\right]$	34.6	34.7	34.8	34.8	34.9	34.6
$FF[\%]$	81.3	81.0	80.1	80.1	77.4	30.9
$\eta[\%]$	20.9	20.9	20.6	20.4	20.0	7.9

This brief study of the effects of a different Δ_{AB} and Δ_{BW} leads to the conclusion that the cell is affected by these CBOs only if the value is unrealistic and outside the

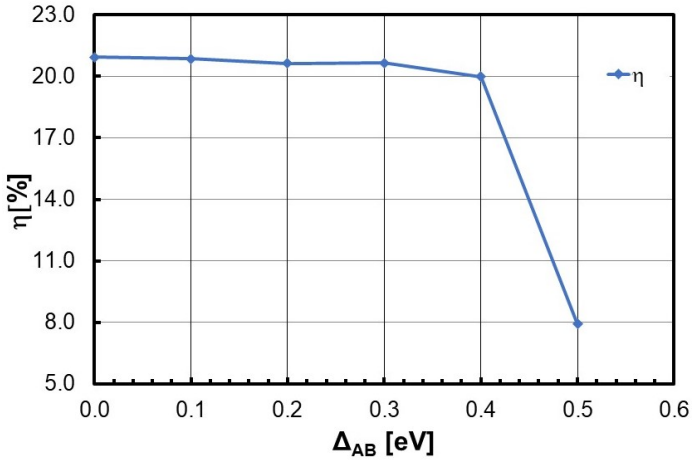

Figure 3.12: Simulated efficiency in function of Δ_{AB}.

boundaries described in the literature.

3.4 Temperature-dependent I-V characteristics

One of the peculiar characteristic of *CIGS* solar cell temperature-dependent current-voltage characteristics (J-V-T), is the presence of roll-over. This effect is a saturation of the forward current of the cell at low temperatures. The J-V-T curves affected by the roll-over have a blocking and non-exponential behaviour.

A complete understanding of this phenomena that may influence the device performance at lower temperature is still incomplete and debated [33]. In literature it is mainly attributed to a Schottky diode at the Molybdenum back contact [34], or deep acceptor-like defects at the interface between the CdS and a defect-chalcopyrite layer [35].

The aim of this section is to interpret the roll-over of J-V-T measured curves by means of numerical simulations [33]; in particular: will be examinated the way the conduction band offsets (CBOs) at hetero-interfaces can affect the current and induce the roll-over. The effect of a non-ohmic contact at the *CIGS/Molybdenum* interface

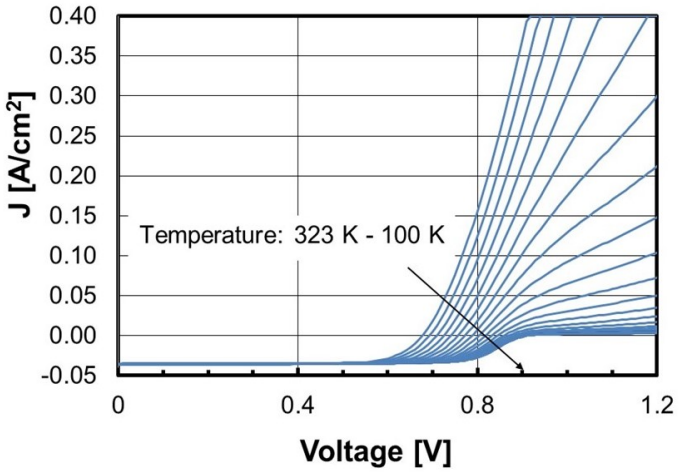

Figure 3.13: Measured J-V-T curves

will be also analyzed.

The ZSW cell was used for this modeling activity and the optical coefficient used are those of EMPA [24] for a *CIGS* with a *CGI* of *0.9*. The measurements shown in Figure 3.13 were performed by the University of Luxemburg.

The J-V curves measured by University of Luxemburg under AM1.5G illumination in the range $323 \div 100K$, reported in Figure 3.13, show remarkable roll-over of the current at low temperature. The following analysis is restricted to this one sample for a quantitative description of the roll-over but, the behavior is common for many alkali-treated cells.

In the simulations shown hereafter, the CBO at different hetero-interfaces was varied in order to discriminate between the effects due to the CBO at the window/buffer, ΔE_{BW}, and buffer/absorber, ΔE_{AB}, heterojunctions.

3.4.1 $\Delta E_{BW} = 0$ and $\Delta E_{AB} = 0$

The first set of simulation is focused on a structure without conduction band offsets at the hetero-interfaces: the simulated J-V curves show no roll-over (see Figure 3.14); the curves only shift with decreasing temperature towards higher voltages, as predicted

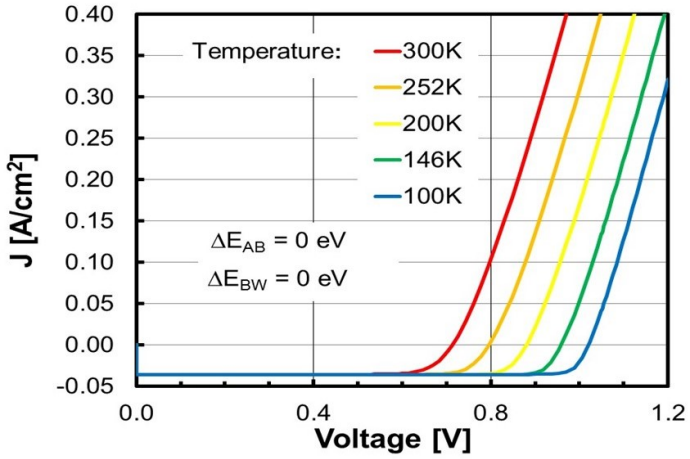

Figure 3.14: Simulated J-V-T curves under illumination for structure without CBOs.

by the classical pn-junction theory.

3.4.2 $\Delta E_{AB} = 0$ and $\Delta E_{BW} < 0$

As described in the section before a negative CBO (cliff) is usually expected at the *ZnO/CdS* interface [21] [22]; $\Delta E_{BW} < 0$ determines the presence of the roll-over at low temperature as shown in Figure 3.15 for the two cases of $\Delta E_{BW} = -0.2eV$ and $-0.4eV$.

The behavior for the two values of ΔE_{BW} is different: for $\Delta E_{BW} = -0.2eV$, the roll-over only appears at the lowest temperature $T = 100K$ (blue dashed curve), while for $\Delta E_{BW} = -0.4eV$ it is already remarkable at a temperature as high as $T = 252K$ (orange solid curve).

The reason why a large negative ΔE_{BW} affects the current flow can be understood looking at the conduction-band diagrams in Figure 3.16: a large $\Delta E_{BW} < 0$ (red curve) increases the barrier to the flow of electrons from the window to the absorber, thus suppressing the diffusion current which dominates the J-V characteristics at voltages higher than V_{OC}.

The comparison with measurements (black curves in Figure 3.15) shows that, in

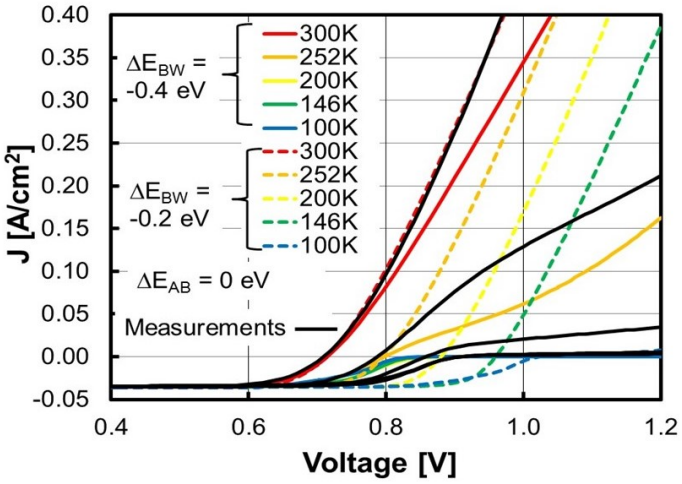

Figure 3.15: Simulated (coloured lines) and measured (black lines) current-voltage characteristics under illumination at different temperatures and for two values of the window-buffer CBO.

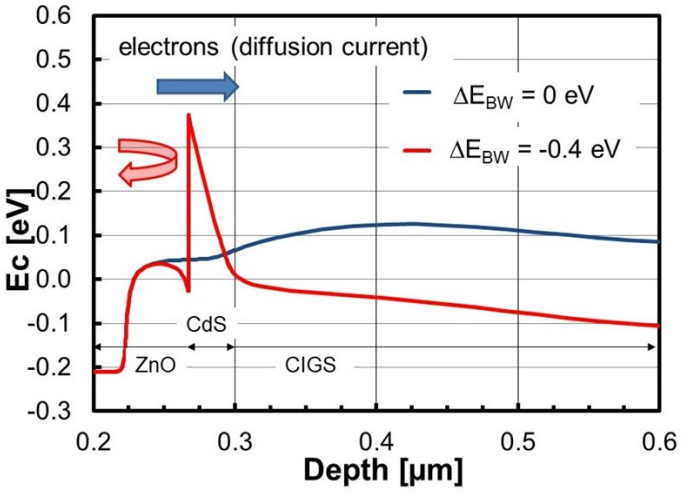

Figure 3.16: Conduction band energy, E_C, versus depth at $V = 1.1V$ under illumination for two values of the window-buffer CBO. $\Delta E_{AB} = 0eV$ $T = 200$ K.

order to obtain a similar roll-over in the simulated currents, ΔE_{BW} must be larger than the expected value (i.e., $\Delta E_{BW} = -0.2eV$), and even then the match between measurements and simulations is only qualitative.

3.4.3 $\Delta E_{BW} = 0$ and $\Delta E_{AB} > 0$

In literature the CBO between *CdS* and *CIGS* is expected to be higher than *0* [23] [31]; as described before it varies with the changing of the *GGI* at surface of the absorber.

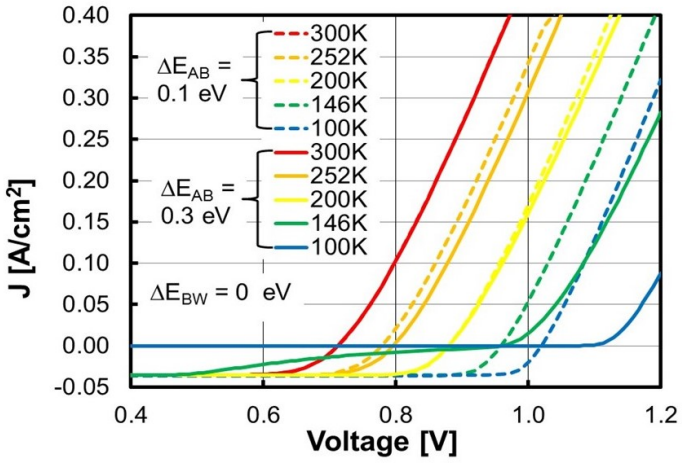

Figure 3.17: Simulated current-voltage characteristics under illumination at different temperatures, for two values of the absorber-buffer CBO.

In the case of positive CBO (spike) only the largest $\Delta E_{AB} = 0.3eV$ (solid curves in Figure 3.17), determines a change of shape in the *J-V* curves, mainly for voltage lower than V_{OC}, where the photo-generated current is reduced for $T < 200K$, while the effect on the roll-over is negligible.

The reduction of the photo-current at low temperature is due to the larger energy barrier seen at the *CdS/CIGS* junction by the photo-generated electrons leaving the absorber as shown by the conduction-band diagrams in Figure 3.18 (blue curve).

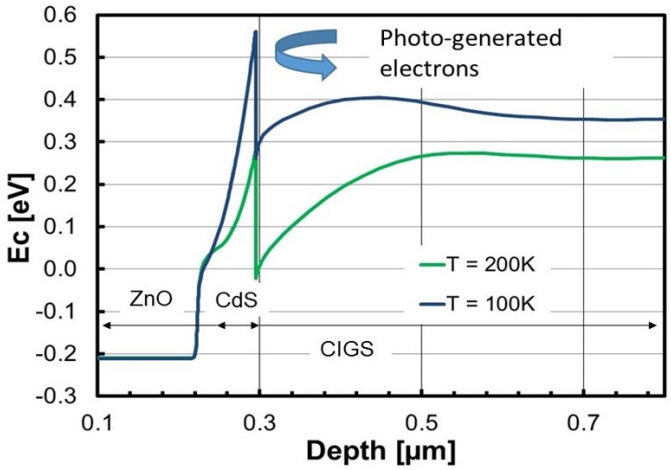

Figure 3.18: Conduction band energy, E_C, versus depth at $V = 0.7V$ under illumination. $\Delta E_{AB} = 0.3eV$, $\Delta E_{BW} = 0eV$.

3.4.4 $\Delta E_{BW} < 0$ and $\Delta E_{AB} > 0$

When CBOs at both hetero-interfaces are taken in account, the effect of ΔE_{BW} on roll-over slightly increases. However, assuming $\Delta E_{AB} = 0.1eV$ and $\Delta E_{BW} = -0.2eV$, does not allow to match the measured roll-over (dashed and solid black curves in Figure 3.19, respectively)

Since the roll-over is mainly influenced by the barrier at the *ZnO/CdS* interface, it was introduced a thermionic emission model for the transport of electrons over the barrier.

The main difference between the thermionic emission model and the drift-diffusion model (standard one) is in the different consideration of the two behaviors of a carriers which cross a barrier. To pass through a barrier the electrons must perform two processes in series: the passage through the depleted region and the emission of them through the barrier. If the critical phenomenon is the first process the most accurate model is the drift-diffusion; instead, if the critical phenomenon is the second one the thermionic emission is the most accurate model.

The simulated currents (orange curves in Figure 3.19) with the thermionic model

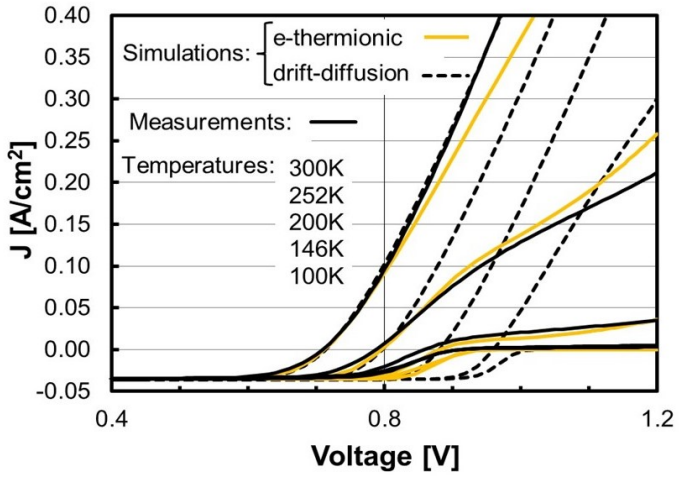

Figure 3.19: Measured and simulated J-V curves under *AM1.5G* illumination at different temperatures. The simulations are performed using either a drift-diffusion or a thermionic model at the buffer-window interface. $\Delta E_{AB} = 0.1eV$, $\Delta E_{BW} = -0.2eV$.

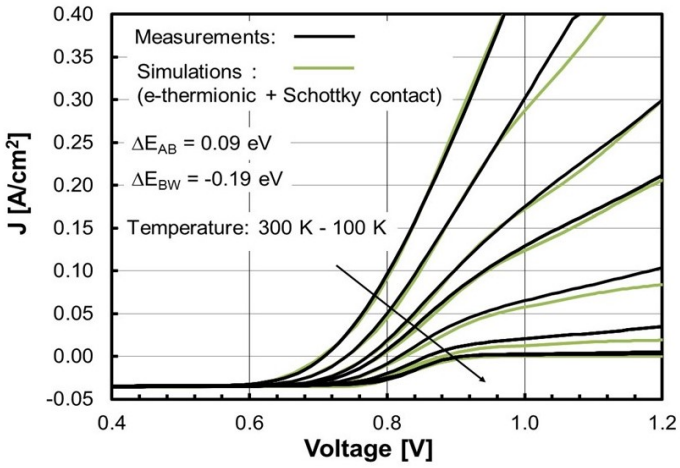

Figure 3.20: Best fit of the current-voltage characteristics under *AM1.5G* illumination. Series resistance optimized on the $300K$ curve.

well reproduce the measured ones, with some deviation at high voltages. However, by including in the model also a Schottky barrier at the rear contact [34] ($E_v - E_f = 125meV$), this latter discrepancy disappears, too, as shown in Figure 3.20.

In conclusion, in this set of simulations the effect of conduction band offsets at window/buffer and buffer/absorber interfaces on the roll-over of J-V-T curves was analyzed in the $300K \div 100K$ range.

The roll-over is mainly controlled by the energy barrier at the window/buffer interface, where the transport of electrons over the barrier can be adequately described by the thermionic-emission theory; a Schottky barrier at the rear contact is also necessary for a complete match with measured data.

3.5 Mobility

In the previous chapter, for the modeling of both the EMPA and ZSW baseline cells, the mobility of electrons within all the materials was fixed at $100cm^2V^{-1}s^{-1}$, instead those for the holes was fixed at $25cm^2V^{-1}s^{-1}$. Initially, it was chosen to equalize mobility in all materials so as not to take into account the possible effect. In this section it is presented a study on the mobility of carriers inside the *CIGS* in order to understand the possible effects.

This set of simulations was based on the EMPA cell simulated with the Minoura optical coefficients [29] for the *CIGS* with a *CGI* of *0.9* and the Hara coefficients [32] for all the other materials. The resulting simulated solar cell has the following parameters:

$$V_{OC} = 0.74V,\ J_{SC} = 34.1\frac{mA}{cm^2},\ FF = 80.1\% \text{ and } \eta = 20.6\%.$$

The change of mobility within *AZnO*, *ZnO* and *CdS* does not produce any variation, while a variation of carriers mobility within the *CIGS* impacts on the parameters of the cell; in Figure 3.21 the change of figures of merit versus the variation of *CIGS* electron mobility is shown.

It is possible to notice a decrease about 5% of efficiency for electron mobility lower than the base value of $100cm^2V^{-1}s^{-1}$, this is due to the decreases of FF and

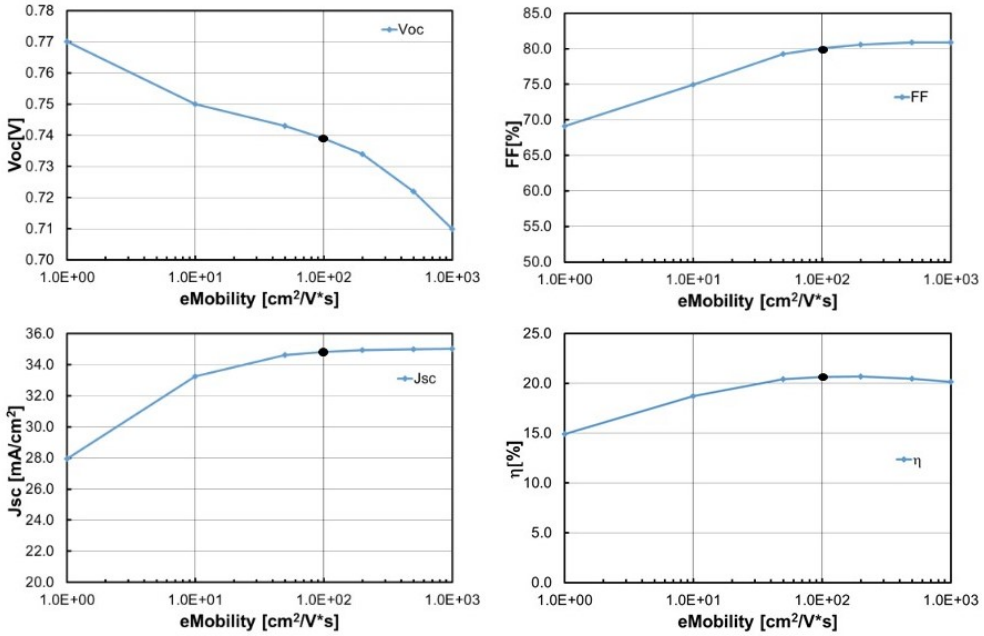

Figure 3.21: Simulated figures of merit in function of electrons mobility. The dots indicate the parameter of the baseline cell.

J_{SC}, instead the variation of V_{OC} is not so significant.

The decrease J_{SC} is due to a non-optimal collection of generated electrons, instead the decrease of FF is due to an increase in the series resistance of the cell because the electrons response is not so quick.

On the other hand the change of parameters of the cell with the variation of hole mobility within the *CIGS* is shown in Figure 3.22. This change does not produce a variation in any of the figures of merits.

This set of simulations are useful to understand how a change in carriers mobility can impact on the figures of merit of the cell. It is possible to conclude that only the variation of electron mobility in the *CIGS* induces changes in the parameter of the cell but, since the literature on the measurement of electron mobility within the *CIGS* is poor, and μ_e also changes with the doping of the material, it was decided to use

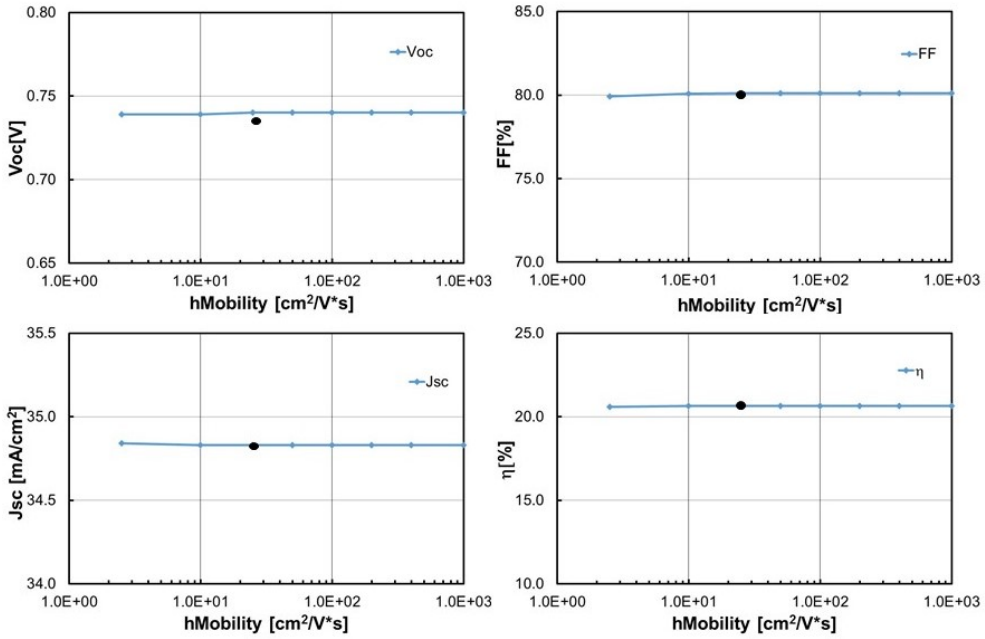

Figure 3.22: Simulated figures of merit in function of holes mobility. The dots indicate the parameter of the baseline cell.

$100 cm^2 V^{-1} s^{-1}$.

3.6 Admittance spectra simulations

A technique used to characterize the *CIGS* solar cells is the admittance spectroscopy [36] [37], even if the interpretation of admittance spectroscopy is a controversial issue.

In this section it will be presented a set of simulations [38] aimed at understanding the effect on the frequency and temperature dependent capacitance curves, *C(f,T)* of :

- conduction band offset at the *CdS/CIGS* interface;
- interfacial distribution of defects between *CIGS* and *CdS*;
- Schottky barrier at the rear contact;

- grain boundaries in the *CIGS*.

This set of simulations is based on the EMPA cell with an ungraded absorber and different doping for *CdS* and *CIGS* which are respectively $1 \cdot 10^{17} cm^{-3}$ and $5 \cdot 10^{15} cm^{-3}$. As the measurements, all the simulations were performed under dark condition.

The typical capacitance measurements performed on a *CIGS* solar cell manufactured by EMPA is shown in Figure 3.23. In the temperature range $123K \div 233K$ the *C(f,T)* curves show a step where the capacitance decreases from a low frequency value C_{LF} to a high frequency value C_{HF}.

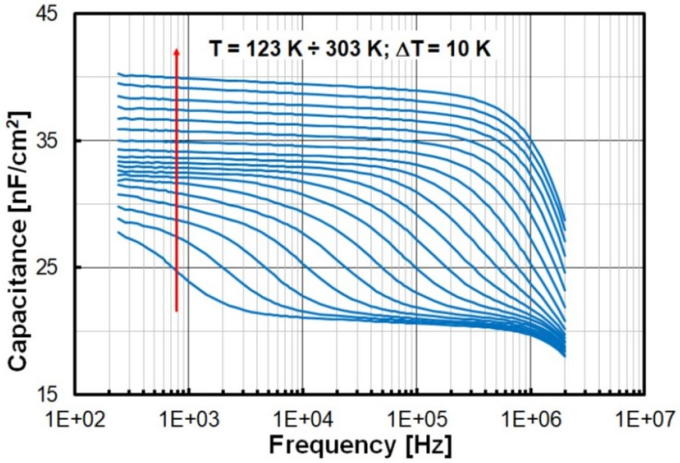

Figure 3.23: Measured capacitance spectra of a RbF PDT cell.

To perform a *C-f* simulation the cell is connected to a voltage generator on which a small signal with a certain frequency is superimposed: the circuit diagram is shown in Figure3.24. The simulation were performed at zero voltage.

3.6.1 Conduction band offset at buffer/absorber interface Δ_{AB}

As described in previous sections, the *CIGS* solar cell is an heterostructure so that the presence of a conduction band offsets are expected at hetero-interface. In this section

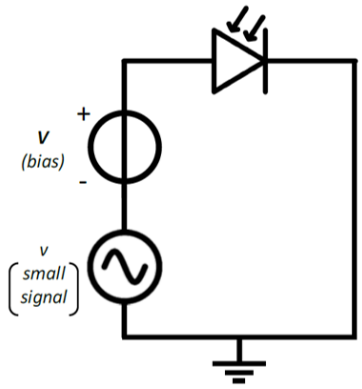

Figure 3.24: Simulated circuit.

the focus is on the CBO formed at *CdS*/*CIGS* interface: its presence expected to give a drop in the capacitance for increasing frequency, at frequency for which the transport over the barrier cannot follow the ac modulating signal.

In Figure 3.25 (a), the simulated capacitance for different values of $\Delta_{AB} \geq 0eV$ at $T = 200K$ are shown in function of frequency. The CBO at the window buffer interface is fixed at $\Delta_{BW} = -0.2eV$. It is possible to note that a capacitance step arises approximately for $\Delta_{AB} > 0.25eV$ and the corresponding inflection frequency, f_0, decreases with increasing Δ_{AB}.

It is possible to explain this effect with the inversion of *CIGS* front surface, which for $\Delta_{AB} > 0.25eV$ becomes n-type because of downward band bending which arises at *CIGS* surface. As shown in Figure 3.26, for $f < f_0$ the low frequency (LF) signal modulates the electron-rich *CIGS* surface (blue curve, point (1)) and to a lesser extent the electrons inside the *i-ZnO*, at the boundary with the *CdS*, (blue curve, point (2)). Opposite behavior is obtained at high frequency (HF), in fact for $f > f_0$ the electrons at the front *CIGS* surface cannot follow the AC signal anymore, while the electron in the *i-ZnO* respond to the AC signal (red curve, point (2)).

In both cases, the charge modulated within the *CdS* is negligible, due to the conduction band offsets and the resulting low concentration of electrons. In this case,

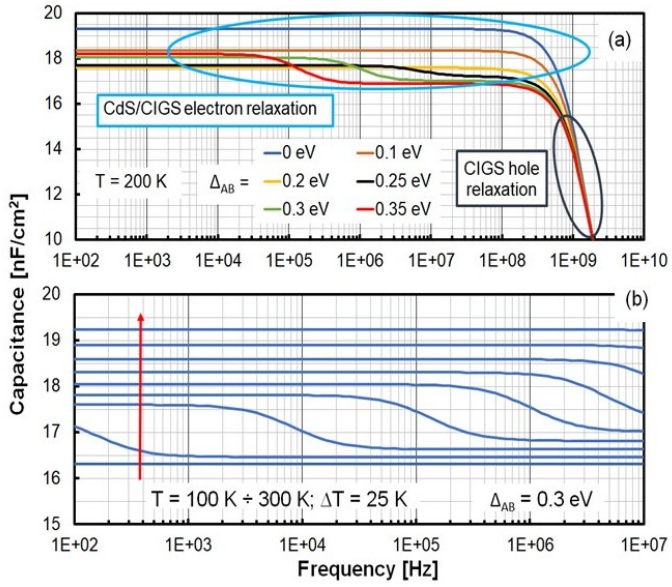

Figure 3.25: Simulated C(f,T) for different (a) conduction band offset at the CdS/CIGS interface and (b) temperatures. $\Delta_{BW} = -0.2eV$.

and also in the following, only the electrons behavior is taken into account because the holes respond to AC signal, at the edge of the depletion region in the *CIGS* (Figure 3.27), as long as its frequency is lower than $1/\tau_D$; where $\tau_D = 2\pi\varepsilon/\sigma$ is the hole dielectric relaxation time, ε is the dielectric constant and σ the conductivity. In this set of simulation at *200K* the hole dielectric relaxation time is $\tau_D = 118ps$ as shown in 3.25 (a).

Depending on the AC signal frequency, charge is thus modulated between the edge of the *CIGS* space-charge layer (holes) and the *CdS/CIGS* interface (electrons, LF case) or the *i-ZnO/CdS* interface (electrons, HF case). Assuming the same ε for all materials it is possible to define:

$$\frac{1}{C_{LF}} = \frac{w_p}{\varepsilon \cdot A} \tag{3.1}$$

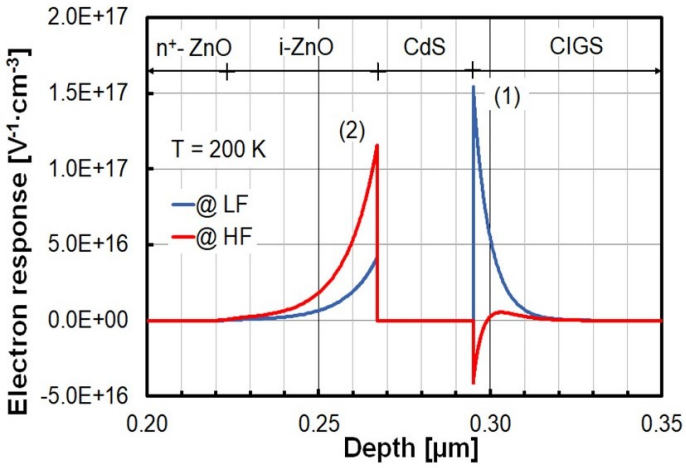

Figure 3.26: Electrons response to the ac signal vs depth for a frequency lower (LF) or higher (HF) than the inflection frequency f_0 of the capacitance step. $\Delta_{AB} = 0.1eV$, $\Delta_{BW} = -0.2eV$.

$$\frac{1}{C_{HF}} = \frac{w_p + w_n}{\varepsilon \cdot A} \tag{3.2}$$

where w_p and w_n are, respectively, the depletion widths on the n- and p-side of the junction, and A is the junction area, so it is possible to calculate:

$$w_n = \left(\frac{1}{C_{HF}} - \frac{1}{C_{LF}}\right) \cdot A \cdot \varepsilon \tag{3.3}$$

The 3.3 connects the step in *C(f)* curve with the n-side space-charge width, and calculate w_n values close to the *CdS* thickness ($t_{CdS} = 28nm$) are obtained for $\Delta_{AB} > 0.25eV$ as reported in table below.

	T=100K	T=200K	T=300K
$\Delta_{AB} = 0.25eV$	8	9	11
$\Delta_{AB} = 0.3eV$	27	28	28
$\Delta_{AB} = 0.35eV$	33	34	34

The simulations were repeated for $\Delta_{AB} = 0.3eV$ with different *CdS* thickness in

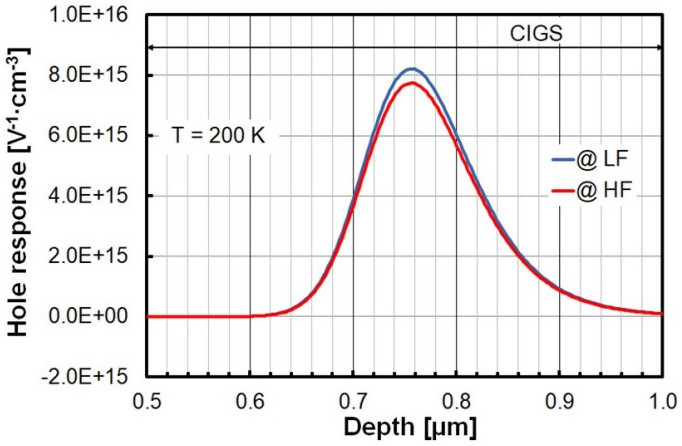

Figure 3.27: Holes response to the ac signal vs depth for a frequency lower (LF) or higher (HF) than the inflection frequency f_0 of the capacitance step. $\Delta_{AB} = 0.1eV$, $\Delta_{BW} = -0.2eV$.

the range $28nm \div 50nm$ finding a perfect correlation between the buffer layer thickness and the capacitance step (Figure 3.28).

$t_{CdS}[nm]$	$w_n[nm]$
28	27
30	29
35	34
40	40
45	45
50	51

It was also found that f_0 is related to the dielectric relaxation time of the electrons inside the *CdS*:

$$\tau_{D,CdS} = \frac{2\pi\varepsilon}{n_{CdS}\mu_{n,CdS}} \tag{3.4}$$

where n_{CdS} is the electron density in the *CdS* at the interface with the *CIGS*, and $\mu_{n,CdS}$ their mobility. Indeed analyzing the Arrhenius plot of $1/\tau_{D,CdS}$ (Figure 3.29

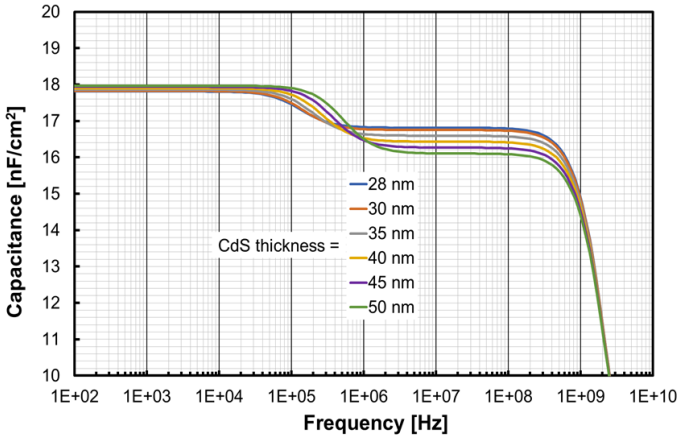

Figure 3.28: Simulated C-f for different thickness of CdS.

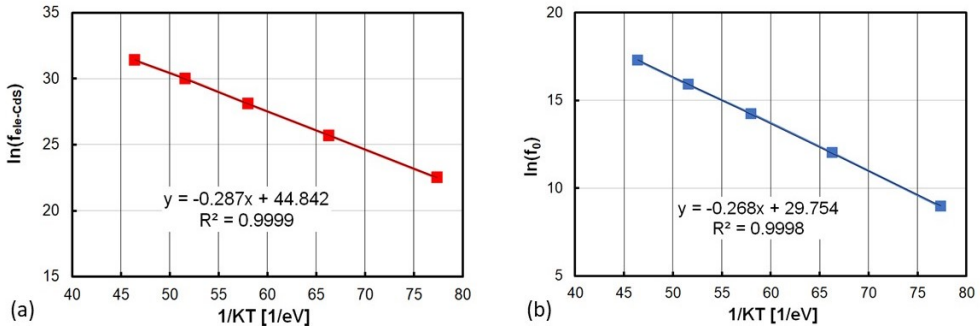

Figure 3.29: Arrhenius plots of $1/\tau_{D,CdS}$ (a) and inflection point f_0 (b)

(a)) for a structure with $\Delta_{AB} = 0.3$, it is possible to extract an activation energy of $E_{A,CdS} = 0.287eV$ which is very close to that extracted from the inflection point of the *C(f,T)* spectra in Figure 3.25 (b), which is $E_{A,Cf} = 0.268eV$ (Figure 3.29 (b)).

This correlation also explain why f_0 is smaller for larger Δ_{AB}: higher Δ_{AB} implies fewer electrons in the *CdS*, hence larger $\tau_{D,CdS}$.

3.6.2 Interfacial defect states

The generally interpretation of the capacitance step assumes a defect at or close to the hetero-interface [34] [37]. Indeed for modulation frequencies lower than the defect thermal emission rate the trap responds to the signal at the depth where the trap energy crosses the quasi-Fermi level, while for higher frequencies the trap does not contribute to the capacitance.

In this subsection it will shown a set of simulations with donor traps located in a *1-nm* thick layer at the *CdS/CIGS* interface. The trap density N_{TD} is varied while the trap energy and also the the electron/hole capture cross-section are fixed at $E_T = 0.2eV$ below the conduction band and $\sigma_{e/h} = 1 \cdot 10^{-16} cm^2$ respectively. The conduction band offsets $\Delta_{AB} = 0.1eV$ and $\Delta_{BW} = -0.2eV$, values that do not induce any step in the *C(f,T)* curves (Figure 3.25 (a)).

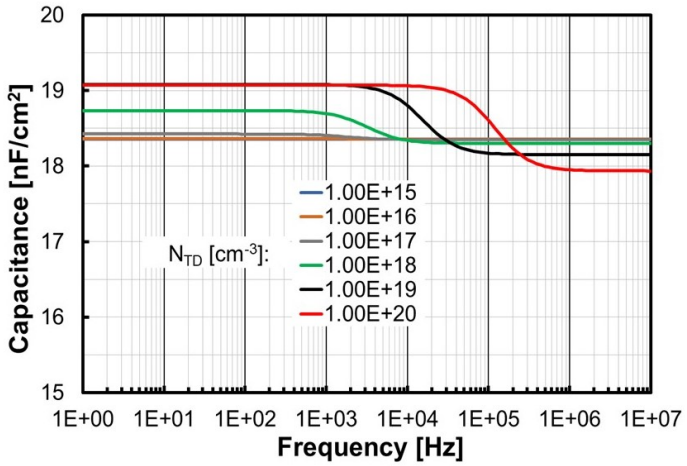

Figure 3.30: Simulated C-f for different concentration of donor defects, N_{TD}, at the CdS/CIGS interface. $t_{CdS} = 28nm$. w_n is calculate as described in the text.

In Figure 3.30 it is possible to note that a capacitance step appears for $N_{TD} \geq 10^{18} cm^{-3}$, and the values of w_n calculated approaches t_{CdS} for $N_{TD} \geq 10^{19} cm^{-3}$, as reported in table below.

$N_{TD}[cm^{-3}]$	$w_n[nm]$
10^{15}	–
10^{16}	–
10^{17}	2
10^{18}	11
10^{19}	22
10^{20}	26

The higher the trap concentration at the interface, the more the capacitance response is dominated by the trapped charge at the *CdS/CIGS* interface, and the extension of the region between the *CdS/CIGS* interface and the edge of the *CIGS* depletion region (w_p) determines C_{LF}. Similar results could be obtained in the case of interfacial acceptor traps.

3.6.3 Schottky barrier at the rear contact

Another possible explanation of the experimentally-observed capacitance step of *C(f,T)* curves is a rear-contact Schottky barrier for holes ϕ_{Bp} (Figure 3.31) [34].

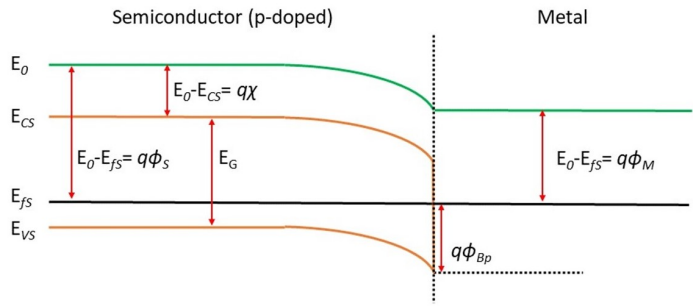

Figure 3.31: Band diagram of a Metal-Semiconductor junction (Schottky barrier).

The simulation of the structure with Schottky barrier for holes are shown in Figure 3.32, but without traps and with CBOs chosen in order to not obtain the step ($\Delta_{AB} = 0.1eV$ and $\Delta_{BW} = -0.2eV$). As it possible to observe, higher ϕ_{Bp} causes larger capacitance step (Figure 3.32 (a)), while the hole recombination velocity at the

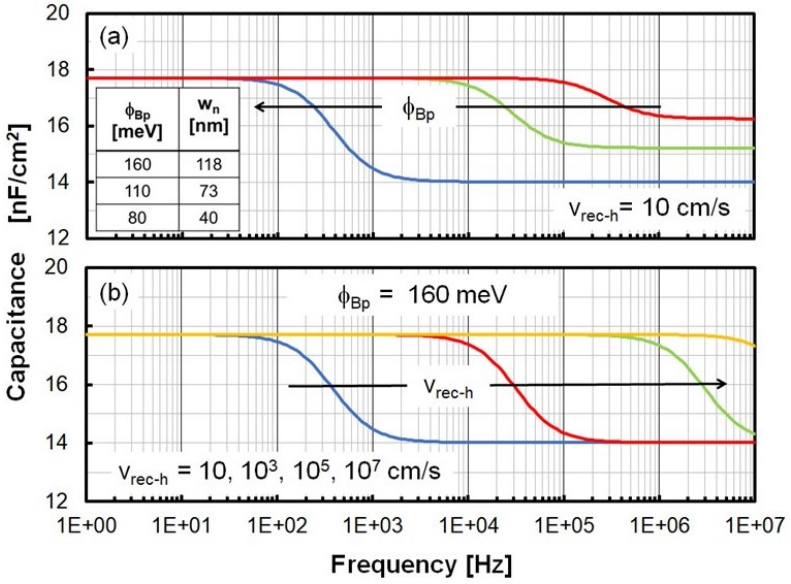

Figure 3.32: Simulated C-f for (a) different Schottky hole barrier height, ϕ_{Bp}, at the rear contact, and (b) $\phi_{Bp} = 160meV$ and different hole recombination velocity, v_{rec-h}, at the rear contact; $T = 125\ K$.

barrier, v_{rec-h}, only affects the inflection frequency, f_0 (Figure 3.32 (b)).

Reported in table in the inset of Figure 3.32 (a) the calculated w_n extracted by eq.3.3, as expected it has no relationship with t_{CdS}, rather in this case the width of the Schottky barrier [34] was obtained. The f_0 in this case discriminates between a regime where the charge at the rear contact responds to the AC signal and a regime where it does not.

3.6.4 Grain Boundaries in the CIGS

To complete the study also the poly-crystalline nature of *CIGS* has been taken in account by considering the presence of defects at the grain boundaries [39] [40] [41] [42].

In order to simulate a realistic structure with GBs, it was considered a grain size

of $1\mu m$ where the GB is modeled by a *2 nm* wide region rich with donor traps which are characterized by an electron/hole capture cross-section of $\sigma_{e/h} = 10^{-18} cm^2$. The distribution of traps was assumed to be Gaussian with peak concentration $N_{DT}^{Peak} = 2 \cdot 10^{20} eV^{-1} cm^{-3}$, peak energy $E_T^{Peak} = 1.1eV$ from the valence band, and standard deviation $w_T = 0.01eV$ so the corresponding integrated defect density is $\phi_{DT0} = 10^{12} cm^{-2}$. With these values the corresponding equilibrium ionized trap density at the GB is $N_{DT0}^{+} = 8.4 \cdot 10^{18} cm^{-3}$ which integrated corresponds to $\phi_{DT0} = 8.4 \cdot 10^{11} cm^{-2}$.

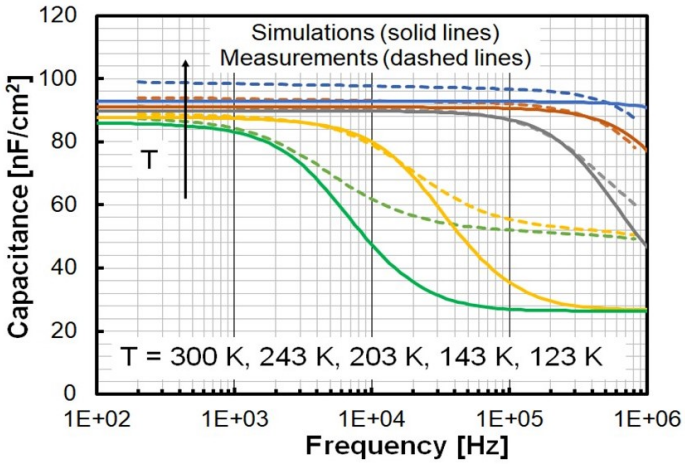

Figure 3.33: Measured (dashed lines) and simulated (solid lines) capacitance spectra of a cell with KF PDT.

Figure 3.33 shows the comparison between simulations and measurements, the fitting is quite good. The N_{DT}^{Peak} and w_t used have been chosen as fitting parameters, instead $E_T^{Peak} = 1.1eV$ is taken from the activation energy extracted from the inflection frequency f_0 of the measured *C(f,T)* spectra.

In this case, a capacitance step appears in the simulated *C(f,T)* curves of Figure 3.33 (solid lines) that is compatible with the measured one, although at the lowest temperatures the measured C_{HF} is significantly larger than the simulated value.

In this case, the extracted w_n is $230nm$ which is very different from the one calculated for the measurements $w_n = 72nm$ but, it is very close to the simulated

depletion width across the GB, which is about 200nm. The depletion region is due to the donor traps which decorate the GB: in fact, the positive charge of ionized defects determines a downward band bending at the GB that repels holes and depletes the surrounding region [41] [42].

It is possible to obtain an opposite behavior if acceptor traps are considered at the GB, in fact no capacitance step arises in the simulations; the possible explanation is the absence of a depletion region because the negative charge of ionized defects determines an upward band bending around the GB so there is an accumulation of holes that are the majority and no formation of depletion region.

This section was dedicated to the analysis of the admittance spectroscopy of *CIGS* solar cells. All the possible origins of the capacitance step were studied and can be summarize as follows:

- high CBO at the CdS/CIGS interface (Δ_{AB});
- high density of defects at the CdS/CIGS interface;
- a Schottky barrier for holes at the rear contact;
- donor-decorated grain boundaries.

It was also demonstrated that the inflection frequency of the capacitance step due to Δ_{AB} is related with the dielectric relaxation time of the electrons in the *CdS*.

Moreover, comparing the w_n extracted, it is possible to observe that, differently from what indicate the theory, a $w_n \approx t_{cdS}$ can be obtained only in two cases: in presence of high Δ_{AB} or high density of defects at the *CdS/CIGS* interface, instead in the other cases $w_n \gg t_{cdS}$.

The same absence of correlation between w_n and t_{CdS} can be find in literature [34] [37], this may indicate that a Schottky barrier or downward-bent GB could be the reason for depletion widths (calculated from measured capacitance step heights) much larger than the *CdS* thickness. This result may help to discriminate among the possible origins of the capacitance step.

Chapter 4

Limiting factors of CIGS solar cells performance

In this chapter the main limiting factors of CIGS solar cells performance will be investigated: non-radiative recombination and optical losses. The effects of traps in the bulk or at the CdS/CIGS interface will be presented; the effect of the presence of an Order Vacancy Compound (OVC) and a KIS layer possibly due to the alkali treatment will be also analyzed. Finally the effect of the grain boundaries on the performance of the cells will be introduced.

4.1 Bulk traps

One of the main causes of the non-radiative recombinations in the cells are the traps in the bulk of the absorber [30] [31]; in this section a set of simulations aim to analyzed the effect of this type of traps on the cells performance will be presented.

This set of simulations is based on both EMPA and ZSW cells, simulated with optical coefficient taken from literature [29] for a *CIGS* with a *CGI* of *0.9*. The cells parameters obtained with these optical values are reported in the following table.

	V_{OC}	J_{SC}	FF	η
EMPA simulated	0.74	34.1	80.1	20.6
ZSW simulated	0.81	34.0	83.6	23.6

4.1.1 EMPA cell

In this subsection only the effect of donor type traps will be analyzed. The effect of variation of the absorber bulk mid-gap defect density is shown in Figures 4.1 4.2 4.3.

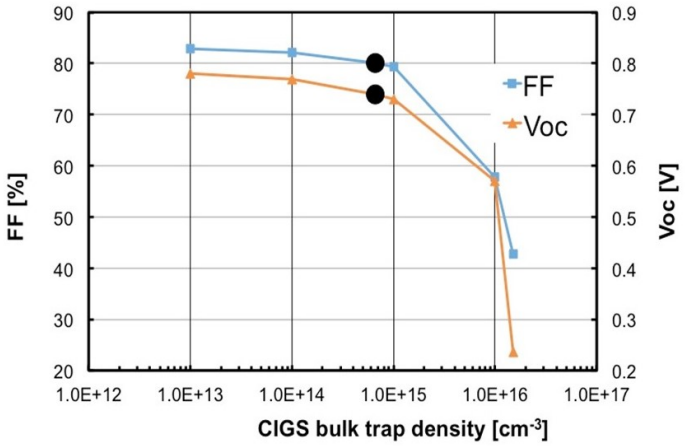

Figure 4.1: Simulated open-circuit voltage (V_{OC}) and FF vs. bulk defect density for the EMPA cell. The black dot marks the baseline cell value.

The black dot in all the figures marks the baseline value of the figures of merit; these values correspond to a baseline donor concentration of $6.67 \cdot 10^{14} cm^{-3}$ which can be translate in a lifetime of $300 ns$.

It is possible to observe from Figure 4.1 that for concentration higher than $1 \cdot 10^{15} cm^{-3}$ the V_{OC} and FF dramatically decrease because the recombination increase, so it is possible to affirm that concentration higher than $1 \cdot 10^{15} cm^{-3}$ are not compatible with high efficiency ($> 20\%$) as shown in Figure 4.3.

It was also studied the effect of the variation of electron capture cross-section of the donor defect. Figure 4.4 shows the EQE of the cell for varying cross-section.

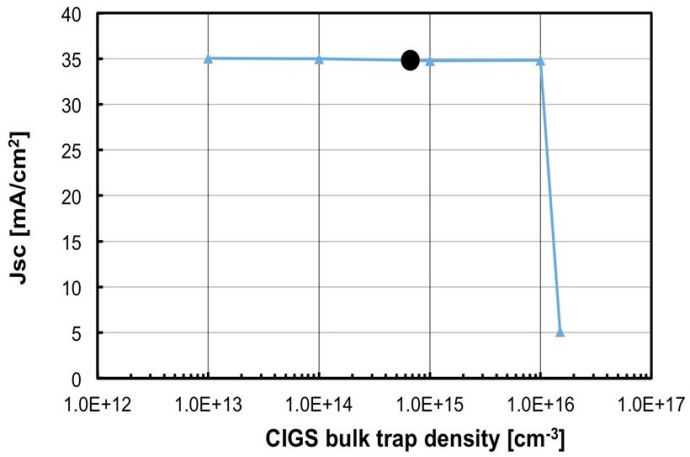

Figure 4.2: Simulated J_{SC} vs. bulk defect density for the EMPA cell. The black dot marks the baseline cell value.

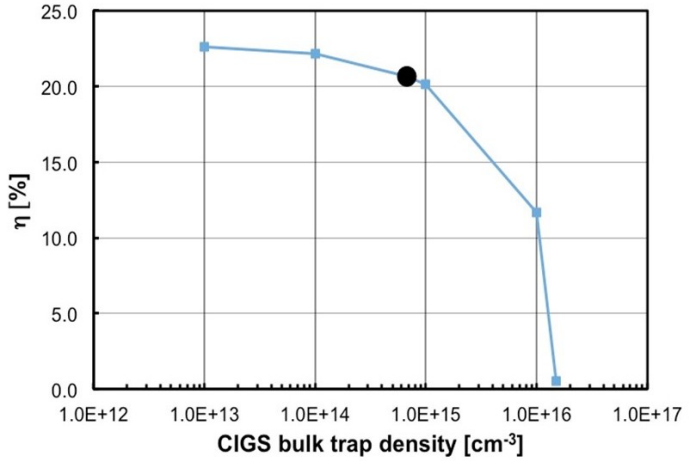

Figure 4.3: Simulated η vs. bulk defect density for the EMPA cell. The black dot marks the baseline cell value.

To complete this analysis on the bulk traps, the effect of the traps energy has been also investigated. In Figure 4.5 the efficiency of the baseline in function of the energy

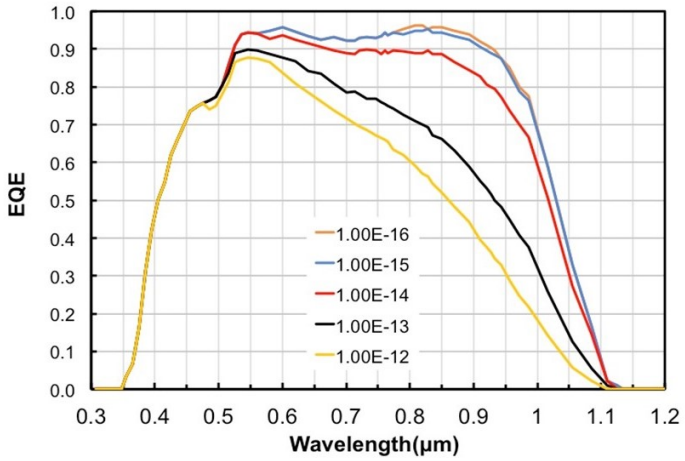

Figure 4.4: Simulated EQE vs. bulk trap electron capture cross-section (legend, in cm^2) for the EMPA cell. The blue line ($10^{-15}cm^2$) corresponds to the baseline cell case.

level is shown: it is possible to observe that the trap defects are influential as far as they are placed within $0.25eV$ of the intrinsic Fermi level ($EnMid = 0$).

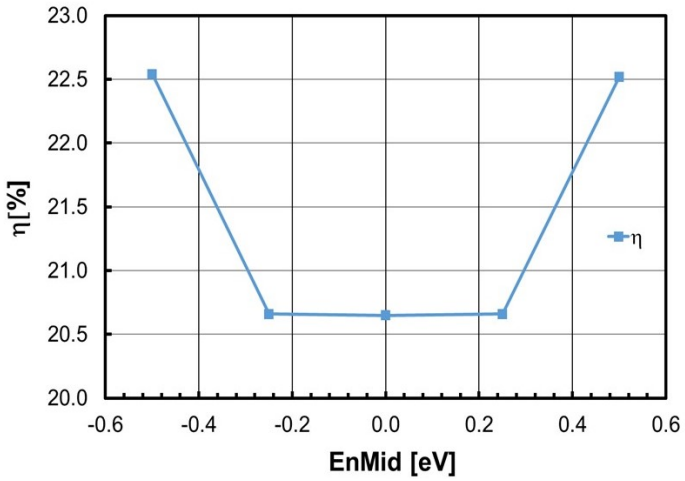

Figure 4.5: Simulated η vs. energy level of bulk traps for EMPA cell.

4.1.2 ZSW cell

One of the main differences between the two baseline cells is the number of bulk traps, indeed in the EMPA cell there is one bulk trap instead in the ZSW cell there are four different bulk traps (two donors and two acceptors).

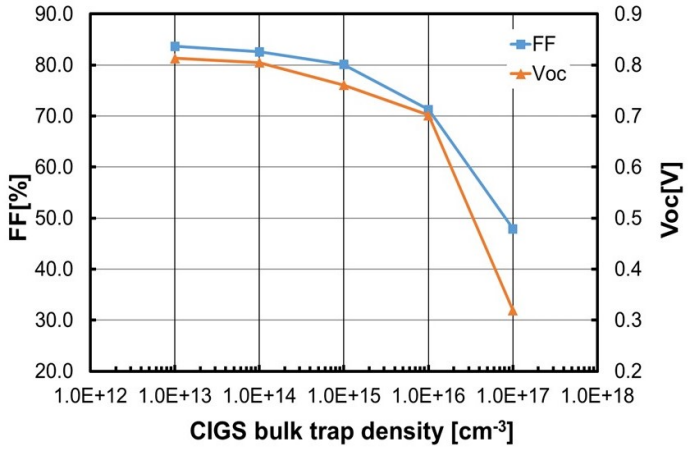

Figure 4.6: Simulated V_{OC} and FF vs. bulk defect density for the ZSW cell.

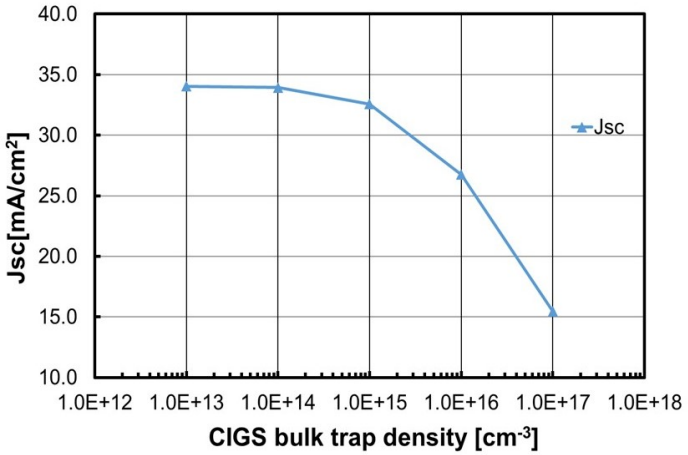

Figure 4.7: Simulated J_{SC} vs. bulk defect density for the ZSW cell.

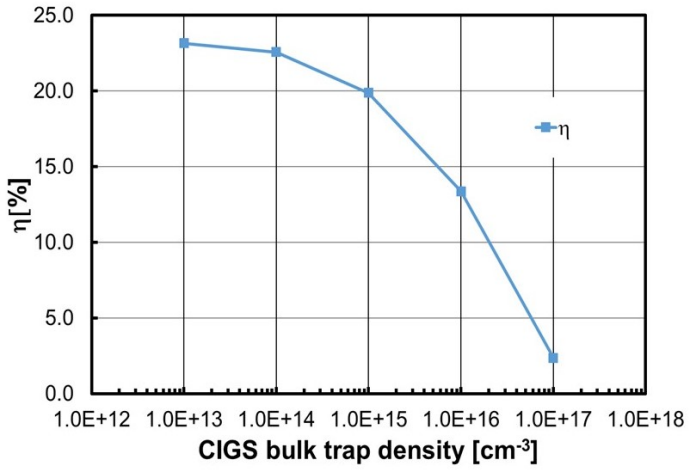

Figure 4.8: Simulated η vs. bulk defect density for the ZSW cell.

For this reason it was decided to vary the concentration of all traps in the same way.

The effect of variation of the absorber bulk defect densities is shown in Figures 4.6, 4.7 and 4.8. In this case V_{OC} and FF have acceptable value up to a concentration of $1 \cdot 10^{15} cm^{-3}$ (Figure 4.6) but, the reduction of Jsc leads to low simulated efficiency. So even in this case it is possible to state that bulk traps density higher than $1 \cdot 10^{15} cm^{-3}$ are not compatible with high efficiency ($> 20\%$) as shown in Figure 4.8. The same happens for EMPA cell as stated before.

4.2 CIGS/Buffer interface traps

In this section one of the main cause of non-radiative recombination in the cell will be analyzed: traps at interface between Buffer and *CIGS* [43] [44]. This set of simulations is based on the EMPA cell simulated with absorption coefficients measured at EMPA [24] for all the materials as presented in Chapter 2. The corresponding figures of merits are:

$$V_{OC} = 0.741V,\ J_{SC} = 36.4 \frac{mA}{cm^2},\ FF = 80.1\% \text{ and } \eta = 21.6\%.$$

In the framework of these simulations, the defect-rich *CIGS/buffer* interface is modelled as a *1-nm* thick layer of *CIGS* with additional traps with respect to the *CIGS* bulk. These traps may be either acceptors or donors, and their default energy level is at mid-gap. Recombination via these interface defects is described by the SRH model [9]:

$$R = \frac{N_{IT} v_{THn} v_{THp} \sigma_{nIT} \sigma_{pIT} (np - n_i^2)}{v_{THn} \sigma_{nIT} (n + n_1) + v_{THp} \sigma_{pIT} (p + p1)} \tag{4.1}$$

with

$$n_1 = n_i \cdot e^{\frac{E_{IT} - E_i}{kT}} \tag{4.2}$$

$$p_1 = n_i \cdot e^{\frac{E_i - E_{IT}}{kT}} \tag{4.3}$$

N_{IT} and E_{IT} are the interface trap density and energy level, v_{THn} and v_{THp} are the electron and hole thermal velocities, σ_{nIT} and σ_{pIT} the electron and hole capture cross-sections, n_i and E_i the intrinsic carrier concentration and intrinsic Fermi level.

The recombination rate of the SRH model can also be written as:

$$R = \frac{np - n_i^2}{\tau_{pIT}(n + n_1) + \tau_{nIT}(p + p_1)} \tag{4.4}$$

with

$$\tau_{nIT} = \frac{1}{N_{IT} v_{THn} \sigma_{nIT}} \tag{4.5}$$

$$\tau_{pIT} = \frac{1}{N_{IT} v_{THp} \sigma_{pIT}} \tag{4.6}$$

τ_{nIT} and τ_{pIT} are the electron and hole lifetime at interface.

It is worthwhile to remember that in EMPA a conduction band offset of $0.3eV$ is considered at the *CdS/CIGS* interface.

4.2.1 Interface acceptor traps

In the literature there are several studies on the interface traps: both acceptors and donors defects are hypothesized, therefore it is necessary to simulate the two cases to better understand the possible effects of different traps. In this section the effects of acceptor traps at interface between buffer and absorber will be analyzed.

4.2.1.1 Acceptor traps with $\sigma_{nIT} = \sigma_{pIT}$

In a first set of simulations, mid-gap interface acceptors (previous simulations, presented in Section 4.1.1, showed that the effect of interface acceptors is largely independent of the trap energy level, as long as the latter is within ±0.25 eV of the intrinsic Fermi level) with equal electron and hole capture cross-sections are considered. Figures 4.9, 4.10, 4.11 and 4.12 show the impact on cell performance of the density of traps in the cases $\sigma_{nIT} = \sigma_{pIT} = 1 \cdot 10^{-16} cm^2$ (red lines) and $\sigma_{nIT} = \sigma_{pIT} = 1 \cdot 10^{-14} cm^2$ (blue lines).

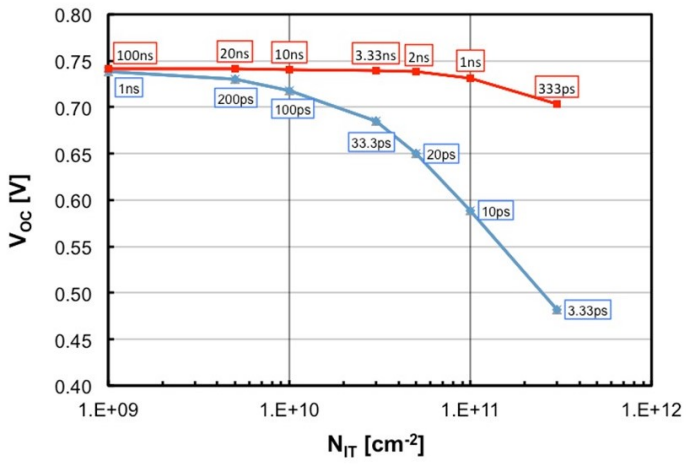

Figure 4.9: Open-circuit voltage as a function of interface acceptor density, with $\sigma_{nIT} = \sigma_{pIT} = 1 \cdot 10^{-16} cm^2$ (red line) and with $\sigma_{nIT} = \sigma_{pIT} = 1 \cdot 10^{-14} cm^2$ (blue line).

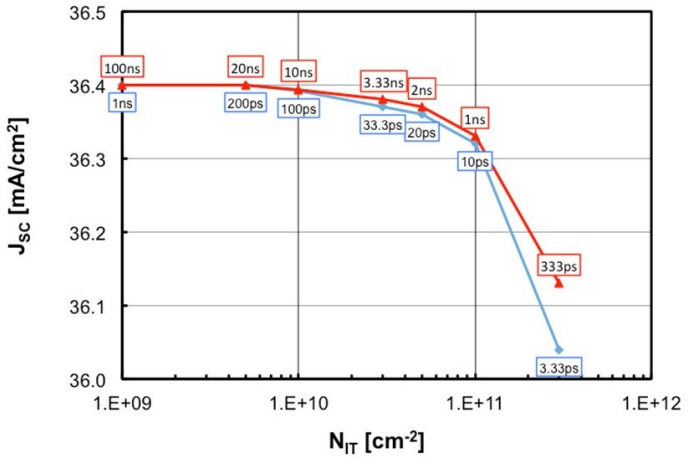

Figure 4.10: Short-circuit current as a function of interface acceptor density, with $\sigma_{nIT} = \sigma_{pIT} = 1 \cdot 10^{-16} cm^2$ (red line) and with $\sigma_{nIT} = \sigma_{pIT} = 1 \cdot 10^{-14} cm^2$ (blue line).

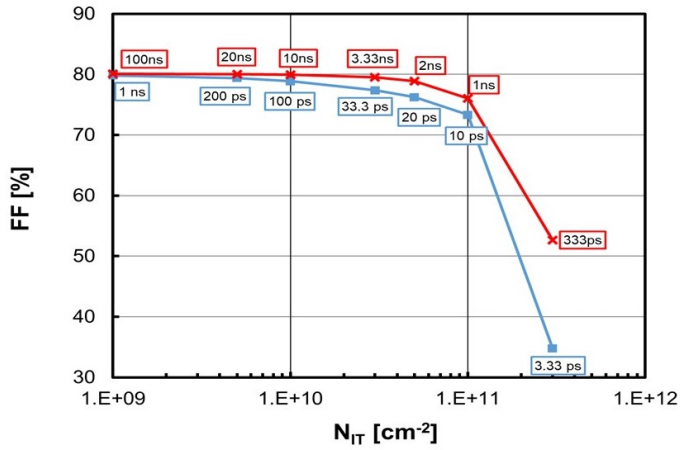

Figure 4.11: Fill factor as a function of interface acceptor density, with $\sigma_{nIT} = \sigma_{pIT} = 1 \cdot 10^{-16} cm^2$ (red line) and with $\sigma_{nIT} = \sigma_{pIT} = 1 \cdot 10^{-14} cm^2$ (blue line).

The value of $\tau_{nIT} = \tau_{pIT}$ corresponding to each value of N_{IT} is indicated in the

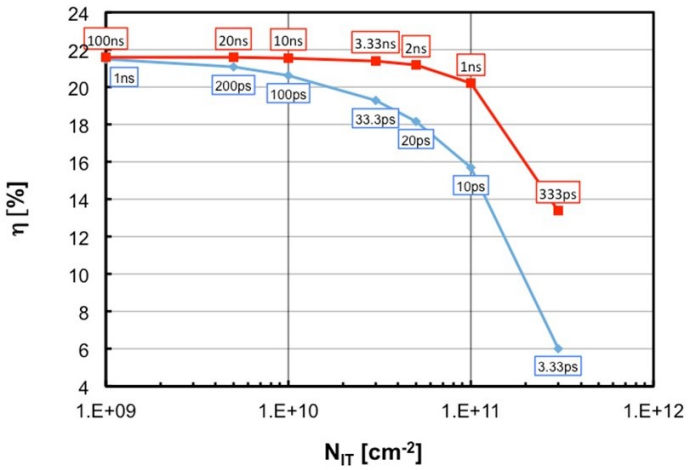

Figure 4.12: Efficiency as a function of interface acceptor density, with $\sigma_{nIT} = \sigma_{pIT} = 1 \cdot 10^{-16} cm^2$ (red line) and with $\sigma_{nIT} = \sigma_{pIT} = 1 \cdot 10^{-14} cm^2$ (blue line).

charts. As expected the curve of $\sigma_{nIT} = \sigma_{pIT} = 1 \cdot 10^{-16} cm^2$ (red lines) is always above the curve of $\sigma_{nIT} = \sigma_{pIT} = 1 \cdot 10^{-14} cm^2$ (blue lines), because in the blu lines the traps concentration is the same of the red lines but the cross-section is larger so the lifetime is lower and the traps have more effect on the figures of merit of the cell. It is possible to conclude that in case of $\sigma_{nIT} = \sigma_{pIT} = 1 \cdot 10^{-16} cm^2$ traps concentration higher than $1 \cdot 10^{11} cm^{-2}$ are not compatible with high efficiency ($> 20\%$), instead for $\sigma_{nIT} = \sigma_{pIT} = 1 \cdot 10^{-14} cm^2$ only traps concentration lower than $1 \cdot 10^{10} cm^{-2}$ are compatible with high efficiency (Figure 4.12).

In a second set of simulations, it was varied the interface acceptor lifetimes $\tau_{nIT} = \tau_{pIT}$ by changing the value of $\sigma_{nIT} = \sigma_{pIT}$, while keeping the density N_{IT} fixed.

The effect on the performance of the cell is illustrated by Figures 4.13, 4.14, 4.15 and 4.16; as expected, V_{OC} suffers due to surface recombination for small lifetimes (Figure 4.13), while the effect of changing lifetimes on J_{SC} is minor (Figure 4.14).

It is interesting to note that, even when lifetimes are so long as not to limit V_{OC} anymore (see Figure 4.13 for lifetimes in excess of a few *ns*), there is a significant

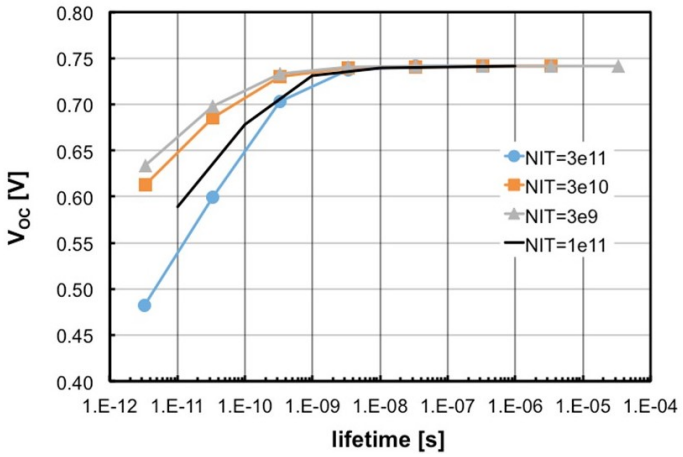

Figure 4.13: Open-circuit voltage as a function of interface acceptor lifetime $\tau_{nIT} = \tau_{pIT}$, for different values of the acceptor density N_{IT} (in cm^{-2} in the legend).

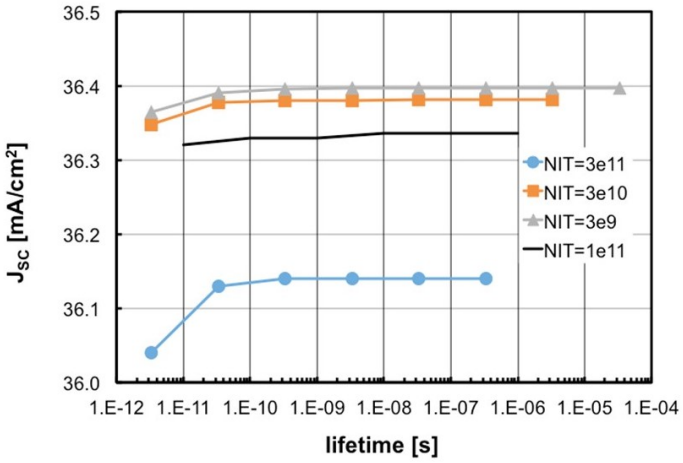

Figure 4.14: Short-circuit current as a function of interface acceptor lifetime $\tau_{nIT} = \tau_{pIT}$, for different values of the acceptor density N_{IT} (in cm^{-2} in the legend).

impact of the trap concentration on FF and, consequently, on the efficiency. This is mostly due to the electro-statics of the surface acceptors: larger N_{IT} means larger

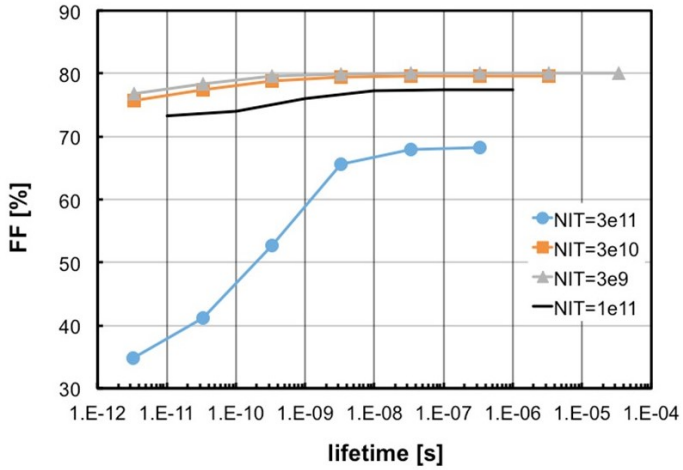

Figure 4.15: Fill Factor as a function of interface acceptor lifetime $\tau_{nIT} = \tau_{pIT}$, for different values of the acceptor density N_{IT} (in cm^{-2} in the legend).

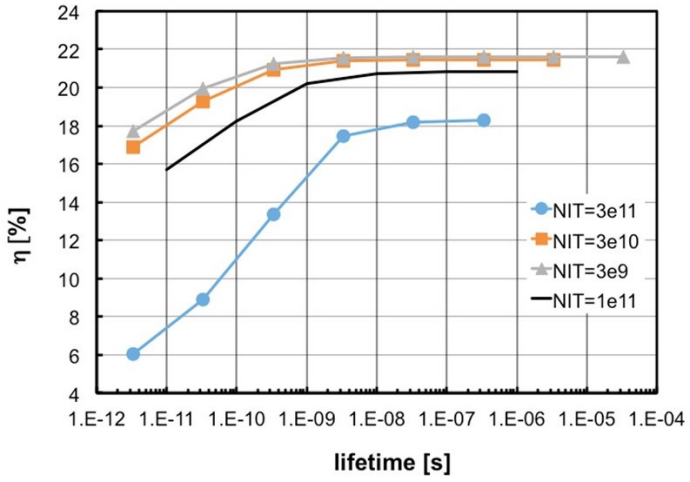

Figure 4.16: Efficiency as a function of interface acceptor lifetime $\tau_{nIT} = \tau_{pIT}$, for different values of the acceptor density N_{IT} (in cm^{-2} in the legend).

trapped negative charge, weaker surface inversion, hence smaller conductance of the top region of the *CIGS* absorber.

4.2.1.2 Acceptor traps with $\sigma_{nIT} \neq \sigma_{pIT}$

It was also evaluated the effect of varying the electron and hole capture cross-sections (i.e., the lifetimes) independently. Figures 4.17 and 4.18 show the effect of a large concentration of interface acceptors ($N_{IT} = 3 \cdot 10^{11} cm^{-2}$) when $\tau_{pIT} = 333ns$ (i.e., a large value) and τ_{nIT} is varied over a few decades.

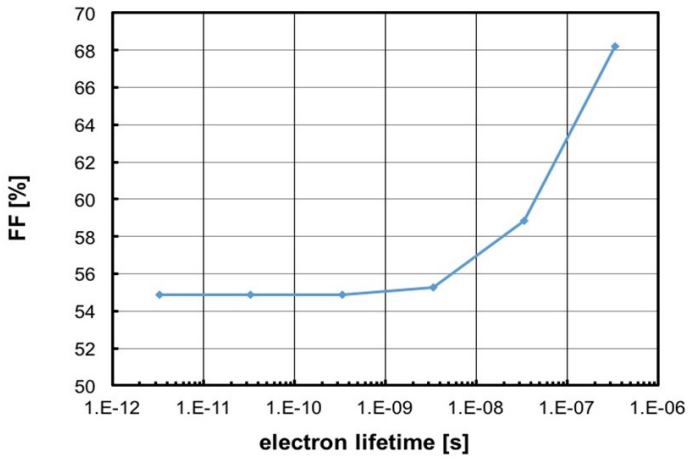

Figure 4.17: Fill factor as a function of interface acceptor electron lifetime τ_{nIT} ($\tau_{pIT} = 333ns$). $N_{IT} = 3 \cdot 10^{11} cm^{-2}$.

No effect is observed on either V_{OC} or J_{SC}, and the efficiency improvement for longer electron lifetimes is entirely due to the increase of *FF*.

These effects can be explained as follows: (1) since the *CIGS* surface is inverted ($\Delta_{AB} = 0.3eV$), holes are minority carriers, and since it was kept $\tau_{pIT} = 333ns$ the recombination rate is low and independent of τ_{nIT} (2) increasing τ_{nIT}, however, i.e., decreasing the electron capture cross-section of the interface traps, de-populates the interface acceptors of electrons; consequently, the surface potential increases, surface inversion is enhanced and the *CIGS* surface region becomes more conductive, hence

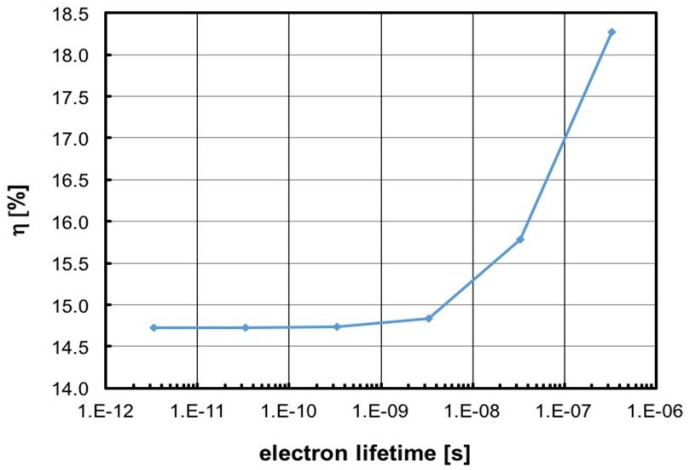

Figure 4.18: Efficiency as a function of interface acceptor electron lifetime τ_{nIT} ($\tau_{pIT} = 333ns$). $N_{IT} = 3 \cdot 10^{11} cm^{-2}$.

larger *FFs* and efficiencies.

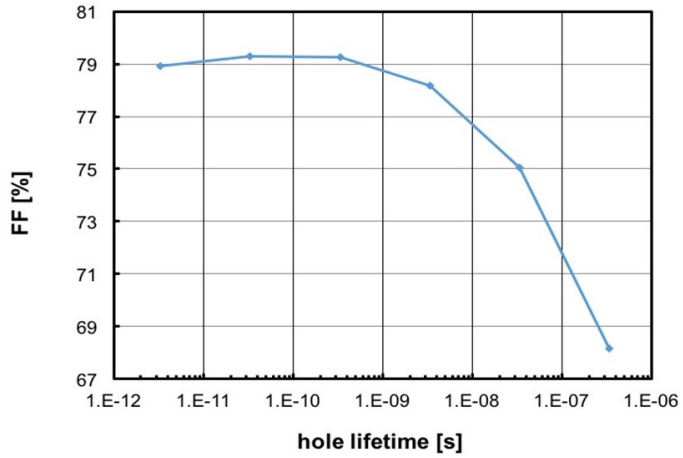

Figure 4.19: Fill factor as a function of interface acceptor hole lifetime τ_{pIT} ($\tau_{nIT} = 333ns$). $N_{IT} = 3 \cdot 10^{11} cm^{-2}$.

On the other hand, Figures 4.19 4.20 show the effect of a large concentration of interface acceptors ($N_{IT} = 3 \cdot 10^{11} cm^{-2}$) when $\tau_{nIT} = 333ns$ (i.e., a large value) and τ_{pIT} is varied over a few decades.

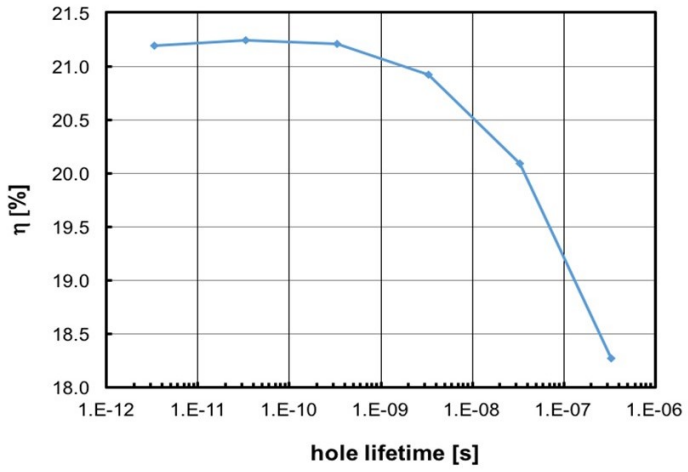

Figure 4.20: Efficiency as a function of interface acceptor hole lifetime τ_{pIT} ($\tau_{nIT} = 333ns$). $N_{IT} = 3 \cdot 10^{11} cm^{-2}$.

The effect is negligible on V_{OC} and very minor on J_{SC}, while a remarkable decrease of FF with increasing hole lifetime drives the efficiency down. Once more, the cause of this behavior can be traced down to the electro-static effect of interface traps, not to recombination - the latter requiring both lifetimes to be small to be significant – since larger τ_{pIT}, so smaller hole capture cross-section, means fewer neutral interface acceptors, weaker downward band bending and surface inversion, and as a consequence less conductive *CIGS* surface.

4.2.2 Interface donor traps

The effect of donor traps (mid-gap) at interface between *CdS* and *CIGS* was analyzed; Figures 4.21, 4.22, 4.23 and 4.24 show the effect on the performance of the cell. In these simulations the trap concentration (N_{IT}) was kept constant and it was varied the cross-section in order to change the lifetimes ($\tau_{pIT} = \tau_{nIT}$).

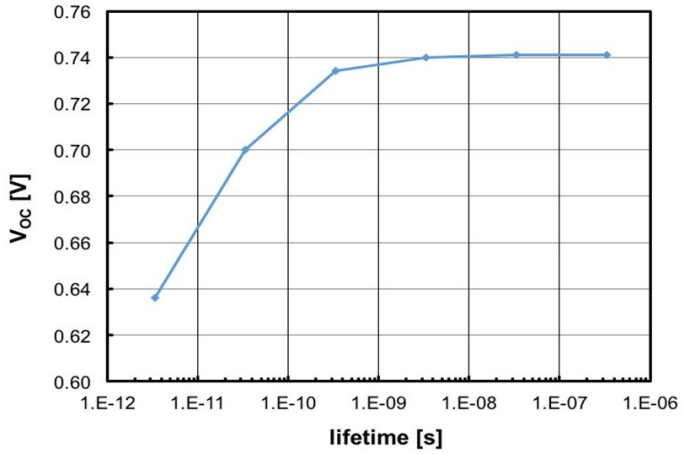

Figure 4.21: Open-circuit voltage as a function of interface donor lifetime $\tau_{pIT} = \tau_{nIT}$. $N_{IT} = 3 \cdot 10^{11} cm^{-2}$.

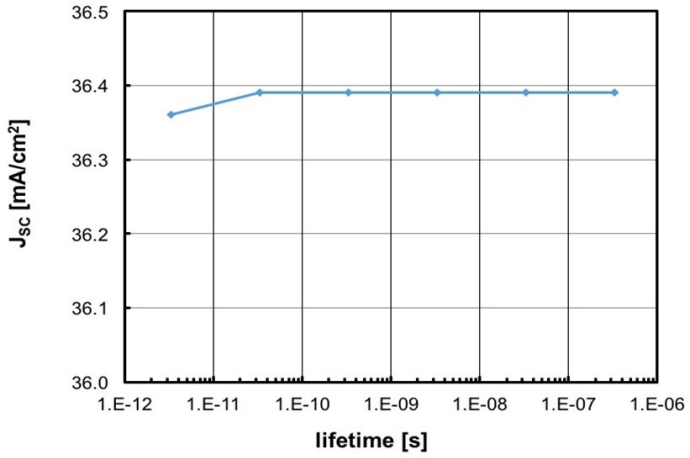

Figure 4.22: Short-circuit current as a function of interface donor lifetime $\tau_{pIT} = \tau_{nIT}$. $N_{IT} = 3 \cdot 10^{11} cm^{-2}$.

Comparing the effect on the cell performance of donor traps (Figures 4.21, 4.22, 4.23 and 4.24) with those of acceptor traps (Figures 4.9, 4.10, 4.11 and 4.12) it is

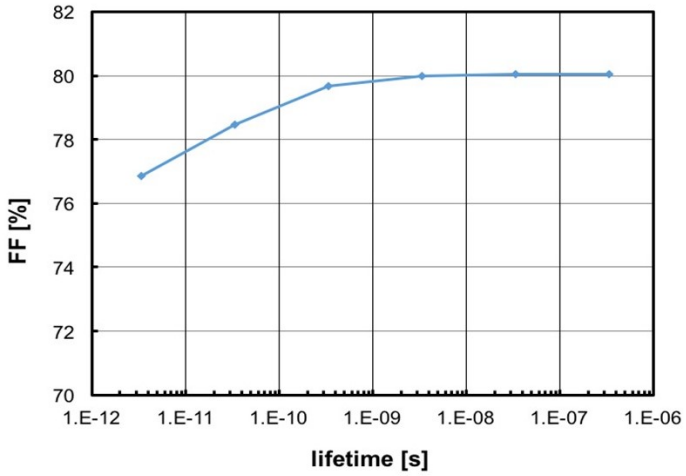

Figure 4.23: Fill Factor as a function of interface donor lifetime $\tau_{pIT} = \tau_{nIT}$. $N_{IT} = 3 \cdot 10^{11} cm^{-2}$.

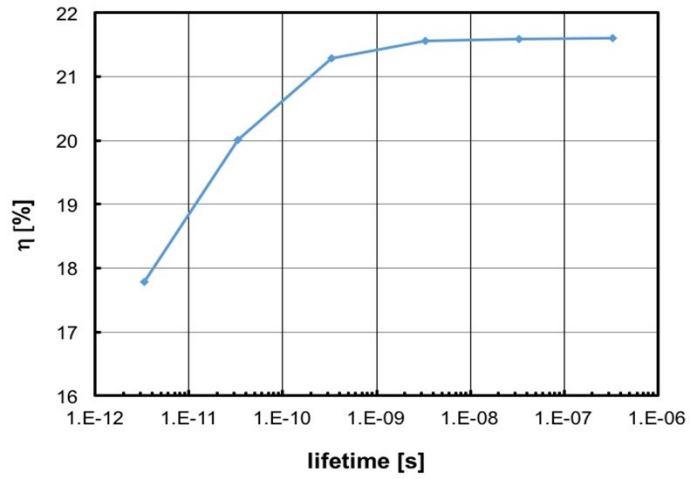

Figure 4.24: Efficiency as a function of interface donor lifetime $\tau_{pIT} = \tau_{nIT}$. $N_{IT} = 3 \cdot 10^{11} cm^{-2}$.

possible to highlight the more benign nature of surface donors, as opposed to surface acceptors.

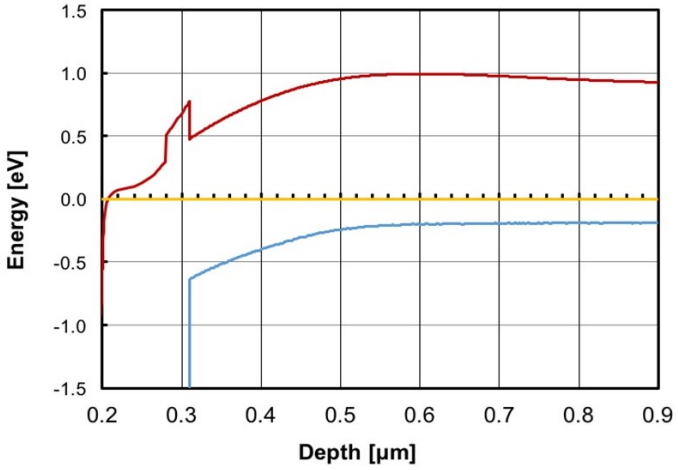

Figure 4.25: Equilibrium band diagram for the case of interface acceptors ($N_{IT} = 3 \cdot 10^{11} cm^{-2}$, $\tau_{pIT} = \tau_{nIT} = 3.3ps$).

This difference is due to a different band-bending, indeed: as shown by the band diagrams in Figures 4.25 and 4.26, positively charged donors contribute to the band down-bending at the *CIGS* surface, which enhances the region with electrons and improves the *FF*.

Moreover, since the surface is inverted and holes are minority carriers, when lifetimes are low, recombination is stronger in the presence of surface acceptors due to larger surface hole concentration: hence the lower V_{OC} observed in Figure 4.9 (blue curve) as compared with Figure 4.21.

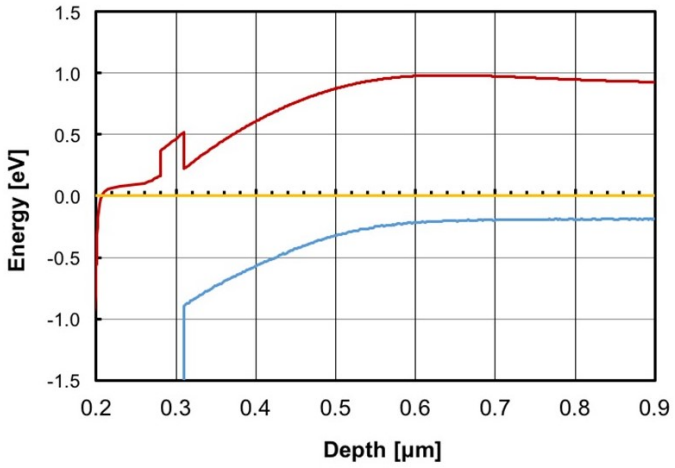

Figure 4.26: Equilibrium band diagram for the case of interface donors ($N_{IT} = 3 \cdot 10^{11} cm^{-2}$, $\tau_{pIT} = \tau_{nIT} = 3.3ps$).

4.3 CIGS/Buffer interface traps in case of alternative (non-CdS) buffers

One of the problem of *CIGS* based solar cells is the presence of *CdS* because it is toxic but, it forms an optimum interface with the *CIGS*; this mean low concentration of traps hence high carriers lifetime. In literature there are a lot of study which aim at removing the *CdS* as buffer and substitute it with other materials [22] [45] [46] [47] [48] [49] [50] [51] [52]: two of the main studied are the *ZnO* and *Zn(O,S)* that will be analyzed in the following of this section.

In this section a set of simulations aimed at studying the effect of interface traps between buffer and *CIGS* in the case of alternative buffers will be presented. These simulations are based on the EMPA cell simulated with absorption coefficients measured at EMPA for the *CIGS*, instead for the other material coefficient taken from literature [32] are used. The figures of merit of the baseline are the following:

$$V_{OC} = 0.741V,\ J_{SC} = 36.4\frac{mA}{cm^2},\ FF = 80.1\% \text{ and } \eta = 21.6\%.$$

In these simulations is replaced the *30 nm-thick CdS* layer of the EMPA structure described in Chapter 2 with either a *ZnO* or a *Zn(O,S)* layer. The conduction band offsets (CBOs) of the different stacks are detailed in table below (a positive conduction band offset means a "spike", a negative one gives a "cliff").

Solar cell stack	CBO CIGS/Buffer [eV]	CBO Buffer/ZnO [eV]
AZnO/i-ZnO/CdS/CIGS	0.3 [53]	-0.2 [22]
AZnO/i-ZnO/ZnO/CIGS	-0.2 [22]	0
ZnO/i-ZnO/Zn(O,S)/CIGS	0.2 [45]	0 [47]

The *Zn(O,S)* was chosen with a molar fraction of *S/Zn=0.28* but, moreover due to the lack of reliable specific data, its optical coefficients are assumed to be equal to those of *ZnO*: therefore, the main indications that these simulations provide are about the effect of different *CIGS/buffer* CBOs on trap-rich interfaces.

4.3.1 ZnO buffer

The first alternative buffer taken into account is the *ZnO*: when it is directly deposited on *CIGS* the band alignment shows a "cliff" between *CIGS* and buffer (conduction band edge is lower in the buffer than in the *CIGS*). In this subsection the cases of acceptor and donor traps at the *CdS/CIGS* interface for two different doping of the buffer will be studied.

4.3.1.1 Acceptor interface traps

The figures of merit for this stack configuration (*AZnO/i-ZnO/ZnO/CIGS*) in function of surface acceptor lifetimes ($\tau_{nIT} = \tau_{pIT}$) are shown in Figures 4.27, 4.28, 4.29 and 4.30. In these simulations the trap concentration was kept constant ($N_{IT} = 3 \cdot 10^{11} cm^{-2}$) and it was varied the cross-section in order to change the lifetimes.

Two values of doping density for the *30 nm-thick ZnO* buffer were considered, which give slightly different band alignments. In order to understand the consequences of replacing the *CdS* buffer with *ZnO*, the charts in Figures 4.27, 4.28, 4.29 and 4.30 can be compared with Figures 4.13, 4.14, 4.15 and 4.16 (blue lines), respectively, and the equilibrium band diagram of Figure 4.31 with that of Figure 4.25.

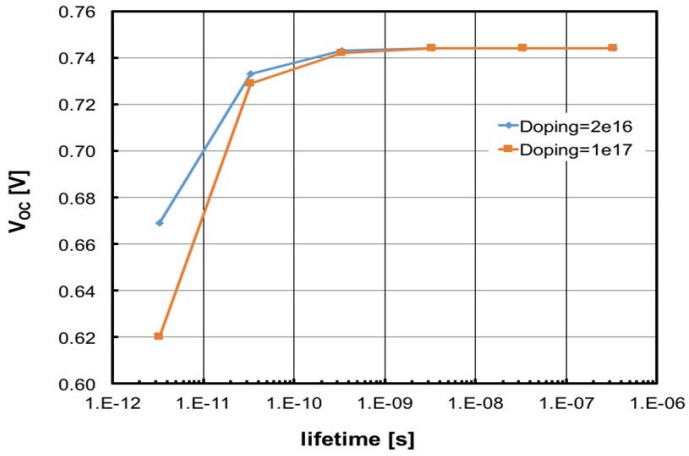

Figure 4.27: Open-circuit voltage as a function of interface acceptor lifetime $\tau_{nIT} = \tau_{pIT}$. $N_{IT} = 3 \cdot 10^{11} cm^{-2}$. Two different values of the buffer doping density were simulated, as shown in the legend.

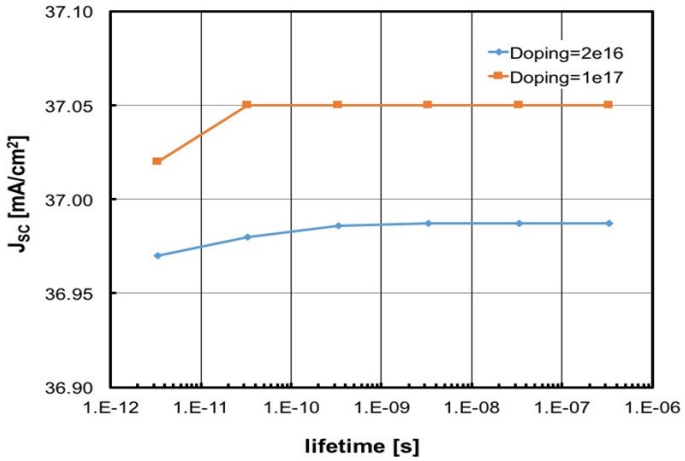

Figure 4.28: Short-circuit current as a function of interface acceptor lifetime $\tau_{nIT} = \tau_{pIT}$. $N_{IT} = 3 \cdot 10^{11} cm^{-2}$. Two different values of the buffer doping density were simulated, as shown in the legend.

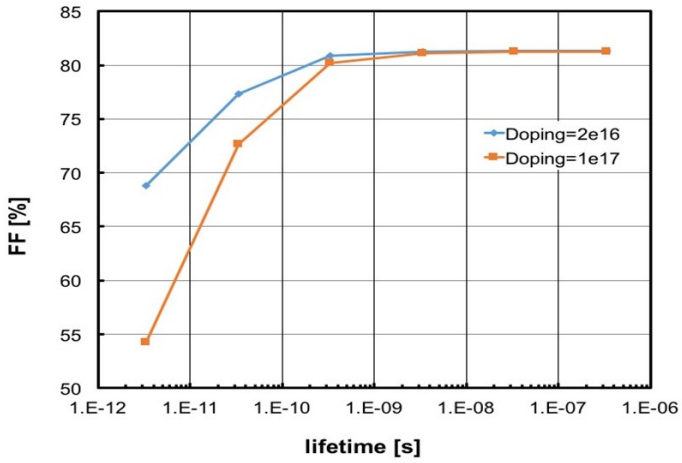

Figure 4.29: Fill factor as a function of interface acceptor lifetime $\tau_{nIT} = \tau_{pIT}$. $N_{IT} = 3 \cdot 10^{11} cm^{-2}$. Two different values of the buffer doping density were simulated, as shown in the legend.

There is a general qualitative similarity of behavior in the two structures (*CdS* buffer and *ZnO* buffer). As far as the observed differences are concerned, it should be pointed out that direct quantitative point-by-point comparison implies the assumption of the same acceptor interface density and lifetimes in the two structures, which is a bold idealization, so the following considerations should therefore be taken with caution.

In the stack with a *ZnO* buffer (Figure 4.27) V_{OC} is more resilient to low recombination lifetimes than that with the *CdS* buffer (Figure 4.13, blue line): due to different band alignments (compare Figure 4.31 with Figure 4.25), the *ZnO-buffered* cell has fewer holes (i.e., minority carriers) at the surface.

The J_{SC}, which is largely independent on lifetime and buffer doping (Figure 4.28), is significantly larger than that of the *CdS* buffer case (Figure 4.14, blue line) thanks to lower parasitic absorption in the *ZnO* buffer.

FF is much improved by the *ZnO* buffer (Figure 4.29 vs. Figure 4.15, blue line), due to the interface "cliff" and Fermi level position facilitating the flow of electrons

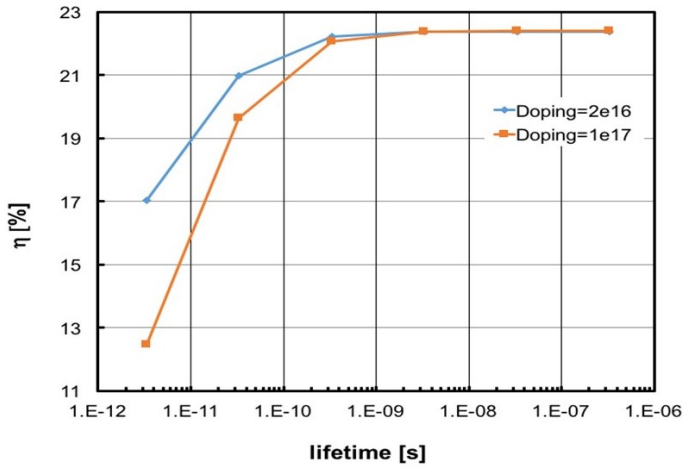

Figure 4.30: Efficiency as a function of interface acceptor lifetime $\tau_{nIT} = \tau_{pIT}$. $N_{IT} = 3 \cdot 10^{11} cm^{-2}$. Two different values of the buffer doping density were simulated, as shown in the legend.

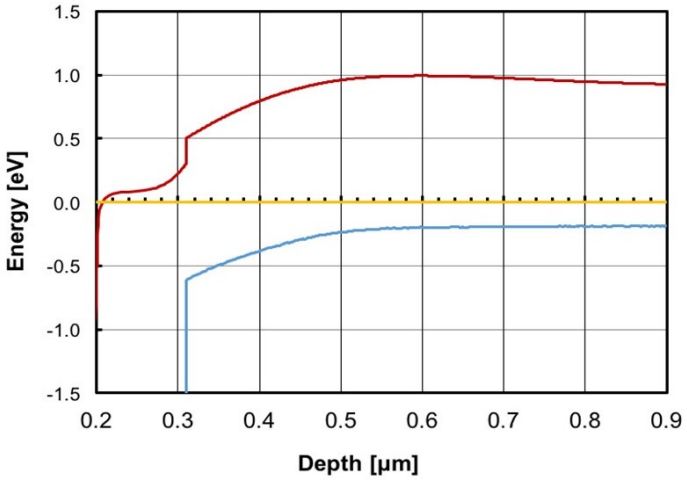

Figure 4.31: Equilibrium band diagram for the case of interface acceptors ($N_{IT} = 3 \cdot 10^{11} cm^{-2}$, $\tau_{nIT} = \tau_{pIT} = 3.3ps$); the buffer doping density is $10^{17} cm^{-3}$.

to the cathode.

Hence it is possible to conclude that thanks to J_{SC} and FF improvements, the efficiency is consistently larger in the *ZnO* buffer case (Figure 4.30 vs. Figure 4.16, blue line).

4.3.1.2 Donor interface traps

In Figures 4.32, 4.33, 4.34 and 4.35 the figures of merit of the *ZnO-buffered* cell are shown in function of donor lifetimes ($\tau_{nIT} = \tau_{pIT}$). Also in this case the trap concentration was kept constant ($N_{IT} = 3 \cdot 10^{11} cm^{-2}$) and it was varied the cross-section in order to change the lifetimes.

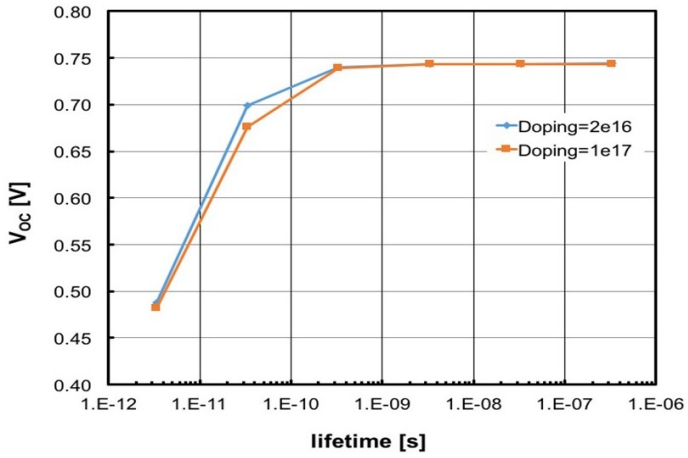

Figure 4.32: Open-circuit voltage as a function of interface donor lifetime $\tau_{nIT} = \tau_{pIT}$. $N_{IT} = 3 \cdot 10^{11} cm^{-2}$. Two different values of the buffer doping density have been simulated, as shown in the legend.

As for the acceptors also for donors, two values of doping for the 30 nm-thick *ZnO* buffer were considered which give slightly different band alignments. In order to understand the consequences of replacing the *CdS* buffer with *ZnO* in case of interface donor traps, the charts in Figures 4.32, 4.33, 4.34 and 4.35 can be compared with Figures 4.21, 4.22, 4.23 and 4.24, respectively, and the equilibrium band diagram of

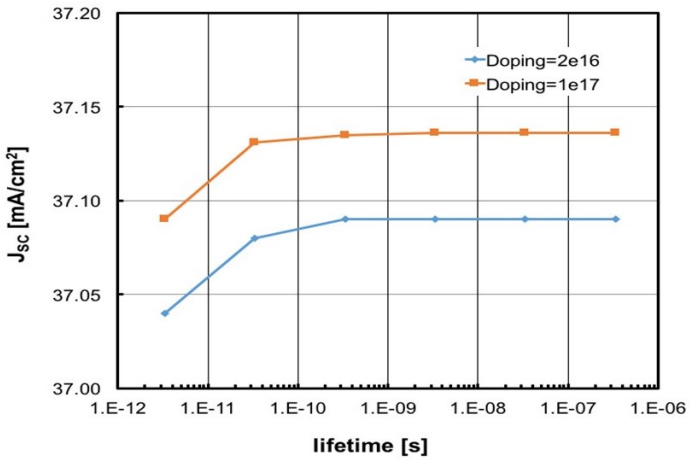

Figure 4.33: Short-circuit current as a function of interface donor lifetime $\tau_{nIT} = \tau_{pIT}$. $N_{IT} = 3 \cdot 10^{11} cm^{-2}$. Two different values of the buffer doping density have been simulated, as shown in the legend.

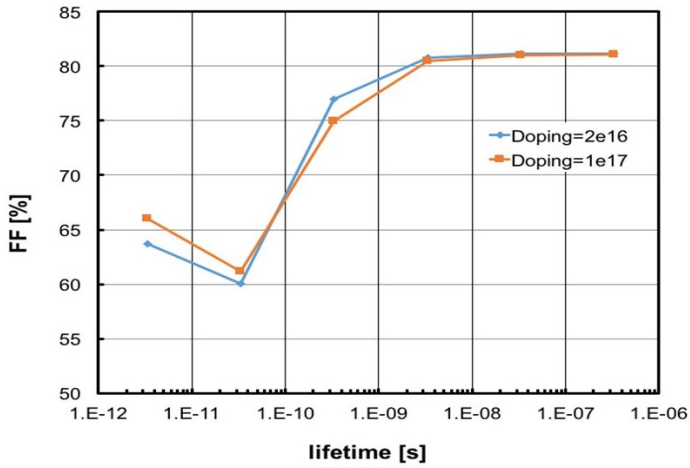

Figure 4.34: Fill factor as a function of interface donor lifetime $\tau_{nIT} = \tau_{pIT}$. $N_{IT} = 3 \cdot 10^{11} cm^{-2}$. Two different values of the buffer doping density have been simulated, as shown in the legend.

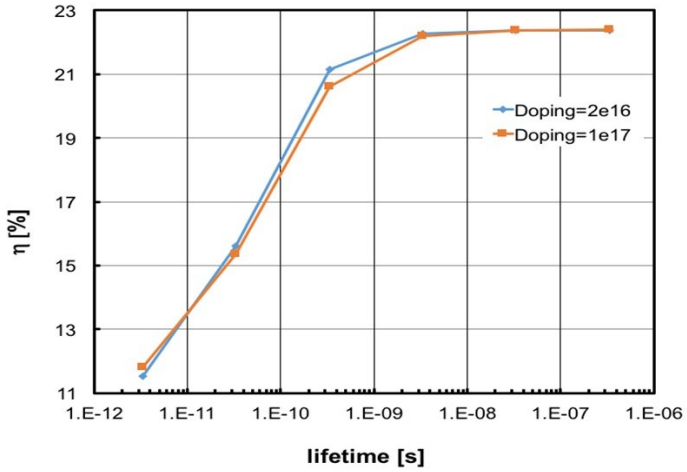

Figure 4.35: Efficiency as a function of interface donor lifetime $\tau_{nIT} = \tau_{pIT}$. $N_{IT} = 3 \cdot 10^{11} cm^{-2}$. Two different values of the buffer doping density have been simulated, as shown in the legend.

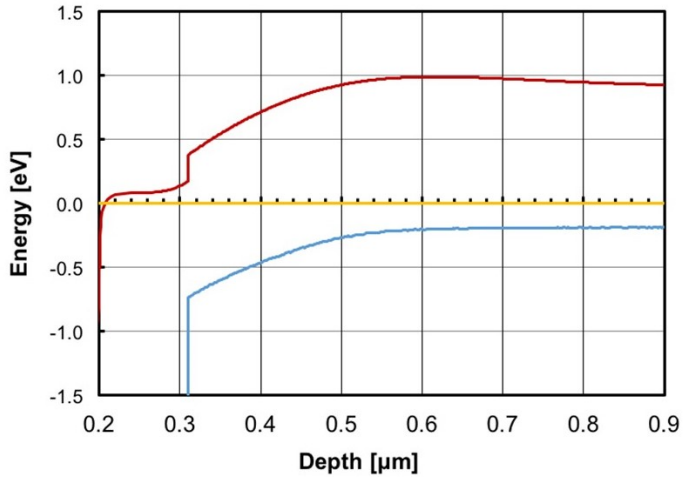

Figure 4.36: Equilibrium band diagram for the case of interface donors ($N_{IT} = 3 \cdot 10^{11} cm^{-2}$, $\tau_{nIT} = \tau_{pIT} = 3.3ps$); the buffer doping density is $1 \cdot 10^{17} cm^{-3}$.

Figure 4.36 with that of Figure 4.26.

Also in this case, direct quantitative point-by-point comparison is totally meaningful only under the assumption that the two structures have the same donor interface density and lifetimes, which is obviously questionable, so the following considerations should therefore be taken with caution.

In the stack with a *ZnO* buffer and interface donors (Figure 4.32) V_{OC} suffers more from low recombination lifetimes than the V_{OC} of the cell with the *CdS* buffer (Figure 4.21); by comparing the band diagram of Figure 4.36 with that of Figure 4.26, it is possible to note the larger surface hole density in the former: since holes are minority carriers at the inverted surface, this results in enhanced recombination.

J_{SC}, which is largely independent on lifetime and buffer doping (Figure 4.33), is significantly larger than that of the *CdS* buffer case (Figure 4.22) thanks to lower parasitic absorption in the *ZnO* buffer exactly as for acceptors.

The *FF* (Figure 4.34 vs. Figure 4.23) is made worse by the *ZnO* buffer when lifetimes are short, due to enhanced recombination in the interface donors, but slightly better when lifetimes are long, thanks to a more favorable band alignment enhancing the electron flow from the absorber to the buffer: see Figure 4.36, where the distance between conduction band and Fermi level at the *CIGS* surface is smaller than that in Figure 4.26. The reduction of *FF* relative to the *CdS* case drives the efficiency down in the presence of significant interface recombination (Figure 4.35 vs. Figure 4.24).

4.3.2 Zn(O,S) buffer

The second alternative buffer taken into account is the *Zn(O,S)*, when it is directly deposited on *CIGS* the band alignment shows a smaller "spike" between *CIGS* and buffer ($0.2eV$ [45]) than in the *CdS* buffer case (conduction band edge is higher in the buffer than in the *CIGS*). As for the *ZnO* alternative buffer also for *Zn(O,S)* will be studied both cases acceptor and donor traps for two different doping of the buffer.

4.3.2.1 Acceptor interface traps

In Figures 4.37, 4.38, 4.39, and 4.40 are shown the figures of merit of the cell for this stack configuration (*ZnO/i-ZnO/Zn(O,S)/CIGS*) in function of surface acceptor lifetimes ($\tau_{nIT} = \tau_{pIT}$). Again, also in this case, the trap concentration was kept constant ($N_{IT} = 3 \cdot 10^{11} cm^{-2}$) and it was varied the cross-section in order to change the lifetimes.

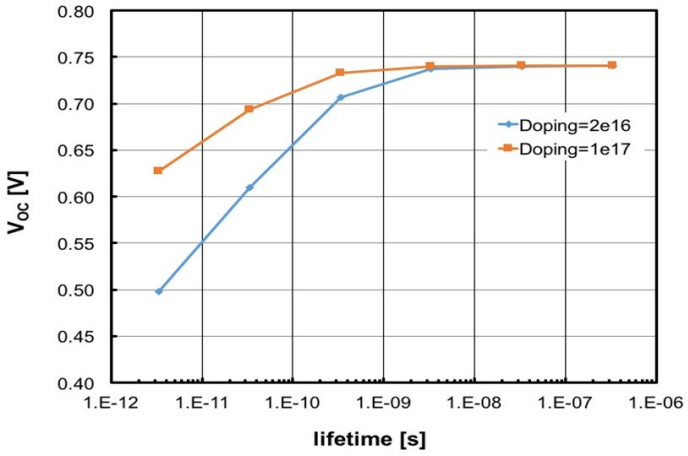

Figure 4.37: Open-circuit voltage as a function of interface acceptor lifetime $\tau_{nIT} = \tau_{pIT}$. $N_{IT} = 3 \cdot 10^{11} cm^{-2}$. Two different values of the buffer doping density have been simulated, as shown in the legend.

Two values of doping for the *30 nm-thick Zn(O,S)* buffer were considered, which give slightly different band alignments. In order to understand the consequences of replacing the *CdS* buffer with *Zn(O,S)* in case of surface acceptor traps, the charts in Figures 4.37, 4.38, 4.39 and 4.40 can be compared with Figures 4.13, 4.14, 4.15 and 4.16 (blue lines), respectively, and the equilibrium band diagram of Figure 4.41 with that of Figure 4.25.

As expected, there is a general qualitative similarity of behavior in the two structures (*CdS* buffer and *Zn(O,S)* buffer). As for the previous studies it should be pointed out that direct quantitative point-by-point comparison implies the assumption of the

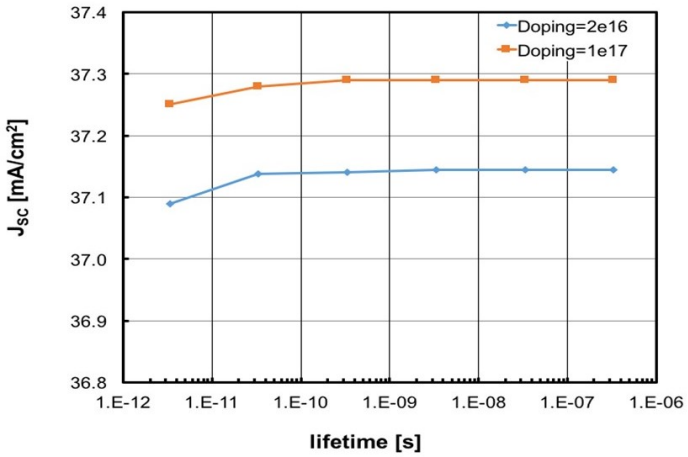

Figure 4.38: Short-circuit current as a function of interface acceptor lifetime $\tau_{nIT} = \tau_{pIT}$. $N_{IT} = 3 \cdot 10^{11} cm^{-2}$. Two different values of the buffer doping density have been simulated, as shown in the legend.

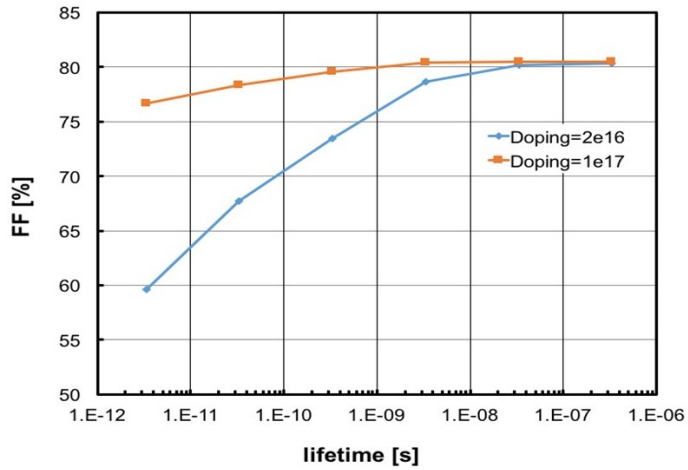

Figure 4.39: Fill factor as a function of interface acceptor lifetime $\tau_{nIT} = \tau_{pIT}$. $N_{IT} = 3 \cdot 10^{11} cm^{-2}$. Two different values of the buffer doping density have been simulated, as shown in the legend.

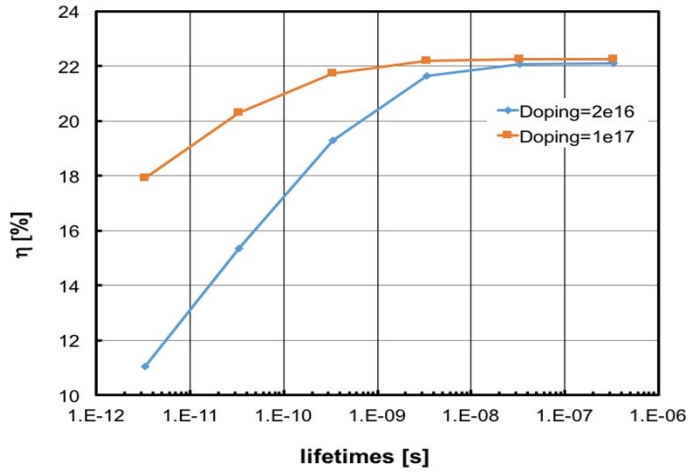

Figure 4.40: Efficiency as a function of interface acceptor lifetime $\tau_{nIT} = \tau_{pIT}$. $N_{IT} = 3 \cdot 10^{11} cm^{-2}$. Two different values of the buffer doping density have been simulated, as shown in the legend.

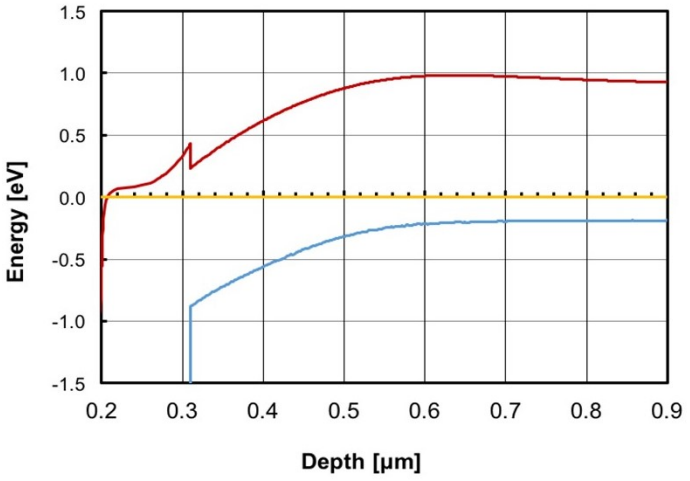

Figure 4.41: Equilibrium band diagram for the case of interface acceptors ($N_{IT} = 3 \cdot 10^{11} cm^{-2}$, $\tau_{nIT} = \tau_{pIT} = 3.3ps$); the buffer doping density is $10^{17} cm^{-3}$.

same acceptor interface density and lifetimes in the two structures, which may not be the case, so the following considerations should therefore be taken with caution.

In the stack with a *Zn(O,S)* buffer (Figure 4.37) V_{OC} is very similar to of the *CdS* buffer case (Figure 4.13, blue line) when the buffer doping is the same ($2\cdot 10^{16} cm^{-3}$), due to similar band alignment; when the *Zn(O,S)* buffer doping is larger ($1\cdot 10^{17} cm^{-3}$), the *CIGS* surface inversion is enhanced (compare Figure 4.41 with Figure 4.25), recombination is inhibited and V_{OC} gets larger.

The J_{SC} is largely independent on lifetime and buffer doping (Figure 4.38), and significantly larger than that of the *CdS* buffer case (Figure 4.14, blue line) thanks to lower parasitic absorption in the *Zn(O,S)* buffer.

FF is much improved by the *Zn(O,S)* buffer (Figure 4.39 vs. Figure 4.15, blue line), thanks to smaller "spike" and more favorable band alignment (particularly in the case of larger *Zn(O,S)* buffer doping) facilitating the flow of electrons to the cathode.

As a consequence of the above-noted improvements, the efficiency is consistently larger in the *Zn(O,S)* buffer case (Figure 4.40 vs. Figure 4.16, blue line).

4.3.2.2 Donor interface traps

In Figures are shown the figures of merit of the cell for the *Zn(O,S)* buffer case in function of surface donor lifetimes ($\tau_{nIT} = \tau_{pIT}$). Exactly as the previous cases also in this the trap concentration was kept constant ($N_{IT} = 3\cdot 10^{11} cm^{-2}$) and it was varied the cross-section in order to change the lifetimes.

Two values of doping for the *30 nm-thick Zn(O,S)* buffer were considered, which give slightly different band alignments. In order to understand the consequences of replacing the *CdS* buffer with *Zn(O,S)* in case of surface donor traps, the charts in Figures 4.42, 4.43, 4.44 and 4.45 can be compared with Figures 4.21, 4.22, 4.23 and 4.24, respectively, and the equilibrium band diagram of Figure 4.46 with that of Figure 4.26.

Again, as the previous studies, direct quantitative point-by-point comparison is totally meaningful only under the assumption that the two structures have the same donor interface density and lifetimes, which is obviously questionable, so the following considerations should therefore be taken with caution.

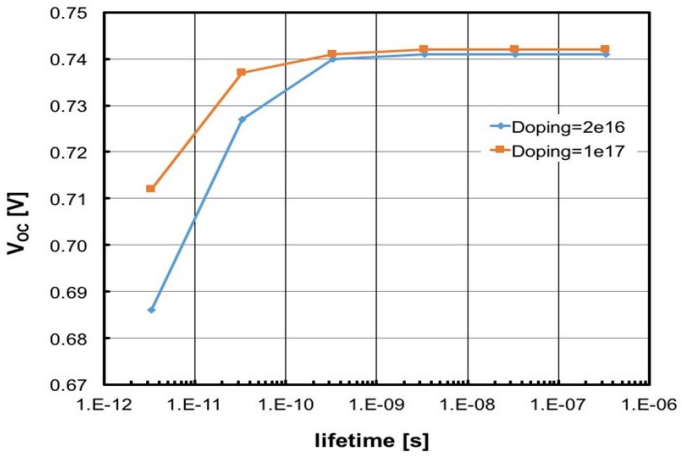

Figure 4.42: Open-circuit voltage as a function of interface donor lifetime $\tau_{nIT} = \tau_{pIT}$. $N_{IT} = 3 \cdot 10^{11} cm^{-2}$. Two different values of the buffer doping density have been simulated, as shown in the legend.

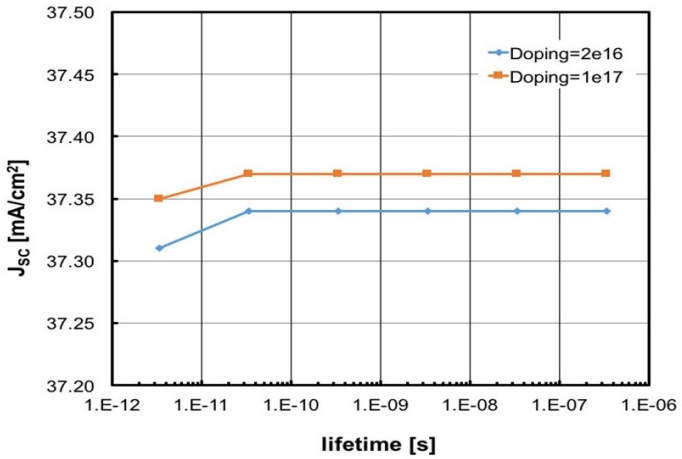

Figure 4.43: Short-circuit current as a function of interface donor lifetime $\tau_{nIT} = \tau_{pIT}$. $N_{IT} = 3 \cdot 10^{11} cm^{-2}$. Two different values of the buffer doping density have been simulated, as shown in the legend.

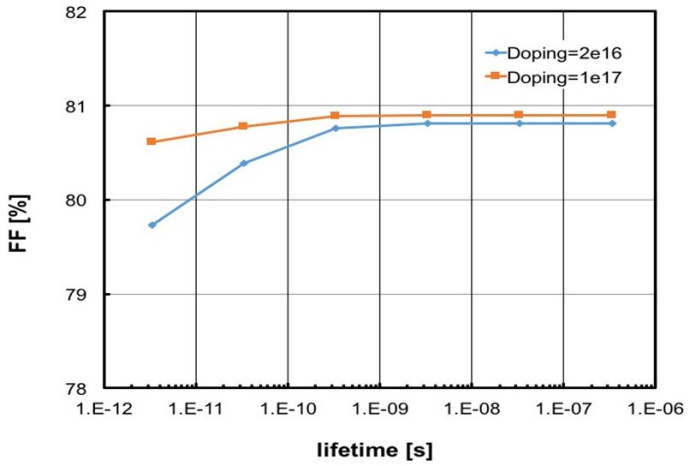

Figure 4.44: Fill factor as a function of interface donor lifetime $\tau_{nIT} = \tau_{pIT}$. $N_{IT} = 3 \cdot 10^{11} cm^{-2}$. Two different values of the buffer doping density have been simulated, as shown in the legend.

The cell with a *Zn(O,S)* buffer and interface donors (Figure 4.42) shows similar V_{OC} to that of the *CdS* buffer case (Figure 4.21), particularly when the buffer doping is the same ($2 \cdot 10^{16} cm^{-3}$), due to similar band alignment; however, by comparing the band diagram of Figure 4.46 with that of Figure 4.26, it is possible to note that for larger *Zn(O,S)* buffer doping ($1 \cdot 10^{17} cm^{-3}$) surface inversion is enhanced, and V_{OC} improves accordingly relative to the *CdS* case.

As usual, the J_{SC} is largely independent on lifetime and buffer doping (Figure 4.43), and significantly larger than that of the *CdS* buffer case (Figure 4.22) thanks to lower parasitic absorption in the *ZnO* buffer.

The *FF* (Figure 4.44 vs. Figure 4.23) is improved by the *Zn(O,S)*, thanks to a more favorable band alignment enhancing surface inversion and facilitating the electron flow from the absorber to the buffer (see Figure 4.46 vs. Figure 4.26).

The improvements described above push the efficiency up in the *Zn(O,S)* buffered cell, relative to the case of *CdS* buffered cell (Figure 4.45 vs. Figure 4.24).

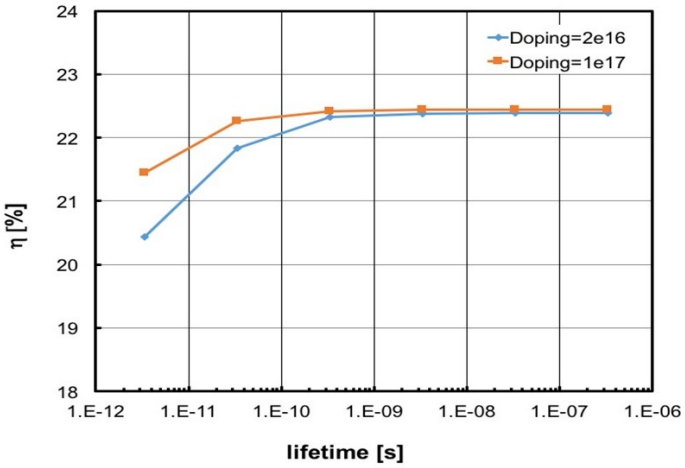

Figure 4.45: Efficiency as a function of interface donor lifetime $\tau_{nIT} = \tau_{pIT}$. $N_{IT} = 3 \cdot 10^{11} cm^{-2}$. Two different values of the buffer doping density have been simulated, as shown in the legend.

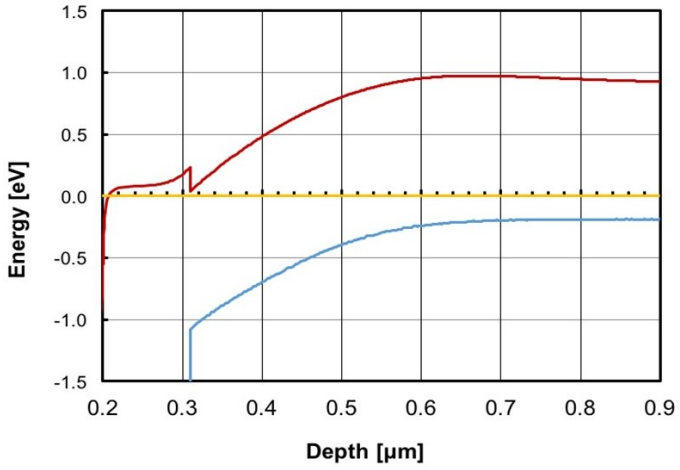

Figure 4.46: Equilibrium band diagram for the case of interface donors ($N_{IT} = 3 \cdot 10^{11} cm^{-2}$, $\tau_{nIT} = \tau_{pIT} = 3.3ps$); the buffer doping density is $10^{17} cm^{-3}$.

4.3.3 Comparison between different buffer

In this concluding section a synthetic comparison between cells with either *CdS*, *ZnO*, and *Zn(O,S)* buffers in case of acceptor or donor interface traps will be shown.

4.3.3.1 Interface acceptors

Assuming equal interface acceptor concentration $N_{IT} = 3 \cdot 10^{11} cm^{-2}$, it is possible to compare the two alternative buffer layers with each other and with the *CdS* baseline, as shown in Tables below.

	CdS	ZnO	Zn(O,S)
$V_{oc}[V]$	0.482	0.669	0.498
$J_{sc}[\frac{mA}{cm^2}]$	36.0	37.0	37.1
$FF[\%]$	34.8	68.8	59.6
$\eta[\%]$	6.04	17.0	11.0

In the table above the figures of merit of the three different cell stack in the case of extremely active interface acceptors ($\tau_{nIT} = \tau_{pIT} = 3.3ps$) are shown due to the effect of different band alignment at buffer7absorber interface. It is possible to note that under these conditions, the "cliff" situation of *ZnO* is the most favorable.

In table below the performance of the three cells in case of interface acceptors with long lifetimes ($\tau_{nIT} = \tau_{pIT} = 3.3ns$) are shown; it is possible to note that the *ZnO* buffered cell has better performance than the others mainly thanks the "cliff" band alignment resulting in high *FF*.

	CdS	ZnO	Zn(O,S)
$V_{oc}[V]$	0.737	0.744	0.737
$J_{sc}[\frac{mA}{cm^2}]$	36.1	37.0	37.1
$FF[\%]$	65.5	81.3	78.7
$\eta[\%]$	17.5	22.4	21.6

Comparing *ZnO* and *Zn(O,S)* structures with high doping density ($1 \cdot 10^{17} cm^{-3}$) in the case of extremely active interface acceptors ($\tau_{nIT} = \tau_{pIT} = 3.3ps$), it is possible

to note in table below that the "spike" band alignment of *Zn(O,S)* (see Figure 4.41) is more benign that those of *ZnO* (Figure 4.31) due to stronger surface inversion.

	ZnO	Zn(O,S)
$V_{oc}[V]$	0.620	0.627
$J_{sc}[\frac{mA}{cm^2}]$	37.0	37.2
$FF[\%]$	54.2	76.7
$\eta[\%]$	12.5	17.9

On the other hand, when interface acceptors have long lifetimes ($\tau_{nIT} = \tau_{pIT} = 3.3ns$) the two stack behave similarly, as shown in the table below.

	ZnO	Zn(O,S)
$V_{oc}[V]$	0.744	0.740
$J_{sc}[\frac{mA}{cm^2}]$	37.0	37.3
$FF[\%]$	81.1	80.4
$\eta[\%]$	22.4	22.2

4.3.3.2 Interface donors

Assuming equal interface donor concentration $N_{IT} = 3 \cdot 10^{11} cm^{-2}$, it is possible to compare the two alternative buffer layers with the *CdS* baseline.

The figures of merits shown in table below are the results of cells with the extremely active interface donors ($\tau_{nIT} = \tau_{pIT} = 3.3ps$). It is possible to note that the "spike" band alignment of *CdS* and *Zn(O,S)* is more favorable than the "cliff" of *ZnO* thanks to stronger surface inversion. Moreover, the *Zn(O,S)* buffered cell performs better than the *CdS* one in all aspects.

	CdS	ZnO	Zn(O,S)
$V_{oc}[V]$	0.636	0.488	0.686
$J_{sc}[\frac{mA}{cm^2}]$	36.4	37.0	37.3
$FF[\%]$	76.9	63.7	79.7
$\eta[\%]$	17.8	11.5	20.4

On the other hand, table below shows the results in the case of long interface donor lifetimes ($\tau_{nIT} = \tau_{pIT} = 3.3ns$), the band alignment appears to be of little importance, and the two cells with alternative buffers slightly outperform the *CdS* cell thanks to reduced parasitic absorption in the buffer.

	CdS	ZnO	Zn(O,S)
$V_{oc}[V]$	0.740	0.743	0.741
$J_{sc}[\frac{mA}{cm^2}]$	36.4	37.1	37.3
$FF[\%]$	80.0	80.7	80.8
$\eta[\%]$	21.6	22.3	22.4

As for the acceptors, comparing structures with high doping density ($1 \cdot 10^{17} cm^{-3}$) for *ZnO* and *Zn(O,S)* in the case of extremely active interface donors ($\tau_{nIT} = \tau_{pIT} = 3.3ps$) the "spike" band alignment of *Zn(O,S)* is much more beneficial than the "cliff" of *ZnO*.

	ZnO	Zn(O,S)
$V_{oc}[V]$	0.482	0.712
$J_{sc}[\frac{mA}{cm^2}]$	37.1	37.3
$FF[\%]$	66.0	80.6
$\eta[\%]$	11.8	21.4

On the other hand, when donor capture times are long ($\tau_{nIT} = \tau_{pIT} = 3.3ns$), the differences between *ZnO* and *Zn(O,S)* structures tend to vanish, and performance tends to saturate.

	ZnO	Zn(O,S)
$V_{oc}[V]$	0.743	0.742
$J_{sc}[\frac{mA}{cm^2}]$	37.1	37.4
$FF[\%]$	80.4	80.9
$\eta[\%]$	22.2	22.4

These simulations lead to the conclusion that for all the configurations of interface acceptor traps (short and long lifetimes) a "cliff" CBO between *CIGS* and buffer performs better than a "spike".

On the other hand, for all the configurations of interface donor traps (short and long lifetimes) the results lead to opposite conclusion that is to say that a "spike" CBO performs better than a "cliff".

4.4 Ordered Vacancy Compound at the CIGS/buffer interface

In literature there are no conclusive evidence for the existence of a Conduction Band Offset (CBO) at the interface between *CdS* and *CIGS*; in fact experimental results mostly yield Valence Band Offset (VBOs), while CBOs are indirectly determined from VBOs and bandgap values, the latter assumed to be equal to their bulk values. Very limited data are available of direct CBO measurements, and they do not support the presence of a significant spike [54].

The CBO spike ($0.1eV$ for ZSW cell and $0.3eV$ for EMPA cell) included in the models of the baseline of this thesis has the aim of taking in account the good quality of the interface between *CdS* and *CIGS* (the downward band bending produced at the interface by the spike-like CBO repels holes from the interface and hinders non-radiative recombination at interface defect centers).

On the other hand, the Cu vacancy at the surface of *CIGS* could produce an Ordered Vacancy Compound (OVC) layer, with larger bandgap than *CIGS* and a VBO. This layer may have in principle the same effect of majority carrier repulsion from the *CIGS* surface as the spike-like CBO, and could therefore explain how the *CdS/CIGS* interface can be so benign even in the absence of a CBO. The simulations of this section aim at exploring this scenario.

This set of simulations is based on EMPA cell simulated with absorption coefficients measured by EMPA [24] for all the materials.

4.4.1 p-doped OVC layer

In a first set of simulations, it was considered the presence of a *10-nm-thick* p-doped ($1 \cdot 10^{16} cm^{-3}$) OVC layer with a larger bandgap than *CIGS* and no CBO (there is a

VBO with the VB being lower in the OVC layer than in the *CIGS*); zero CBO has been considered between the OVC layer and the *CdS*, too.

It was studied the effect of either mid-gap acceptors or mid-gap donors in the OVC layer, with capture cross sections $\sigma_{nIT} = \sigma_{pIT} = 10^{-15} cm^2$ and variable concentration. Three cases were studied with different VBO between the OVC layer and the absorber, namely: *100, 200, and 280 meV*, corresponding with OVC bandgap values of *1.22, 1.32, and 1.40 eV*, respectively. Figure 4.47 shows the equilibrium band diagrams for the three cases.

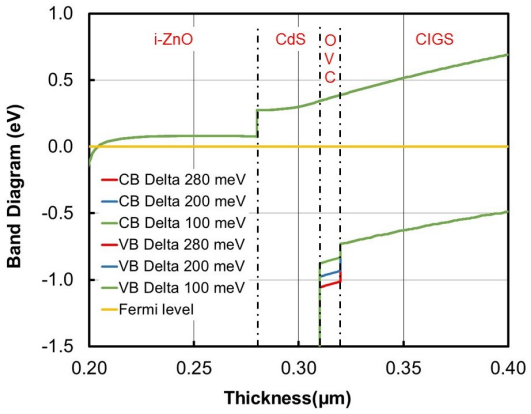

Figure 4.47: Equilibrium band diagrams for the structures with p-doped OVC layer.

The effect of acceptor traps in the structures of Figure 4.47 is illustrated by Figures 4.48 and 4.49.

As expected, the effect of interface acceptors, which mostly affect V_{OC} and FF, becomes less severe for increasing VBO: for a *200 meV* VBO, the cell can tolerate a defect density as large as $1 \cdot 10^{17} cm^{-3}$ with less than 0.5% absolute efficiency degradation.

The figures of merit of the cell in case of mid-gap donor defects in the OVC is described in Figures 4.50 and 4.51 .

Qualitatively, the dependence of the performance of the cell on the OVC defect density and VBO is the same as for acceptor defects. Quantitatively, it is somewhat less

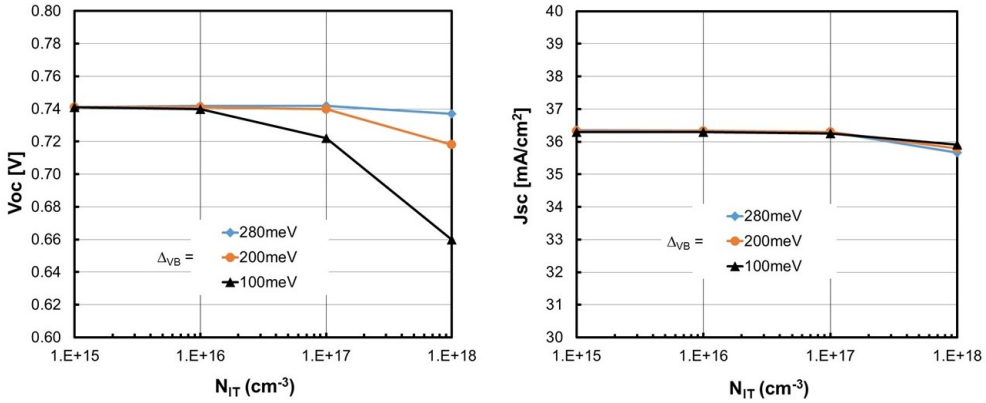

Figure 4.48: Simulated V_{OC} and J_{SC} as a function of acceptor defect concentration in the OVC. Δ_{VB} is the VBO between the OVC and the CIGS absorber.

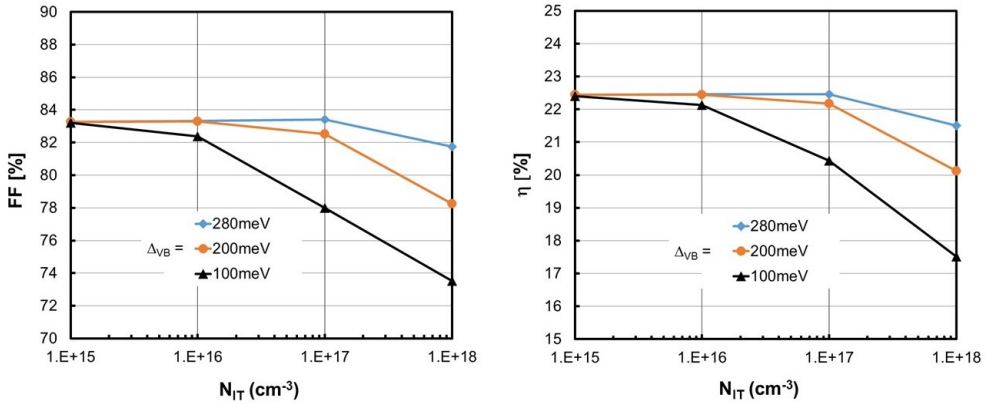

Figure 4.49: Simulated FF and η as a function of acceptor defect concentration in the OVC. Δ_{VB} is the VBO between the OVC and the CIGS absorber.

severe, in fact the band diagrams of Figure 4.47 show that mid-gap defects lie below the Fermi level at equilibrium, and are therefore occupied by electrons: while donors will be neutral, acceptors will be negatively charged; therefore, acceptor defects will push the bands upward, thus increasing the hole concentration in the OVC, which is shown by Figure 4.47 to be the limiting concentration for non-radiative recombination.

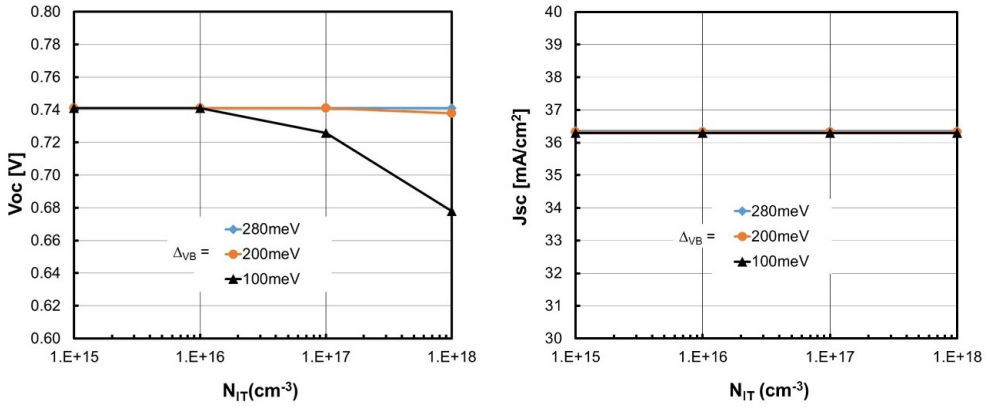

Figure 4.50: Simulated V_{OC} and J_{SC} as a function of donor defect concentration in the OVC. Δ_{VB} is the VBO between the OVC and the CIGS absorber.

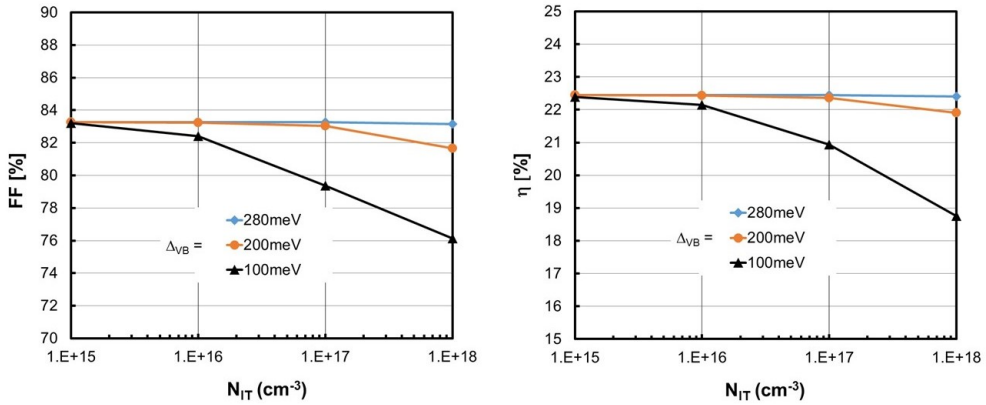

Figure 4.51: Simulated FF and η as a function of donor defect concentration in the OVC. Δ_{VB} is the VBO between the OVC and the CIGS absorber.

4.4.2 n-doped OVC layer

In a second set of simulations, we have considered a *10-nm-thick* n-doped ($1 \cdot 10^{16} cm^{-3}$) OVC. Apart from the dopant type, all the other features of the OCV are the same as described in section before. The effect of acceptor traps in the OVC on the perfor-

mance of the cell is shown in Figure 4.52 and 4.53; instead the effect of donor defects in the OVC is shown in Figure .

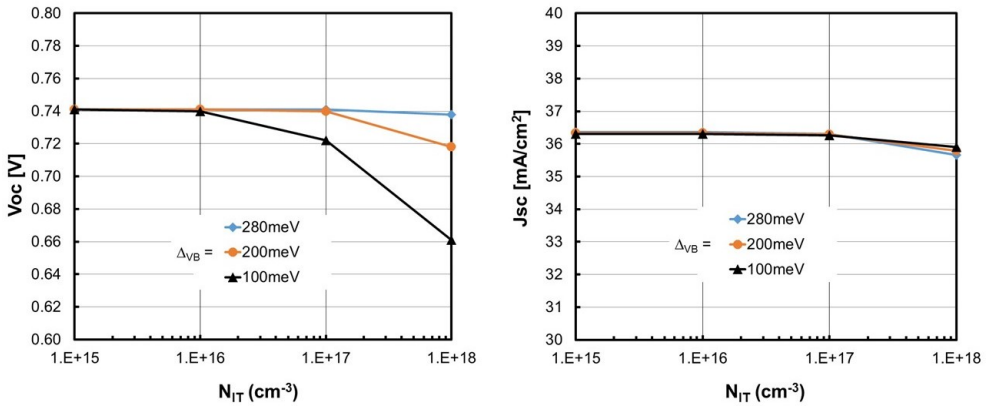

Figure 4.52: Simulated V_{OC} and J_{SC} for the cells with n-doped OVC, as a function of acceptor defect concentration in the OVC. Δ_{VB} is the VBO between the OVC and the CIGS absorber.

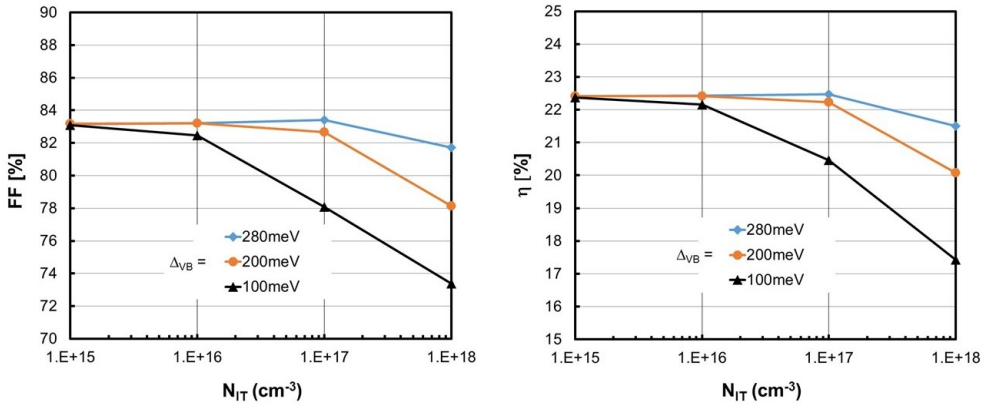

Figure 4.53: Simulated FF and η for the cells with n-doped OVC, as a function of acceptor defect concentration in the OVC. Δ_{VB} is the VBO between the OVC and the CIGS absorber.

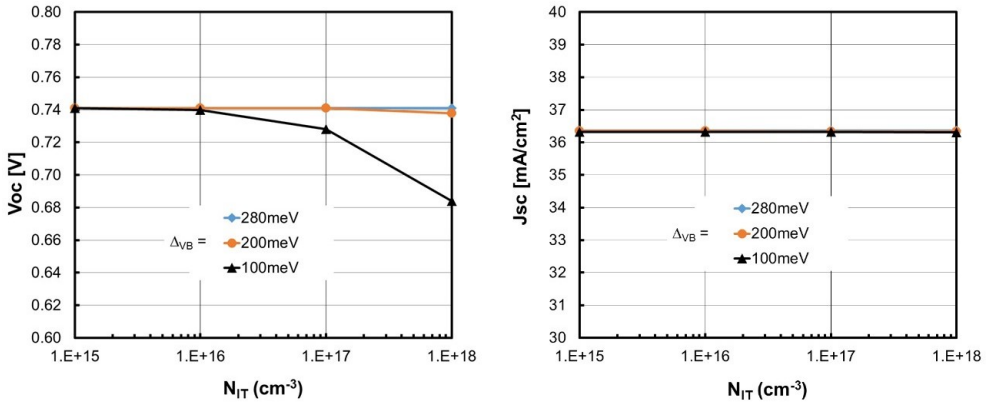

Figure 4.54: Simulated V_{OC} and J_{SC} for the cells with n-doped OVC, as a function of donor defect concentration in the OVC. Δ_{VB} is the VBO between the OVC and the CIGS absorber.

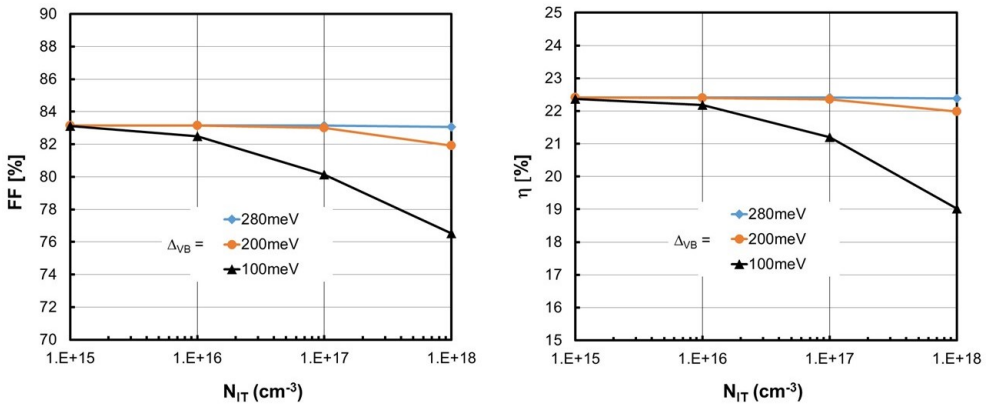

Figure 4.55: Simulated FF and η for the cells with n-doped OVC, as a function of donor defect concentration in the OVC. Δ_{VB} is the VBO between the OVC and the CIGS absorber.

The results are very similar to those obtained in the p-doped OVC case, the reason for this similarity is that the very thin (*10 nm*) OVC is sandwiched between the much thicker *CIGS* layer (which has the same doping density) and thicker and more heavily

doped n-layers (buffer and window): consequently, its band alignment is dictated by the much larger charge in the adjoining layers on either side, and rather independent of its own doping type.

It is possible to conclude that these simulations shown that the presence of either a p-doped or an n-doped *10-nm-thick* Ordered Vacancy Compound between *CdS* and *CIGS* with lower valence band than *CIGS* (VBO ranging from *100 to 280 meV*) can account for state-of-the-art cell performance even in the presence of significant defect concentration (both acceptor and donor type) in the OVC and zero CBO between *CdS* and OVC and between OVC and *CIGS*.

4.5 $KInSe_2$ layer at the interface between buffer and absorber

One of the most used solution to increment the efficiency of the *CIGS* solar cells is the Post-Deposition Treatment (PDT) with Alkali fluorides [1] [2], but as a consequence of this treatment a thin surface layer of $Alk - InSe_2$ may form at the absorber surface [55]. Calculations from University of Aalto [56] support this theory and provide some detail about the bandgap of these $Alk - InSe_2$ layers and band offsets with *CIGS*. It is therefore of interest to study with numerical simulations what might be the effects brought about by these layers on the cell characteristics and performance.

This set of simulations is focuses on the case of a $KInSe_2$ (KIS) layer, and considers the EMPA cell as baseline simulated with optical coefficients provided by EMPA for all the layers [24].

Three thickness values were considered for the *KIS* layer (*5, 10, and 20nm*) and a *KIS* bandgap of *2.53eV*, based on calculations from Aalto. Different values for *KIS* electron affinity were also considered; these lead to study a range of CBO with *CIGS* (and *CdS*). The schematic cross section of the cells is shown in Figure 4.56, together with a simplified drawing of the conduction band alignment.

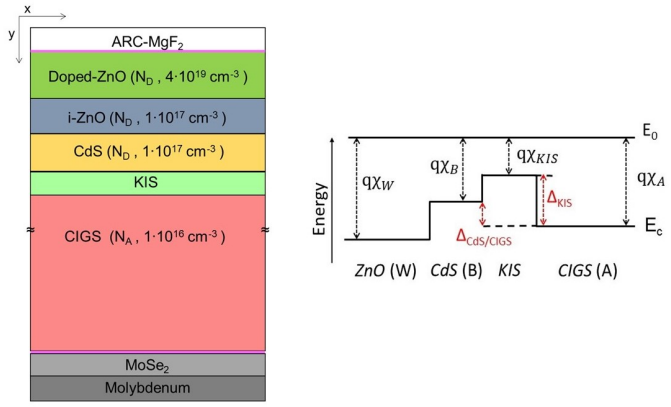

Figure 4.56: Schematic cross-section and conduction band alignment of the structures with interfacial KIS layer. $\chi_{ZnO} = 4.5eV$, $\chi_B = 4.3eV$, $\chi_A = 4.6eV$..

4.5.1 Variable *KIS* thickness and electron affinity

In a first set of simulations it was analyzed the effects of a trap-free *KIS* layer with varying thickness and electron affinity χ_{KIS} on the room temperature cell performance. Figures 4.57 and 4.58 show the dependence of the figures of merit of the cell on these two parameters.

Since the electron affinity of *CdS* buffer is $\chi_B = 4.3eV$ and that of *CIGS* is $\chi_A = 4.6eV$, the minimum value of $\chi_{KIS} = 4.1eV$, results in a cliff *CBO = -0.2eV* with *CdS* and a spike *CBO = 0.5eV* with *CIGS*; instead the maximum value of $\chi_{KIS} = 5.1eV$, results in a spike *CBO = 0.8eV* with *CdS* and a cliff *CBO = -0.5eV* with *CIGS*.

Predictably, while V_{OC} is practically unaffected by the variation of χ_{KIS}, instead *FF* is dramatically degraded at the extremes of the χ_{KIS} range due to large barriers for electron collection either at the *CIGS/KIS* interface (low χ_{KIS}) or at the *KIS/CdS* interface (high χ_{KIS}).

The range of χ_{KIS} values compatible with the room temperature behavior measured KF-PDT cells is $4.3eV \leq \chi_{KIS} \leq 4.7eV$ (this range corresponds with $-0.1eV \leq CBO_{KIS/CIGS} \leq 0.3eV$, and $0.4eV \geq CBO_{CdS/KIS} \geq 0eV$); in this range, the effect

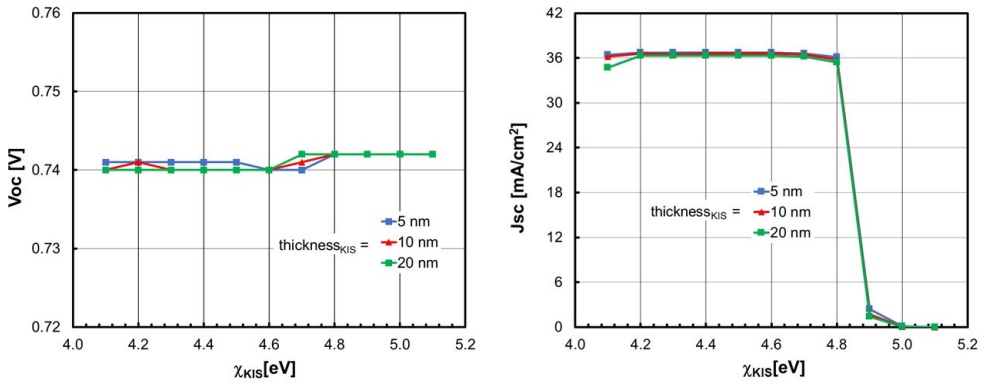

Figure 4.57: V_{OC} and J_{SC} for the cells with trap-free interfacial KIS layer, as a function of the KIS electron affinity and for three thickness values.

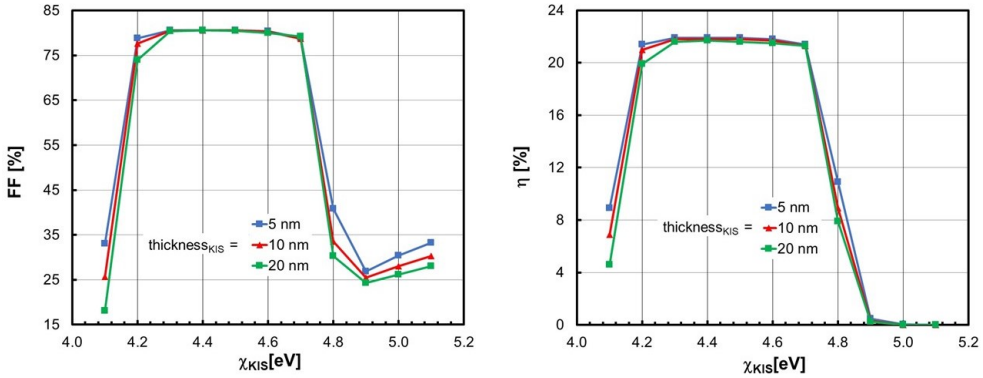

Figure 4.58: FF and η for the cells with trap-free interfacial KIS layer, as a function of the KIS electron affinity and for three thickness values.

of the thickness of *KIS* is negligible.

4.5.2 Variable KIS electron affinity and acceptor traps in the KIS

In another sets of simulations it was fixed the *KIS* thickness at *5nm*, varied its electron affinity in the range compatible with good cell performance ($4.3eV \leq \chi_{KIS} \leq 4.7eV$),

and considered the presence of *KIS* acceptor defects ($\sigma_n = \sigma_p = 10^{-14} cm^2$) uniformly distributed in the energy range corresponding with the *CIGS* bandgap: Figure 4.59 illustrates three exemplary cases.

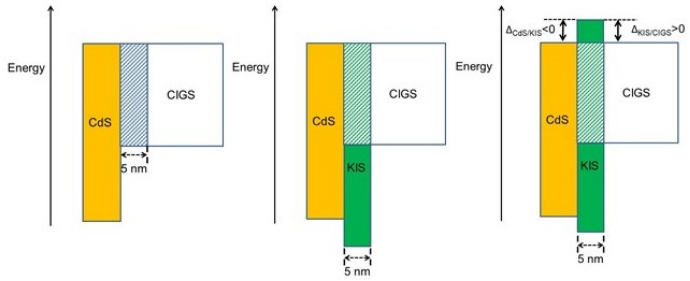

Figure 4.59: Schematic band alignment for three exemplary cases. Left: no KIS; center: no CBO between KIS and the adjoining layers; right: KIS forms a cliff CBO with CdS and a spike CBO with CIGS. The hatched areas indicate the energy distribution of acceptor defects.

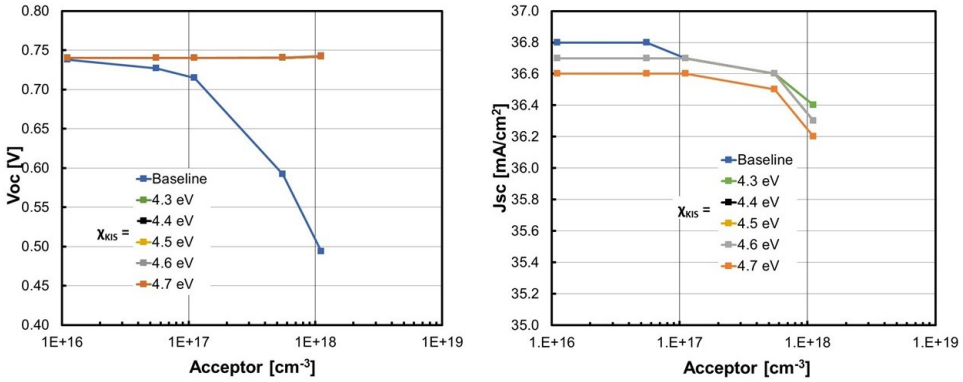

Figure 4.60: V_{OC} and J_{SC} for the cells with interfacial KIS layer with acceptor defects, as a function of the defect density and KIS electron affinity.

The performance figures of merit as a function of acceptor defect density and for several values of the *KIS* electron affinity in the range $4.3eV \leq \chi_{KIS} \leq 4.7eV$ are

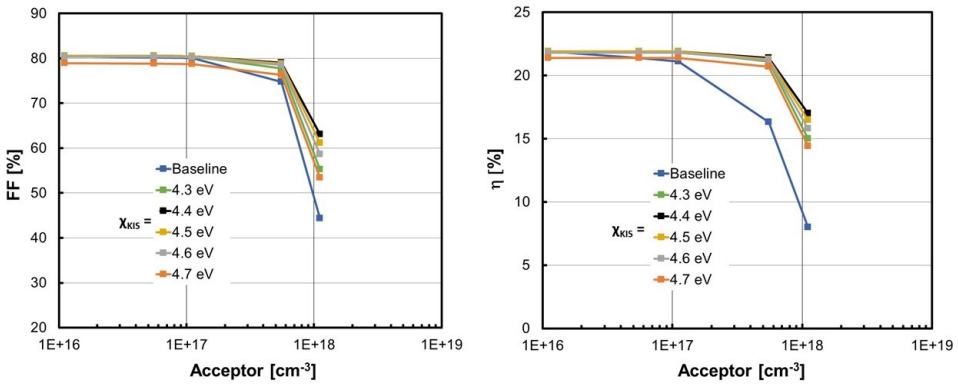

Figure 4.61: FF and η for the cells with interfacial KIS layer with acceptor defects, as a function of the defect density and KIS electron affinity.

given in Figures 4.60 and 4.61.

The results show that, unlike the reference cell with no *KIS*, the cells with *KIS* are unaffected by the presence of interface acceptor defects up to a concentration of $5 \cdot 10^{17} cm^{-3}$, which corresponds with a unit-area concentration of $2.5 \cdot 10^{11} cm^{-2}$. This effect is due to the larger *KIS* bandgap and particularly to the lower valence band reducing the number of interface holes available for non-radiative recombination.

From these sets of simulation it is possible to conclude that the presence of a thin (*5-20nm*) $KInSe_2$ (*KIS*) layer with larger bandgap than *CIGS* between the absorber and buffer can have beneficial effects on the cell performance, in terms of neutralization of the activity of interface defects, if its electron affinity is in the range $4.3eV \leq \chi_{KIS} \leq 4.7eV$ (this range corresponds with $-0.1eV \leq CBO_{KIS/CIGS} \leq 0.3eV$, and $0.4eV \geq CBO_{CdS/KIS} \geq 0eV$). Outside the range described before the performance degraded dramatically due to large barriers for electron collection either at the *CIGS/KIS* interface (low χ_{KIS}) or at the *KIS/CdS* interface (high χ_{KIS}).

4.6 Lateral inhomogeneities of absorber composition and voids

Measurements carried out at EMPA (TEM, EDX, SEM) have indicated the presence of two structural defects: inhomogeneities in the lateral distribution of *In*, *Ga*, *Cu* and voids of material. The inhomogeneities appear to be more pronounced for *In* and *Ga*, and concentrated in the surface and notch regions of the *GGI* profile, instead the voids appear often at the surface between *CdS* and *CIGS*. These defects could be limiting factors of the *CIGS* based solar cell, so in this section is reported the study on the inhomogeneities and voids in order to understand their effects on the performance of the cell.

This modeling activity is based on the EMPA cell simulated with optical coefficients measured at EMPA for all the materials [24].

4.6.1 Lateral inhomogeneities

Based on the preliminary results of the measurements performed at EMPA, it was decided that the inhomogeneous structure to be modeled would feature:

- a high-GGI columnar region extending for 30% of the structure width;
- a low-GGI columnar region extending for the remaining 70% of the structure width.

The overall *Ga* and *In* content of the inhomogeneous structure would be the same as in the baseline homogeneous structure, so the weighted average of the *GGI* ratio of the two portions of the inhomogeneous structure would be equal to the average *GGI* in the baseline homogeneous structure.

For simplicity and clarity of interpretation of the results, it was decided that the *GGI* profile of Figure 2.5 be modeled by a piece-wise linear approximation. The maximum difference between the *high GGI* and *low GGI* values was set at *0.1*, based on preliminary measurement results.

Three scenarios were simulated:

1. "notch inhomogeneity": the *GGI* inhomogeneity is maximum (*0.1* difference) at the notch, zero at the peak of the *GGI* profile and at the surface of the absorber, as well as at the back;

2. "surface inhomogeneity": the *GGI* inhomogeneity is maximum (*0.1* difference) at the surface and peak positions, zero at the notch of the *GGI* profile and at the back;

3. "notch+surface inhomogeneity": the *GGI* inhomogeneity is maximum (*0.1* difference) at the surface, peak and notch positions, zero at the back.

The local value of *GGI* determines the local value of absorber bandgap and its optical coefficients. In the simulations described below, unless otherwise specified, the total width of the structures is *100 nm*. This means that the inhomogeneous structures have a *30 nm* wide *high GGI* region and a *70 nm* wide *low GGI* region.

4.6.1.1 Notch inhomogeneity

The first set of simulations was focused on Notch inhomogeneity, in Figure 4.62 is shown the simulated *GGI* profiles for the low and *high GGI* regions of the inhomogeneous structure, together with the *GGI* profile of the uniform (homogeneous) baseline structure.

Three cases were studied:

- ideal *CdS/CIGS* interface;

- interface *CdS/CIGS* decorated by a high concentration of midgap acceptor traps;

- interface *CdS/CIGS* decorated by low concentration of acceptors but large capture cross section (thus yielding the same recombination velocity as in case above, but with negligible effects of surface trapped charge).

In Figure 4.63 is shown a 2D map of the recombination rate in the dark at $35 mA/cm^2$ in the inhomogeneous structure with ideal interface; the larger electron density around the notch region results in significantly larger recombination in the

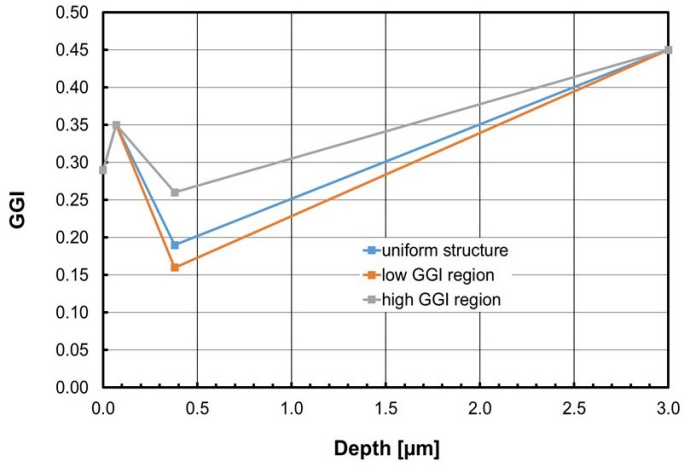

Figure 4.62: Simulated *GGI* profiles for the case of the "notch inhomogeneity", and for the baseline uniform structure. The inhomogeneous structure has low *GGI* over 70% of its width, high *GGI* over the remaining 30%.

low GGI (right) region; the corresponding 1D recombination rate vs. depth profile in the two regions is shown in Figure 4.64.

The recombination maps for the case of large concentration of interface acceptors are given in Figures 4.65 and 4.66: in this case interface recombination is clearly dominant.

The simulated figures of merit of the inhomogeneous cell in case of ideal interface are shown in the table below, together with the cases of the baseline homogeneous structure and two reference cases of homogeneous cells featuring the *high GGI* and *low GGI* profiles of Figure 4.62.

	Uniform	Inhomogeneous	High GGI uniform	Low GGI uniform
$V_{OC}[V]$	0.724	0.719	0.746	0.713
$J_{SC}[\frac{mA}{cm^2}]$	37.1	37.0	35.5	37.6
$FF[\%]$	83.3	83.0	83.8	82.9
$\eta[\%]$	22.4	22.1	22.2	22.3

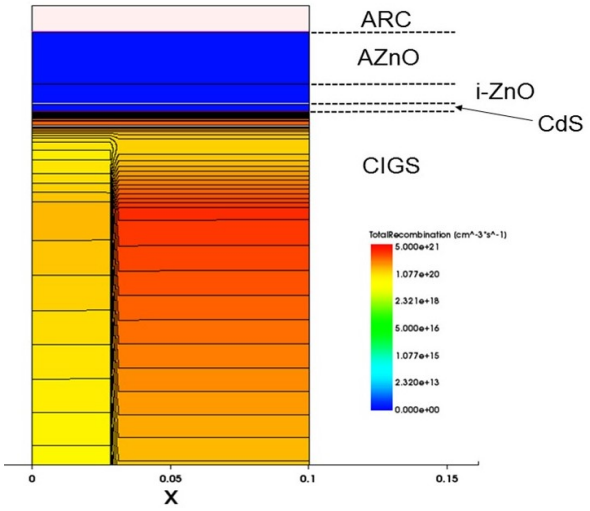

Figure 4.63: 2D map of the recombination rate in the dark at $35 mA/cm^2$ in the inhomogeneous structure with ideal interface.

The case where the interface is decorated by a high concentration of mid-gap acceptor traps is given in table below.

	Uniform	Inhomogeneous	High GGI uniform	Low GGI uniform
$V_{OC}[V]$	0.678	0.676	0.681	0.676
$J_{SC}[\frac{mA}{cm^2}]$	37.1	37.0	35.5	37.6
$FF[\%]$	79.1	79.0	79.3	78.9
$\eta[\%]$	19.9	19.8	19.2	20.1

In table below are shown the figures of merit of the structure in the case where the concentration of interface acceptors is 10^4 times lower, but the traps have 10^4 times larger capture cross section, thus yielding the same recombination velocity as in previous table, but with negligible effects of surface trapped charge.

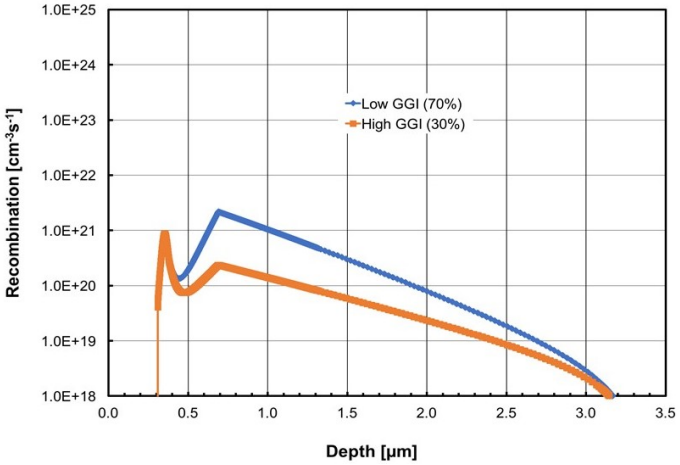

Figure 4.64: Recombination rate vs. depth in the dark at $35mA/cm^2$ in the inhomogeneous structure with ideal interface; the recombination rate is taken in the middle section of the two regions.

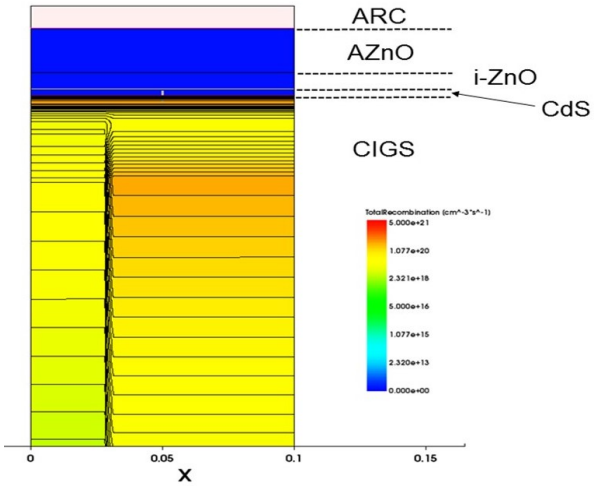

Figure 4.65: 2D map of the recombination rate in the dark at $35mA/cm^2$ in the inhomogeneous structure with large concentration of interface acceptors.

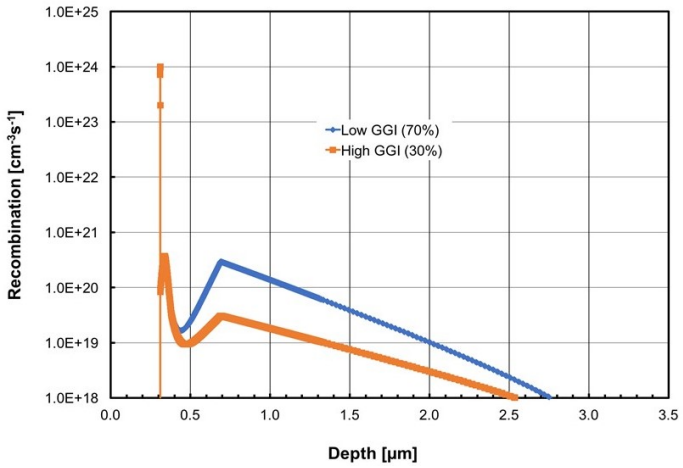

Figure 4.66: Recombination rate vs. depth in the dark at $35mA/cm^2$ in the inhomogeneous structure with large concentration of interface acceptors; the recombination rate is taken in the middle section of the two regions.

	Uniform	Inhomogeneous	High GGI uniform	Low GGI uniform
$V_{OC}[V]$	0.710	0.707	0.722	0.703
$J_{SC}[\frac{mA}{cm^2}]$	37.1	37.0	35.5	37.6
$FF[\%]$	82.3	82.2	82.3	82.2
$\eta[\%]$	21.7	21.5	21.1	21.8

The results lead to conclude that the performance loss due to the *GGI* inhomogeneity is moderate in all cases.

Electrons are observed to flow from the *high GGI* region to the *low GGI* region all the way from the bulk of the absorber to the notch depth; only at the surface, where the *GGI* profiles merge, is the electron flow reversed. The drift component of the electron current due to the conduction band offset therefore seems to dominate over the diffusion component caused by larger generation in the *low GGI* region. The plots of electron current density (Figure 4.67) and electron density (Figure 4.68) at J_{sc} conditions vs. depth confirm this, with the inhomogeneous structure showing larger current and electron concentration disparity between the two sections than the two

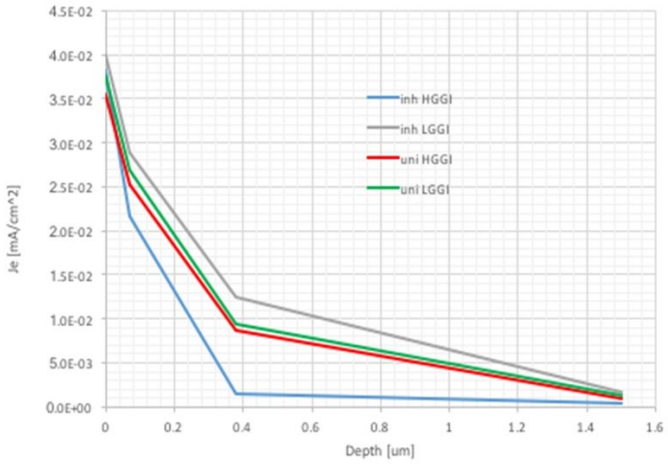

Figure 4.67: Electron current density vs. depth in the absorber for the low *GGI* (grey line) and high *GGI* (blue line) regions of the inhomogeneous structure, and for the two reference structures with uniform low *GGI* (green line) and uniform high *GGI* (red line).

homogeneous ones between one another. On the other hand, a small hole current is seen to flow from the *low GGI* region to the *high GGI* region all across the boundary, consistently with the larger optical generation in the *low GGI* region and the absence of a valence band offset.

4.6.1.2 Surface inhomogeneity

The second set of simulations was focused on surface inhomogeneity, in Figure 4.69 is shown the simulated *GGI* profiles for the *low* and *high GGI* regions of the inhomogeneous structure, together with the *GGI* profile of the uniform (homogeneous) baseline structure.

The simulated figures of merit of the inhomogeneous cell are shown in the tables below, together with the cases of the baseline homogeneous structure and two reference cases of homogeneous cells featuring the *high GGI* and *low GGI* profiles of Figure 4.69.

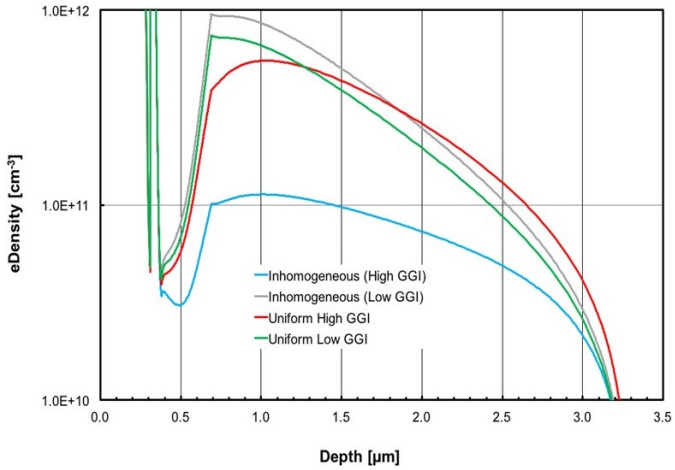

Figure 4.68: Electron density vs. depth in the absorber for the low *GGI* (grey line) and high *GGI* (blue line) regions of the inhomogeneous structure, and for the two reference structures with uniform low *GGI* (green line) and uniform high *GGI* (red line).

The case of ideal CdS/CIGS interface is reported in Table below.

	Uniform	Inhomogeneous	High GGI uniform	Low GGI uniform
$V_{OC}[V]$	0.724	0.724	0.726	0.723
$J_{SC}[\frac{mA}{cm^2}]$	37.1	37.1	36.8	37.2
$FF[\%]$	83.3	83.3	81.9	83.3
$\eta[\%]$	22.4	22.4	21.9	22.4

The case where the interface is decorated by a high concentration of mid-gap acceptor traps is given in the following Table;

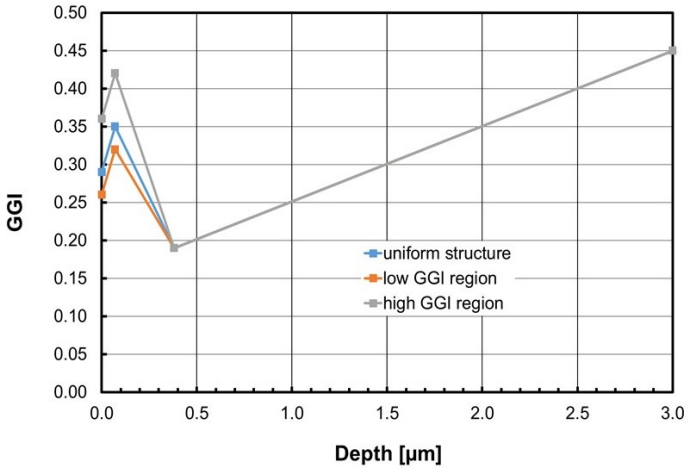

Figure 4.69: Simulated GGI profiles for the case of the "surface inhomogeneity", and for the baseline uniform structure. The inhomogeneous structure has low GGI over 70% of its width, high GGI over the remaining 30%.

	Uniform	Inhomogeneous	High GGI uniform	Low GGI uniform
$V_{OC}[V]$	0.678	0.678	0.682	0.676
$J_{SC}[\frac{mA}{cm^2}]$	37.1	37.1	36.8	37.2
$FF[\%]$	79.1	79.2	77.3	79.4
$\eta[\%]$	19.9	19.9	19.4	20.0

In the last table is shown case where the concentration of interface acceptors is 10^4 times lower, but the traps have 10^4 times larger capture cross section, thus yielding the same recombination velocity as in previous table, but with negligible effects of surface trapped charge.

	Uniform	Inhomogeneous	High GGI uniform	Low GGI uniform
$V_{OC}[V]$	0.710	0.709	0.716	0.707
$J_{SC}[\frac{mA}{cm^2}]$	37.1	37.1	36.8	37.2
$FF[\%]$	82.3	82.4	81.0	82.4
$\eta[\%]$	21.7	21.7	21.4	21.7

From this set of simulations it is possible to conclude that qualitatively the behavior is the same as in the case of the notch inhomogeneity, but with even smaller quantitative effects.

4.6.1.3 Notch+surface inhomogeneity

The last case analyzed for the lateral inhomogeneities puts together "notch" and "surface" inhomogeneity; the Figure 4.70 shown the simulated *GGI* profiles for the *low* and *high GGI* regions of the inhomogeneous structure, together with the *GGI* profile of the uniform (homogeneous) baseline structure.

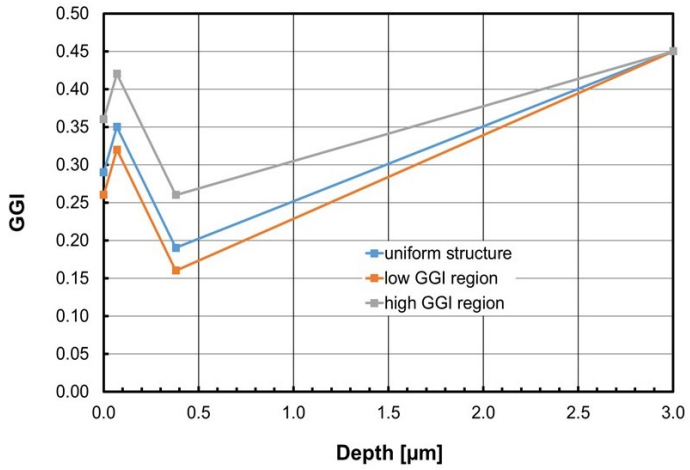

Figure 4.70: Simulated GGI profiles for the case of the “notch+surface inhomogeneity”, and for the baseline uniform structure. The inhomogeneous structure has low GGI over 70% of its width, high GGI over the remaining 30%.

The simulated figures of merit of the inhomogeneous cell are shown in the tables below, together with the cases of the baseline homogeneous structure and two reference cases of homogeneous cells featuring the *high GGI* and *low GGI* profiles of Figure 4.70. The first table shows the performances of the structures in case of ideal *CdS/CIGS* interface.

	Uniform	Inhomogeneous	High GGI uniform	Low GGI uniform
$V_{OC}[V]$	0.724	0.719	0.749	0.712
$J_{SC}[\frac{mA}{cm^2}]$	37.1	37.0	35.1	37.7
$FF[\%]$	83.3	83.2	83.0	83.0
$\eta[\%]$	22.4	22.1	21.8	22.3

The case where the interface is decorated by a high concentration of mid-gap acceptor traps is given in table below.

	Uniform	Inhomogeneous	High GGI uniform	Low GGI uniform
$V_{OC}[V]$	0.678	0.676	0.685	0.673
$J_{SC}[\frac{mA}{cm^2}]$	37.1	37.0	35.1	37.7
$FF[\%]$	79.1	79.2	78.1	79.2
$\eta[\%]$	19.9	19.8	18.8	20.1

The last table shows the case where the concentration of interface acceptors is 10^4 times lower, but the traps have 10^4 times larger capture cross section, thus yielding the same recombination velocity as in previous table, but with negligible effects of surface trapped charge.

	Uniform	Inhomogeneous	High GGI uniform	Low GGI uniform
$V_{OC}[V]$	0.710	0.706	0.730	0.700
$J_{SC}[\frac{mA}{cm^2}]$	37.1	37.0	35.1	37.7
$FF[\%]$	82.3	82.4	81.5	82.3
$\eta[\%]$	21.7	21.5	20.9	21.7

Even in the case of non-homogeneous "surface + notch" the results are comparable but with even smaller quantitative effects to the "notch" case, this confirms that the *GGI* notch value is the most influential parameter. So from these studies it is possible to conclude that lateral inhomogeneities are not a limiting factor for the performance of the cell because their effect is always small.

4.6.2 Voids

Based on the preliminary results of the measurements performed at EMPA, it was decided to simulate two structures that differ in the position of the void:

- void at the interface between *CdS* and *CIGS*;
- void inside the *CIGS*.

All structures were studied with 3D cylindrical-symmetry simulation and the void is simulated as an air-filled hole in the *CIGS*, so the optical and electrical parameters of air are used for the void volume. The *CdS/CIGS* interface was considered ideal.

In the simulations described below the radius of the structures is *500 nm*, this value was carried out from the EMPA measurements.

4.6.2.1 Void at the CIGS surface, defects decorate the void walls

In Figure 4.71 is shown the simulated structure in case of void at the interface between *CdS* and *CIGS*; the results presented in this section were obtained considering recombination velocity ranging from $10^2 cm/s$ to $10^6 cm/s$ on the walls of the void.

The following table shows the figures of merit of the cell as a function of the recombination velocity; the case in which it is zero represents the baseline structure without void.

Recombination Velocity [cm/s]	$V_{OC}[V]$	$J_{SC}[\frac{mA}{cm^2}]$	$FF[\%]$	$\eta[\%]$
0	0.742	36.9	80.6	22.0
$1 \cdot 10^2$	0.741	36.8	80.6	22.0
$1 \cdot 10^3$	0.736	36.8	80.2	21.7
$2 \cdot 10^3$	0.732	36.8	79.9	21.5
$3 \cdot 10^3$	0.728	36.8	79.6	21.3
$4 \cdot 10^3$	0.724	36.8	79.4	21.2
$1 \cdot 10^4$	0.709	36.8	78.4	20.4
$1 \cdot 10^5$	0.648	36.7	74.6	17.7
$1 \cdot 10^6$	0.587	36.2	71.1	15.1

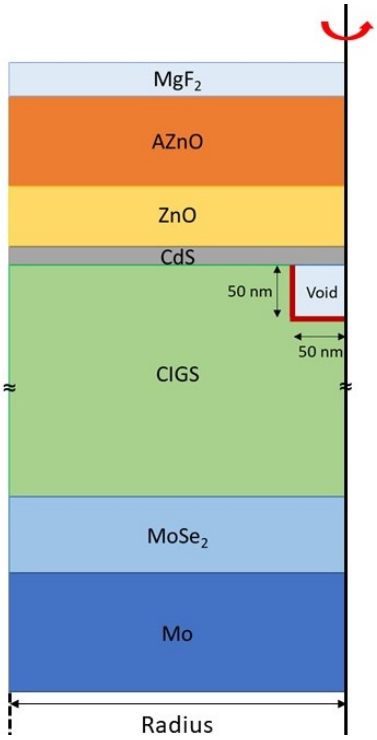

Figure 4.71: Structure with void at the surface. Recombination velocity on the walls of the void (marked by the red lines) was varied. The right side wall is the cylindrical symmetry axis.

In Figures 4.72 and 4.73 are shown the figures of merit of the cell in function of the recombination velocity (V_S) on the wall of the void. From these results it is possible to conclude that the void at *CdS/CIGS* interface is a limiting factor of the performance of the cell and it is not compatible with high efficiency for $V_S > 1 \cdot 10^4 cm/s$.

4.6.2.2 Void 50 nm below the CIGS surface, defects decorate the void walls

In Figure 4.71 is shown the simulated structure in case of void situated at *50 nm* below the surface of *CIGS*; the results presented in this section were obtained considering recombination velocity ranging from $10^2 cm/s$ to $10^6 cm/s$ on the walls of the void.

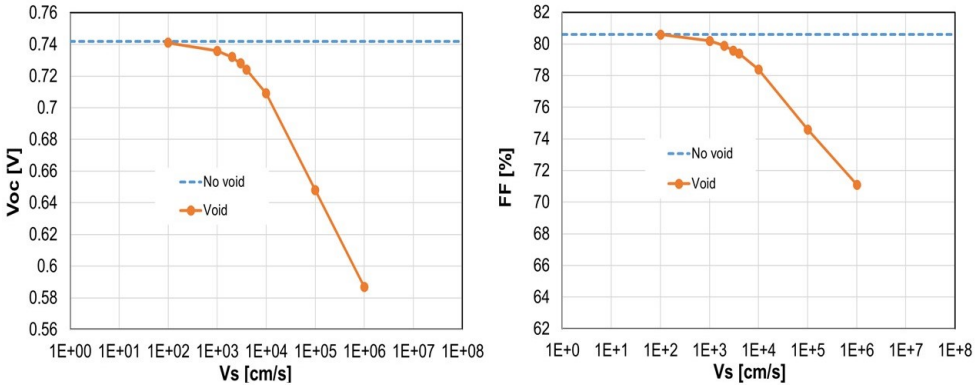

Figure 4.72: V_{OC} and FF as a function of recombination velocity V_S on the wall of the void.

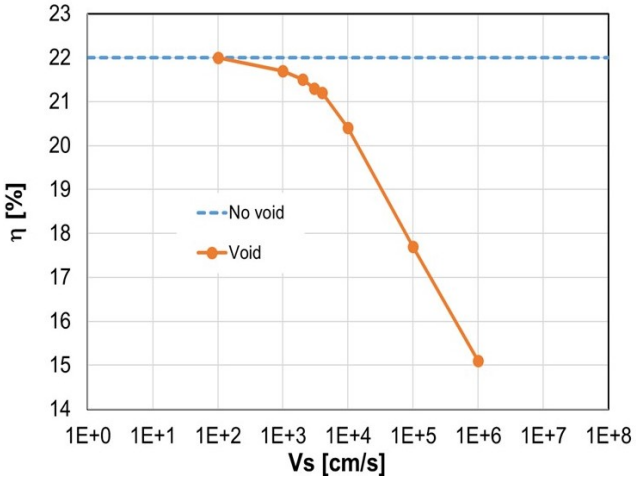

Figure 4.73: η as a function of recombination velocity V_S on the wall of the void.

The following table shows the figures of merit of the cell as a function of the recombination velocity; the case in which it is zero represents the baseline structure without void.

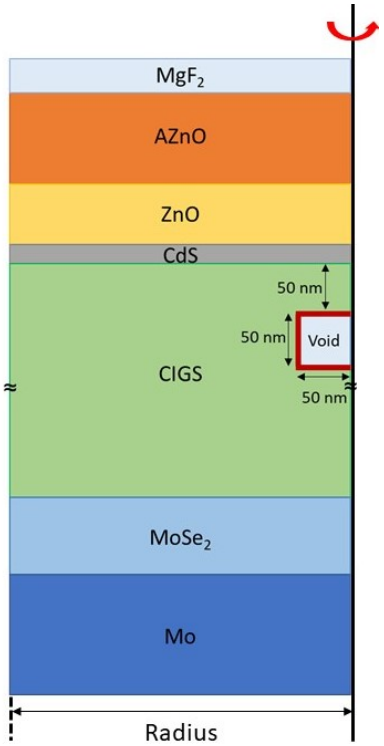

Figure 4.74: Structure with void 50*nm* below the surface. Recombination velocity on the walls of the void (marked by the red lines) is varied. The right side wall is the cylindrical symmetry axis.

Recombination Velocity [cm/s]	$V_{OC}[V]$	$J_{SC}[\frac{mA}{cm^2}]$	$FF[\%]$	$\eta[\%]$
0	0.742	36.9	80.6	22.0
$1\cdot 10^2$	0.741	36.8	80.6	22.0
$1\cdot 10^3$	0.737	36.8	80.3	21.8
$2\cdot 10^3$	0.733	36.8	80.0	21.6
$3\cdot 10^3$	0.729	36.8	79.8	21.4
$4\cdot 10^3$	0.726	36.8	79.6	21.3
$1\cdot 10^4$	0.711	36.8	78.7	20.6
$1\cdot 10^5$	0.652	36.7	75.2	18.0
$1\cdot 10^6$	0.591	36.2	71.0	15.2

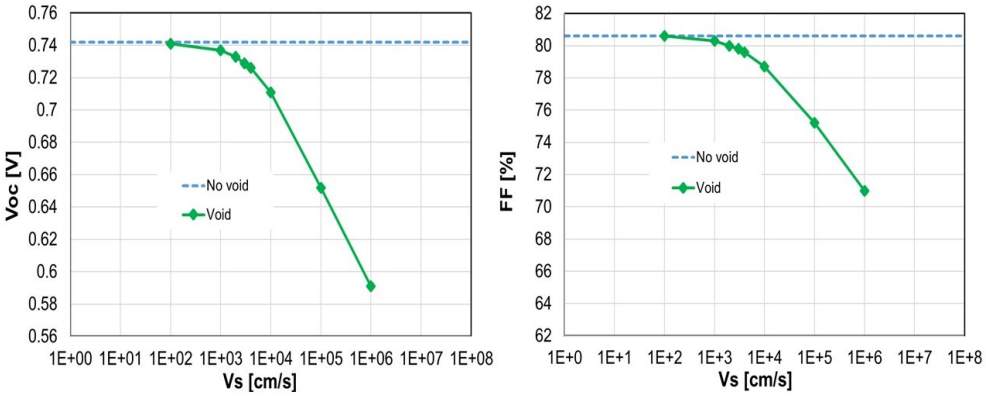

Figure 4.75: V_{OC} and FF as a function of recombination velocity V_S on the wall of the void in case of void 50nm below the *CIGS* surface.

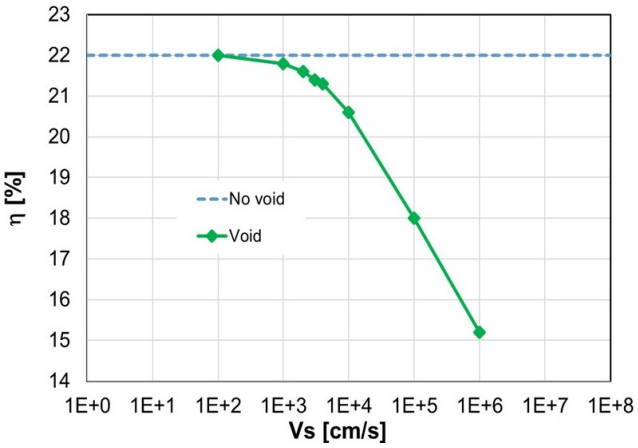

Figure 4.76: η as a function of recombination velocity V_S on the wall of the void in case of void 50nm below the *CIGS* surface.

In Figures 4.75 and 4.76 are shown the figures of merit of the cell in function of the recombination velocity (V_S) on the wall of the void. These results are comparable with the case of void at *CIGS* surface, so it is possible to conclude that also the void at 50nm below the the surface of *CIGS* is a limiting factor of the performance of the cell and it is not compatible with high efficiency for $V_S > 1 \cdot 10^4 cm/s$.

At the end of these studies on the lateral inhomogeneities of the *GGI* profile and the material voids it is possible to conclude that the voids have a negative effect on the cell performances because they introduce a new defect, which is not taken into consideration in the baseline, that increases the recombinations; on the other hand, the effect of inhomogeneity is negligible in most cases.

4.7 Grain Boundaries

Even if polycrystalline *CIGS* solar cells have reached efficiencies up to 22.9% [26], the presence of grain boundaries (GBs) could be detrimental for the efficiency, as shown in many studies [39] [40] [41] [42]; therefore, the effect of the presence of GB in a cell was analyzed, in particular it was investigated whether a strong band-bending, upwards or downwards, caused by GB can coexist with high efficiency.

The simulations were based on the EMPA cell simulated with optical coefficients measured at EMPA for all the materials [24]. These optical values give the following figures of merit for the baseline without GB:

$$V_{OC} = 0.742V \; J_{SC} = 36.8\frac{mA}{cm^2} \; FF = 80.6\% \; \eta = 22\%$$

All structures were studied with 3D cylindrical-symmetry simulations, so there is the grain with *500 nm* of radius which is surrounded by the grain boundary *2 nm* wide (Figure 4.77).

It is possible to induce the band-bending in two different ways: fixed charge or traps; therefore, three scenarios were simulated:

- fixed charge in the grain boundary to simulate only the field effect;
- traps in the grain boundary with small cross-section;
- traps in the grain boundary with large cross-section to take into account also the recombination effect.

The fixed charge in the first scenario and the traps in the last two were chosen to simulate a range from $-600meV$ to $+600meV$ of band-bending (Δ_{CPD}) due to the grain boundary; this values were taken from INL measurements.

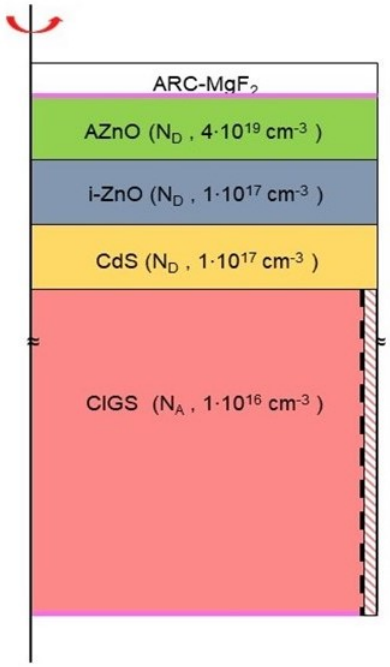

Figure 4.77: Simulated structure in presence of Grain Boundary.

4.7.1 Fixed charge in the grain boundary

The preliminary study on the effect of grain boundary on the performance of the solar cells was focused on the presence of a fixed charge inside the GB in order to reproduce the band-bending measured from INL but, at the same time, excluding the effect of recombinations.

The band-bending (Δ_{CPD}) was calculated with the cell in dark condition and it is the difference between the band in the grain and that in the grain boundary.

In Figures 4.78 and 4.79 are shown the figures of merit of the cell in function of the Δ_{CPD}; a positive fixed charge simulates a downward band-bending, instead a negative fixed charge simulates an upward band-bending.

It is possible to note that a positive band-bending, corresponding to a GB decorated with a negative charge has no effect on the V_{OC} and FF, while in the case of downward

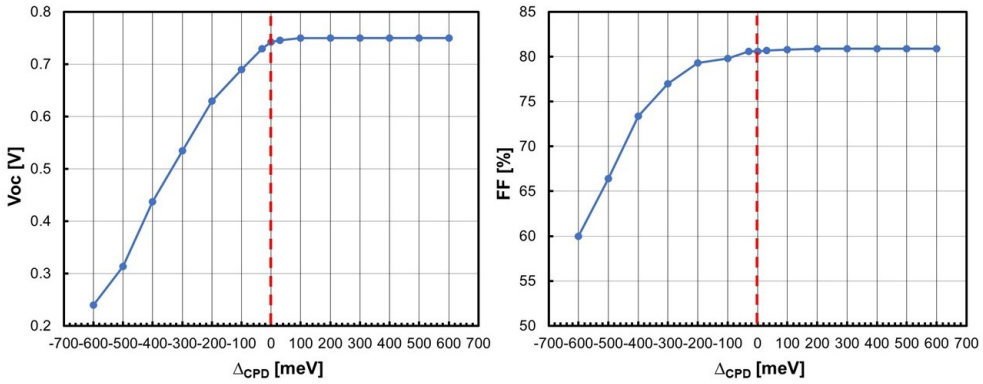

Figure 4.78: V_{OC} and FF as a function of band-bending (Δ_{CPD}).

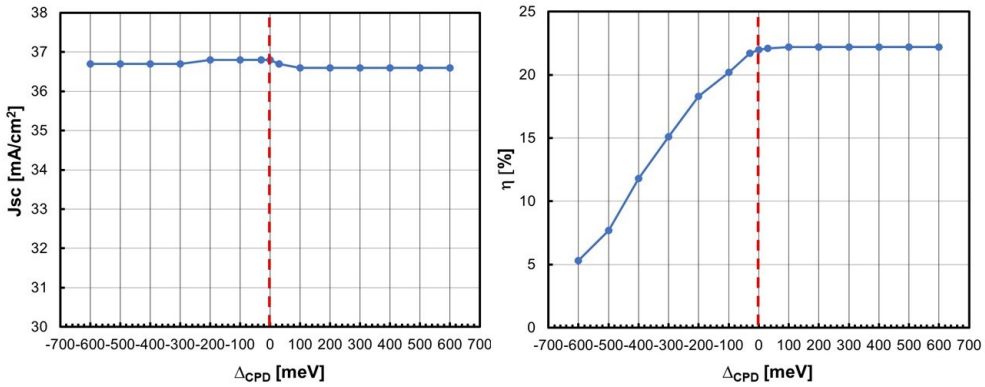

Figure 4.79: J_{SC} and η as a function of band-bending (Δ_{CPD}).

band bending the V_{OC} and FF reduce the more Δ_{CPD} becomes negative. On the other hand, the J_{SC} seems almost unaffected by both the fixed charge, so it is possible to conclude that the efficiency of the cell is controlled by V_{OC} and FF.

In order to understand the observed behavior, it is useful to look the I-V curves simulated for different Δ_{CPD} (Figure 4.80).

In case of negative fixed charge, so upward band-bending, the J-V curves are superimposed, instead for the case of positive FC, so negative CPD, the J-V characteristics are larger the more Δ_{CPD} becomes negative and the behavior of the curves

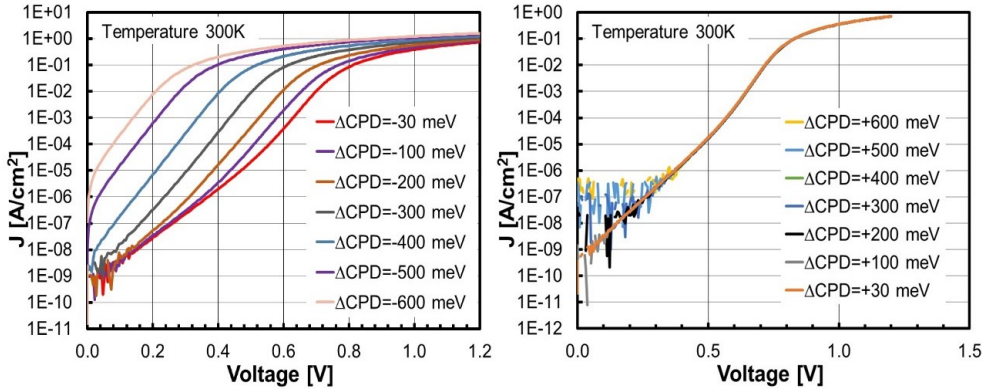

Figure 4.80: Simulated J-V curve for different Δ_{CPD}.

completely changes impacting on the FF and V_{OC}.

The different behavior is due to the grain interior which becomes depleted of holes with the increasing of Δ_{CPD} as possible to observe in the band diagram (Figure 4.81); instead the grain boundary becomes rich of electrons with the increasing of Δ_{CPD}.

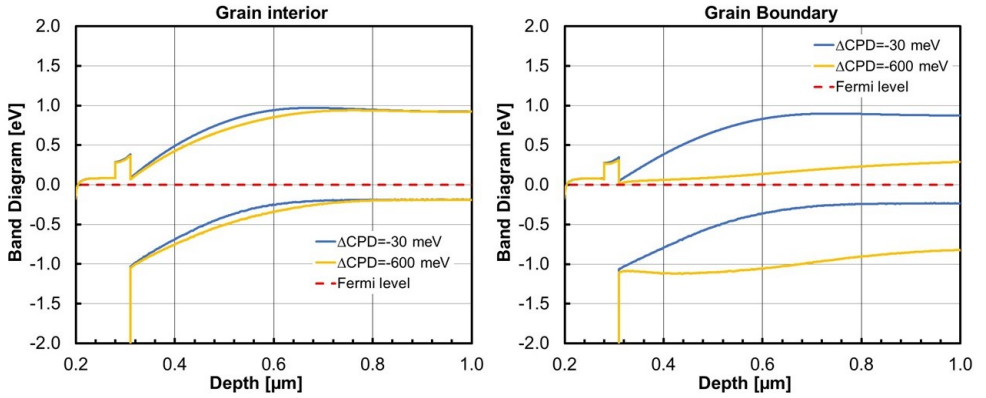

Figure 4.81: Equilibrium band diagram of the grain interior and grain boundary for two Δ_{CPD} $(-30meV, -600meV)$.

Because of the band-banding at the grain boundary the grain interior becomes more n-type and the built-in barrier at the p-n junction reduces, this increases the dark

current that reduce the V_{OC} and the FF. Therefore it is possible to conclude that the decreases of open-circuit voltage and fill-factors are not induced by the recombinations but, from the depletion of the grain interior which is caused by the band-bending due to the grain boundary.

4.7.2 Traps in the grain boundary

The second part of the study on the effect of grain boundaries on the performance of the cell was focused on the simulation of the GB with traps instead of fixed charge. Two different configurations of traps were simulated:

- traps with low capture cross-section ($1 \cdot 10^{-20} cm^2$) in order to simulate only the field effect due to the ionized traps and exclude the recombinations;
- traps with large capture cross-section ($1 \cdot 10^{-16} cm^2$) in order to take into account both the field effect and the recombinations effect.

The concentration of defects is the same in both the cases and it was chosen in order to achieve the wanted Δ_{CPD}.

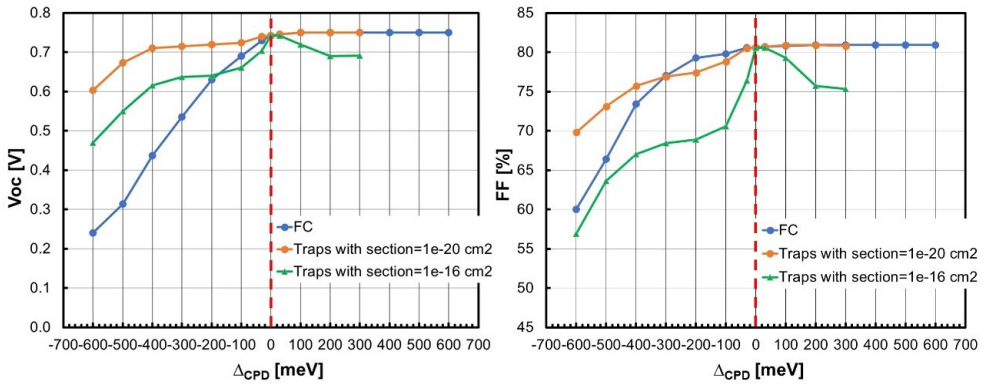

Figure 4.82: V_{OC} and FF as a function of Δ_{CPD} for three different cases: FC in the grain boundary (blu line), traps with small cross-section ($1 \cdot 10^{-20} cm^2$ orange line) and traps with large capture cross-section ($1 \cdot 10^{-16} cm^2$ green line)

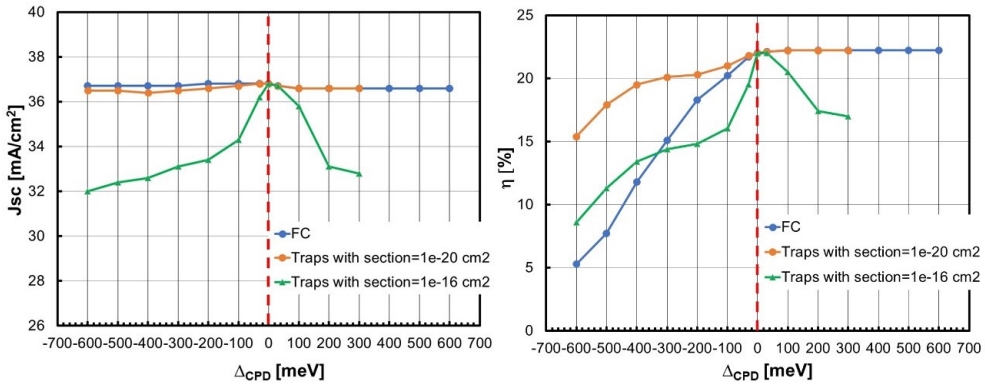

Figure 4.83: J_{SC} and η as a function of Δ_{CPD} for three different cases: FC in the grain boundary (blu line), traps with small cross-section ($1 \cdot 10^{-20} cm^2$ orange line) and traps with large capture cross-section ($1 \cdot 10^{-16} cm^2$ green line)

In Figures 4.82 and 4.83 the comparison of the performance parameters of the cell is shown for the three cases: Fixed charge, Traps with low cross-section ($1 \cdot 10^{-20} cm^2$), and Traps with large cross-section ($1 \cdot 10^{-16} cm^2$).

Considering the two cases with the traps, as expected, V_{OC} is more degraded in the case of a large capture section such as FF; instead if these cases are compared with the one with a fixed charge, it is possible to observe that the effect of a FC is worse than in the case of trap at a constant Δ_{CPD}.

The reason why at fixed Δ_{CPD} the effect of FC is generally worst than traps of low capture cross section is that the CPD in case of fixed charge is unaffected by the light instead in case of traps the traps ionization is different under illumination or in the dark, for this reason the Δ_{CPD} reduces mitigating the effect of GB.

In Figure 4.84 the comparison between FC and traps is shown in terms of band diagram under light and in the dark. Exactly as described before in the case of traps $\Delta_{CPD,Light} \ll \Delta_{CPD,Dark}$, instead in case of FC $\Delta_{CPD,Light} = \Delta_{CPD,Dark}$.

At the end of this study it is possible to conclude that an upward band-bending $\Delta_{CPD} > 0$ reduces V_{OC}, FF and η only if due to traps with large cross-section; instead a downward band-bending $\Delta_{CPD} < 0$ reduces always V_{OC}, FF and η the more Δ_{CPD}

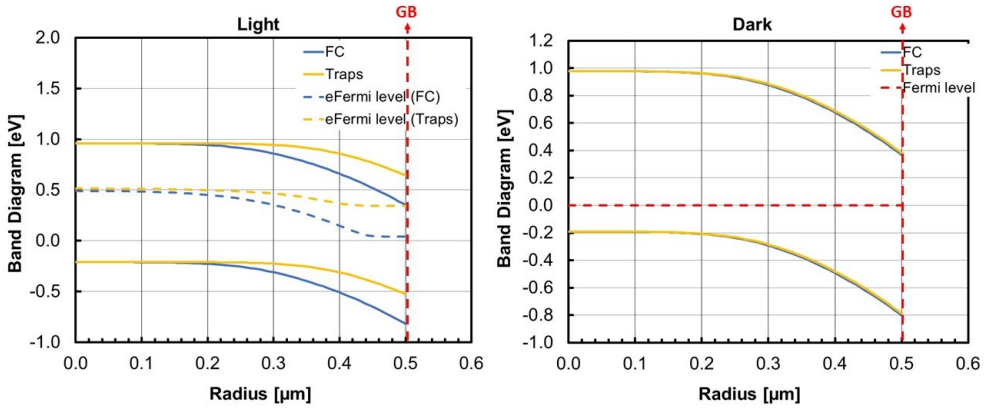

Figure 4.84: Band diagram in the dark and under light condition for two cases: FC inside the Grain Boundary (blu lines) and Traps inside the Grain Boundary (yellow lines)

becomes negative. The last mention is focused on the *J-V* curves which are very different from measured ones in case of FC at the GB so it is more probable that in the GBs there are traps with low cross-section in order to justify the J-V behavior and the high efficiency.

4.8 Optical losses in CIGS solar cells

Up to this point all the limiting factors of the performance of the *CIGS*-based solar cells mentioned in this chapter are related in some way to the non-radiative recombination but, as described in the introduction, the decrease in efficiency could also be related to optical losses.

In this section will be presented a study focused on the optical losses of the two cells, EMPA and ZSW, used as baseline in this thesis.

A critical step of the path to accurate optical modeling of the cells under test is the choice of optical coefficient spectra for the various materials. This step is not trivial at all, mainly due to the wide dispersion of the data available in the literature. In the way to obtain a good match between measured and simulated structures it was chosen

an optical coefficient spectra taken from literature [32] for all the materials in the stack, except for the *CIGS* absorber, for which it was used optical coefficient spectra measured at EMPA [24]. In the simulations of this section it was always considered $CGI = 0.9$, so the optical coefficients are those corresponding with this *Cu* content.

4.8.1 ZSW cell

In Figure 4.85 are shown the measured and simulated EQE spectra for the ZSW cell, the match is quite good, the only difference is an overestimate in the central part of the spectrum.

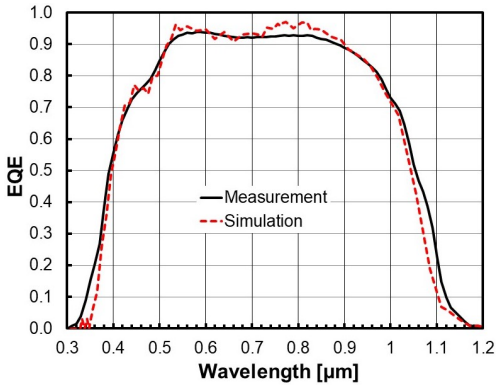

Figure 4.85: Measured and simulated EQE spectra for the ZSW record cell.

The detailed analysis on the optical losses in each layer of the structure is shown in Figure 4.86.

In Figure 4.86 the distance between each line and the one immediately above indicates the corresponding loss: black line: reflection loss; blue line: *Al-doped ZnO* window loss; light blue line: *i-ZnO* loss; red line with dots: *CdS* buffer loss; green line: *CIGS* absorption; the distance between the green line and the EQE (black dashed line) marks the collection losses. In table below are listed the calculated value for each optical loss.

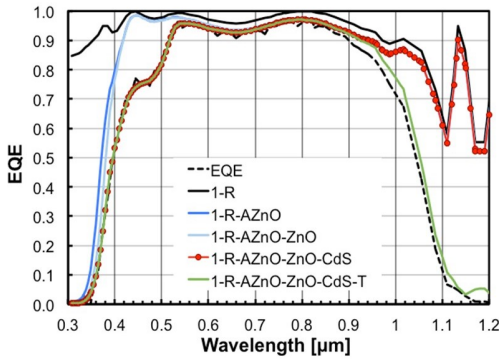

Figure 4.86: Simulated EQE spectrum for the ZSW record cell, together with the absorption loss of each individual layer.

Loss contribution	$J_{SC}[\frac{mA}{cm^2}]$	$\delta J_{SC}[\frac{mA}{cm^2}]$	$deltaJ_{SC}[\%]$
Reflection	47.92	–	–
AZnO	45.77	-2.15	-4.5
i-ZnO	45.62	-0.15	-0.3
CdS	43.97	-1.65	-3.4
Transmission	36.40	-7.57	-15.8
Collection	35.40	-1.00	-2.1

As expected it is possible to conclude that the most part of the optical losses are in the window layer (*-4.5%*) and in the buffer layer (*-3.4%*), instead the transmission losses are not considered because are impossible to recover for the reason that they are formed from photons with too low energy to be absorbed by the *CIGS*.

4.8.2 EMPA cell

The same analysis was done for the EMPA cell, so in Figure 4.87 are shown the measured and simulated EQE spectra, the match also in this case is quite good and the only difference is an overestimation of the absorption in the NIR range.

The detailed analysis on the optical losses in each layer of the structure is shown in Figure 4.88.

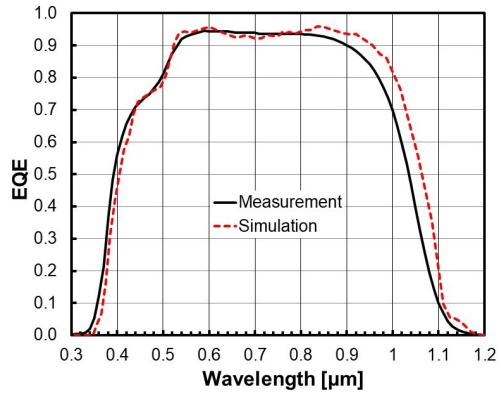

Figure 4.87: Measured and simulated EQE spectra for the EMPA record cell.

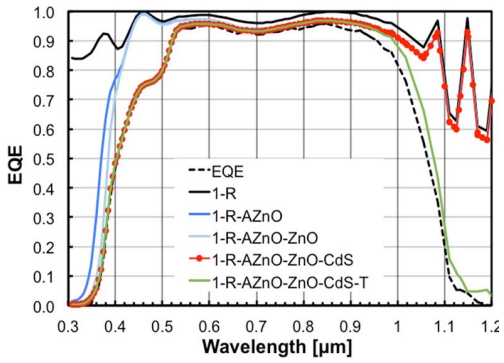

Figure 4.88: Simulated EQE spectrum for the EMPA record cell, together with the absorption loss of each individual layer.

As for the ZSW cell, in Figure 4.88 the distance between each line and the one immediately above indicates the corresponding loss: black line: reflection loss; blue line: *Al-doped ZnO* window loss; light blue line: *i-ZnO* loss; red line with dots: *CdS* buffer loss; green line: *CIGS* absorption; the distance between the green line and the EQE (black dashed line) marks the collection losses. In table below are listed the calculated value for each optical loss.

Loss contribution	$J_{SC}[\frac{mA}{cm^2}]$	$\delta J_{SC}[\frac{mA}{cm^2}]$	$deltaJ_{SC}[\%]$
Reflection	48.57	–	–
AZnO	46.59	-1.98	-4.1
i-ZnO	46.34	-0.25	-0.5
CdS	44.64	-1.70	-3.5
Transmission	37.47	-7.17	-14.8
Collection	36.16	-1.31	-2.7

Also in the case of EMPA cell is possible to conclude that that the most part of the optical losses are in the window layer (*-4.1%*) and in the buffer layer (*-3.5%*); the transmission losses are not considered for the same reason described in the ZSW cell.

From these analysis is possible to resume that for both the cells the layer which causes the highest optical loss is the window one; this is unexpected because the *AZnO* (*3.3eV*) has an higher band-gap than the *CdS* (*2.4eV*) so the absorption should be lower, instead for its thickness and for a tail of absorption at low energies [32] it results the worst layer from an optical point of view. The possible solution to these losses is to change the materials which compose the window and the buffer layer, this changing will be analyzed in the next chapter.

Chapter 5

New solutions to increase the efficiency of the cells

In this chapter some possible solution to increase the efficiency of the thin-film CIGS solar cells will be presented. Initially the focus will be on the interface between CdS and CIGS where point contact can be introduced, then the presence of point contact at the back of the cell (CIGS/Molibdenum) will be analyzed. The possible increase of efficiency due to the insertion of a reflector at the back of the cell will be analyzed as well. Finally a study on buffer alternative to CdS will be presented.

5.1 Front Point Contact

As written in the previous chapter, one of the limiting factors of the thin-film *CIGS* solar cells are the non-radiative recombinations at the interface between the buffer and the absorber layers. In order to reduce this negative effect, the introduction of surface passivation and point contacts which can help to boost the cell performance [57], similarly to the case of advanced PERC cells [58] in silicon solar cell technology will be analyzed.

These simulations are based on the EMPA cell simulated with absorption coefficients measured at EMPA for the *CIGS* [24], instead for the other material coefficient

taken from literature [32] are used, so the figures of merit of the baseline are:

$$V_{OC} = 0.741V,\ J_{SC} = 36.4\frac{mA}{cm^2},\ FF = 80.1\% \text{ and } \eta = 21.6\%.$$

The simulated cell is based on the passivation plus local opening geometry achievable by the Self-Assembled Alkali-Template (SALT) technique at EMPA [59], and it is shown in Figure 5.1.

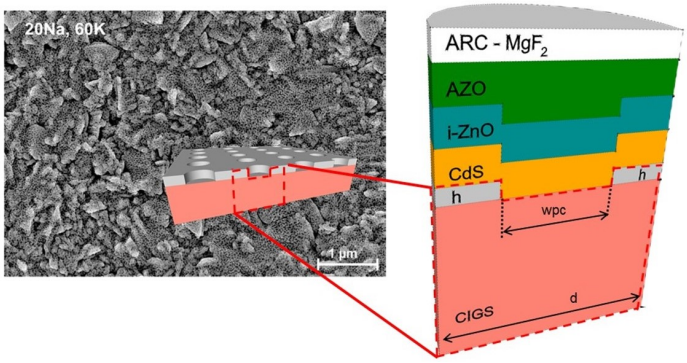

Figure 5.1: Left: SEM micrograph of *CIGS* nano-patterned surface; right: schematic cross-section of the 3D simulated cell.

The passivation layer thickness h, the point contact width wpc, and pitch d are varied in order to evaluate their effect on cell performance. When $h = 0$, the *CdS* covers the whole *CIGS* surface, and the cell structure is the standard one.

In this set of simulations it was used cylindrical-symmetry 3D simulations since the point contact is inherently a 3D structure: a 2D simulation would describe a line contact extending indefinitely in the third dimension, with significant underestimation of the contact resistance for a given wpc value.

As far as interface recombination is concerned, two scenarios for the *CdS/CIGS* interface were examined:

- ideal interface (no trap centers);
- non-ideal interface (with trap centers).

The passivation is modeled as a transparent layer with $Eg = 5eV$, forming a conduction band spike ($\Delta E_C = 0.5eV$) at the interface with *CIGS*. It is worth pointing out that the exact value of the energy gap of the passivation layer used in simulation is not very relevant, since passivation is considered to be transparent.

5.1.1 Chemical passivation

Starting from the ideal-case bulk-limited cell ($\eta = 21.6\%$), in order to simulate a case of surface-limited cell, either acceptor or donor traps were introduced, with a density of $1 \cdot 10^{10} \div 1 \cdot 10^{11} cm^{-2}$ at the *CdS/CIGS* interface, corresponding to surface recombination velocity of $1 \cdot 10^{3} \div 1 \cdot 10^{4} cm/s$.

All traps are energetically located at the *CIGS* mid-gap: in fact, simulations presented in previously chapter have shown that the effect of both interface acceptor-like and donor-like defects is largely independent of the trap energy level as long as the latter is within $\pm 0.3eV$ from the intrinsic Fermi level.

As listed in table below, the lowest efficiency $\eta = 15.9\%$ is obtained for acceptor defects of density $N_{AT} = 1 \cdot 10^{11} cm^{-2}$, due to a larger reduction of both V_{OC} and FF caused by enhanced surface recombination and defect-induced band bending.

	$N_{AT}[cm^{-2}]$	$V_{OC}[V]$	$J_{SC}[\frac{mA}{cm^2}]$	$FF[\%]$	$\eta[\%]$
Reference (ideal interface)	0	0.74	35.6	82.1	21.6
	$D - 1 \cdot 10^{11}$	0.67	35.3	80.0	18.9
	$D - 1 \cdot 10^{10}$	0.72	35.3	81.3	20.7
	$A - 1 \cdot 10^{11}$	0.59	35.3	75.9	15.9
	$A - 1 \cdot 10^{10}$	0.72	35.3	81.0	20.5
	Neutral defects	0.67	35.3	80.0	18.9
	Negatively charged defects-$1 \cdot 10^{11}$	0.74	35.3	79.4	20.7

In order to decouple the effect of recombination from that of band bending due to charged interface defects, separate cases were also simulated:

- neutral recombination centers;
- negatively charged (i.e., acceptor-type) interface defects with low enough capture cross section to make surface recombination negligible.

As expected, the negatively charge defects affect FF (-2.7% absolute) due to a change in the band bending, leaving V_{OC} unchanged, while the neutral recombination centers reduce V_{OC} ($-0.07V$) and, as a consequence, FF.

In the presence of acceptor traps, these two effects, namely, the different band bending due to negatively-charged acceptors and trap-assisted surface recombination, combine to reduce the efficiency of the cell to the 15.9% minimum observed in previous table.

With reference to the interface-limited cell with $1 \cdot 10^{11} cm^{-2}$ acceptors, in order to identify the optimum passivation layer thickness and point contact layout that give the largest efficiency recovery, several structures were simulated with different passivation thickness: $h = 5nm, 10nm, 25nm$; all these values are compatible with the Atomic Layer Deposition (ALD) technique [60]. For each value of h, three values of the point contact pitch were considered: $d = 50nm, 100nm, and 250nm$. Moreover, for each combination of h and d, the point contact width wpc was varied between $5nm$ and $(d - 10nm)$.

The best performance, with $\eta = 19.3\%$, is reached with a point contact width $wpc = 20nm$ and closely spaced ($d = 50nm$) point contacts. The best efficiency obtained for each value of h and the corresponding combination of d and wpc is shown in table below.

$h[nm]$	$V_{OC}[V]$	$J_{SC}[\frac{mA}{cm^2}]$	$FF[\%]$	$\eta[\%]$
5	0.70	35.5	78.1	19.3
10	0.69	35.5	76.7	18.7
15	0.66	35.4	72.5	16.9

The complete set of the figures-of-merit of the cell is shown as a function of wpc and for different values of d, in the case of $h = 10nm$, in Figure 5.2.

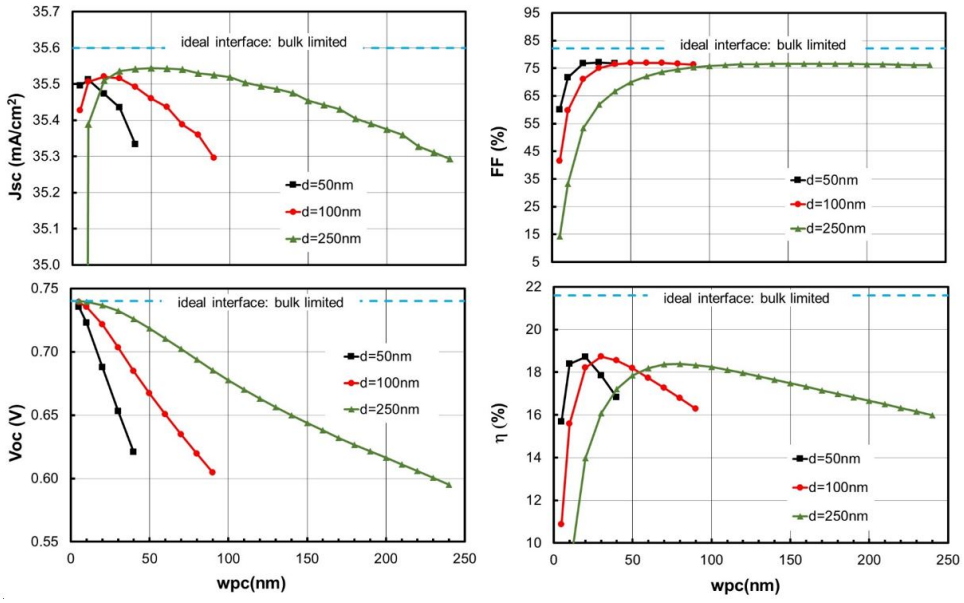

Figure 5.2: Simulated cell parameters vs. point contact width, *wpc*, for varying pitch, *d*. Non-ideal interface ($N_{AT} = 10^{11} cm^{-2}$). $h = 10nm$, $d = 50nm$, $wpc = 10nm$. The reference line indicates the case of absence of interface states and passivation.

Even with the optimal configuration ($h = 5nm$), the efficiency recovery - about *3.4%* absolute, offered by surface passivation with point contacts does not restore the ideal bulk-limited case efficiency ($\eta = 21.6\%$).

In fact, contrary to V_{OC}, which completely recovers the loss due to the defective *CdS/CIGS* interface, the fill factor (*78.1%*) remains lower than that of the ideal-interface solar cell (*82.1%*). As shown by Figure 5.2 (top right), the fill factor (*FF*) is severely degraded for narrow point contacts, due to the increased resistance of the current path in the absorber and through the point contact openings, despite the carrier diffusion length being in the micrometer range for both electrons and holes. The parasitic resistance of point contacts increases with passivation thickness, too, because the *CdS* thickness covering the point contact corners, which is equal to $(30nm - h)$, as seen in previous table, is reduced for higher *h*.

On the other hand, Figure 5.2 shows that increasing *wpc*, starting from values in the low nanometer range, makes the cell tend toward the surface-limited case, due to insufficient passivation of the interface defects. The performance degradation for increasing *wpc* can be expected to be gentler for less defective interfaces. This means that the success of the passivation-with-point-contacts strategy depends on the trade-off between the beneficial effect of surface defects passivation, which is maximum for narrow point contacts and wide pitch, and the detrimental effect of series resistance, which is aggravated when the point contacts are narrower and wider apart.

Since the series resistance introduced by the passivation layer with point contacts is the factor limiting the cell performance, it was evaluated the effect of increasing the doping densities. It can be expected that the more conductive the *CIGS* and *CdS* layers, the less will the cell suffer from series resistance effects, thus enhancing the benefit of point contacts.

It was considered as reference the cell with $h = 10nm$, $d = 50nm$, $wpc = 10nm$ and it was simulated the illuminated behavior for different values of the *CIGS* acceptor doping density keeping the *CdS* donor doping density fixed at $2 \cdot 10^{16} cm^{-3}$. Similarly was done for different values of *CdS* donor doping keeping the *CIGS* doping density fixed at $1 \cdot 10^{16} cm^{-3}$ (Figure 5.3).

In Figure 5.3 the results of simulation with different doping of *CIGS* and *CdS* are shown, it is possible to conclude that while increasing the *CdS* doping (5.3, black line) does prove successful owing to reduction of the parasitic series resistance of the point contact path and improved band alignment [61], instead higher *CIGS* doping (5.3, orange line) lowers the *FF* due to unfavorable combination of doping and band alignment [61]. In both cases, the effect of increased doping is marginal on V_{OC} and J_{SC}, and *FF* controls the cell performance.

The presence of passivation on top of the *CIGS* makes the *CdS* redundant outside of the point contact areas, and suggests the possibility of removing the *CdS* everywhere except in the point contacts, thus increasing the photon inflow and the External Quantum Efficiency (EQE). Thus, it was chosen the cell with $h = 10nm, wpc = 10nm, d = 50nm$, and removed the *CdS* from the passivation top, leaving everything else unchanged. The simulated efficiency improves from *18.4%* to *21.0%*, not only

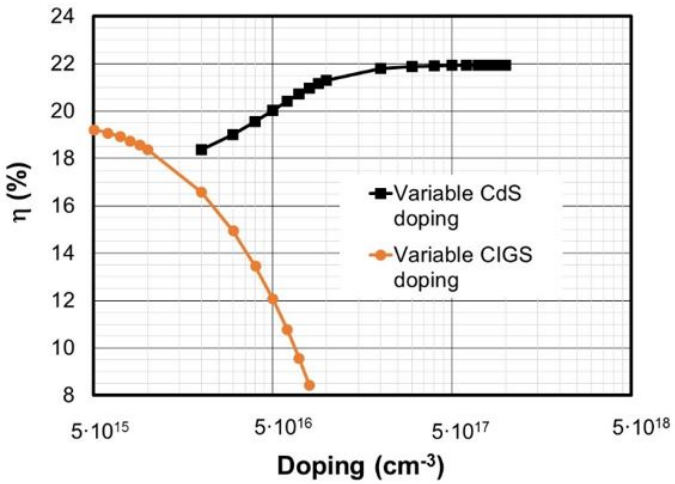

Figure 5.3: Simulated efficiency versus either CIGS acceptor doping density (orange line), or CdS donor doping density (black line). Non-ideal interface.

due the expected reduction of absorption losses in the *CdS* (corresponding to a J_{SC} increase of $+1mA/cm^2$), but also to the improvement of *FF* (+7% absolute), the latter mainly attributed to the series resistance (extracted from the slopes of the *I-V* curve near V_{OC}) decreasing from $3.10\Omega\cdot cm^2$ to $1.55\Omega\cdot cm^2$ when the *CdS* is removed from the top of the passivation layer and is replaced by more conductive *ZnO*.

5.1.2 Field-effect passivation

The previous analysis was based on a perfect passivation of interface defects, that is, defect-free passivation-layer/absorber interface. In that case the passivation with point contact arrangement allows to recover the cell efficiency significantly, but not so much as to attain the bulk-limited $\eta = 21.6\%$.

A different solution which can decrease the recombination at the *CIGS* surface is the reduction of the density of one type of carrier by means of the electric field induced by the charge within the passivation. The best choice can be the introduction of a positive charge, which attracts electrons at the surface, favours the photo-current flow

and moves the *CIGS* surface deeper into inversion thus reducing the recombination.

In order to evaluate this effect, it was considered the presence of a fixed positive charge density, Q_f, inside the passivation layer, which is varied in the range $1 \cdot 10^{10}$ – $1 \cdot 10^{13} cm^{-2}$. Positive Q_f are reported in HfO_2 layers, in $SiO_2/HfO_2/Al_2O_3$ stacks depending on the thicknesses of different materials, or in as-deposited Al_2O_3 [62] [63] [64].

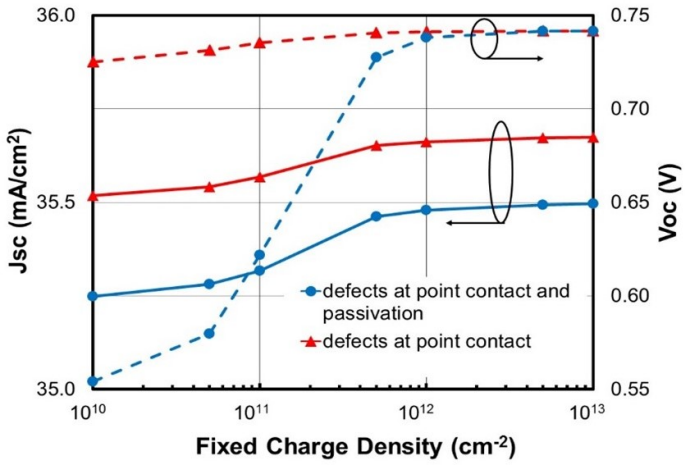

Figure 5.4: Simulated J_{SC} and V_{OC} vs. fixed charge density inside the passivation layer with $h = 10nm$, $wpc = 10nm$, $d = 50nm$ for the two scenarios of acceptor interface states with density $10^{11} cm^{-2}$ at point contact only (triangles) and all over the *CIGS* surface (circles).

Two scenarios were examined for the case of the most detrimental acceptor traps density, $N_{AT} = 1 \cdot 10^{11} cm^{-2}$:

- acceptor traps are present only at the buffer/absorber interface, so only in the point contact openings, which corresponds to ideal chemical passivation at the absorber/passivation interface;

- acceptor traps are present all over the *CIGS* surface, in order to simulate the case of ineffective chemical passivation.

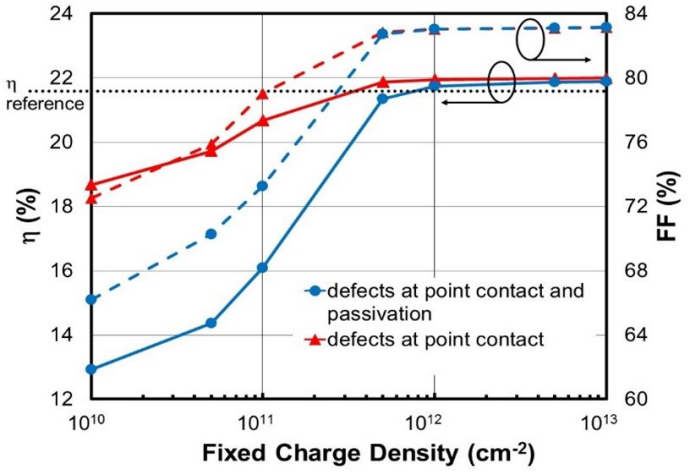

Figure 5.5: Simulated FF and η vs. fixed charge density inside the passivation layer with $h = 10nm$, $wpc = 10nm$, $d = 50nm$ for the two scenarios of acceptor interface states with density $10^{11}cm^{-2}$ at point contact only (triangles) and all over the *CIGS* surface (circles). The reference line indicates the case of absence of interface states and passivation.

In Figures 5.4 and 5.5 are shown the simulated cell parameters in function of fixed charge inside the passivation for the two scenarios of acceptor interface states; the reference line indicates the case of absence of interface states and passivation.

As shown (Figures 5.4 and 5.5) even with ideal chemical passivation of defects (red triangles), the efficiency improve by almost 3.6% absolute in the case of additional field-effect passivation induced by positive Q_f mainly by the increase of FF, slightly surpassing the bulk-limited cell with no passivation (reference dotted line).

The positive Q_f reduces the barrier seen by photo-generated electrons leaving the absorber, as shown in in Figure 5.6 for $V = 0.4V$ (corresponding to the Maximum Power Point, MPP, in the case of $Q_f = 0cm^{-2}$), and also favors the accumulation of electrons at the inverted passivation/absorber interface (Figure 5.7) thereby reducing the resistance of the current path inside the absorber: consequently, FF increases and so does efficiency.

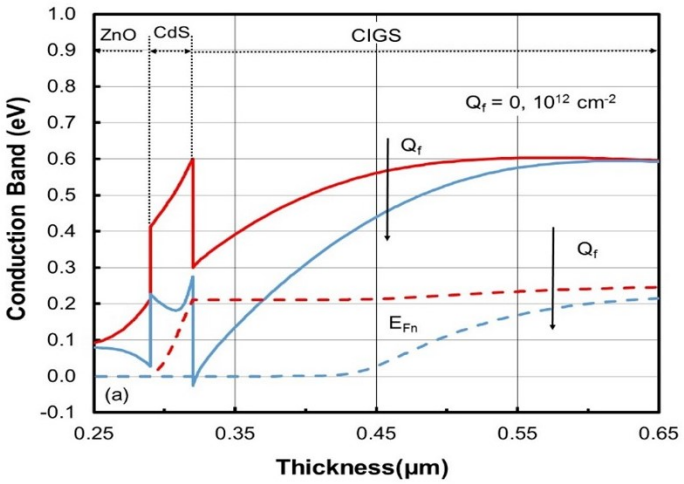

Figure 5.6: Conduction band energy in the point contact area in the case of acceptor interface states $N_{AT} = 10^{11} cm^{-2}$ all over the *CIGS* surface and $Q_f = 0, 10^{12} cm^{-2}$. E_C (solid lines) and corresponding electron Fermi energy, E_{Fn} (dashed lines) versus depth at $V = 0.4V$ (corresponding to the MPP for the case of $Q_f = 0$).

Not surprisingly, the benefit of field-effect passivation is even larger in the case of inefficient chemical passivation of defects: the 12.5% efficiency obtained with $Q_f = 0$ jumps to 21.9%, if positive $Q_f > 5 \cdot 10^{11} cm^{-2}$ is present at the passivation/absorber interface (Figure 5.5, circles).

The efficiency improvement is due to the increase of both V_{OC} $(+180mV)$ and FF (+18% absolute), respectively originating from the inhibition of recombination and the improved band alignment at the *CIGS* surface. The presence of field-effect passivation helps relaxing the requirements on point contact size: in fact in the presence of positive fixed charge density $Qf = 1 \cdot 10^{12} cm^{-2}$, local openings through the passivation in the range $5 \div 20nm$ practically give the same cell efficiency, as shown in Figure 5.8.

In these sections the effects of both chemical and field-effect passivation were analyzed, the obtained results lead to conclude that in the presence of surface-limited cells, with strongly defective *buffer/CIGS* interface, the use of surface passivation in combination with point contacts can help the cell recover most of the performance

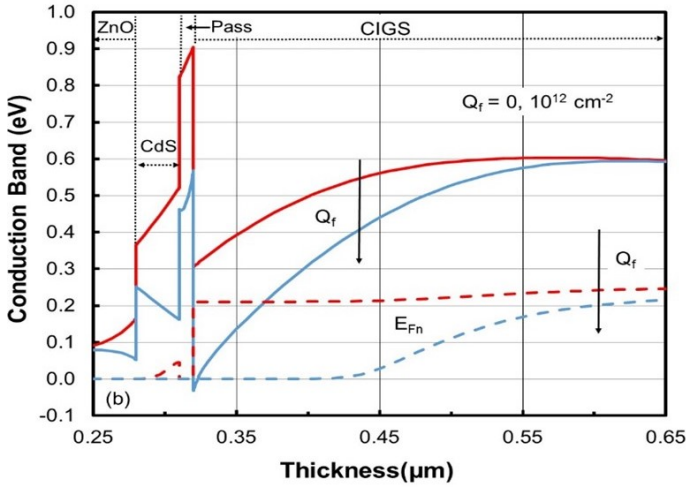

Figure 5.7: Conduction band energy in the passivated area, in the case of acceptor interface states $N_{AT} = 10^{11} cm^{-2}$ all over the *CIGS* surface and $Q_f = 0, 10^{12} cm^{-2}$.

loss due to interface states, provided that the passivation is effective in removing the surface defects. Nanometer-scale point contact openings with pitch of a few tens of nanometers give the best results for the structures considered.

It was identified that the fill factor is the main performance bottleneck and it was showed that lower series resistances (leading to higher fill factor), can be obtained with thin passivation layer and high doping density ($\geq 1 \cdot 10^{17} cm^{-3}$) of buffer layer, but also removing the *CdS* from the top of the passivation.

In the end it was also showed that positive charge in the order of $1 \cdot 10^{12} cm^{-2}$ within the passivation can improve the efficiency of a cell with ideal chemical passivation by about 3.4% absolute, mainly thanks to better fill-factor. This field-effect passivation is even more effective in the case of inefficient chemical passivation. The positive charge also helps relaxing the requirements on the point contact geometry: point contact widths up to $20nm$ can be used without significant efficiency loss.

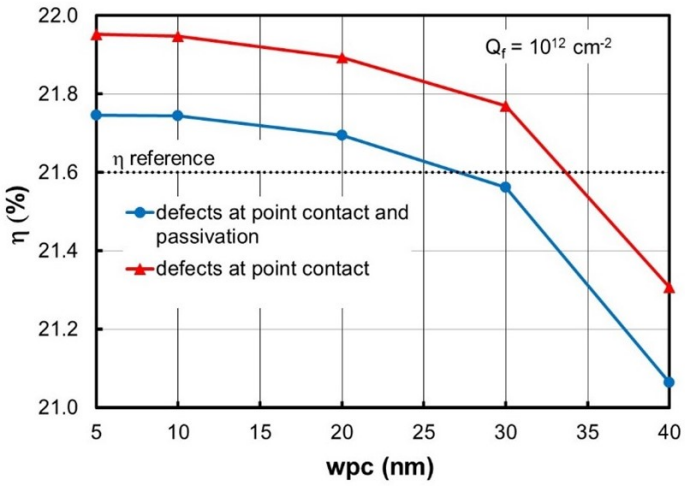

Figure 5.8: Simulated cell efficiency versus point contact width, *wpc*, for the two scenarios of acceptor interface states ($N_{AT} = 10^{11} cm^{-2}$) at point contact only (red triangles) and all over the *CIGS* surface (blue circles) in the case of fixed charge density $Q_f = 10^{12} cm^{-2}$ inside the passivation ($h = 10nm$, $d = 50nm$). The reference line indicates the case of absence of interface states and passivation.

5.2 Back-side point contact

The back surface recombinations are one of the causes of the non-radiative recombination that negatively affects the performance of the solar cells. In order to reduce their impact on the figures of merit, in this section will be presented a study on the potential advantages of rear-surface passivation in solar cells from the point of view of back-surface recombination and photo-generated carrier collection to give indications on the best geometries for back-side contact openings in a passivation layer [65].

The rear surface passivation consists of a passivation layer that reduces interface recombination by lowering the interface trap density (chemical passivation) and altering the interface carrier concentration by means of an electric field induced by the passivation charge (field-effect passivation) [66] [67]; point contact openings are clearly necessary to let the current flow through the rear metal contact. A $10nm$ thick

Al_2O_3 was considered as passivating material [66], and it was analyzed the effect of both chemical and field-effect passivation on the cell performance.

The simulation of this section are based on the EMPA cell simulated without contact resistance and with absorption coefficients measured at EMPA for the *CIGS* [24], instead for the other material coefficient taken from literature [32] are used, so the figures of merit of the baseline are:

$$V_{OC} = 0.742V,\ J_{SC} = 36.5\frac{mA}{cm^2},\ FF = 80.6\% \text{ and } \eta = 21.9\%.$$

All the simulations described hereafter are cylindrical symmetry 3D simulations, since the point contact is inherently a 3D structure: a 2D simulation would describe a line contact extending indefinitely in the third dimension, with significant underestimation of the contact resistance.

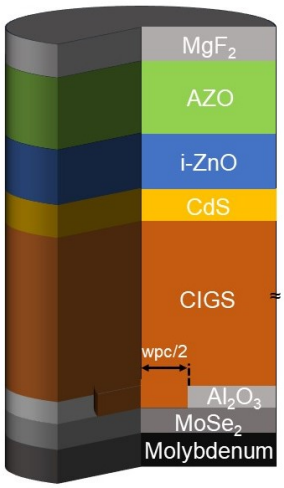

Figure 5.9: Back point contact: simulated cell structure.

The modeled solar cell is shown in Figure 5.9; cells with circular back-side point contacts of different diameter, *wpc*, contact specific resistance R_C ranging from 10^{-5} or $10^{-4}\Omega cm^2$ to $10^{-1}\Omega cm^2$ were simulated. The point contact pitch was kept fixed at $2\mu m$.

High recombination velocity, $v_R = 10^6 cm/s$ was assumed at the rear contact, while different scenarios were considered for the $Al_2O_3/CIGS$ interface:

- ideal chemical passivation, no electrical passivation: $v_S = 0cm/s, Q_f/q = 0cm^{-2}$;
- mild chemical passivation, no electrical passivation: $v_S = 10^6 cm/s, Q_f/q = 0cm^{-2}$ (worst case);
- mild chemical passivation, mild electrical passivation: $v_S = 10^6 cm/s, Q_f/q = -10^{12} cm^{-2}$;
- intermediate chemical passivation, mild electrical passivation: $v_S = 10^4 cm/s$, $Q_f/q = -10^{12} cm^{-2}$;
- mild chemical passivation, intermediate electrical passivation: $v_S = 10^6 cm/s$, $Q_f/q = -5 \cdot 10^{12} cm^{-2}$ (likely case);
- intermediate chemical passivation, intermediate electrical passivation: $v_S = 10^4 cm/s, Q_f/q = -5 \cdot 10^{12} cm^{-2}$;
- mild chemical passivation, strong electrical passivation: $v_S = 10^6 cm/s, Q_f/q = -10^{13} cm^{-2}$.

The mild chemical passivation scenario is based on published results [68] showing that the effect of Al_2O_3 surface passivation is minor (*35%*) in terms of surface state density reduction, but may be very significant thanks to negative passivation charge density in excess of $3 \cdot 10^{12} cm^{-2}$.

5.2.1 Ideal chemical passivation, no electrical passivation

The first simulated scenario is based on ideal chemical passivation ($v_S = 0cm/s$) and no electrical passivation ($Q_f/q = 0cm^{-2}$); the results are summarized in table below for point contact width ranging from $100nm$ to $2\mu m$ (since the point contact pitch is $2\mu m$, $wpc = 2\mu m$ means that there is no back-side passivation) and specific contact resistance ranging from 10^{-4} to $10^{-1} \Omega \cdot cm^2$.

$wpc[nm]$	$R_C[\Omega\cdot cm^2]$	$V_{OC}[V]$	$J_{SC}[\frac{mA}{cm^2}]$	$FF[\%]$	$\eta[\%]$
100	10^{-4}	0.747	37.0	80.0	22.1
100	10^{-3}	0.747	37.0	78.4	21.7
100	10^{-2}	0.747	36.9	63.2	17.4
100	10^{-1}	0.747	17.9	25.1	3.4
250	10^{-4}	0.746	36.9	80.5	22.2
250	10^{-3}	0.746	36.9	80.3	22.1
250	10^{-2}	0.746	36.9	77.8	21.4
250	10^{-1}	0.746	36.9	54.1	14.8
400	10^{-4}	0.745	36.9	80.6	22.2
400	10^{-3}	0.745	36.9	80.5	22.2
400	10^{-2}	0.745	36.9	79.6	21.9
400	10^{-1}	0.745	36.9	69.9	19.2
550	10^{-4}	0.745	36.9	80.7	22.1
550	10^{-3}	0.745	36.9	80.7	22.1
550	10^{-2}	0.745	36.9	80.6	22.1
550	10^{-1}	0.745	36.9	80.1	22.0
700	10^{-4}	0.744	36.8	80.7	22.1
700	10^{-3}	0.744	36.8	80.7	22.1
700	10^{-2}	0.744	36.8	80.6	22.1
700	10^{-1}	0.744	36.8	80.3	22.0
2000	10^{-4}	0.742	36.5	80.6	21.9
2000	10^{-3}	0.742	36.5	80.6	21.9
2000	10^{-2}	0.742	36.5	80.6	21.9
2000	10^{-1}	0.742	36.5	80.2	21.7

As expected, thanks to the thick absorber layer and *GGI* grading, the back-side interface recombination is not a severe performance limiter in the non-passivated cell ($wpc = 2000nm$), and the V_{OC} improvement in the passivated structures is minor. With the sole exception of narrow ($wpc = 100nm$) and very resistive ($R_C = 10^{-1}\Omega\cdot cm^2$) point contacts, J_{SC} was slightly improved by the passivation with point contacts arrangement. FF, on the other hand, is sensitive to the parasitic series resistance

increase caused by the presence of passivation with point contact openings, and is the main efficiency limiter for narrow point contacts.

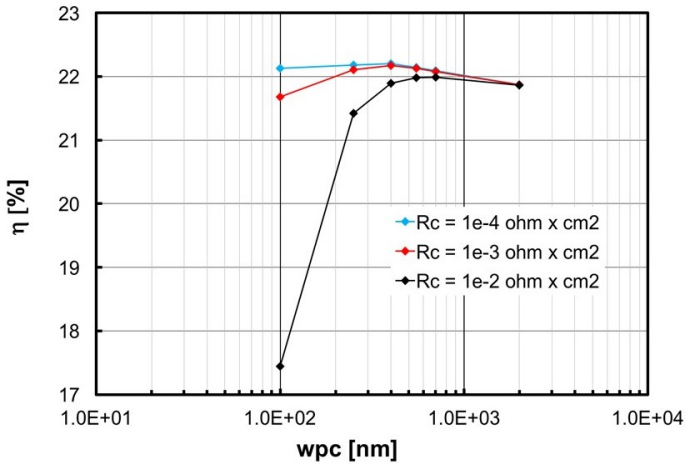

Figure 5.10: Cell efficiency vs. point contact width, for different values of the point contact specific resistance, for the case of ideal chemical passivation and no electrical passivation ($v_S = 0cm/s$, $Q_f/q = 0cm^{-2}$) at the $CIGS/Al_2O_3$ back-side interface.

The effects of wpc and R_C on the cell efficiency are summarized in Figure 5.10 and it is possible to conclude that in the case of ideal chemical passivation ($v_S = 0cm/s$) and no electrical passivation ($Q_f/q = 0cm^{-2}$) the passivation with point contacts solution is beneficial, with:

- $550nm \leq wpc \leq 700nm$, for $R_C = 10^{-2}\Omega \cdot cm^2$;
- $250nm \leq wpc \leq 700nm$, for $R_C = 10^{-3}\Omega \cdot cm^2$ (optimum value: $400nm$);
- $100nm \leq wpc \leq 700nm$, for $R_C = 10^{-4}\Omega \cdot cm^2$ (optimum value: $400nm$).

5.2.2 Mild chemical passivation, no electrical passivation

The second scenario analyzed is also the worst case and it is based on mild chemical passivation ($v_S = 10^6 cm/s$) and no electrical passivation ($Q_f/q = 0cm^{-2}$).

$wpc[nm]$	$R_C[\Omega\cdot cm^2]$	$V_{OC}[V]$	$J_{SC}[\frac{mA}{cm^2}]$	$FF[\%]$	$\eta[\%]$
100	10^{-4}	0.741	36.3	79.8	21.5
100	10^{-3}	0.741	36.3	78.3	21.1
100	10^{-2}	0.741	36.3	63.3	17.0
100	10^{-1}	0.741	17.8	25.1	3.3
250	10^{-4}	0.741	36.3	80.4	21.7
250	10^{-3}	0.741	36.3	80.2	21.6
250	10^{-2}	0.741	36.3	77.7	20.9
250	10^{-1}	0.741	36.2	54.3	14.6
400	10^{-4}	0.741	36.5	80.6	21.8
400	10^{-3}	0.741	36.5	80.5	21.8
400	10^{-2}	0.741	36.5	79.6	21.5
400	10^{-1}	0.741	36.4	69.9	18.9
550	10^{-4}	0.741	36.5	80.6	21.8
550	10^{-3}	0.741	36.5	80.5	21.8
550	10^{-2}	0.741	36.5	80.0	21.6
550	10^{-1}	0.741	36.5	74.9	20.3
700	10^{-4}	0.741	36.5	80.6	21.8
700	10^{-3}	0.741	36.5	80.6	21.8
700	10^{-2}	0.741	36.5	80.2	21.7
700	10^{-1}	0.741	36.5	77.1	20.9
2000	10^{-4}	0.742	36.5	80.6	21.9
2000	10^{-3}	0.742	36.5	80.6	21.9
2000	10^{-2}	0.742	36.5	80.6	21.9
2000	10^{-1}	0.742	36.5	80.2	21.7

The results are summarized in table above for point contact width ranging from $100nm$ to $2\mu m$ (since the point contact pitch is $2\mu m$, $wpc = 2\mu m$ means that there is no back-side passivation) and specific contact resistance ranging from 10^{-4} to $10^{-1}\Omega\cdot cm^2$.

Due to limited effect of the passivation, in this scenario V_{OC} is the same in all the simulate structures. With the sole exception of narrow ($wpc = 100nm$) and very

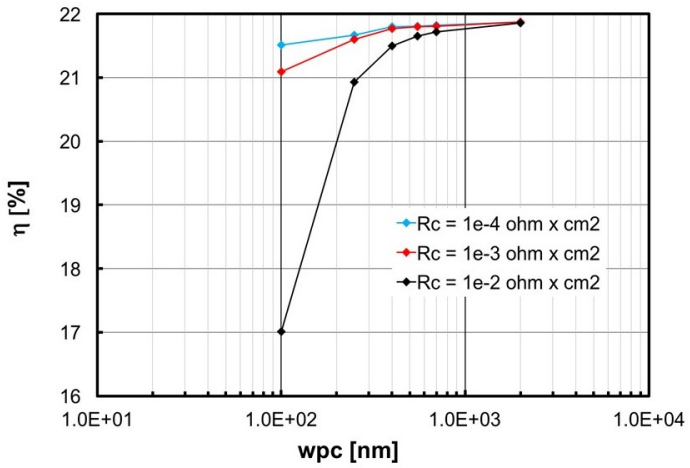

Figure 5.11: Cell efficiency vs. point contact width, for different values of the point contact specific resistance, for the case of mild chemical passivation and no electrical passivation ($v_S = 10^6 cm/s$, $Q_f/q = 0 cm^{-2}$) at the $CIGS/Al_2O_3$ back-side interface.

resistive ($R_C = 10^{-1}\Omega \cdot cm^2$), J_{SC} is almost independent of the point contact geometry, too. Exactly as the previous case, the FF is sensitive to the parasitic series resistance increase caused by the presence of passivation with point contact openings, and its value determined the observed changes of efficiency.

In Figure 5.11 the effects of wpc and R_C on the cell efficiency are summarized; it shows that in the worst case scenario ($v_S = 10^6 cm/s, Q_f/q = 0 cm^{-2}$) passivation with point contacts is generally not convenient but, if $R_C \leq 10^{-3}\Omega \cdot cm^2$ and $wpc \geq 550nm$, it is not harmful either.

5.2.3 Mild chemical passivation, mild electrical passivation

The third scenario studied is based on mild chemical passivation ($v_S = 10^6 cm/s$) and mild electrical passivation ($Q_f/q = -10^{12} cm^{-2}$); the results are summarized in table below for point contact width ranging from $100nm$ to $2\mu m$ (since the point contact pitch is $2\mu m$, $wpc = 2\mu m$ means that there is no back-side passivation) and specific contact resistance ranging from 10^{-4} to $10^{-1}\Omega \cdot cm^2$.

$wpc[nm]$	$R_C[\Omega\cdot cm^2]$	$V_{OC}[V]$	$J_{SC}[\frac{mA}{cm^2}]$	$FF[\%]$	$\eta[\%]$
100	10^{-4}	0.742	36.5	80.3	21.7
100	10^{-3}	0.742	36.5	78.7	21.3
100	10^{-2}	0.742	36.4	63.6	17.2
100	10^{-1}	0.742	17.8	25.1	3.3
250	10^{-4}	0.742	36.5	80.5	21.8
250	10^{-3}	0.742	36.5	80.3	21.7
250	10^{-2}	0.742	36.5	77.8	21.1
250	10^{-1}	0.742	36.3	54.3	14.6
400	10^{-4}	0.742	36.6	80.6	21.9
400	10^{-3}	0.742	36.6	80.5	21.9
400	10^{-2}	0.742	36.6	79.5	21.6
400	10^{-1}	0.742	36.6	69.9	19.0
550	10^{-4}	0.742	36.6	80.6	21.9
550	10^{-3}	0.742	36.6	80.6	21.9
550	10^{-2}	0.742	36.6	80.0	21.8
550	10^{-1}	0.742	36.6	74.9	20.4
700	10^{-4}	0.742	36.6	80.6	21.9
700	10^{-3}	0.742	36.6	80.6	21.9
700	10^{-2}	0.742	36.6	80.3	21.8
700	10^{-1}	0.742	36.6	77.1	21.0
2000	10^{-4}	0.742	36.5	80.6	21.9
2000	10^{-3}	0.742	36.5	80.6	21.9
2000	10^{-2}	0.742	36.5	80.6	21.9
2000	10^{-1}	0.742	36.5	80.2	21.7

As for the previous case, due to limited effect of the passivation, in this scenario V_{OC} is the same in all the simulate structures and, with the sole exception of narrow ($wpc = 100nm$) and very resistive ($R_C = 10^{-1}\Omega\cdot cm^2$), also J_{SC} is almost independent of the point contact geometry. As expected the FF is sensitive to the parasitic series resistance increase caused by the presence of passivation with point contact openings, and its value determined the observed changes of efficiency.

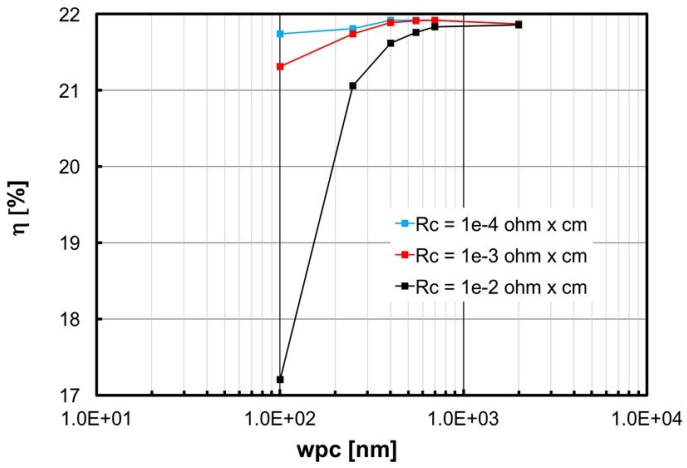

Figure 5.12: Cell efficiency vs. point contact width, for different values of the point contact specific resistance, for the case of mild chemical passivation and mild electrical passivation ($v_S = 10^6 cm/s$, $Q_f/q = -10^{12} cm^{-2}$) at the $CIGS/Al_2O_3$ back-side interface.

Overall, these results are very similar to those of the mild chemical passivation ($v_S = 10^6 cm/s$) and no electrical passivation ($Q_f/q = 0 cm^{-2}$) scenario indicating that for this chemical passivation a negative charge density $Q_f/q = -10^{12} cm^{-2}$ is not enough to provide significant electrical passivation.

The effects of wpc and R_C on the cell efficiency are summarized in Figure 5.12 and it is possible to conclude that in the case of mild chemical passivation and mild electrical passivation ($v_S = 10^6 cm/s$, $Q_f/q = -10^{12} cm^{-2}$) passivation with point contacts may be very marginally beneficial, provided that $R_C \leq 10^{-3} \Omega \cdot cm^2$ and $400nm \leq wpc \leq 700nm$.

5.2.4 Intermediate chemical passivation, mild electrical passivation

An intermediate chemical passivation ($v_S = 10^4 cm/s$) and mild electrical passivation ($Q_f/q = -10^{12} cm^{-2}$) are analyzed in the fourth scenario; the results are summarized in table below for point contact width ranging from $100nm$ to $2\mu m$ (since the point

contact pitch is $2\mu m$, $wpc = 2\mu m$ means that there is no back-side passivation) and specific contact resistance ranging from 10^{-4} to $10^{-1}\Omega \cdot cm^2$.

$wpc[nm]$	$R_C[\Omega \cdot cm^2]$	$V_{OC}[V]$	$J_{SC}[\frac{mA}{cm^2}]$	$FF[\%]$	$\eta[\%]$
100	10^{-4}	0.748	37.0	80.4	22.2
100	10^{-3}	0.748	37.0	78.8	21.8
100	10^{-2}	0.748	36.9	63.5	17.5
100	10^{-1}	0.748	17.9	25.1	3.4
250	10^{-4}	0.747	36.9	80.6	22.2
250	10^{-3}	0.747	36.9	80.4	22.2
250	10^{-2}	0.747	36.9	77.9	21.5
250	10^{-1}	0.747	36.8	54.1	14.9
400	10^{-4}	0.747	37.0	80.7	22.3
400	10^{-3}	0.747	37.0	80.6	22.3
400	10^{-2}	0.747	37.0	79.6	22.0
400	10^{-1}	0.747	37.0	69.9	19.3
550	10^{-4}	0.746	37.0	80.7	22.2
550	10^{-3}	0.746	37.0	80.6	22.2
550	10^{-2}	0.746	37.0	80.1	22.1
550	10^{-1}	0.746	36.9	74.9	20.7
700	10^{-4}	0.745	36.9	80.7	22.2
700	10^{-3}	0.745	36.9	80.7	22.2
700	10^{-2}	0.745	36.9	80.4	22.1
700	10^{-1}	0.745	36.9	80.3	21.2
2000	10^{-4}	0.742	36.5	80.6	21.9
2000	10^{-3}	0.742	36.5	80.6	21.9
2000	10^{-2}	0.742	36.5	80.6	21.9
2000	10^{-1}	0.742	36.5	80.2	21.7

Thanks to the contribution of the electrical passivation (negative interface charge) V_{OC} improves by a few mV as the passivation coverage increases; the reduction of recombination results in general increase of J_{SC}, too. As in all the cases before, the

FF decreases significantly for narrow *wpc* and large R_C, due to the parasitic series resistance increase caused by the presence of passivation with point contact openings.

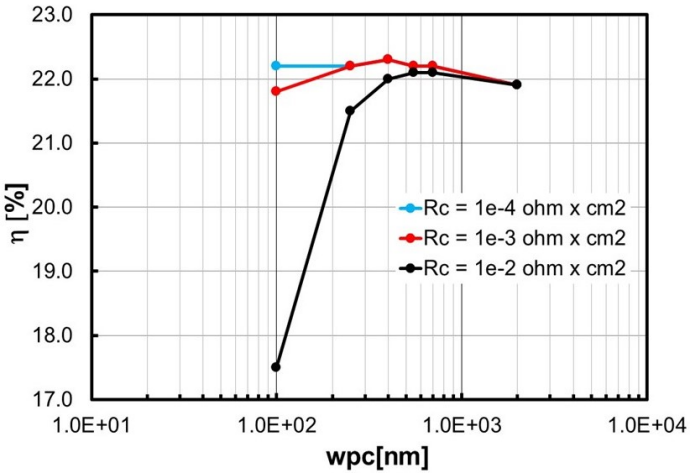

Figure 5.13: Cell efficiency vs. point contact width, for different values of the point contact specific resistance, for the case of intermediate chemical passivation and mild electrical passivation ($v_S = 10^4 cm/s$, $Q_f/q = -10^{12} cm^{-2}$) at the $CIGS/Al_2O_3$ back-side interface.

Figure 5.13 shows that, in the case of intermediate chemical passivation and mild electrical passivation ($v_S = 10^4 cm/s, Q_f/q = -10^{12} cm^{-2}$), passivation with point contacts may be beneficial for:

- $400nm \leq wpc \leq 700nm$ for $R_C = 10^{-2} \Omega \cdot cm^2$;
- $250nm \leq wpc \leq 700nm$ for $R_C = 10^{-3} \Omega \cdot cm^2$;
- $100nm \leq wpc \leq 700nm$ for $R_C = 10^{-4} \Omega \cdot cm^2$.

5.2.5 Mild chemical passivation, intermediate electrical passivation

The fifth scenario was focused on mild chemical passivation ($v_S = 10^6 cm/s$) and intermediate electrical passivation ($Q_f/q = -5 \cdot 10^{12} cm^{-2}$); the results are summarized

in table below for point contact width ranging from $100nm$ to $2\mu m$ (since the point contact pitch is $2\mu m$, $wpc = 2\mu m$ means that there is no back-side passivation) and specific contact resistance ranging from 10^{-4} to $10^{-1}\Omega \cdot cm^2$.

$wpc[nm]$	$R_C[\Omega \cdot cm^2]$	$V_{OC}[V]$	$J_{SC}[\frac{mA}{cm^2}]$	$FF[\%]$	$\eta[\%]$
100	10^{-4}	0.748	37.1	80.5	22.3
100	10^{-3}	0.748	37.1	78.9	21.9
100	10^{-2}	0.748	37.0	63.6	17.6
100	10^{-1}	0.748	18.0	25.1	3.4
250	10^{-4}	0.748	37.0	80.6	22.3
250	10^{-3}	0.748	37.0	80.4	22.3
250	10^{-2}	0.748	37.0	77.9	21.6
250	10^{-1}	0.748	36.9	54.1	14.9
400	10^{-4}	0.747	37.1	80.7	22.4
400	10^{-3}	0.747	37.1	80.6	22.3
400	10^{-2}	0.747	37.1	79.6	22.1
400	10^{-1}	0.747	37.0	69.9	19.4
550	10^{-4}	0.747	37.0	80.7	22.3
550	10^{-3}	0.747	37.0	80.6	22.3
550	10^{-2}	0.747	37.0	80.1	22.2
550	10^{-1}	0.747	37.0	75.0	20.7
700	10^{-4}	0.746	37.0	80.7	22.2
700	10^{-3}	0.746	37.0	80.7	22.2
700	10^{-2}	0.746	37.0	80.4	22.2
700	10^{-1}	0.746	37.0	77.2	21.3
2000	10^{-4}	0.742	36.5	80.6	21.9
2000	10^{-3}	0.742	36.5	80.6	21.9
2000	10^{-2}	0.742	36.5	80.6	21.9
2000	10^{-1}	0.742	36.5	80.2	21.7

As the previous case, thanks to the contribution of the electrical passivation (negative interface charge) V_{OC} improves by a few mV as the passivation coverage increases.

Reduced recombination results in general increase of J_{SC}, too. FF, on the other hand, is a monotonically decreasing function of decreasing wpc and increasing R_C, due to the parasitic series resistance increase caused by the presence of passivation with point contact openings. Overall, the results are similar to those of the intermediate chemical passivation and mild electrical passivation scenario, which shows that negative charge density of $Q_f/q = -5 \cdot 10^{12} cm^{-2}$ has the same passivating effect of a two orders of magnitude reduction of v_S (from $10^6 cm/s$ to $10^4 cm/s$).

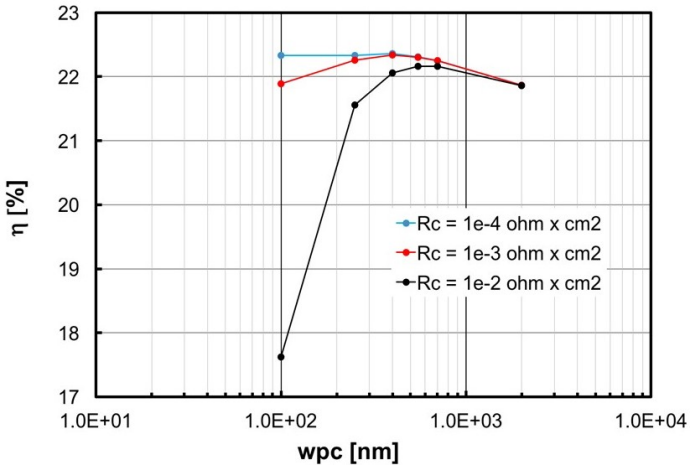

Figure 5.14: Cell efficiency vs. point contact width, for different values of the point contact specific resistance, for the case of mild chemical passivation and intermediate electrical passivation ($v_S = 10^6 cm/s$, $Q_f/q = -5 \cdot 10^{12} cm^{-2}$) at the $CIGS/Al_2O_3$ back-side interface.

In Figure 5.14 is shown the effects of wpc and R_C on the cell efficiency for the likely case of mild chemical passivation and intermediate electrical passivation ($v_S = 10^6 cm/s$, $Q_f/q = -5 \cdot 10^{12} cm^{-2}$), passivation with point contacts is beneficial, with:

- $550nm \leq wpc \leq 700nm$, for $R_C = 10 - 2\Omega \cdot cm^2$;
- $250nm \leq wpc \leq 700nm$, for $R_C = 10 - 3\Omega \cdot cm^2$ (optimum value: 400 nm);

- $100nm \leq wpc \leq 700nm$, for $R_C = 10 - 4\Omega \cdot cm^2$ (optimum value: 400 nm).

5.2.6 Intermediate chemical passivation, intermediate electrical passivation

The sixth scenario studied the case of intermediate chemical passivation ($v_S = 10^4 cm/s$) and intermediate electrical passivation ($Q_f/q = -5 \cdot 10^{12} cm^{-2}$).

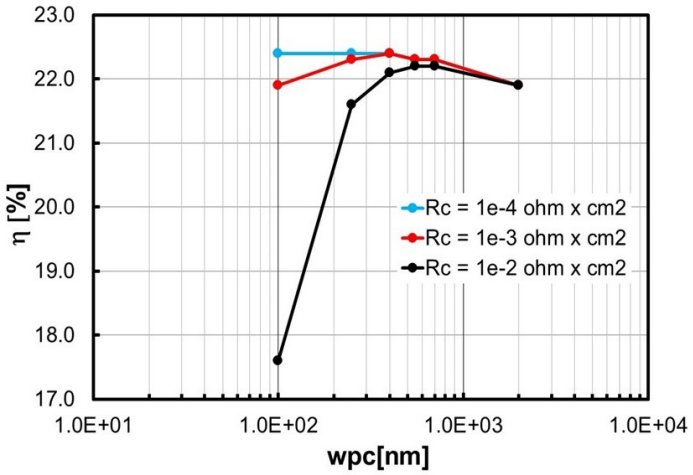

Figure 5.15: Cell efficiency vs. point contact width, for different values of the point contact specific resistance, for the case of intermediate chemical passivation and intermediate electrical passivation ($v_S = 10^4 cm/s$, $Q_f/q = -5 \cdot 10^{12} cm^{-2}$) at the $CIGS/Al_2O_3$ back-side interface.

The results are summarized in table below for point contact width ranging from $100nm$ to $2\mu m$ (since the point contact pitch is $2\mu m$, $wpc = 2\mu m$ means that there is no back-side passivation) and specific contact resistance ranging from 10^{-4} to $10^{-1}\Omega \cdot cm^2$.

$wpc[nm]$	$R_C[\Omega \cdot cm^2]$	$V_{OC}[V]$	$J_{SC}[\frac{mA}{cm^2}]$	$FF[\%]$	$\eta[\%]$
100	10^{-4}	0.749	37.1	80.5	22.4
100	10^{-3}	0.749	37.1	78.9	21.9
100	10^{-2}	0.749	37.0	63.6	17.6
100	10^{-1}	0.749	18.0	25.1	3.4
250	10^{-4}	0.748	37.0	80.7	22.4
250	10^{-3}	0.748	37.0	80.4	22.3
250	10^{-2}	0.748	37.0	77.9	21.6
250	10^{-1}	0.748	36.9	54.1	14.9
400	10^{-4}	0.748	37.1	80.7	22.4
400	10^{-3}	0.748	37.1	80.6	22.4
400	10^{-2}	0.748	37.1	79.6	22.1
400	10^{-1}	0.748	37.1	69.9	19.4
550	10^{-4}	0.747	37.0	80.7	22.3
550	10^{-3}	0.747	37.0	80.6	22.3
550	10^{-2}	0.747	37.0	80.1	22.2
550	10^{-1}	0.747	37.0	75.0	20.7
700	10^{-4}	0.745	37.0	80.7	22.3
700	10^{-3}	0.745	37.0	80.7	22.3
700	10^{-2}	0.745	37.0	80.4	22.2
700	10^{-1}	0.745	37.0	77.2	21.3
2000	10^{-4}	0.742	36.5	80.6	21.9
2000	10^{-3}	0.742	36.5	80.6	21.9
2000	10^{-2}	0.742	36.5	80.6	21.9
2000	10^{-1}	0.742	36.5	80.2	21.7

Exactly as the two last cases analyzed, thanks to the contribution of the electrical passivation (negative interface charge) V_{OC} improves by a few mV as the passivation coverage increases. Reduced recombination results in general increase of J_{SC}, too. FF, as always, decreases significantly for narrow wpc and large R_C, due to the parasitic series resistance increase caused by the presence of passivation with point contact openings.

The effects of wpc and R_C on the cell efficiency are summarized in Figure 5.15, it shows that in the case of intermediate chemical passivation and intermediate electrical passivation ($v_S = 10^4 cm/s$, $Q_f/q = -5 \cdot 10^{12} cm^{-2}$), passivation with point contacts may be beneficial for:

- $400nm \leq wpc \leq 700nm$, for $R_C = 10 - 2\Omega \cdot cm^2$;
- $250nm \leq wpc \leq 700nm$, for $R_C = 10 - 3\Omega \cdot cm^2$;
- $100nm \leq wpc \leq 700nm$, for $R_C = 10 - 4\Omega \cdot cm^2$.

5.2.7 Mild chemical passivation, strong electrical passivation

The last hypothesized scenario analyzes the case of mild chemical passivation ($v_S = 10^6 cm/s$) and strong electrical passivation ($Q_f/q = -10^{13} cm^{-2}$).

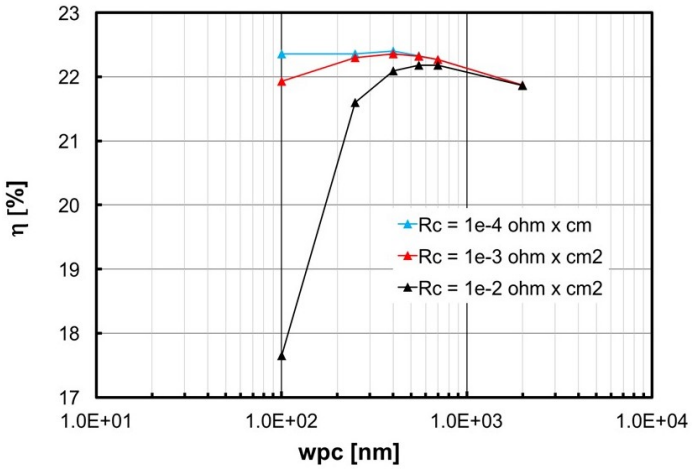

Figure 5.16: Cell efficiency vs. point contact width, for different values of the point contact specific resistance, for the case of mild chemical passivation and strong electrical passivation ($v_S = 10^6 cm/s$, $Q_f/q = -10^{13} cm^{-2}$) at the $CIGS/Al_2O_3$ back-side interface.

$wpc[nm]$	$R_C[\Omega\cdot cm^2]$	$V_{OC}[V]$	$J_{SC}[\frac{mA}{cm^2}]$	$FF[\%]$	$\eta[\%]$
100	10^{-4}	0.749	37.1	80.5	22.4
100	10^{-3}	0.749	37.1	79.0	21.9
100	10^{-2}	0.749	37.0	63.6	17.6
100	10^{-1}	0.749	18.0	25.1	3.4
250	10^{-4}	0.748	37.0	80.7	22.4
250	10^{-3}	0.748	37.0	80.4	22.3
250	10^{-2}	0.748	37.0	77.9	21.6
250	10^{-1}	0.748	36.9	54.1	15.0
400	10^{-4}	0.748	37.1	80.7	22.4
400	10^{-3}	0.748	37.1	80.6	22.4
400	10^{-2}	0.748	37.1	79.6	22.1
400	10^{-1}	0.748	37.1	69.9	19.4
550	10^{-4}	0.747	37.0	80.7	22.3
550	10^{-3}	0.747	37.0	80.6	22.3
550	10^{-2}	0.747	37.0	80.1	22.2
550	10^{-1}	0.747	37.0	75.0	20.7
700	10^{-4}	0.746	37.0	80.7	22.3
700	10^{-3}	0.746	37.0	80.7	22.3
700	10^{-2}	0.746	37.0	80.4	22.2
700	10^{-1}	0.746	37.0	77.2	21.3
2000	10^{-4}	0.742	36.5	80.6	21.9
2000	10^{-3}	0.742	36.5	80.6	21.9
2000	10^{-2}	0.742	36.5	80.6	21.9
2000	10^{-1}	0.742	36.5	80.2	21.7

The results are summarized in table above for point contact width ranging from $100nm$ to $2\mu m$ (since the point contact pitch is $2\mu m$, $wpc = 2\mu m$ means that there is no back-side passivation) and specific contact resistance ranging from 10^{-4} to $10^{-1}\Omega\cdot cm^2$.

The obtained results for the case mild chemical passivation ($v_S = 10^6 cm/s$) and strong electrical passivation ($Q_f/q = -10^{13}cm^{-2}$) are very similar to the case

of intermediate chemical passivation and intermediate electrical passivation ($v_S = 10^4 cm/s$, $Q_f/q = -5 \cdot 10^{12} cm^{-2}$), indeed thanks to the contribution of the electrical passivation (negative interface charge) V_{OC} improves by up to $7mV$ as the passivation coverage increases. There is also a general increase of J_{SC} due to the reduction of recombination. *FF*, as usual, is a monotonically decreasing function of decreasing *wpc* and increasing R_C, due to the parasitic series resistance increase caused by the presence of passivation with point contact openings.

The effects of *wpc* and R_C on the cell efficiency are summarized in Figure 5.16, it shows that in the case of mild chemical passivation and strong electrical passivation ($v_S = 10^6 cm/s$, $Q_f/q = -10^{13} cm^{-2}$), passivation with point contacts is beneficial, with:

- $550nm \leq wpc \leq 700nm$, for $RC = 10 - 2\Omega \cdot cm^2$;
- $250nm \leq wpc \leq 700nm$, for $RC = 10 - 3\Omega \cdot cm^2$ (optimum value: 400 nm);
- $100nm \leq wpc \leq 700nm$, for $RC = 10 - 4\Omega \cdot cm^2$ (optimum value: 400 nm).

5.2.8 Comparison and summary

The sections before describe the application of 3D numerical simulation to the optimization of *CIGS* solar cells with passivated back-side interface and point contacts with $2\mu m$ pitch. The effects of both chemical and field-effect passivation are analyzed for several combinations of point contact diameter (*wpc*) and specific contact resistance (R_C).

Qualitatively, there are three effects playing a role, the combination of which determines the impact on efficiency:

- CIGS back interface passivation, whether chemical or electrical, increasing V_{OC};
- enhanced light reflection of Al_2O_3 relative to $MoSe_2/Mo$, increasing J_{SC};
- increased series resistance at the point contact, reducing *FF*.

Quantitatively, due to the thick ($3\mu m$) absorber and back **GGI** grading, the beneficial effects (increase of V_{OC} J_{SC}) are limited. In particular, the effect of reflection on the J_{SC} turns out to be negligible. The compositional grading increasing the Gallium content toward the back-side also contributes to reducing the effects of back-side interface recombination.

Based on what was described before for a structure with Al_2O_3 passivation and $2\mu m$ pitch, it is possible to summarise the obtained results as follow:

- point contacts can be convenient provided that $R_C \leq 10^{-2}\Omega \cdot cm^2$ (back contact specific resistance), more significantly so if $R_C \leq 10^{-3}\Omega \cdot cm^2$;
- in the worst case scenario of mild chemical passivation plus no electrical passivation, passivation with point contacts is generally not convenient but, if $R_C \leq 10^{-3}\Omega \cdot cm^2$ and $wpc \geq 550nm$ (point contact diameter), not harmful, either;
- in the case of mild chemical passivation plus mild electrical passivation, passivation with point contacts is very marginally beneficial, provided that $R_C \leq 10^{-3}\Omega \cdot cm^2$ and $400nm \leq wpc \leq 700nm$;
- in the cases of ideal chemical passivation plus no electrical passivation, the most likely case of mild chemical passivation plus intermediate electrical passivation, and the best case of mild chemical passivation plus strong electrical passivation, passivation with point contacts gives optimum results with: $550nm \leq wpc \leq 700nm$ for $R_C \leq 10^{-2}\Omega \cdot cm^2$, and $wpc = 400nm$ for $R_C \leq 10^{-3}\Omega \cdot cm^2$;
- in the cases of intermediate chemical passivation plus mild electrical passivation, and intermediate chemical passivation plus intermediate electrical passivation, passivation with point contacts is beneficial, with:
  - $400nm \leq wpc \leq 700nm$, for $R_C = 10^{-2}\Omega \cdot cm^2$;
  - $250nm \leq wpc \leq 700nm$, for $R_C = 10^{-3}\Omega \cdot cm^2$;
  - $100nm \leq wpc \leq 700nm$, for $R_C = 10^{-4}\Omega \cdot cm^2$.

5.3 Back reflector

There are many technical solutions to obtain an increased absorption or a reduction of power losses in the solar cells: the point contact at the front and at the back of the structure or the nano-structured back contact [69] [70] [71] [72] but, the easier solution one is a back mirror with high reflective material [73] [74] [75] [76] [77] in order to improve the optical path of photon inside the absorber layer to increase the absorption. In this section it will be presented a set of simulations aims to study the effect on the performance of the cell of a high reflective back contact. The purpose is to understand if the back mirror is only useful for *CIGS* thickness lower than $1\mu m$ or if this solution can be incorporated in the record cells with an improvement that justifies this effort.

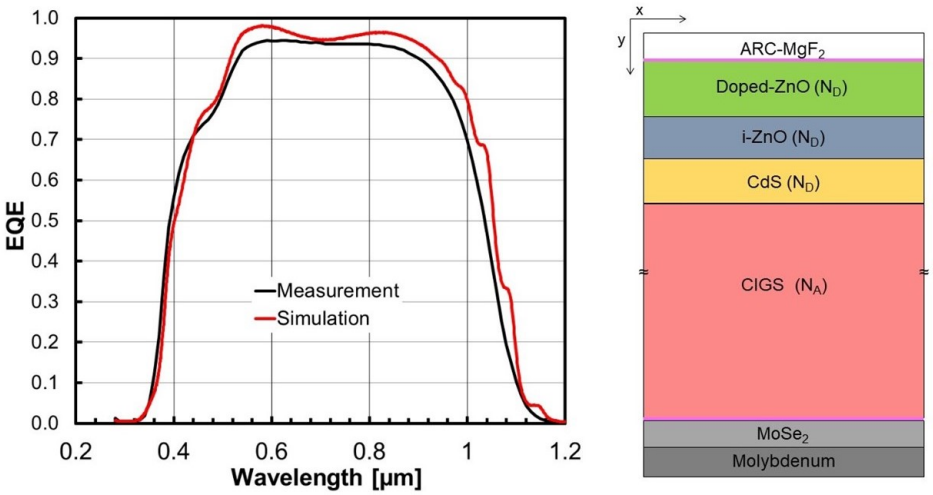

Figure 5.17: Left: comparison between measurement and simulation; right: simulated structure.

The simulation of this section are based on the EMPA cell simulated with absorption coefficients measured at EMPA for all the materials [24], so the figures of merit of the baseline are:

$$V_{OC} = 0.741V,\ J_{SC} = 36.8\frac{mA}{cm^2},\ FF = 80.6\% \text{ and } \eta = 21.9\%.$$

In Figure 5.17 are shown the EQE comparison between measured and simulated cell (left), and the simulated structure (right).

5.3.1 Structures with ideal reflector

In order to understand if the back-mirror solution is useful to improve the record cell J_{SC} the first set of simulations was focused on an ideal reflector that can be assumed as the upper limit.

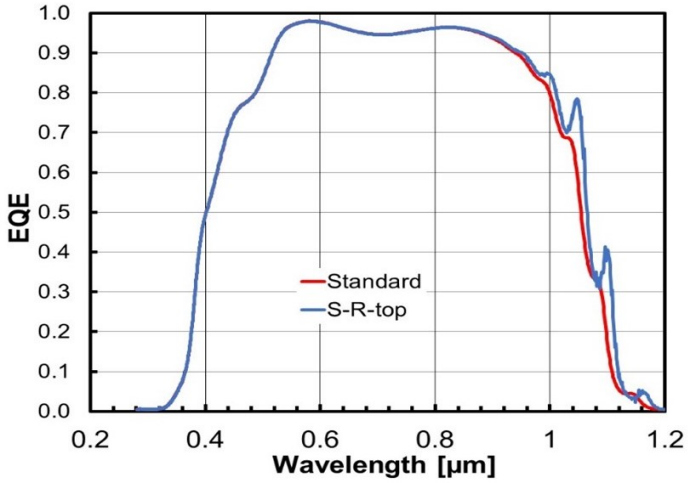

Figure 5.18: EQE comparison between standard structure and the one with ideal rear reflector on $MoSe_2$

Structure	$MoSe_2$	*Mo*	*Reflector*	$J_{SC}[\frac{mA}{cm^2}]$	$\Delta J_{SC}[\frac{mA}{cm^2}]$	$\eta[\%]$
Standard (S)	100	500	–	36.82	–	21.9
S-R-top	100	500	on $MoSe_2$	37.44	+0.62	22.4
S-R	100	500	under Mo	36.81	-0.01	21.9
10/500-R	10	500	under Mo	36.81	-0.01	21.9
10/20-R	10	20	under Mo	37.15	+0.33	22.2
0/20-R	0	20	under Mo	37.16	+0.34	22.2
0/5-R	0	5	under Mo	37.27	+0.45	22.3

In table above the results of efficiency and J_{SC} of simulated structures are listed which differ only by the thickness of $MoSe_2$ and *Molybdenum* on the ideal reflector. From these results it is possible to conclude that the absorption of back contact is relevant indeed a reduction of $MoSe_2$ or *Molybdenum* thickness causes an increment of ΔJ_{SC}.

The main indication of these results is that in the best case, ideal reflector on $MoSe_2$ (*S-R-top* Figure 5.18), the J_{SC} increment with respect to the standard structure is $\Delta J_{SC} = 0.66 \frac{mA}{cm^2}$.

5.3.2 Structures with real reflector materials

In this section the structures with real reflectors will be analyzed, the study was limited to four different materials: Gold (Au [70] [76] [78]), Aluminum (Al [69] [70] [73]), Titanium Nitride (TiN [73]) and Zirconium Nitride (ZrN [73] [79] [80]).

Structure	$MoSe_2$	*Mo*	*Reflector*	$J_{SC}[\frac{mA}{cm^2}]$	$\Delta J_{SC}[\frac{mA}{cm^2}]$	$\eta[\%]$
R-Au-1	0	0	Au [81]	37.28	+0.46	22.3
MSMR-Au-1	10	5	Au [81]	37.13	+0.31	22.2
MSMR-Au-2	10	20	Au [81]	36.90	+0.08	22.0
MSMR-Au-3	30	20	Au [81]	36.86	+0.04	22.0
R-Al-1	0	0	Al [82]	37.22	+0.40	22.2
MSMR-Al-1	10	5	Al [82]	37.14	+0.32	22.2
MSMR-Al-2	10	20	Al [82]	36.96	+0.14	22.1
MSMR-Al-3	30	20	Al [82]	36.92	+0.10	22.0
R-TiN-1	0	0	TiN [83]	37.03	+0.21	22.1
MSMR-TiN-1	10	5	TiN [83]	36.92	+0.10	22.0
MSMR-TiN-2	10	20	TiN [83]	36.81	-0.01	21.9
MSMR-TiN-3	30	20	TiN [83]	36.77	-0.05	21.9
R-ZrN-1	0	0	ZrN [84]	36.92	+0.10	22.1
MSMR-ZrN-1	10	5	ZrN [84]	36.85	+0.03	22.0
MSMR-ZrN-2	10	20	ZrN [84]	36.80	-0.05	21.9
MSMR-ZrN-3	30	20	ZrN [84]	36.75	-0.07	21.9

The choice is restricted to these reflectors because in literature a back mirrors are always obtained by employing one of these materials.

In table above the efficiency and short-circuit current (Figure 5.19) of simulated structures are listed which differ for the thickness of $MoSe_2$ and *Molybdenum* on the four reflectors; four structures for each of the four materials were take into account.

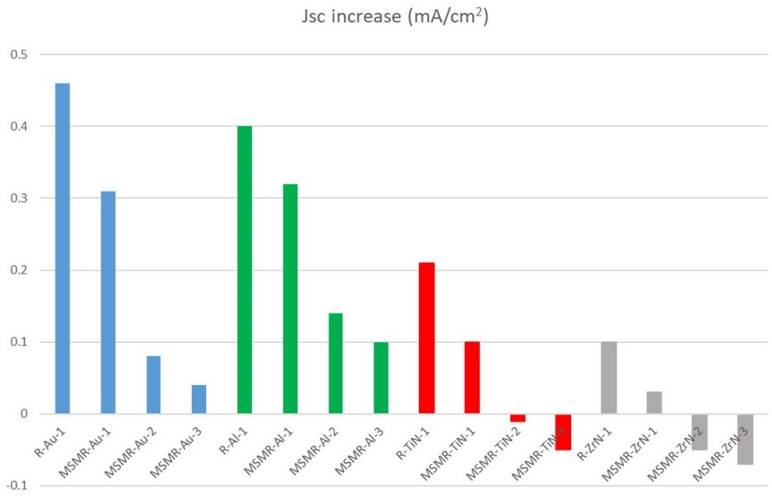

Figure 5.19: J_{SC} increase of the four real reflector for different structures

In Figure 5.20 is shown the comparison between the EQE of the different materials in case of the structure without $MoSe_2$ and *Molybdenum*, so the reflector directly under the *CIGS*.

From these results it is possible to conclude that *Au* and *Al* outperform *TiN* and *ZrN* as mirror materials, and the differences between Aluminum and Gold are never dramatic (Figure 5.21). Considering modeling uncertainties these simulations indicate that either *Au* or *Al* can be used as back mirror material.

5.3.3 Structures with *AZO* spacer and *Al* mirror

Since *Au* is known to diffuse significantly into the upper layers at processing temperatures and significant diffusion can be expected for *Al* as well, so in this section will

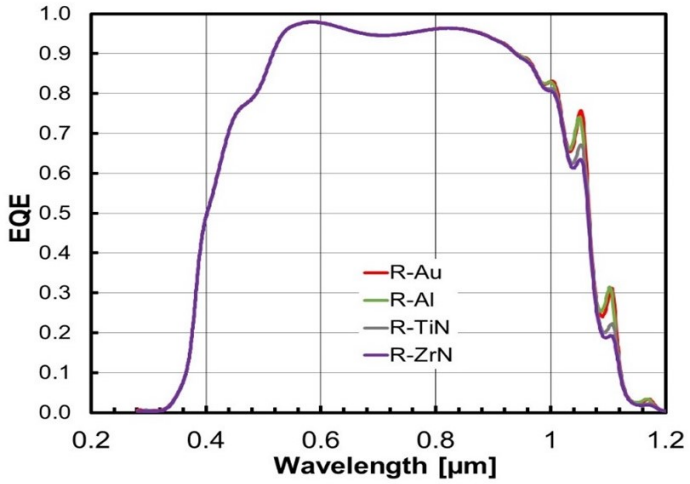

Figure 5.20: EQE comparison between the different materials in case of the structure without $MoSe_2$ and Molybdenum, so the reflector directly under the *CIGS*.

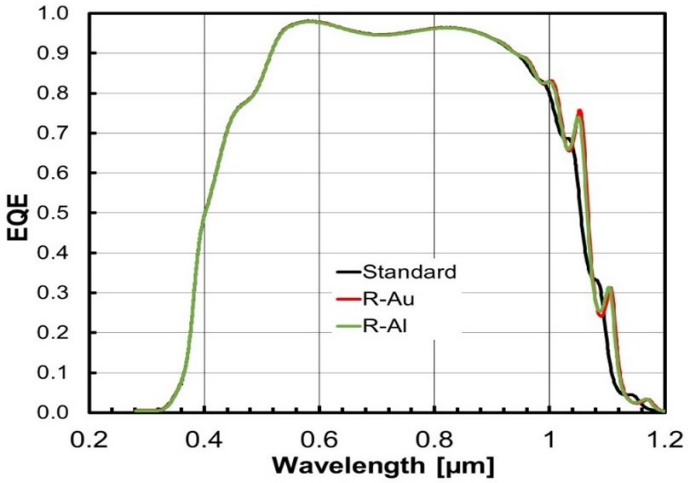

Figure 5.21: EQE comparison between *Au* and *Al* in case of the reflector directly under the *CIGS*.

be presented a set of simulation focused on the structure were the mirror is separated from the upper layer by a spacer of *AZnO* (*AZO*) [85] of variable thickness.

All the simulations in this section take into account an *Al* mirror because it produce the same ΔJ_{SC} of gold but it is cheaper.

Structure	$MoSe_2$	*Mo*	*Spacer*	$J_{SC}[\frac{mA}{cm^2}]$	$\Delta J_{SC}[\frac{mA}{cm^2}]$	$\eta[\%]$
MS10-AZO10	10	0	10	37.19	+0.37	22.2
MS10-AZO100	10	0	100	37.24	+0.42	22.2
MS10-AZO200	10	0	200	37.24	+0.42	22.2
MS10-AZO300	10	0	300	37.10	+0.28	22.2
MS10M5-AZO10	10	5	10	37.07	+0.25	22.1
MS10M5-AZO100	10	5	100	36.80	-0.02	21.9
MS10M5-AZO200	10	5	200	36.78	-0.04	21.9
MS10M5-AZO250	10	5	250	36.91	+0.09	22.0
MS10M5-AZO275	10	5	275	37.02	+0.20	22.1
MS10M5-AZO300	10	5	300	37.06	+0.24	22.1
MS10M5-AZO325	10	5	325	36.99	+0.17	22.1
MS10M5-AZO350	10	5	350	36.90	+0.08	22.0

In table above the results of simulated structures in presence of a spacer are summarized, different thickness of $MoSe_2$, *Molybdenum* and *AZO* were simulated in order to find the best configuration to obtain the highest reflectance at the back contact.

In Figure 5.22 the behavior of J_{SC} as a function of the thickness of the spacer is shown; from this graph and previous table it is possible to observe that the performance of the structures with $MoSe_2(10nm)/Mo(5nm)/AZO/mirror$ stacks (Figure 5.22) indicating that the *AZO* spacer thickness of 300*nm* is expected to provide, in addition to sufficient *Al* diffusion blocking, optimum optical performance.

A possible explanation of why the structure with 300*nm* of *AZO* is the best solution from a point of view of reflection could be the constructive interference inside the cell. In Figure 5.23 are shown the reflectance for three different thickness of spacer, it is possible to note that in the NIR region the reflectance of *MS10M5-AZO300* is the

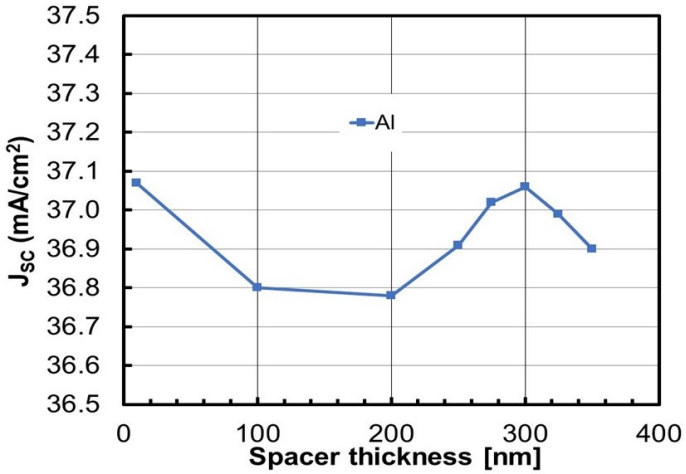

Figure 5.22: Simulated J_{SC} in function of the spacer (*AZnO*) thickness. (Simulated thickness range: $10 \div 350nm$)

highest one.

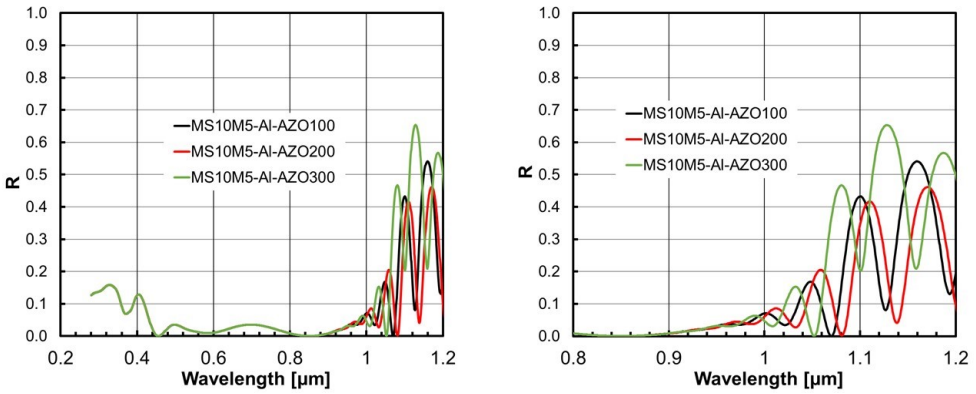

Figure 5.23: Reflectance comparison between the structures with spacer (*AZnO*) thick *100nm*, *200nm* and *300nm*

A direct consequence of the increase of reflectance in the NIR region is the increment of the EQE in the same range of frequencies; it is possible to observe this

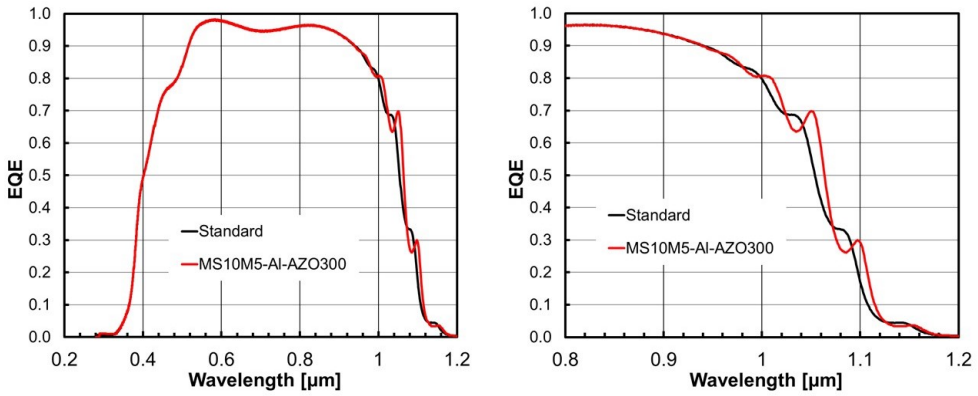

Figure 5.24: EQE comparison between the standard structure and the one with *Al* back reflector and spacer (*AZnO*) *300nm* thick.

behavior in Figure 5.24 where is shown a comparison between the EQEs of standard structure and *MS10M5-AZO300* structure.

As a final comment, it can be pointed out that the relative advantages offered by light trapping via backside mirror would get significantly larger in the case of thinner *CIGS* layers than the thick ($3\mu m$) absorbers simulated but, also in this case the increase of J_{SC} is not negligible indeed in case of ideal reflector $\Delta J_{SC} = +0.66 mA/cm^2$ and in a real case $\Delta J_{SC} = +0.24 mA/cm^2$.

5.4 Alternative Window and Buffer layers

The last part of this Thesis was dedicated to the study of the substitution of window and buffer layers in order to increase the performance of the thin-film CIGS solar cell [57].

This section deals with the performance of cells in which the standard n-side stack made of *CdS* buffer, *i-ZnO* high-resistance interlayer and *Al-doped ZnO (AZO)* window has been replaced with one featuring buffer materials with larger bandgap than that of the *CdS*, in order to reduce parasitic absorption and increase J_{SC}, in combination with a novel *ZnMgO* window interlayer, followed by the *AZO*.

In a first set of simulations, it was considered a *Zn(O,S)* buffer and a $Zn_{1-x}Mg_xO$ window with varying composition ($x = 0.17 \div 0.40$), in order to determine the optimum *Mg* mole fraction.

Next, it was studied the behavior of cells with $Zn_{0.83}Mg_{0.17}O$ window and as a buffer either *Zn(O,S)*, with varying thickness, or $Cd_{1-x}Zn_xS$, with varying composition.

For all the simulations in this section it was used as baseline the ZSW cell simulated with optical coefficient measured by EMPA for the *CIGS* [24] and coefficient from the paper by Hara [32] for other materials. Optical coefficients for *ZnMgO* were provided by ZSW: they were wavelength-shifted to account for the specific composition of the simulations; for *Zn(O,S)* were used the *ZnO* coefficients from the paper by Hara [32]; for *CdZnS* were used the *CdS* coefficients from the paper by Hara [32], wavelength-shifted to account for the specific *Zn* mole fraction of different simulations.

In all of the simulations of this section the *buffer/absorber* interface, as well as the other hetero-interfaces, has been considered ideal, hence the large efficiency values.

5.4.1 *Zn(O,S)* buffer with $Zn_{1-x}Mg_xO$ window interlayer

In the first set of simulations it was analyzed a structure where *i-ZnO* and *CdS* were replaced by, respectively, $Zn_{1-x}Mg_xO$ and *Zn(O,S)*. In these simulations it was varied the composition of *ZnMgO* in order to determine the optimum *Mg* mole fraction. In Figure 5.25 is shown the simulated structure and in table below are described the main material properties of the structures.

	AZnO	$Zn_{1-x}Mg_xO$	*Zn(O,S)*	*CIGS*
x	–	Var (0.17 ÷ 0.4)	–	–
$Eg[eV]$	3.3	Var (3.6 ÷ 4.1)	3	Graded
$\chi[eV]$	4.8	Var (4.3 ÷ 3.8)	4.4	4.6
$Doping[cm^{-3}]$	$4\cdot 10^{19}$	$1\cdot 10^{17}$	$1\cdot 10^{17}$	$8\cdot 10^{16}$

Five values of *Mg* mole fraction in the $Zn_{1-x}Mg_xO$ were considered: $x = 0.17, 0.22, 0.26, 0.33, 0.40$; these correspond with $Zn_{1-x}Mg_xO$ electron affinities $\chi = 4.30, 4.17, 4.10, 3.96, 3.80$ *eV*, respectively [22] [46].

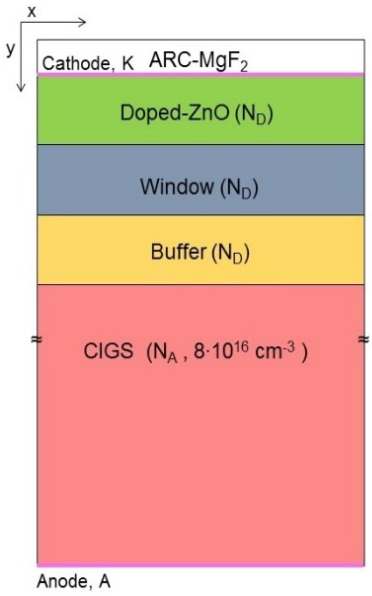

Figure 5.25: Schematic cross-section of the structures with $Zn_{1-x}Mg_xO$ window interlayer and *Zn(O,S)* buffer.

In Figures 5.26 and 5.27 is shown the effect of varying the $Zn_{1-x}Mg_xO$ composition on the figures of merit of the cell; it is possible to observe that small values of $x < 0.25$ are required for optimum performance. As x gets larger, so do both the bandgap of $Zn_{1-x}Mg_xO$ and its CBO with the *CdS* buffer, which hinders photogenerated electron collection and kills the fill factor.

For this reason, it was chosen $x = 0.17$ as the optimum *Mg* mole fraction in the $Zn_{1-x}Mg_xO$ in the simulations that follow.

It is worth noticing that, in case a larger active donor concentration can be obtained in the *AZO*, with respect to the $4 \cdot 10^{19} cm^{-3}$ of Figures , the constraint on x relaxes, because the large n-doping density of the *AZO* layer pulls the $Zn_{1-x}Mg_xO$ bands down and makes the effect of its CBO spike with *CdS* less harmful: when the *AZO* active donor concentration reaches $4 \cdot 10^{20} cm^{-3}$, optimum performance can be obtained for $x < 0.35$.

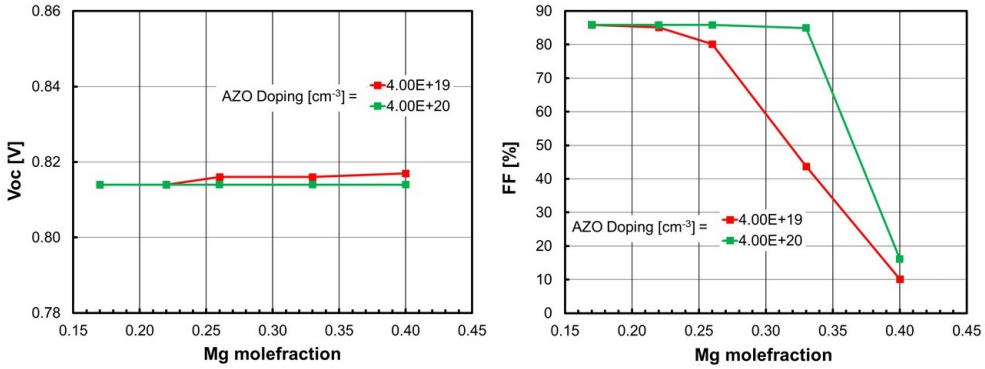

Figure 5.26: V_{OC} and FF for the cells with $Zn_{1-x}Mg_xO$ window interlayer and *Zn(O,S)* buffer, as a function of the *Mg* mole fraction x for two different *AZnO* doping

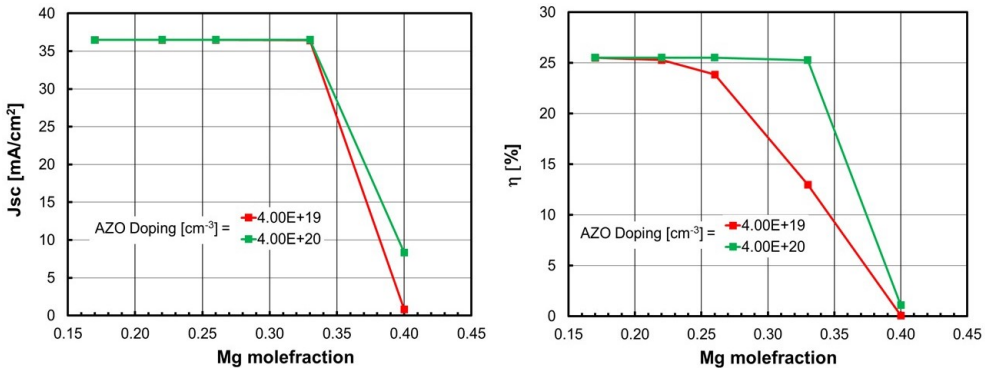

Figure 5.27: J_{SC} and η for the cells with $Zn_{1-x}Mg_xO$ window interlayer and *Zn(O,S)* buffer, as a function of the *Mg* mole fraction x for two different *AZnO* doping

5.4.2 *Zn(O,S)* buffer with $Zn_{0.83}Mg_{0.17}O$ window interlayer of varying thickness

Having fixed a $Zn_{1-x}Mg_xO$ layer composition yielding optimum performance ($x = 0.17$), it was explored a range of window interlayer thickness values ($30 \div 100nm$) to ascertain their impact on the behavior of the cell.

In table below are reported the main material properties of the structures.

	AZnO	$Zn_{1-x}Mg_xO$	*Zn(O,S)*	*CIGS*
x	–	0.17	–	–
$Eg[eV]$	3.3	3.6	3	Graded
$\chi[eV]$	4.8	4.3	4.4	4.6
$Doping[cm^{-3}]$	$4\cdot 10^{19}$	$1\cdot 10^{17}$	$1\cdot 10^{17}$	$8\cdot 10^{16}$

Observing the behavior of the figures of merit of the cell (Figures 5.28 and 5.29) due to the variation of the window interlayer thickness, it is clear that in the range explored the performance of the cell is practically independent of the $Zn_{0.87}Mg_{0.13}O$ layer thickness, which allows for significant design tolerance.

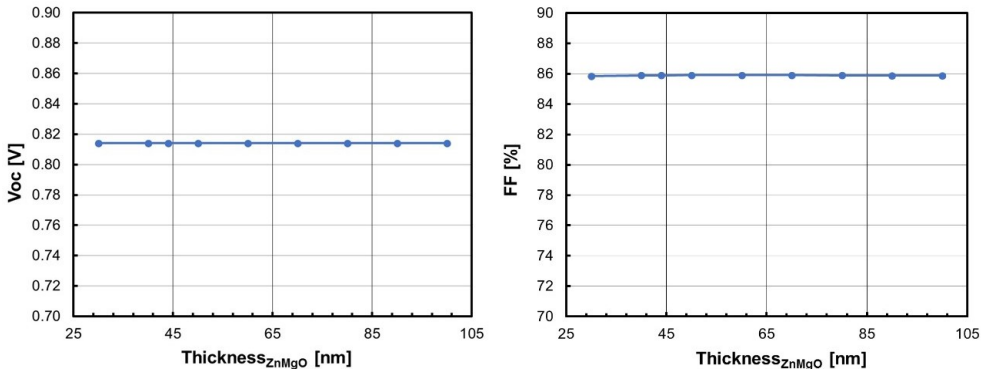

Figure 5.28: V_{OC} and FF for the cells with $Zn_{0.87}Mg_{0.13}O$ window interlayer and *Zn(O,S)* buffer, as a function of the $Zn_{0.87}Mg_{0.13}O$ thickness

The very slight increase of J_{SC} observed as the window interlayer thickness is increased from *30* to $70nm$ can be partly explained by more favorable optical transmission through the top stack: Figure 5.30 shows the reflectance and EQE spectra for the cells with *30* and $70nm$ $Zn_{0.87}Mg_{0.13}O$ thickness: reduced reflection in the $850 \div 1050nm$ range in the latter locally enhances the EQE.

Perhaps more importantly, the $70nm$ $Zn_{0.87}Mg_{0.13}O$ gives a slightly more favorable band alignment, with lower CB in the buffer and window spikes, which facilitates electron collection by the cathode: the band diagrams are shown in Figure 5.31.

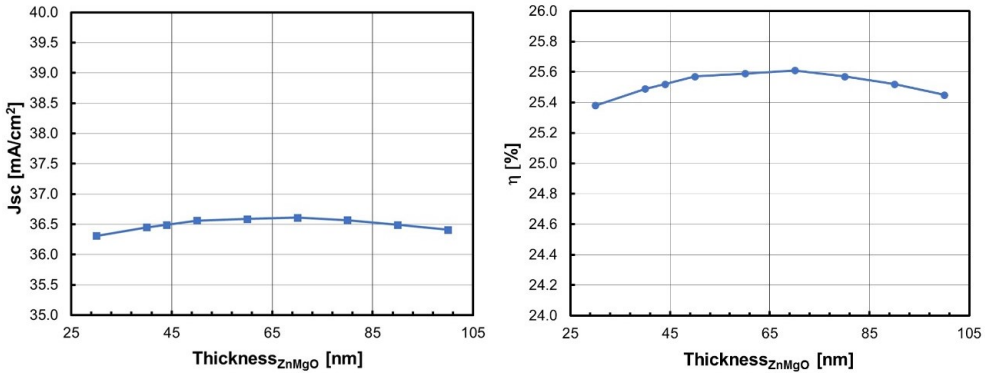

Figure 5.29: J_{SC} and η for the cells with $Zn_{0.87}Mg_{0.13}O$ window interlayer and *Zn(O,S)* buffer, as a function of the $Zn_{0.87}Mg_{0.13}O$ thickness

5.4.3 $Cd_{1-x}Zn_xS$ buffer with $Zn_{0.83}Mg_{0.17}O$ window interlayer

The second buffer material analyzed is the $Cd_{1-x}Zn_xS$, it was chosen to study it because it is one of the most used to replacing the standard *CdS* buffer [86] [87] [88], in order to reduce parasitic photon absorption, by increasing the *Zn* mole fraction *x*.

Three values of *Zn* mole fraction in the $Cd_{1-x}Zn_xS$ were considered: $x = 0$ *(CdS), 0.1, 0.2, 0.3*; these correspond with $Cd_{1-x}Zn_xS$ electron affinities χ = *4.50, 4.43, 4.33, 4.23 eV*, respectively.

In table below are reported the main material properties of the structures.

	$AZnO$	$Zn_{1-x}Mg_xO$	$Cd_{1-x}Zn_xS$	$CIGS$
x	–	0.17	Var (0 ÷ 0.3)	–
$Eg[eV]$	3.3	3.6	Var (2.4 ÷ 2.67)	Graded
$\chi[eV]$	4.8	4.3	Var (4.5 ÷ 4.23)	4.6
$Doping[cm^{-3}]$	$4\cdot 10^{19}$	$1\cdot 10^{17}$	$1\cdot 10^{17}$	$8\cdot 10^{16}$

In Figure are shown the figures of merit of the cell in function of the *Zn* mole fraction of the $Cd_{1-x}Zn_xS$; it is possible to note that the moderate increase of the bandgap (270*meV* over the whole range of *x* values) of the buffer results in modest but non-negligible J_{SC} improvement. This results in a correspondingly modest increase

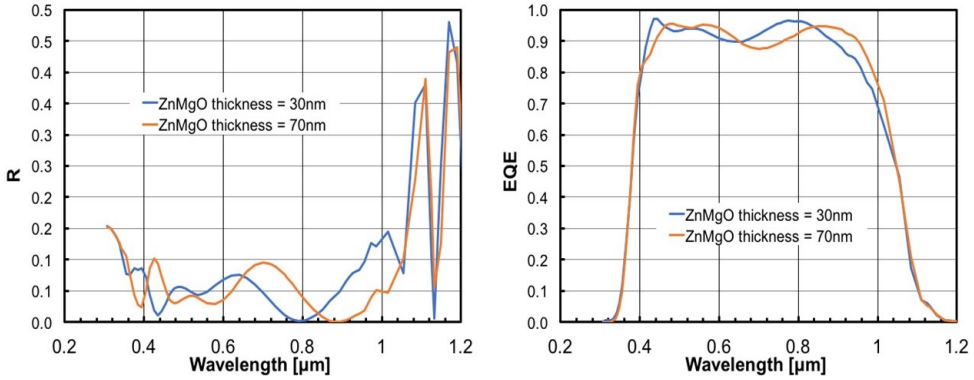

Figure 5.30: Reflectance and EQE spectra for the cells with 30*nm* and 70*nm* $Zn_{0.87}Mg_{0.13}O$ window interlayer and *Zn(O,S)* buffer.

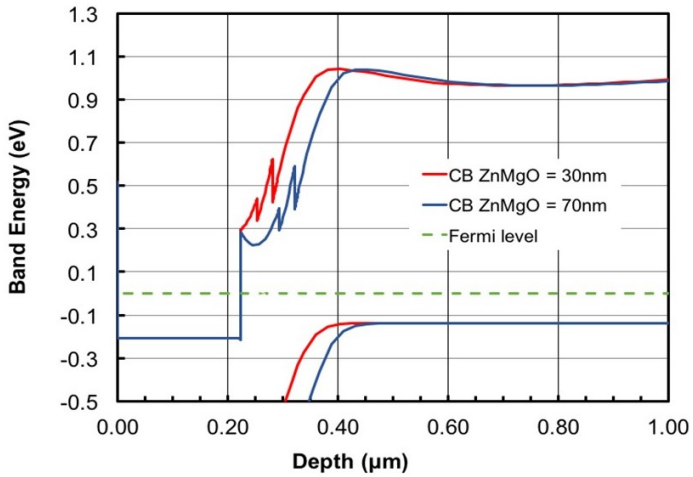

Figure 5.31: Equilibrium band diagram for the cells with 30*nm* and 70*nm* $Zn_{0.87}Mg_{0.13}O$ window interlayer and *Zn(O,S)* buffer.

of the efficiency, until, for the large value of $x = 0.3$, the spike-like CBO between buffer and absorber becomes large enough (*0.33 eV*) to negatively affect *FF* and, consequently, the efficiency.

In this section were studied a different window layer (*ZnMgO*) and two alternative

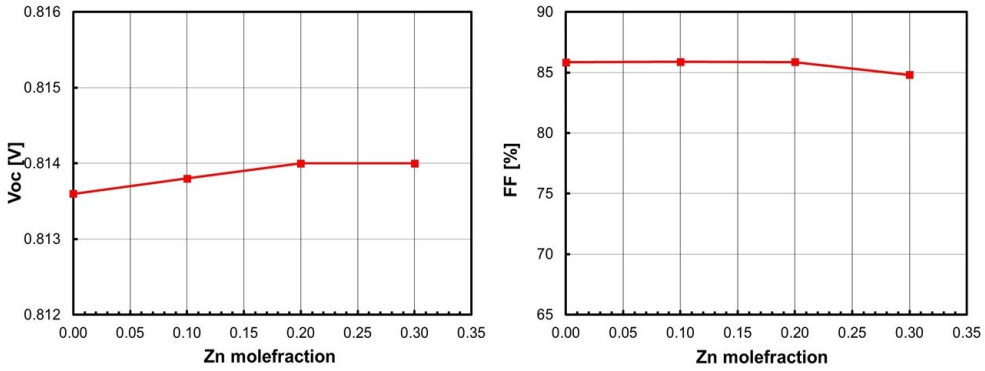

Figure 5.32: Simulated V_{OC} and FF for the cells with $Zn_{0.83}Mg_{0.17}O$ window interlayer and $Cd_{1-x}Zn_xS$ buffer, as a function of the buffer Zn mole fraction x.

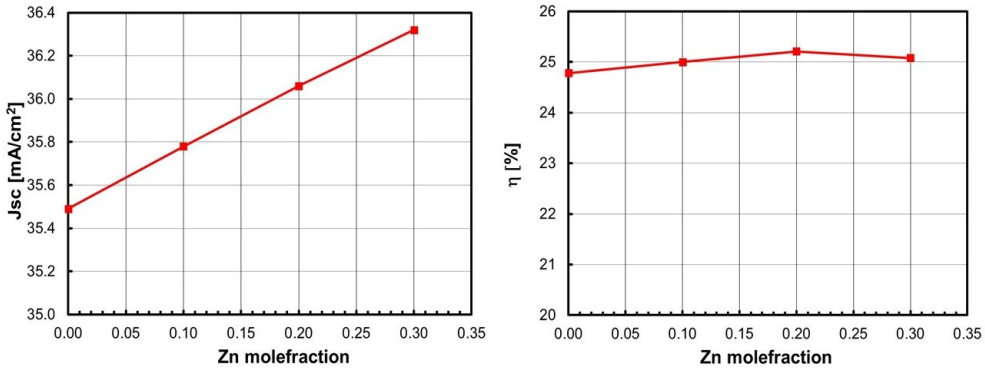

Figure 5.33: Simulated J_{SC} and η for the cells with $Zn_{0.83}Mg_{0.17}O$ window interlayer and $Cd_{1-x}Zn_xS$ buffer, as a function of the buffer Zn mole fraction x.

buffers (*Zn(O,S), CdZnS*) to the baseline structure.

It was demonstrated that a $Zn_{1-x}Mg_xO$ high-resistance window interlayer is compatible with *Zn(O,S)* buffer and *AZO TCO* and it is possible to yield high performance as long as the Mg mole fraction x is low enough ($x < 0.25$). It was also shown that for $x = 0.17$ there is a broad, rather flat efficiency maximum for varying interlayer thickness, centered around $65nm$. In the end using an interlayer of $Zn_{0.83}Mg_{0.17}O$ it was shown that the use of $Cd_{1-y}Zn_yS$ buffer ($y = 0 \div 0.3$) produce a slight performance

improvement for *Zn* mole fraction up to $y = 0.2$ thanks to the reduction of parasitic absorption.

5.5 Front point contact in case of alternative buffers

The last technique that will be analyzed to increase the performance of the cells is based on the union of two previously studied solutions: point contact, in particular the field effect passivation, and alternative buffers.

In order to evaluate the effectiveness of field-effect passivation in combination with buffer materials alternative to *CdS*, it was simulated the front contact nanostructured *CIGS-based* solar cell of Section 5.1 (Figure 5.1) *($h = 10$ nm, $d = 50$ nm, $wpc = 10$ nm*), with several buffer materials alternative to *CdS*.

These simulations are based on the EMPA cell simulated with absorption coefficients measured at EMPA for the *CIGS* [24], instead for the other material were used coefficient taken from literature [32], so the figures of merit of the baseline are:

$$V_{OC} = 0.741V,\ J_{SC} = 36.4\frac{mA}{cm^2},\ FF = 80.1\% \text{ and } \eta = 21.6\%.$$

The mainly focus of these simulations is on the effect of the different conduction band offsets (CBOs) at the hetero-interfaces. The CBOs at the *ZnO/buffer* and *buffer/CIGS* interfaces used in our simulations come from the literature and are summarized in table below together with the simulated cell figures of merit for the two cases of $Q_f = 0$ (no field-effect passivation) and $Qf = 1 \div 5 \cdot 10^{12} cm^{-2}$ (optimum field-effect passivation). In both cases, no chemical passivation of defects was considered at the passivation/*CIGS* interface.

For the $Zn_{1-x}Mg_xO$, it was considered the case of low *Mg* concentration ($x = 0.19$), as previous studies showed that larger x necessitates nearly degenerate or degenerate $Zn_{1-x}Mg_xO$ to achieve good efficiency. The optical complex refractive indexes of the studied buffer materials come from the literature (for In_2S_3) [89], from unpublished measured data (for $Zn_{0.81}Mg_{0.19}O$), or are the same as for *ZnO* (for the *Zn(O,S)*).

Solar cell stack	$CBO_{CIGS/Buffer}$ (eV)	$CBO_{Buffer/ZnO}$ (eV)	Q_f (cm^{-2})	J_{sc} (mA/cm^2)	V_{oc} (V)	FF (%)	η (%)
ZnO/i-ZnO/CdS/CIGS	0.3	-0.2	0	35.2	0.55	64.8	12.6
			10^{12}	35.5	0.74	83.0	21.7
ZnO/i-ZnO/In_2S_3/CIGS (Na containing)	-0.25	-0.2	0	33.9	0.72	81.1	19.9
			$5{\cdot}10^{12}$	35.4	0.73	83.1	21.6
ZnO/i-ZnO/ZnO/CIGS	-0.2	0	0	36.0	0.70	75.3	19.0
			$5{\cdot}10^{12}$	36.6	0.73	83.1	22.3
ZnO/i-ZnO/Zn(O,S)/CIGS, S/(S+O)=0.28	0.2	0	0	36.4	0.61	76.4	17.1
			10^{12}	36.6	0.74	83.1	22.5
ZnO/i-ZnO/$Zn_{0.81}Mg_{0.19}O$/CIGS	0.2	-0.35	0	36.0	0.64	25.5	5.9
			10^{12}	36.5	0.73	83.0	22.3

In Figure 5.34 are shown the simulated cell efficiency, η,(bars) and corresponding open circuit voltage, V_{OC}, (symbols) in function of buffer materials for different values of the passivation charge. Interface acceptors, $N_{AT} = 10^{11} cm^{-2}$, are present all over the *CIGS* surface.

From these results it is possible to observe that in the cases of $CBO_{CIGS/Buffer} > 0$ (*CdS* [53], *Zn(O, S)* [45], $Zn_{0.81}Mg_{0.19}O$ [22]), positive $Q_f \geq 10^{12} cm^{-2}$ is sufficient to hinder recombination at the defective CIGS surface for all studied materials, boosting V_{OC} (Figure 5.34, symbols) irrespective of the conduction-band offset value at the buffer/absorber heterojunction. Moreover, the concentration of electrons, which are majority carriers at the inverted *passivation/CIGS interface*, is raised by the positive charge and the barrier seen by photo-generated electrons leaving the absorber is reduced, so that the *FF* monotonically increases with Q_f. The combination of the two factors leads the efficiency (Figure 5.34, bars) up to and beyond 21.6%.

On the other hand, in the presence of a cliff ($CBO_{CIGS/Buffer} < 0$) at the *buffer/CIGS interface* (In_2S_3 [89] and *ZnO* [22]), the barrier to the flow of photo-generated electrons from the absorber to the buffer layer is removed, as shown by conduction band diagram of *ZnO-buffered* cell depicted in Figure 5.35 , and *FF* is higher than that of $CBO_{CIGS/Buffer} > 0$ case, even when $Q_f = 0$, and increases further with positive Q_f due to the increased band-bending under the point-contact

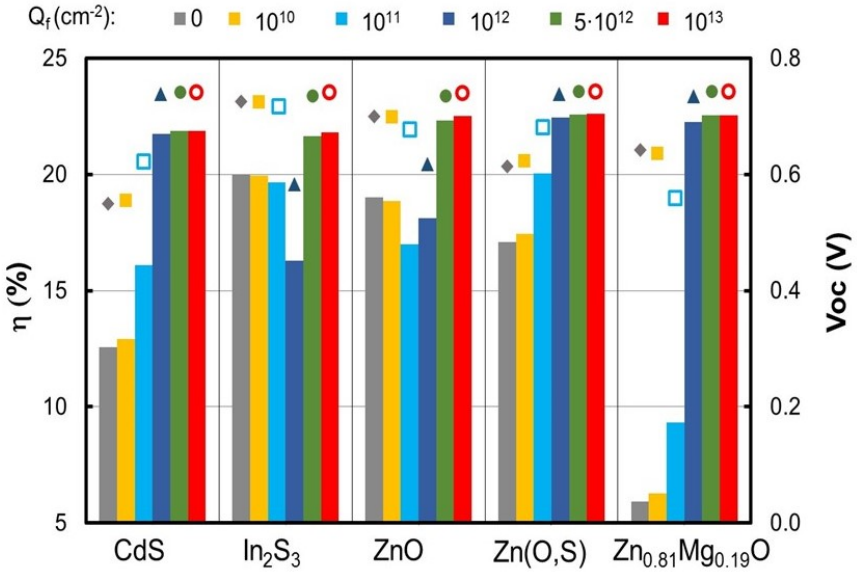

Figure 5.34: Simulated cell efficiency, η (bars) and corresponding open circuit voltage, V_{OC}, (symbols) vs. buffer material for different values of the passivation charge; $h = 10nm$, $wpc = 10nm$, $d = 50nm$. Interface acceptors, $N_{AT} = 10^{11}cm^{-2}$, are present all over the *CIGS* surface. In the case of *Zn(O,S)*, $S/Zn = 0.28$.

(Figure 5.35) and passivation (Figure 5.36), the latter mainly reducing the series resistance of the current path. As the positive Q_f increases, the downward band-bending of the conduction band enhances the interface acceptor trap ionization and at the same time repels holes (minority carriers) at the surface: the competing effects of increased inversion (hindering recombination) and enhanced trap ionization (promoting recombination) determine the non-monotonic V_{OC} dependence on the fixed charge density, as shown by data in previous table. The high V_{OC} and FF when $Q_f = 0$ combine to give the *19%* efficiency of the *ZnO/i-ZnO/CIGS* stack (*19.9%* for $ZnO/i - ZnO/In_2S_3/CIGS$). In the case of *ZnO* (In_2S_3) buffer, the minimum V_{OC} is reached for $Q_f = 10^{12}cm^{-2}$, beyond which the electric field induced by Q_f is high enough to push away the holes from the *CIGS* surface; the recombination

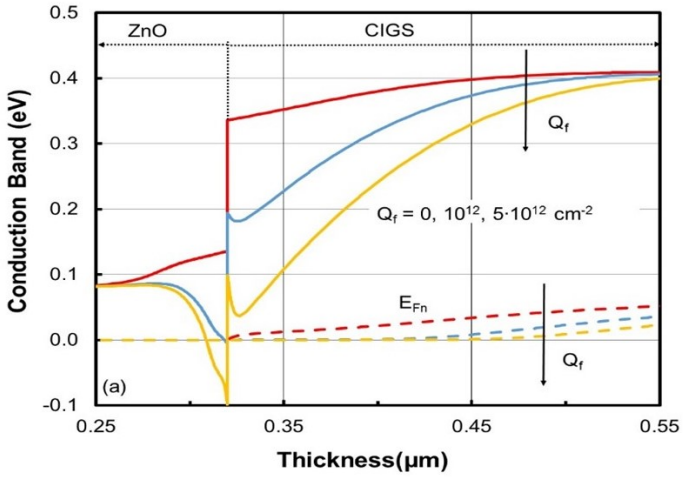

Figure 5.35: Conduction band energy in the point contact area in the case of acceptor interface states with density $10^{11}cm^{-2}$ all over the *CIGS* surface (circles) and $Q_f = 0, 10^{12}, 5\cdot 10^{12}cm^{-2}$. E_C (solid lines) and corresponding electron Fermi energy, E_{Fn}, (dashed lines) versus depth at $V = 0.59V$ (corresponding to the *MPP* for the case of $Q_f = 0$).

decreases again and V_{OC} starts to increase like for the other buffer materials boosting the efficiency to *22.3%* for *ZnO* and *21.6%* for In_2S_3.

In conclusion it is possible to affirm that when the positive charge within the passivation is sufficiently high (in the range $10^{12} \div 5\cdot 10^{12}cm^{-2}$), the benefit of field-effect passivation also applies to cells having unfavorable conduction-band offset (i.e., cliff or low spike) at the buffer/CIGS interface, yielding efficiencies over *21%* for all samples, and allowing more flexibility in the choice of the buffer layer.

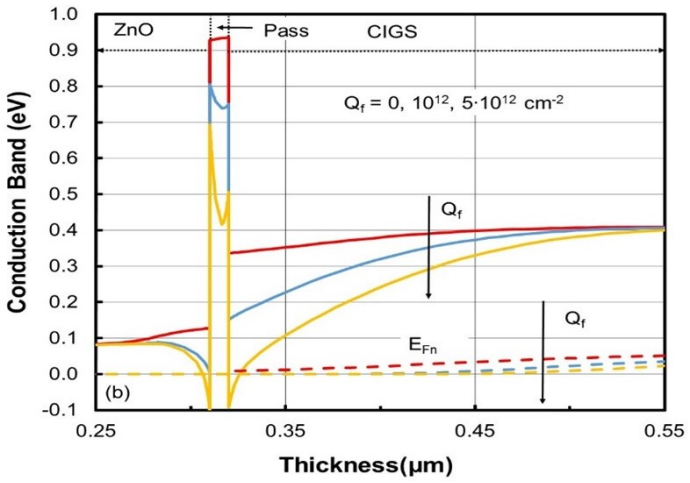

Figure 5.36: Conduction band energy in the passivated area in the case of acceptor interface states with density $10^{11}cm^{-2}$ all over the *CIGS* surface (circles) and $Q_f = 0, 10^{12}, 5\cdot 10^{12}cm^{-2}$. E_C (solid lines) and corresponding electron Fermi energy, E_{Fn}, (dashed lines) versus depth at $V = 0.59V$ (corresponding to the *MPP* for the case of $Q_f = 0$).

Conclusions

The main aims of this thesis were to study thin-film *CIGS* solar cells, provide a good model for simulating record cells, understand the main limiting factors and propose new solutions to increase their efficiency.

First of all, the photovoltaic effect and the behavior of the p-n junction were introduced mainly focusing on the structure of thin-film *CIGS* solar cells.

A brief description of the simulator and the models used, both electrical (Drift-diffusion) and optical (Transfer Matrix Method TMM) was given, and the models of the two record cells of EMPA and ZSW on which this work is based were introduced.

The effect of *CIGS* properties on cell performance was studied, starting from a variation of the Gallium profile (*GGI*), and the variation of the conduction band offsets. In particular it was demonstrated that the increase of *GGI* at the molybdenum side of the *CIGS* absorber is expected to give the best efficiency thanks to the increase of carriers collection. Then it was analyzed another important aspect related to the composition of the material, i.e., the *Cu* content inside *CIGS* (*CGI*). Four samples with different average *CGI* were simulated and it was observed that the absorption of the cells increases with the rise of *CGI*, up to a *Cu* concentration of *0.85*, after which the increment of J_{SC} is slight.

It was also studied the behavior of the temperature dependent *J-V* characteristics, which show a saturation at low temperatures (roll-over). It was analyzed the effect of conduction band offsets at *window/buffer* and *buffer/absorber* interfaces on the roll-over and it was demonstrated that it is mainly controlled by the energy barrier at the *window/buffer* interface, where the transport of electrons over the barrier can be

adequately described by the thermionic-emission theory.

Another particular effect due to the properties of *CIGS* is the capacitance step in the admittance spectroscopy signatures, it was observed that this could be related to the presence of:

- high CBO at the *CdS/CIGS* interface (Δ_{AB});
- high density of defects at the *CdS/CIGS* interface;
- a Schottky barrier for holes at the rear contact;
- donor-decorated grain boundaries.

From this study it was also found that there is no correlation between w_n and t_{CdS} in many experimental studies, so this may indicate that a Schottky barrier or downward-bent GB could be the reason for depletion widths (calculated from measured capacitance step heights) much larger than the *CdS* thickness.

In the second part of this work the attention was shifted on the limiting factors of the solar cells, both non-radiative recombinations and optical losses were analyzed. One of the main causes of non-radiative recombination inside the cell are due to bulk traps and for this reason it was studied their effect on the performance of the cells. It was showed that traps concentration higher than $1 \cdot 10^{15} cm^{-3}$ are not compatible with high efficiency ($> 20\%$). Moreover it was observed that trap defects are influential as far as they are placed within $0.25eV$ of the intrinsic Fermi level.

Another cause of non-radiative recombinations are the interface traps at *CIGS /Buffer* surface, both donor and acceptor types were studied and it was observed that the surface donors are more benign than surface acceptors; furthermore it was found that in case of acceptors even when carriers lifetimes are so high as not to limit V_{OC} anymore there is a significant impact of the trap concentration on FF and, consequently, on the efficiency. This is mostly due to the electro-statics of the surface acceptors: larger N_{IT} (Interface trap concentration) means larger trapped negative charge, weaker surface inversion, hence smaller conductance of the top region of the *CIGS* absorber.

The last possible cause of non-radiative recombination analyzed is the presence of grain boundaries, which are peculiar of the material and could be rich of traps, so their presence was also studied in order to understand if a strong band-bending, upwards or downwards, caused by GB, can coexist with high efficiency. It was observed that an upward band-bending reduces V_{OC}, FF and η only if due to traps with large cross-section, instead a downward band-bending reduces always V_{OC}, FF and η the more it becomes negative; in addiction it was showed that *J-V* curves are very different from measured one in case of *FC* at the GB so it is more probable that in the grain boundaries there are traps with low cross-section in order to justify the *J-V* behavior and the high efficiency. To conclude the analysis of electrical limiting factors of the cells the effect of the presence of a $KInSe_2$ (*KIS*) layer due to the Post-Deposition Treatment (PDT) with Alkali fluoride was studied and it was found that it can have beneficial effects on the cell performance, in terms of neutralization of the activity of interface defects, if its electron affinity is in the range $4.3eV \leq \chi_{KIS} \leq 4.7eV$; outside the range described before the performance drastically reduced due to large barriers for electron collection either at the *CIGS/KIS* interface (low χ_{KIS}) or at the *KIS/CdS* interface (high χ_{KIS}).

Also the optical losses were taken into account and were analyzed for both the record cells observing that the layer which causes the highest optical loss is the *window* one; this is unexpected because the *AZnO* ($3.3eV$) has an high band-gap so the absorption should be low, instead for its thickness and for a tail of absorption at low energies it results the worst layer from an optical point of view.

The last part of this thesis is dedicated to the possible solutions to increase the efficiency of thin-film *CIGS* solar cells; electrical and optical solutions were analyzed. The first solution is the introduction of surface passivation and point contacts which can help to boost the cell performances reducing the non-radiative recombinations at the interface between *CIGS* and buffer. The effects of both chemical and field-effect passivation were analyzed and the obtained results showed that in presence of surface-limited cells the use of surface passivation in combination with point contacts can help the cell recover most of the performance loss due to interface states. It was also showed that positive charge in the order of $1 \cdot 10^{12} cm^{-2}$ within the passivation can

improve the efficiency of a cell and it helps to relaxing the requirements on the point contact geometry.

The same solution was simulated at the back of the cell, so back-side point contact were taken into account in order to reduce back-surface recombination and increase the photo-generated carrier collection; also in this case it was analyzed the effect of both chemical and field-effect passivation on the cell performance. A lot of possible cases were studied and it was observed that there are three effects playing a role, the combination of which determines the impact on efficiency:

- *CIGS* back interface passivation, whether chemical or electrical, increasing V_{OC};
- enhanced light reflection of Al_2O_3 relative to $MoSe_2/Mo$, increasing J_{SC};
- increased series resistance at the point contact, reducing *FF*.

due to the thick ($3\mu m$) absorber and back *GGI* grading, the beneficial effects (increase of V_{OC} J_{SC}) are limited.

After that the introduction of a back reflector was analyzed in order to obtain an increased absorption and a reduction of power losses in the solar cells; the study was limited to four different materials: Gold (*Au*), Aluminum (*Al*), Titanium Nitride (*TiN*) and Zirconium Nitride (*ZrN*). It was showed that *Au* and *Al* outperform *TiN* and *ZrN* as mirror materials and the differences between Aluminum and Gold are never dramatic, so both can be used as back mirror materials. In addition, it is possible to affirm that the relative advantages offered by light trapping via backside mirror would get significantly larger in the case of thinner *CIGS* layers than the thick ($3\mu m$) absorbers simulated but, also in this case, the increase of J_{SC} is not negligible.

The last solution analyzed is the substitution of window and buffer layers with alternative material in order to increase the absorption and reduce the optical losses. The window layer was substituted by $ZnMgO$, instead the buffer layer was replaced by *Zn(O,S)* or *CdZnS*. It was demonstrated that a $Zn_{1-x}Mg_xO$ high-resistance window interlayer is compatible with *Zn(O,S)* buffer and *AZO TCO* and it is possible to yield high performance as long as the *Mg* mole fraction x is low enough ($x < 0.25$). It was

also showed that using an interlayer of $Zn_{0.83}Mg_{0.17}O$ the use of $Cd_{1-y}Zn_yS$ buffer ($y = 0 \div 0.3$) produce a slight performance improvement for Zn mole fraction up to $y = 0.2$ thanks to the reduction of parasitic absorption.

To conclude, it is possible to affirm that this work is useful to better understand some behaviors of thin-film *CIGS* solar cells and to understand what the more promising solution to boost the cell efficiency is.

Bibliography

[1] A. Chirilă, P. Reinhard, F. Pianezzi, P. Bloesch, A.R. Uhl, C. Fella, L. Kranz, D. Keller, C. Gretener, H. Hagendorfer and others. Potassium-induced surface modification of $Cu(In,Ga)Se_2$ thin films for high-efficiency solar cells. *Nature materials*, 12(12):1107, 2013.

[2] P. Jackson, R. Wuerz, D. Hariskos, E. Lotter, W. Witte and M. Powalla. Effects of heavy alkali elements in $Cu(In,Ga)Se_2$ solar cells with efficiencies up to 22.6%. *physica status solidi (RRL) – Rapid Research Letters*, 10(8):583–586. URL: https://onlinelibrary.wiley.com/doi/abs/10.1002/pssr.201600199, doi:10.1002/pssr.201600199.

[3] BP. Bp statistical review of world energy, 2015. Available online. URL: https://www.bp.com/en/global/corporate/energy-economics/statistical-review-of-world-energy.html.

[4] A.E. Becquerel. Recherches sur les effets de la radiation chimique de la lumiere solaire au moyen des courants electriques. *CR Acad. Sci*, 9(145):1, 1839.

[5] H. Hertz. On the photoelectric effect. *Ann Phys*, 31:983–1000, 1887.

[6] D. M. Chapin, C.S. Fuller and G. L. Pearson. A new silicon p-n junction photocell for converting solar radiation into electrical power. *Journal of Applied Physics*, 25(5):676–677, 1954.

[7] PVEducation. Pveducation, 2018. Available online. URL: https://www.pveducation.org/index.php.

[8] Wikipedia contributors. P–n junction — Wikipedia, the free encyclopedia, 2018. Available online. URL: https://en.wikipedia.org/w/index.php?title=P%E2%80%93n_junction&oldid=834302918.

[9] R.S. Muller, T.I. Kamins and M. Chan. *Device Electronics for Integrated Circuits*. Wiley, 2003. URL: https://books.google.it/books?id=lhNnQgAACAAJ.

[10] X. Sun, T. Silverman, R. Garris, C. Deline and M.A. Alam. An Illumination and Temperature-Dependent Analytical Model for Copper Indium Gallium Diselenide (CIGS) Solar Cells. *IEEE Journal of Photovoltaics*, 6(5):1298–1307, 2016.

[11] A. Luque and S. Hegedus. *Handbook of photovoltaic science and engineering*. John Wiley & Sons, 2011.

[12] F. Kessler and D. Rudmann. Technological aspects of flexible CIGS solar cells and modules. *Solar Energy*, 77(6):685–695, 2004.

[13] A. Chirilă, S. Buecheler, F. Pianezzi, P. Bloesch, C. Gretener, A.R. Uhl, C. Fella, L. Kranz, J. Perrenoud, S. Seyrling and others. Highly efficient $Cu(In,Ga)Se_2$ solar cells grown on flexible polymer films. *Nature materials*, 10(11):857, 2011.

[14] P. Reinhard, A. Chirilă, P. Blosch, F. Pianezzi, S. Nishiwaki, S. Buecheler and A.N. Tiwari. Review of progress toward 20% efficiency flexible CIGS solar cells and manufacturing issues of solar modules. In *Photovoltaic Specialists Conference (PVSC), Volume 2, 2012 IEEE 38th*, pages 1–9. IEEE, 2012.

[15] W. Shockley and J.H. Queisser. Detailed balance limit of efficiency of p-n junction solar cells. *Journal of applied physics*, 32(3):510–519, 1961.

[16] S.H. Wei, S.B. Zhang and A. Zunger. Effects of Ga addition to $CuInSe_2$ on its electronic, structural, and defect properties. *Applied physics letters*, 72(24):3199–3201, 1998.

[17] D. L. Pulfrey. *Understanding modern transistors and diodes*. Cambridge University Press, 2010.

[18] G. Sozzi, S. Di Napoli, R. Menozzi, R. Carron, E. Avancini, B. Bissig, S. Buecheler and A.N. Tiwari. Analysis of Ga grading in CIGS absorbers with different Cu content. In *Photovoltaic Specialists Conference (PVSC), 2016 IEEE 43rd*, pages 2279–2282. IEEE, 2016.

[19] Synopsys. Synopsys sentaurus tcad, 2018. Available online. URL: `https://www.synopsys.com/`.

[20] D.A. Neamen and others. *Semiconductor physics and devices*, volume 3. McGraw-Hill New York, 1997.

[21] L. Weinhardt, C. Heske, E. Umbach, T.P. Niesen, S. Visbeck and F. Karg. Band alignment at the i-ZnO/CdS interface in $Cu(In,Ga)(S,Se)_2$ thin-film solar cells. *Applied physics letters*, 84(16):3175–3177, 2004.

[22] T. Törndahl, C. Platzer-Björkman, J. Kessler and M. Edoff. Atomic layer deposition of $Zn_{1-x}Mg_xO$ buffer layers for $Cu(In,Ga)Se_2$ solar cells. *Progress in Photovoltaics: Research and applications*, 15(3):225–235, 2007.

[23] H. Kashiwabara, Y. Hayase, K. Takeshita, T. Okuda, S. Niki, K. Matsubara, K. Sakurai, A. Yamada, S. Ishizuka and N. Terada. Study of changes of electronic and structural nature of CBD-CDS/CIGS interface with Ga concentration. In *Photovoltaic Energy Conversion, Conference Record of the 2006 IEEE 4th World Conference on*, volume 1, pages 495–498. IEEE, 2006.

[24] R. Carron, E. Avancini, T. Feurer, B. Bissig, P.A. Losio, R. Figi, C. Schreiner, M. Bürki, E. Bourgeois, Z. Remes and others. Refractive indices of layers and optical simulations of $Cu(In,Ga)Se_2$ solar cells. *Science and Technology of advanced MaTerialS*, (just-accepted):1–44, 2018.

[25] P. Jackson, D. Hariskos, R. Wuerz, O. Kiowski, A. Bauer, T.M. Friedlmeier and M. Powalla. Properties of $Cu(In,Ga)Se_2$ solar cells with new record efficiencies

up to 21.7%. *physica status solidi (RRL)–Rapid Research Letters*, 9(1):28–31, 2015.

[26] Solar Frontier. Solar frontier achieves world record thin-film solar cell efficiency of 22.9%, 2017. Press release. URL: `http://www.solar-frontier.com/eng/news/2017/1220_press.html`.

[27] E. Avancini, R. Carron, B. Bissig, P. Reinhard, R. Menozzi, G. Sozzi, S. Di Napoli, T. Feurer, S. Nishiwaki and S. Buecheler. Impact of compositional grading and overall Cu deficiency on the near-infrared response in $Cu(In,Ga)Se_2$ solar cells. *Progress in Photovoltaics: Research and Applications*, 25(3):233–241, 2017.

[28] P. Jackson, D. Hariskos, R. Wuerz, W. Wischmann and M. Powalla. Compositional investigation of potassium doped $Cu(In,Ga)Se_2$ solar cells with efficiencies up to 20.8%. *physica status solidi (RRL)–Rapid Research Letters*, 8(3):219–222, 2014.

[29] S. Minoura, T. Maekawa, K. Kodera, A. Nakane, S. Niki and H. Fujiwara. Optical constants of $Cu(In,Ga)Se_2$ for arbitrary Cu and Ga compositions. *Journal of Applied Physics*, 117(19):195703, 2015.

[30] R. Klenk. Characterisation and modelling of chalcopyrite solar cells. *Thin solid films*, 387(1-2):135–140, 2001.

[31] T. Minemoto, T. Matsui, H. Takakura, Y. Hamakawa, T. Negami, Y. Hashimoto, T. Uenoyama and M. Kitagawa. Theoretical analysis of the effect of conduction band offset of window/CIS layers on performance of CIS solar cells using device simulation. *Solar Energy Materials and Solar Cells*, 67(1-4):83–88, 2001.

[32] T. Hara, T. Maekawa, S. Minoura, Y. Sago, S. Niki, and H. Fujiwara. Quantitative Assessment of Optical Gain and Loss in Submicron-Textured $CuIn_{1-x}Ga_xSe_2$ Solar Cells Fabricated by Three-Stage Coevaporation. *Physical Review Applied*, 2(3):034012, 2014.

[33] G. Sozzi, S. Di Napoli, R. Menozzi, F. Werner, S. Siebentritt, P. Jackson and W. Witte. Influence of conduction band offsets at window/buffer and buffer/absorber interfaces on the roll-over of J-V curves of CIGS solar cells. In *Proceedings of the 44th IEEE Photovoltaic Specialists Conference*, page 628, 2017.

[34] T. Eisenbarth, T. Unold, R. Caballero, C. Kaufmann and H.W. Schock. Interpretation of admittance, capacitance-voltage, and current-voltage signatures in $Cu(In,Ga)Se_2$ thin film solar cells. *Journal of Applied Physics*, 107(3):034509, 2010.

[35] M. Topič, F. Smole and J. Furlan. Examination of blocking current-voltage behaviour through defect chalcopyrite layer in $ZnO/CdS/Cu(In,Ga)Se_2/Mo$ solar cell. *Solar energy materials and solar cells*, 49(1-4):311–317, 1997.

[36] J.T. Heath, J.D. Cohen and W.N. Shafarman. Bulk and metastable defects in $CuIn_{1-x}Ga_xSe_2$ thin films using drive-level capacitance profiling. *Journal of Applied Physics*, 95(3):1000–1010, 2004.

[37] A. Niemegeers, M. Burgelman, R. Herberholz, U. Rau, D. Hariskos and H.W. Schock. Model for electronic transport in $Cu(In,Ga)Se_2$ solar cells. *Progress in Photovoltaics: Research and Applications*, 6(6):407–421, 1998.

[38] G. Sozzi, S. Di Napoli, R. Menozzi, T.P. Weiss, S. Buecheler and A.N. Tiwari. Interpretation of admittance signatures in $Cu(In,Ga)Se_2$ solar cells. In *Proceedings of the 45th IEEE Photovoltaic Specialists Conference*, 2018.

[39] G. Sozzi, F. Troni and R. Menozzi. Numerical analysis of the effect of grain size and defects on the performance of CIGS solar cells. *Proc. CS-ManTech*, pages 353–356, 2010.

[40] G. Sozzi, R. Mosca, M. Calicchio, R. Menozzi. Anomalous dark current ideality factor (n>2) in thin-film solar cells: the role of grain-boundary defects. In *Photovoltaic Specialist Conference (PVSC), 2014 IEEE 40th*, pages 1718–1721. IEEE, 2014.

[41] C. Persson and A. Zunger. Anomalous Grain Boundary Physics in Polycrystalline $CuInSe_2$: The Existence of a Hole Barrier. *Physical review letters*, 91(26):266401, 2003.

[42] R. Baier, C. Leendertz, D. Abou-Ras, M. Lux-Steiner, and S. Sadewasser. Properties of electronic potential barriers at grain boundaries in $Cu(In,Ga)Se_2$ thin films. *Solar Energy Materials and Solar Cells*, 130:124–131, 2014.

[43] R. Scheer. Activation energy of heterojunction diode currents in the limit of interface recombination. *Journal of Applied Physics*, 105(10):104505, 2009.

[44] P. Reinhard, B. Bissig, F. Pianezzi, E. Avancini, H. Hagendorfer, D. Keller, P. Fuchs, M. Döbeli, C. Vigo, P. Crivelli and others. Features of KF and NaF postdeposition treatments of $Cu(In,Ga)Se_2$ absorbers for high efficiency thin film solar cells. *Chemistry of Materials*, 27(16):5755–5764, 2015.

[45] C. Platzer-Björkman, T. Törndahl, D. Abou-Ras, J. Malmström, J. Kessler and L. Stolt. Zn (O, S) buffer layers by atomic layer deposition in $Cu(In,Ga)Se_2$ based thin film solar cells: band alignment and sulfur gradient. *Journal of Applied Physics*, 100(4):044506, 2006.

[46] X. Li, A. Kanevce, J.V. Li, I. Repins, B. Egaas and R. Noufi. Impact of $Zn_{1-X}Mn_XO$ on $Cu(In,Ga)Se_2$ thin-film solar cells. In *Photovoltaic Specialists Conference (PVSC), 2009 34th IEEE*, pages 000305–000308. IEEE, 2009.

[47] C. Persson, C. Platzer-Björkman, J. Malmström, T. Törndahl and M. Edoff. Strong valence-band offset bowing of $ZnO_{1-x}S_x$ enhances p-type nitrogen doping of ZnO-like alloys. *Physical review letters*, 97(14):146403, 2006.

[48] N. Naghavi, S. Spiering, M. Powalla, B. Cavana and D. Lincot. High-efficiency copper indium gallium diselenide (CIGS) solar cells with indium sulfide buffer layers deposited by atomic layer chemical vapor deposition (ALCVD). *Progress in Photovoltaics: Research and Applications*, 11(7):437–443, 2003.

[49] P.M.P. Salomé, J. Keller, T. Törndahl, J.P. Teixeira, N. Nicoara, R.R. Andrade, D.G. Stroppa, J.C. González, M. Edoff, J.P. Leitão and others. CdS and $Zn1 - xSn_xO_y$ buffer layers for CIGS solar cells. *Solar Energy Materials and Solar Cells*, 159:272–281, 2017.

[50] N. Naghavi, D. Abou-Ras, N. Allsop, N. Barreau, S. Bücheler, A. Ennaoui, C.-H. Fischer, C. Guillen, D. Hariskos, J. Herrero, R. Klenk, K. Kushiya, D. Lincot, R. Menner, T. Nakada, C. Platzer-Björkman, S. Spiering, A.N. Tiwari, and T. Törndahl. Buffer layers and transparent conducting oxides for chalcopyrite $Cu(In,Ga)(S,Se)_2$ based thin film photovoltaics: present status and current developments. *Progress in Photovoltaics: Research and Applications*, 18(6):411–433. URL: `https://onlinelibrary.wiley.com/doi/abs/10.1002/pip.955`, `arXiv:https://onlinelibrary.wiley.com/doi/pdf/10.1002/pip.955`, `doi:10.1002/pip.955`.

[51] T. Kobayashi, T. Kumazawa, Z.J.L. Kao and T. Nakada. $Cu(In,Ga)Se_2$ thin film solar cells with a combined ALD-Zn(O,S) buffer and MOCVD-ZnO:B window layers. *Solar Energy Materials and Solar Cells*, 119:129–133, 2013.

[52] N. Naghavi, D. Abou-Ras, N. Allsop, N. Barreau, S. Bücheler, A. Ennaoui, C.H. Fischer, C. Guillen, D. Hariskos, J. Herrero and others. Buffer layers and transparent conducting oxides for chalcopyrite $Cu(In,Ga)(S,Se)_2$ based thin film photovoltaics: present status and current developments. *Progress in Photovoltaics: Research and Applications*, 18(6):411–433, 2010.

[53] M. Gloeckler and J.R. Sites. Efficiency limitations for wide-band-gap chalcopyrite solar cells. *Thin Solid Films*, 480:241–245, 2005.

[54] M. Morkel, L. Weinhardt, B. Lohmüller, C. Heske, E. Umbach, W. Riedl, S. Zweigart and F. Karg. Flat conduction-band alignment at the $CdS/CuInSe_2$ thin-film solar-cell heterojunction. *Applied Physics Letters*, 79(27):4482–4484, 2001.

[55] C.P. Muzzillo and T.J. Anderson. Surface and bulk effects of K in $Cu1-xK_xIn1-yGa_ySe_2$ solar cells. *Solar Energy Materials and Solar Cells*, 179:362–371, 2018.

[56] M. Malitckaya, H.P. Komsa, V. Havu, M.J. Puska. Effect of alkali metal atom doping on the $CuInSe_2$-based solar cell absorber. *The Journal of Physical Chemistry C*, 121(29):15516–15528, 2017.

[57] G. Sozzi, S. Di Napoli, R. Menozzi, B. Bissig, S. Buecheler A.N. Tiwari. Impact of front-side point contact/passivation geometry on thin-film solar cell performance. *Solar Energy Materials and Solar Cells*, 165:94–102, 2017.

[58] Z. Wang, P. Han, H. Lu, H. Qian, L. Chen, Q. Meng, N. Tang, F. Gao, Y. Jiang, J. Wu and others. Advanced PERC and PERL production cells with 20.3% record efficiency for standard commercial p-type silicon wafers. *Progress in Photovoltaics: Research and Applications*, 20(3):260–268, 2012.

[59] P. Reinhard, B. Bissig, F. Pianezzi, H. Hagendorfer, G. Sozzi, R. Menozzi, C. Gretener, S. Nishiwaki, S. Buecheler and A.N. Tiwari. Alkali-templated surface nanopatterning of chalcogenide thin films: a novel approach toward solar cells with enhanced efficiency. *Nano letters*, 15(5):3334–3340, 2015.

[60] G. Dingemans, M.M. Mandoc, S. Bordihn, M.C.M. Van De Sanden and W.M.M. Kessels. Effective passivation of Si surfaces by plasma deposited $SiO_x/a-SiN_x:H$ stacks. *Applied Physics Letters*, 98(22):222102, 2011.

[61] G. Sozzi, F. Troni and R. Menozzi. On the combined effects of window/buffer and buffer/absorber conduction-band offsets, buffer thickness and doping on thin-film solar cell performance. *Solar Energy Materials and Solar Cells*, 121:126–136, 2014.

[62] A. Morato, B. Vermang, H. Goverde, E. Cornagliotti, G. Meneghesso, J. John and J. Poortmans. Electrical characterization of ALD $Al_2O_3-HfO_2$ and PECVD Al_2O_3 passivation layers for p-type CZ-Silicon PERC solar cells. In *Photovoltaic*

Specialists Conference (PVSC), 2012 38th IEEE, pages 001077–001082. IEEE, 2012.

[63] D.K. Simon, P.M. Jordan, T. Mikolajick and I. Dirnstorfer. On the control of the fixed charge densities in Al_2O_3-based silicon surface passivation schemes. *ACS applied materials & interfaces*, 7(51):28215–28222, 2015.

[64] R. Kotipalli, B. Vermang, J. Joel, R. Rajkumar, M. Edoff and D. Flandre. Investigating the electronic properties of $Al_2O_3/Cu(In,Ga)Se_2$ interface. *AIP Advances*, 5(10):107101, 2015.

[65] G. Sozzi, S. Di Napoli, M. Carrisi and R. Menozzi. Assessing the impact of rear point-contact/passivation on CIGS cells with different absorber thickness and grading. In *Proceedings of the 45th IEEE Photovoltaic Specialists Conference*, 2018.

[66] B. Vermang, V. Fjällström, X. Gao and M. Edoff. Improved Rear Surface Passivation of $Cu(In,Ga)Se_2$ Solar Cells: A Combination of an Al_2O_3 Rear Surface Passivation Layer and Nanosized Local Rear Point Contacts. *IEEE Journal of Photovoltaics*, 4(1):486–492, 2014.

[67] P.M.P. Salomé, B. Vermang, R. Ribeiro-Andrade, J.P. Teixeira, J.M.V. Cunha, M.J. Mendes, S. Haque, J. Borme, H. Águas, E. Fortunato and others. Passivation of interfaces in thin film solar cells: Understanding the effects of a nanostructured rear point contact layer. *Advanced Materials Interfaces*, 5(2):1701101, 2018.

[68] W.W. Hsu, J.Y. Chen, T.H. Cheng, S.C. Lu, W.S. Ho, Y.Y. Chen, Y.J. Chien and C.W. Liu. Surface passivation of $Cu(In,Ga)Se_2$ using atomic layer deposited Al_2O_3. *Applied Physics Letters*, 100(2):023508, 2012.

[69] M. Schmid. Review on light management by nanostructures in chalcopyrite solar cells. *Semiconductor Science and Technology*, 32(4):043003, 2017.

[70] J. Goffard, A. Cattoni, F. Mollica, M. Jubault, C. Colin, J.F. Guillemoles, D. Lincot, N. Naghavi and S. Collin. Multi-resonant light trapping in ultrathin

CIGS solar cells. In *Photovoltaic Specialists Conference (PVSC), 2016 IEEE 43rd*, pages 1455–1458. IEEE, 2016.

[71] J. Goffard, C. Colin, F. Mollica, A. Cattoni, C. Sauvan, P. Lalanne, J.F. Guillemoles, N. Naghavi and S. Collin. Light trapping in ultrathin CIGS solar cells with nanostructured back mirrors. *IEEE Journal of Photovoltaics*, 7(5):1433–1441, 2017.

[72] R. Kotipalli, O. Poncelet, G. Li, Y. Zeng, L.A. Francis, B. Vermang and D. Flandre. Addressing the impact of rear surface passivation mechanisms on ultra-thin $Cu(In,Ga)Se_2$ solar cell performances using SCAPS 1-D model. *Solar Energy*, 157:603–613, 2017.

[73] O. Poncelet, R. Kotipalli, B. Vermang, A. Macleod, L.A. Francis and D. Flandre. Optimisation of rear reflectance in ultra-thin CIGS solar cells towards > 20% efficiency. *Solar Energy*, 146:443–452, 2017.

[74] N. Naghavi, F. Mollica, J. Goffard, J. Posada, A. Duchatelet, M. Jubault, F. Donsanti, A. Cattoni, S. Collin, P.P. Grand and others. Ultrathin $Cu(In,Ga)Se_2$ based solar cells. *Thin Solid Films*, 633:55–60, 2017.

[75] P. Casper, R. Hünig, G. Gomard, O. Kiowski, C. Reitz, U. Lemmer, M. Powalla and M. Hetterich. Optoelectrical improvement of ultra-thin $Cu(In,Ga)Se_2$ solar cells through microstructured MgF_2 and Al_2O_3 back contact passivation layer. *physica status solidi (RRL)–Rapid Research Letters*, 10(5):376–380, 2016.

[76] Z.J. Li-Kao, N. Naghavi, F. Erfurth, J.F. Guillemoles, I. Gérard,A. Etcheberry, J.L. Pelouard, S. Collin, G. Voorwinden and D. Lincot, Daniel. Towards ultrathin copper indium gallium diselenide solar cells: proof of concept study by chemical etching and gold back contact engineering. *Progress in Photovoltaics: Research and Applications*, 20(5):582–587, 2012.

[77] J. Krc, M. Sever, A. Campa, Z. Lokar, B. Lipovsek and M. Topic. Optical confinement in chalcopyrite based solar cells. *Thin Solid Films*, 633:193–201, 2017.

[78] J.J. Schermer, G.J. Bauhuis, P. Mulder, E.J. Haverkamp, J. Van Deelen, A.T.J. Van Niftrik and P.K. Larsen. Photon confinement in high-efficiency, thin-film III–V solar cells obtained by epitaxial lift-off. *Thin Solid Films*, 511:645–653, 2006.

[79] J. Malmström, S. Schleussner and L. Stolt. Enhanced back reflectance and quantum efficiency in $Cu(In,Ga)Se_2$ thin film solar cells with a ZrN back reflector. *Applied physics letters*, 85(13):2634–2636, 2004.

[80] S. Schleussner, T. Kubart, T. Törndahl and M. Edoff. Reactively sputtered ZrN for application as reflecting back contact in $Cu(In,Ga)Se_2$ solar cells. *Thin Solid Films*, 517(18):5548–5552, 2009.

[81] S. Babar and J.H. Weaver. Optical constants of Cu, Ag, and Au revisited. *Applied Optics*, 54(3):477–481, 2015.

[82] E. Shiles, T. Sasaki, M. Inokuti and D.Y. Smith. Self-consistency and sum-rule tests in the Kramers-Kronig analysis of optical data: applications to aluminum. *Physical Review B*, 22(4):1612, 1980.

[83] E. Valkonen, C.G. Ribbing and J.E. Sundgren. Optical constants of thin TiN films: thickness and preparation effects. *Applied optics*, 25(20):3624–3630, 1986.

[84] H.M. Benia, M. Guemmaz, G. Schmerber, A. Mosser and J.C. Parlebas. Optical properties of non-stoichiometric sputtered zirconium nitride films. *Applied surface science*, 211(1-4):146–155, 2003.

[85] P.J. Rostan, J. Mattheis, G. Bilger, U. Rau and J.H. Werner. Formation of transparent and ohmic $ZnO : Al/MoSe_2$ contacts for bifacial $Cu(In,Ga)Se_2$ solar cells and tandem structures. *Thin Solid Films*, 480:67–70, 2005.

[86] J. Song, S.S. Li, L. Chen, R. Noufi, T.J. Anderson and O.D. Crisalle. Investigation of CdZnS buffer layers on the performance of $CuInGaSe_2$ and CuGaSe2 solar

cells. In *Photovoltaic Energy Conversion, Conference Record of the 2006 IEEE 4th World Conference on*, volume 1, pages 534–537. IEEE, 2006.

[87] R.L. Garris, L.M. Mansfield, B. Egaas and K. Ramanathan. Low-Cd CIGS solar cells made with a hybrid CdS/Zn(O,S) buffer layer. *IEEE Journal of Photovoltaics*, 7(1):281–285, 2017.

[88] J. Chantana, T. Kato, H. Sugimoto and T. Minemoto. Thin-film $Cu(In,Ga)(Se,S)_2$-based solar cell with (Cd,Zn)S buffer layer and $Zn_{1-x}Mg_xO$ window layer. *Progress in Photovoltaics: Research and Applications*, 25(6):431–440, 2017.

[89] J. Sterner, J. Malmström and L. Stolt. Study on ALD $In_2S_3/Cu(In,Ga)Se_2$ interface formation. *Progress in Photovoltaics: Research and Applications*, 13(3):179–193, 2005.